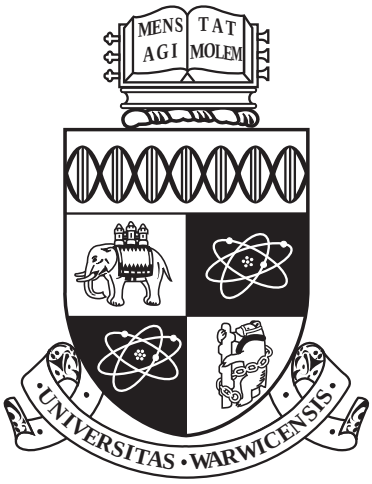

Surfactant entrapment in the wake behind an oil droplet rising in an aqueous medium

by

Andrew C. Bishop

Thesis

Submitted to the University of Warwick

for the degree of

Doctor of Philosophy

School of Engineering

....

THE UNIVERSITY OF
WARWICK

Contents

List of Tables

List of Figures

Acknowledgments

This project would not have been possible without the help, support, and guidance of many people. Firstly I have to thank my supervisors, Petr Denissenko and Peter Thomas, who guided me through this project. Without their support and occasional foot up the backside this project would not have been successful.

My thanks go to the EPSRC, without whose funding this project would not have been possible. I would also like to thank all of the technicians in the School of Engineering, specifically Huw and Bill amongst others, who always managed to find time to help me out despite their busy workloads.

I would like to thank my parents who, while not necessarily understanding why I chose to do a PhD, are a constant source of support and encouragement in everything that I do. I could not ask for more supportive parents.

I couldn't have achieved this project without the support of Liz. Over the past few months she has put up with my eccentricities, taken care of me at home, and has proofread countless hundreds of pages.

Lastly I would like to thank the fluids research group for the memorable antics, especially on our annual 'hiking' trip, and all of the friends I have made over my time at university for all of the great times we have had that have seen me through to completion.

Declarations

This thesis is submitted to the University of Warwick in support of my application for the degree of Doctor of Philosophy. It has been composed by myself and has not been submitted in any previous application for any degree.

The work presented (including data generated and data analysis) was carried out by the author.

Parts of this thesis have been published by the author:

A.C. Bishop, P.J. Thomas, and P. Denissenko. Surfactant concentration and its effect on the flow field inside an oil droplet rising in an aqueous medium: LIF and PIV measurements. In P. Vorobieff, C.A. Brebbia, and J.L. Munoz-Cobo, editors, *Computational Methods in Multiphase Flow VIII,* pages 463. WIT Press, Southampton, 1st edition, 2015.

Abstract

This project uses experimental techniques to explore the effects of surface active agent (surfactant) adsorption on a droplet of oil suspended in a flow. The fluorescent surfactant Rhodamine-6G was used to enable the use of optical techniques to visualise the build-up of surfactant at the rear of the droplet and its effects on the internal circulation within the droplet. This was done to enable an exploration of how surfactant accumulates behind a droplet with the aim of predicting the behaviour based on the internal circulation for non-fluorescent surfactants.

An experiment was designed along with calibration procedures in order to utilise the non-intrusive measurement techniques laser-induced fluorescence and particle image velocimetry to measure the volume of surfactant held behind the droplet, the angle of the visible cap caused by the build-up of Rhodamine-6G, and the cap angle of the stagnant region obtained by measuring the velocity of the circulation within the droplet.

Laser-induced fluorescence (LIF) was used to visualise the development of a surfactant-rich cap that formed at the rear of the oil droplet as it rose through an aqueous solution, with different bulk concentrations of surfactant. The aqueous solution soluble surfactant, adsorbed to the forwards facing part of the droplet, was transported around to the rear where it accumulated in a surfactant cap before being swept back into the flow behind the droplet. The fluorescent properties of Rhodamine-6G were utilised to measure the size of the visible surfactant cap angle and the volume of surfactant stored within the cap. The results showed that increased concentrations of surfactant caused a larger volume of surfactant to be held behind the droplet with larger droplets resulting in smaller surfactant cap angles.

Particle image velocimetry (PIV) was used to explore the effects of surfactant at the interface on the internal circulation within the droplet. As surfactant accumulated an area of very low velocity at the rear of the droplet appeared. This was quantified by measuring the tangential velocity around the droplet with the area of low velocity signifying the presence of a stagnant cap. Measuring the internal velocity around the droplet close to the interface showed that the stagnant cap angle had large growth over the initial region of the tank, with larger droplets resulting in smaller surfactant cap angles.

The visible cap angle measured by LIF was related to the stagnant cap angle measured by PIV to compare how the results for each technique developed over the height of the tank. The angles for both techniques exhibited the same trends as the droplet height increased, although they showed different magnitudes revealing that the experimental procedure could be improved in the future to obtain better agreement.

Chapter 1

Introduction

Surface active agents (surfactants) have been around for many years and are used in a wide range of industries, from the oil industry through to the food and pharmaceutical industries (Porter [1991]). Surfactants have the unique property of being both hydrophilic and hydrophobic and so are attracted to interfaces. Surfactant molecules adhere to the interface by the process of adsorption. When situated at an interface of a multiphase system, surfactant molecules lower the interfacial tension between two phases. This gives surfactants the ability to stabilise emulsions, to apply chemical treatments to interfaces, or to act as a detergent, amongst many other uses.

When a droplet containing surfactant is subjected to a flow, it is well known that the flow sweeps the surfactant around to the rear of the droplet (Eastoe and Dalton [2000], Wegener and Paschedag [2012]). This creates an interfacial gradient around the droplet. Marangoni forces operate along the interfacial gradient, opposing the transportation of surfactant to the rear of the droplet. This reduces the terminal velocity of the droplet in the flow as well as creating a rigid cap of surfactant molecules at the rear of the droplet (Cuenot et al. [1997]). The formation of this stagnant surfactant cap at the rear of the droplet impedes any internal circulation that the droplet may possess (Chang and Chung [1987]).

The majority of surfactants do not possess optical properties, such as fluorescence. This prevents any direct measurements of the quantity of surfactant held at the interface of the droplet. Previous experimental work from the literature rely on measuring the velocity of the droplet in order to link the drag coefficient of the droplet to the size of the immobile region caused by the surfactant cap at the rear of the droplet (Palaparthi et al. [2006]). The optical properties of a fluorescent surfactant, such as Rhodamine-6G, could be utilised to directly visualise the interface

of a droplet in a flow to determine the concentration profile of surfactant around the interface. Existing adsorption isotherms as well as existing theoretical models rely on the droplet having a steady-state, where the adsorption rate is in equilibrium with the desorption rate. Very little work has been done looking into how a surfactant cap at the rear of the droplet develops over time from the creation of the droplet up until a steady state has been achieved.

The internal circulation within droplets has been visualised (Horton et al. [1965]). In this visualisation the internal eddies are observed to shrink and shift position towards the front of the droplet with an increase in the size of the surfactant cap at the rear of the droplet. Theoretical work was attempted to model this shift of the eddies centre point (Harper [1982]) based on the drag coefficient of a droplet which showed very little agreement with the experimental data. Therefore an experiment that can link the size of the surfactant cap at the rear of the droplet to the size of the internal eddies would be beneficial. Using an optical non-intrusive technique to measure the internal circulation within a droplet should make it possible to develop the link with the size of the surfactant cap, with the ultimate aim of being able to deduce the size of the surfactant cap for surfactants with no optical properties based just on the patterns of internal circulation within the droplet.

Rhodamine-6G is a chemical that is often used as a fluorescent dye in experiments (Kuhn and Jensen [2012], Hamdullahpur et al. [1987], Yang et al. [2015], André and Bardet [2015]) to allow the use of lasers to visualise flow patterns and concentration gradients. However Rhodamine-6G has surface active properties (Ren et al. [2014]) and adsorbs to an interface (Liu and Zhang [2007]), so can be classified as a surfactant. Due to the commonness of using Rhodamine-6G as a laser dye rather than a surfactant, there has been very little research into the relevant surface active properties and so values for these properties are scarce.

This project will primarily explore the development of a surfactant rich cap behind a droplet using laser-induced fluorescence (LIF). This experiment will utilise the natural fluorescence properties of Rhodamine-6G to measure the visible angle of the surfactant cap that forms at the rear of the droplet, allowing an improvement of the understanding behind the effect that Rhodamine-6G has on the interface of a multiphase experiment.

As the majority of surfactants do not have fluorescent properties it would be desirable to measure the angle of the surfactant cap from surfactant adsorbed to the interface by measuring a parameter not reliant on fluorescence. The internal circulation within the droplet will be measured using particle image velocimetry (PIV) as a second optical non-intrusive technique. The decrease in the size of the

eddies within the droplet will be measured in an attempt to form a link between the quantity of surfactant adsorbed to the interface and the size of the internal eddies.

The internal circulation of a droplet can be obtained by seeding the fluid of the droplet with tracer particles. The displacement of these tracer particles can be measured using particle image velocimetry to generate instantaneous vector fields. Observations of the vector fields would allow the development of the stagnant region at the rear of the droplet caused by the immobility of the interface due to the formation of a surfactant cap at the rear of the droplet to be explored.

1.1 Aims and objectives

The aim of this project is to investigate the process of adsorption of surfactant to the interface of a droplet of oil in a flow and its effects on the internal circulation within the droplet. This aim is split into individual objectives. These are to:

- Develop an understanding of the fluid dynamics of an oil droplet in a flow, the adsorption mechanisms of an oil droplet rising through a surfactant-rich aqueous solution, and the properties of surfactants. These areas were identified as key principles related to the project.
- Design an experiment to use optical techniques to non-intrusively explore the adsorption of surfactant to a droplet interface. This experiment needs to be adaptable in order to explore the external interface of the droplet using the fluorescence of the surfactant Rhodamine-6G, as well as the internal circulation within the droplet. The experiment needs to optimize optical techniques so as not to interfere with the adsorption dynamics at the interface. Two different techniques are identified to perform the different tasks of observing the external interface and the internal circulation.
- Develop a calibration protocol to reduce experimental irregularities and link qualitative pixel intensities to quantitative concentration values.
- Process the obtained images. Both of the experimental techniques will provide raw data in different forms. The experiments observing the quantity of surfactant at the interface will gather data by measuring the fluorescence at the interface, whereas the internal circulation measurements will consist of instantaneous vector fields. Processing methods will need to be developed for both of these data sets in order to extract information on the surfactant cap angle and volume of surfactant held behind the droplet, as well as the size of the stagnant region within the droplet.

- Explore the effects of changing the surfactant concentration at different positions in the tank for droplets with different radii. The variables to be explored will be the size of the visual surfactant cap observed by laser-induced fluorescence along with the volume of surfactant held behind the droplet, and the size of the stagnant cap observed using particle image velocimetry to measure the internal flow within the droplet.

- Relate the size of the surfactant cap obtained by observing fluorescent measurements in LIF to the size of the stagnant cap measured using PIV. Achieving this link would dispose of the requirement for a fluorescent surfactant in future research.

Chapter 2 investigates the background relating to the proposed experiments along with an exploration of previous research that has been performed in this area. This gave an idea of the range of mechanisms working together in this research as well as ensuring that the experiments to be performed were original research and not duplicating any known work.

Chapter 3 presents the experiment designed to investigate the adsorption of surfactant to a droplet in a flow. The experiment utilised the fluorescent properties of Rhodamine-6G to visualise surfactant build-up around the droplet interface. A second independent experiment was performed using the same controllable parameters in which the oil droplet was seeded with tracer particles. The aim of this experiment was to track the internal circulation within the oil droplet. As the droplet rises these internal eddies should shrink indicating the presence of a developing stagnant cap related to the surfactant build-up around the droplet. The parameters that were controlled and changed in the experiment are discussed along with how the setup changed between the two experiments.

Chapter 4 discusses calibration techniques developed to reduce experimental irregularities and to allow the extraction of quantitative results from the data.

Chapter 5 presents an example of the raw data gathered from both the LIF and PIV experiments, before discussing the processing methods applied to each set of data in order to produce a parameter that could be compared between the different measurement techniques.

The LIF results are analysed in Chapter 6 and the PIV results are analysed in Chapter 7. An in-depth discussion of the results obtained for each set of experiments occurs before an exploration of the link between the two different experimental techniques is performed in Chapter 8.

Finally Chapter 9 provides an overview of the work along with a discussion of lessons learnt from these experiments with proposals on how the experiment could be improved in the future and ideas for the direction future research should take.

Chapter 2

Literature review

This project draws together aspects from fluid dynamics, mass transfer, and surface active chemistry. This chapter explores the background relevant to this work to link together these different aspects as well as reviewing existing related work. The project was split into its basic components to understand the fundamental principles at work. These are then linked together to gain a more complete understanding of the mechanisms at work in the proposed experiments.

The first component to be considered was that of an oil droplet rising through a clean aqueous solution (a solution without contamination), to give a fundamental view of the fluid dynamics involved. From here the chemistry and operation of surfactants are described with an explanation of different types of surfactant and the effects they have on interfacial behaviour. Surfactant adheres to the oil-water interface by the process of adsorption. Different adsorption mechanisms and effects are described to enable an investigation into the available literature on how surfactants interact with a rising droplet of oil, and how this affects the behaviour of the droplet and the droplet interface. The final section of this chapter describes the adsorption properties of the surfactant proposed for this research, Rhodamine-6G, in order to validate the use of Rhodamine-6G as a surfactant and to attempt to extract usable adsorption data relevant to the proposed experiments.

2.1 Droplet Behaviour

Understanding the behaviour of a droplet of oil rising through a pure aqueous solution was a fundamental component of this research. The topics that needed to be investigated were the flow regime of the system - whether turbulent or laminar flow existed, whether the flow would detach from the droplet, whether there would be

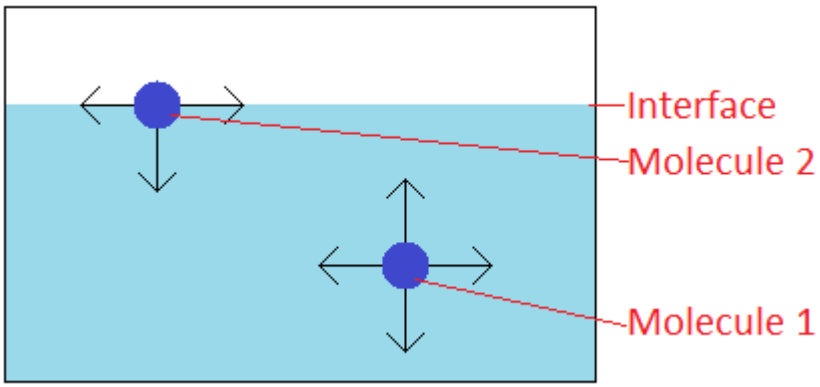

Figure 2.1: Examples of forces acting on molecules within the bulk of a fluid (Molecule 1) and at the interface (Molecule 2).

any internal circulation within the droplet, and whether this potential internal flow would affect the rising speed of the droplet.

This section describes the relationship between two phases that results in droplets maintaining a spherical shape, the effects of the Reynolds number on the flow regime of the system along with a prediction of the flow regime for the proposed experiments, and the differences between a droplet rising in a flow containing no internal circulation against a droplet with complete internal circulation.

2.1.1 Droplet shape

The force responsible for the shape of the interface of an immiscible volume of fluid with a second phase is the interfacial tension. Interfacial tension is a measurement of the force per unit length acting on a fluid. For a fluid in equilibrium each of the constituent molecules of the fluid interact with each other. Deep within the bulk of the fluid (Molecule 1 in Figure 2.1) an equal force is exerted on the molecule in all directions by the surrounding interacting molecules so all of the forces are balanced. However a molecule at the interface (Molecule 2 in Figure 2.1) is not completely surrounded by identical molecules so experiences an unbalanced force. This pulls these molecules back towards the bulk of the fluid, causing the interface to form a shape with the smallest interfacial area. This is the driving force behind the spherical shape of oil droplets suspended in an aqueous solution. The interfacial tension is affected by the temperature, with increasing temperatures leading to a decrease in interfacial tension (Streeter [1961]).

When a flow is introduced past a spherical droplet the shape can be dis-

torted. This distortion is a function of the ratio between the viscous stresses and the interfacial stresses (Guido et al. [1999]). This ratio is the capillary number, Ca, (Awad [2012]) given by

$$Ca = \frac{\mu U}{\sigma}, \tag{2.1}$$

where μ is the dynamic viscosity, U is the flow speed in relation to the droplet, and σ is the interfacial tension. The lower this capillary number, the less deformation there would be.

2.1.2 Flow regime

To understand the flow regime of the continuous fluid, the droplet will be assumed to be a non-deformable sphere with an immobile interface within a flow. This neglects any potential internal circulation within the droplet so that the flow of the continuous phase can be assessed. It is important to understand the flow regime around the droplet to know whether the flow separates from the droplet, as well as understanding the behaviour of the droplet wake. The flow regime depends on the Reynolds number, with low Reynolds numbers giving laminar flow and high Reynolds numbers giving turbulent flow as determined by Blevins [1977] for the flow around a two-dimensional cylinder shown in Figure 2.2. The Reynolds number, Re, is a dimensionless quantity given by the ratio between inertial and viscous forces given by

$$Re = \frac{\rho U L}{\mu}, \tag{2.2}$$

where ρ is the density of the continuous phase, U is a characteristic velocity (in this case the velocity of the flow in relation to the droplet), L is a characteristic length (in this case the diameter of the droplet), and μ is the dynamic viscosity of the continuous phase.

For the experiments proposed in this work the continuous phase fluid had a high viscosity with a droplet diameter in the region of 5mm and a rising speed of approximately 5-10mm/s. This gave a Reynolds number $Re \simeq 0.1$. This falls within the laminar flow regime, with no separation between the fluid and the droplet (Zdravkovich [1997]).

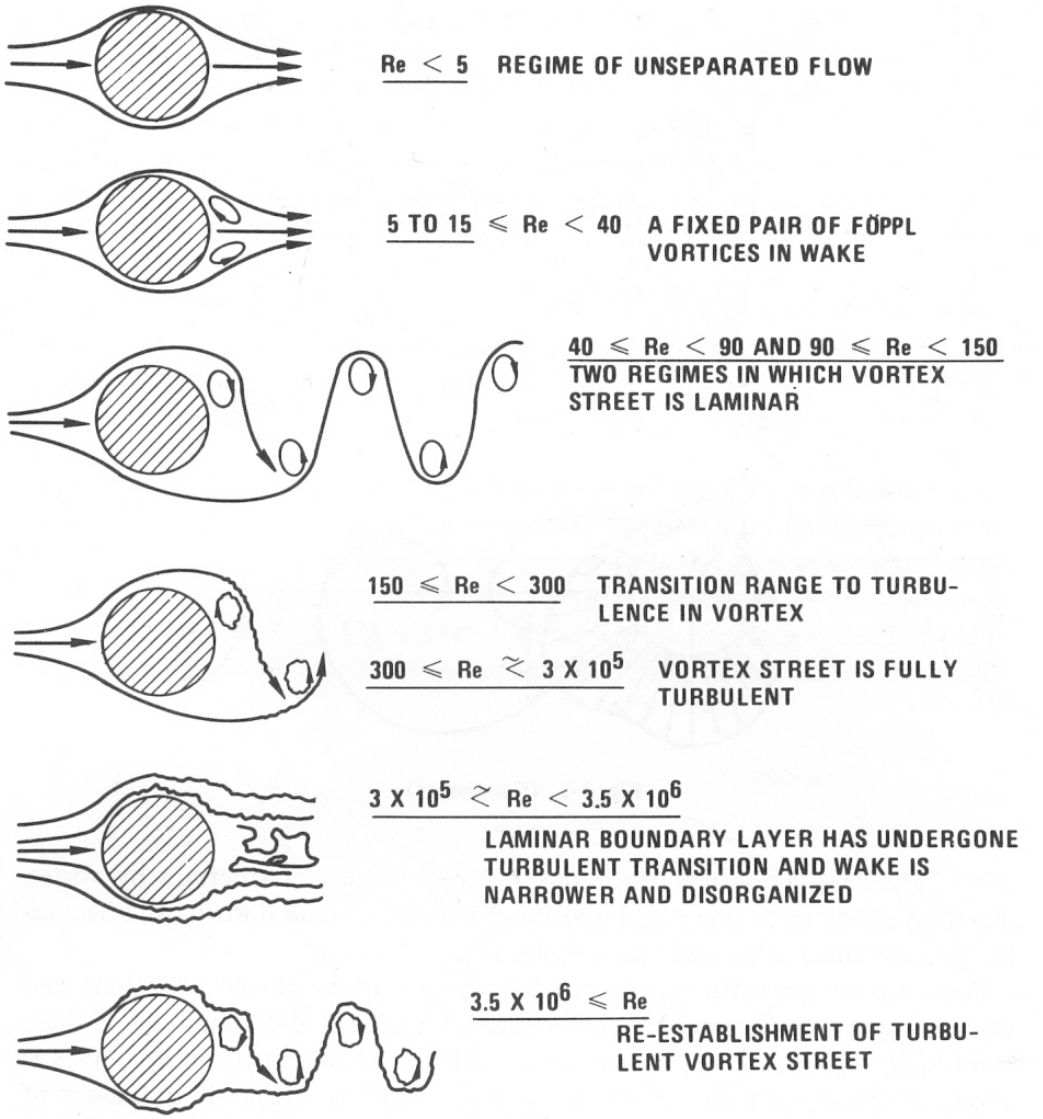

Figure 2.2: Potential flow regimes with associated Reynolds numbers for an infinitely long cylinder in a flow (Blevins [1977]).

2.1.3 Droplet with rigid interface in a flow

There are three different regimes with regard to the effects of surfactants adsorbing to the interface that can influence the behaviour of a droplet in a flow (Palaparthi et al. [2006]). The first regime is where the droplet interface is completely covered in surfactant. This completely immobilises any potential movement of the interface so that there is no internal circulation within the droplet, so this regime can be modelled as a solid spherical object within a flow. The second regime is where there are no contaminants at the interface so the interface is mobile (Palaparthi et al. [2006]). The third regime is a combination of these two scenarios such that the interface is partial mobile, potential affecting any internal flow that the droplet might possess (Palaparthi et al. [2006]).

The following sections will initially disregard surfactants by firstly considering the most simple case of a solid spherical object subjected to a flow. This will be built upon by removing the rigidity conditions on the interface so that the droplet interface has complete mobility and the flow within the droplet can be considered. The final regime of a partially immobile droplet interface will be considered later in the chapter after the mechanisms of surfactants have been introduced and discussed.

Stokes' law for the drag on a solid sphere rising in a solution (Tritton [1988]) can be applied for a flow past a rigid spherical droplet with a very low Reynolds number. This drag force, F_D, is given by (Crowe et al. [2012])

$$F_D = 6\pi\mu r U, \tag{2.3}$$

in which μ is the dynamic viscosity of the continuous phase, r is the radius of the droplet, and U is the velocity of the flow past the droplet.

The droplet reaches a terminal velocity when the drag forces balance the gravitational forces. In the proposed experiments the density of the dispersed oil phase is less than the density of the aqueous continuous phase and so the droplet rises through the continuous phase with a buoyancy force opposed by the drag force as shown in Figure 2.3.

The buoyancy force, F_B, is a function of the density difference between the droplet and the fluid of the continuous phase and is given by (Lamb [1932])

$$F_B = (\rho_c - \rho_d) g \frac{4}{3}\pi r^3, \tag{2.4}$$

where ρ_c is the density of the continuous phase, ρ_d is the density of the droplet, g is the acceleration due to gravity, and r is the droplet radius.

The terminal rising velocity, U, of a rigid spherical droplet rising through a

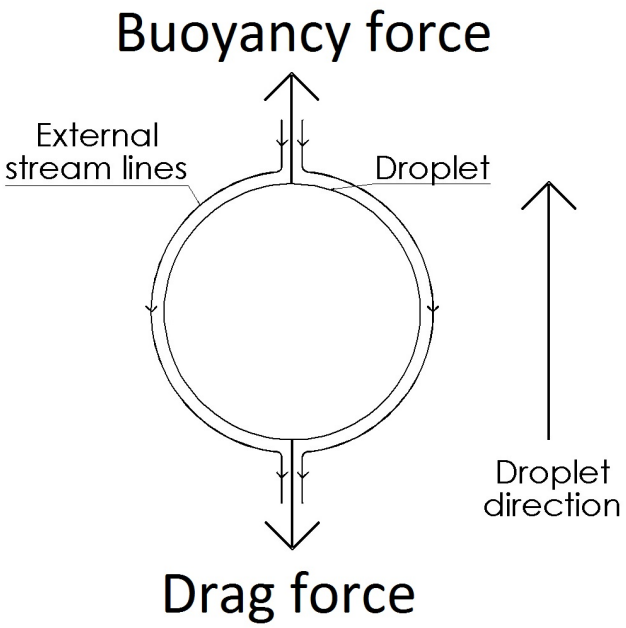

Figure 2.3: Forces acting on a rigid spherical droplet in a flow.

solution with a very low Reynolds number is achieved by equating this buoyancy force to the drag force (Lamb [1932], Levich [1962]) giving

$$U = \frac{2\Delta\rho}{9\mu} g r^2, \tag{2.5}$$

where $\Delta\rho$ is the density difference between the two phases, μ is the dynamic viscosity, g is the acceleration due to gravity, and r is the droplet radius.

2.1.4 Droplet with mobile interface in a flow

The assumption that surfactant completely covers the interface of a droplet in a flow, rendering the interface immobile, is not realistic. The assumption that the droplet would rise like a rigid sphere can be dropped to develop an understanding of a droplet with a mobile interface. This section will develop an understanding of a droplet in a flow containing no surfactant so that the interface of the droplet has complete mobility and recirculation eddies form within the droplet. These eddies are formed by the continuous phase accelerating the interface of the droplet towards the rear of the droplet. The droplet fluid at the interface meets at the rear of the droplet and recirculates back up the centre, as shown in Figure 2.4. This creates a velocity gradient across each hemisphere of the droplet resulting in the formation of

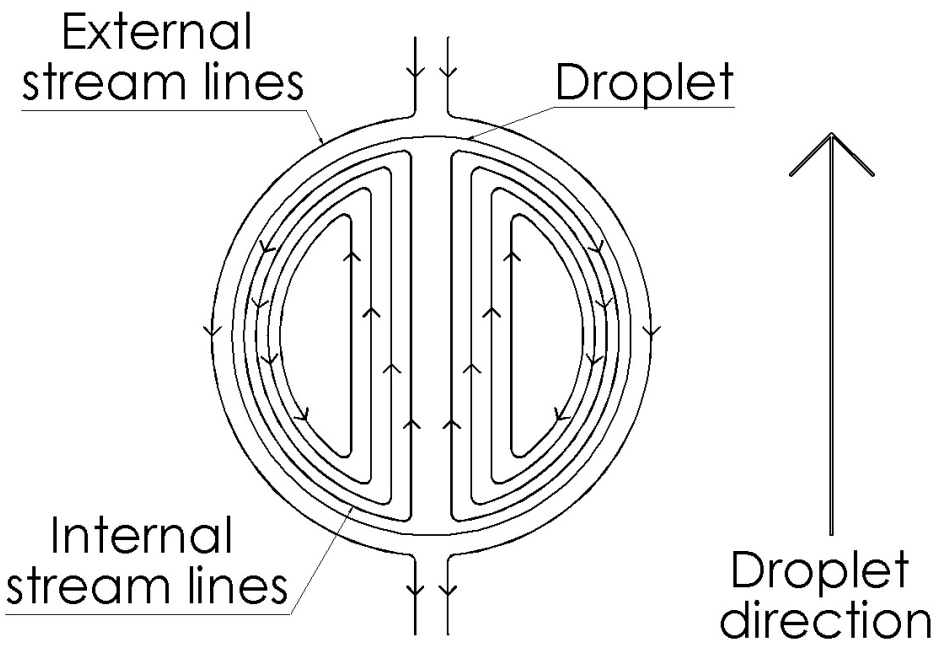

Figure 2.4: Droplet with a completely mobile interface in a flow. Reproduced from McDonald [1954].

eddies.

This internal circulation can propel the droplet through the continuous phase allowing the terminal velocity of the droplet to reach a velocity up to one and a half times that of a droplet with a rigid interface (Griffith [1962]). The terminal velocity, U, of a droplet with a mobile interface is a function of the viscosities of both phases and is given by (Bond [1927])

$$U = \frac{2\Delta\rho}{9\mu_c} g r^2 \left(\frac{3\mu_d + 3\mu_c}{3\mu_d + 2\mu_c}\right), \tag{2.6}$$

where $\Delta\rho$ is the density difference between the phases, g is the gravitational acceleration, r is the droplet radius, μ_d is the dynamic viscosity of the dispersed phase (the droplet), and μ_c is the dynamic viscosity of the continuous phase. It is possible for a spherical droplet rising in a flow in which no contaminants are present (so the interface is completely mobile) to rise with the same terminal velocity as a spherical rigid particle given by Equation 2.5 (Griffith [1962]).

Harper [1972] gives an in-depth review of the established theory of the motion of bubbles and droplets through liquids. The author describes the mechanisms behind both bubbles and droplets at low and high Reynolds numbers for the scenario in which the interfacial tension is constant — there is no adsorption of surfactant.

This section describes the findings of the author for the droplets with a low Reynolds number as proposed for the experiments in this work.

The experiments proposed for this research consist of an immiscible droplet rising through a fluid. Each of the fluid phases in this multiphase system possess a different density, viscosity, and surface tension. These parameters have been combined in past work (Harper [1972], Hu and Kinter [1955]) to produce a non-dimensionalised parameter given by the Morton number (Bhaga and Weber [1981]), M, that can be used to characterise the physical properties of the system. The higher the value of M, the more prone the droplet is to deformation. M_c is the non-dimensional parameter for the continuous phase given by

$$M_c = \frac{g\mu_c^4 \Delta\rho}{\rho_c^2 \sigma^3}, \tag{2.7}$$

where g is the acceleration due to gravity, μ_c is the dynamic viscosity of the continuous phase, ρ_c is the density of the continuous phase with $\Delta\rho$ the difference in density between the two phases, and σ is the interfacial tension between the two phases.

The introduction of a flow past the droplet introduces a flow velocity parameter into the system. This can be combined with the physical parameters of the fluids to produce further non-dimensionalised parameters that are commonly used to characterise the system. These were identified as the Reynolds number, drag coefficient, and Weber number. The drag coefficient, C_D, is used to calculate the drag forces exerted on the droplet, with a higher drag coefficient leading to a larger drag force and so a lower terminal velocity. The final non-dimensionalised parameter is the Weber number, We, and is a measure of the inertial forces in the system to the interfacial forces (Hewitt et al. [1997]). It is used to characterise the distortion of the droplet due to the flow field, with greater values leading to a higher level of distortion. These parameters are given by

$$C_{Dc} = \frac{8gr\Delta\rho}{3\rho_c U^2}, \tag{2.8}$$

$$We_c = \frac{2\rho_c U^2 r}{\sigma}, \tag{2.9}$$

where U is the velocity of the droplet in relation to the flow, r is the droplet radius, ρ is the density, μ is the dynamic viscosity, g is the gravitational acceleration, and σ is the interfacial tension. The subscript relates to physical properties associated with the fluids, with the continuous phase denoted with c and the physical properties

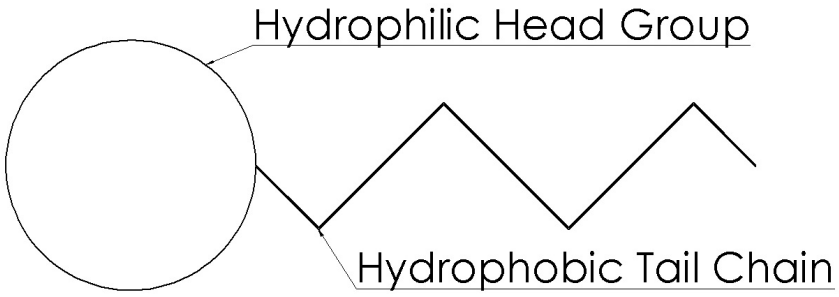

Figure 2.5: Common representation of a surfactant molecule.

of the dispersed phase denoted with d. The subscripts relating to the continuous phase and the dispersed phase in Equations 2.7 to 2.9 can be interchanged to find the related non-dimensionalised parameters of the dispersed phase. However the parameters relating to the dispersed phase are not useful and are rarely used (Harper [1972]).

2.2 Surface active agents (surfactants)

Surfactants are molecules that interact with an interface lowering the interfacial tension. The molecules are amphiphilic in nature, consisting of two segments so are attracted to oil-water interfaces (Atkins and de Paula [2009]). The two segments of a surfactant molecule are the hydrophilic head - a segment that is attracted to the water phase, and a hydrophobic tail - a segment that is soluble in an oil phase (Barnes and Gentle [2005]). This is shown in the representation of a surfactant molecule in Figure 2.5.

The hydrophilic head segment is the largest physical part of the molecule (Porter [1991]) and gives the surfactant the potential to carry a charge. Surfactants are categorised on the charge of the polar hydrophilic head. There are four different categories (Holmberg et al. [2003]):

- anionic - in which the hydrophilic head segment is polar carrying a negative charge,
- cationic - where the hydrophilic head segment is again polar, carrying a positive charge,
- non-ionic - where the hydrophilic head segment of the molecule is neutral as it carries no charge,

- zwitterionic - where the hydrophilic head group carries dual polarity, having both positive and negative charge.

Surfactants have different uses based on the polarity of the polar head segment. Anionic surfactants are the most commonly available surfactants and are used in most detergents. Cationic surfactants bond well with surfaces that carry a negative charge so are often used to chemically treat materials as well as being used as emulsifiers. Non-ionic surfactants are most commonly used as emulsifiers. Zwitterionic surfactants are the least common as they are expensive to manufacture. They are dermatologically 'friendly' making them commonly used in the pharmaceutical industry (Morrison and Ross [2002]).

The hydrophobic segment of the molecule is most commonly constructed from hydrocarbon chains. These hydrocarbons are soluble in the oil phase of a multiphase system and non-soluble in the aqueous phase. The length of the hydrocarbon chain dictates how well the molecule bonds with the oil phase (Witten and Pincus [2010]). The longer the chain the better the interaction.

Figure 2.5 demonstrates the simplest form of a surfactant molecule. Surfactants can carry a far more complex structure such as the hydrophilic head segment possessing multiple hydrophobic tails, or a single string of hydrocarbons having a hydrophilic head at each end of the string (Farn [2006]).

2.2.1 Surfactant strength

For a multiphase system containing an oil phase and a water phase, the strength of a surfactant can be calculated using the hydrophilic-lipophilic balance (HLB) system. The HLB value is calculated in different ways based on the molecular structure and mass of the molecule (Myers [1988]). The HLB value can range between 1 and 20. The higher the HLB value, the stronger the surfactant interacts with the aqueous phase. Surfactants with a HLB value between 3 and 6 are dominated by the hydrophobic segment of the molecule so are soluble within the oil phase and are used to create water-in-oil emulsions. Surfactants with a HLB value between 7 and 9 are dispersible within water and are used as wetting agents. A HLB value between 8 and 18 means that the surfactant is soluble within the aqueous phase and are used to create oil-in-water emulsions (Griffin [1949]).

In the proposed experiments the surfactant to be used, Rhodamine-6G, is soluble in water. This means that the hydrophilic head is the dominating influence of the molecule. While the hydrophobic tail segment of the surfactant is soluble within an oil phase, the surfactant will disperse throughout the aqueous phase. The

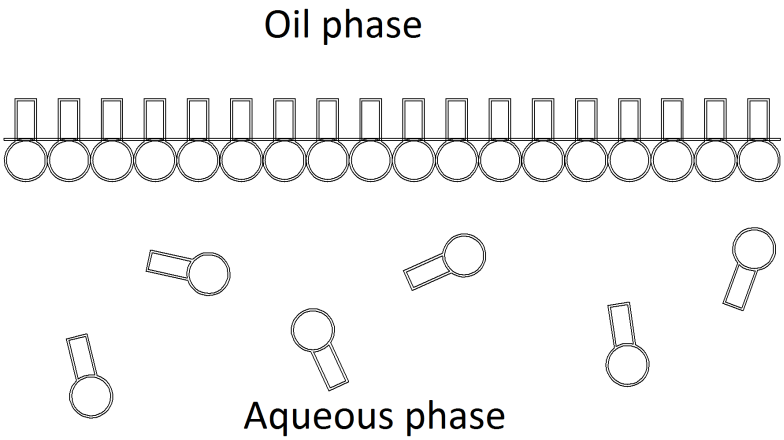

Figure 2.6: Example of surfactant forming a monolayer at the oil-aqueous interface of a multiphase system.

equilibrium positioning for a surfactant molecule is at an interface. The surfactant molecules adsorb to the interface until a monolayer is formed. While excess surfactant can be dispersed in the aqueous phase, no surfactant molecules cross the interface to disperse entirely within the oil phase. The formation of a monolayer is demonstrated in Figure 2.6.

So far the discussed behaviour of surfactants has been relevant to low concentrations of surfactant mixed into a multiphase system. There is a critical concentration associated with surfactants known as the critical micelle concentration (CMC) above which the surfactant molecules interact with each other. As the concentration of surfactant increases towards the CMC, the interfacial tension of the fluid will decrease drastically (Farn [2006]). Above the CMC there is very little change in the interfacial tension. This is due to the excess surfactant molecules clumping together to form aggregates, called micelles, in which the hydrophobic segments bond together within the centre with the hydrophilic segments forming a solid layer around the outside and so shielding the hydrophobic tails from the aqueous solution. These micelles form a stable structure and so have a very long break-up time scale. This means they do not have a large influence on the behaviour of the interface.

The most common form of aggregation of surfactant molecules is shown in Figure 2.7 in which a spherical micelle is formed. Stronger concentrations can lead to larger shapes being formed, including cylindrical shapes, and planes of interlinked surfactant molecules (Morrison and Ross [2002]).

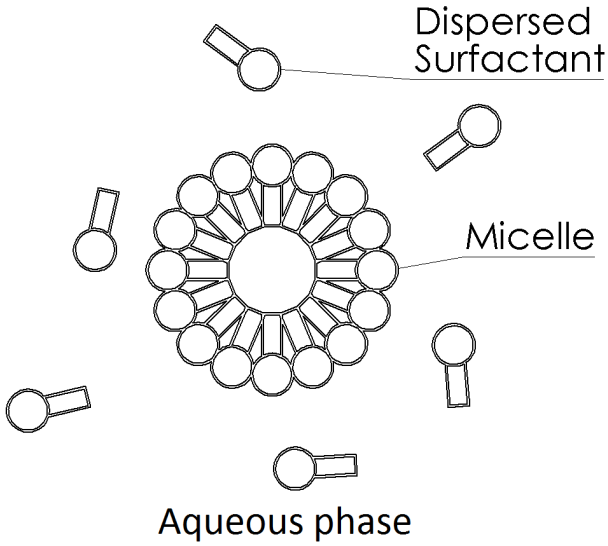

Figure 2.7: Example of excess surfactant molecules in the aqueous phase clumping together to form a micelle.

2.2.2 Stationary droplet with surfactant

If a neutrally buoyant droplet of oil is placed within an aqueous solution containing surfactant, the surfactant dispersed throughout the aqueous phase diffuses through the aqueous phase to adsorb at the interface of the droplet, as shown in Figure 2.8.

Each surfactant molecule occupies an area of the interface. When a sufficient volume of surfactant molecules has been adsorbed so that a monolayer of surfactant molecules has formed around the interface, there is no more physical space on the interface for surfactant molecules to adsorb to, and so an equilibrium is reached.

As surfactants lower the interfacial tension (Defay et al. [1966]), less energy is needed to expand the interface. As the interface expands, the surfactant molecules are diluted and so the interfacial tension begins to rise. An equilibrium point is reached where the size of the interface is balanced by the interfacial tension caused by the surfactant.

Decreasing the interfacial tension around the droplet increases the capillary and Weber numbers. This makes the droplet more prone to deformation in a flow.

2.2.3 Droplet with surfactant in a flow

A flow around a droplet containing a monolayer of surfactant at the interface causes the surfactant to be swept around to the rear of the droplet (Lotfi et al. [2014]) as

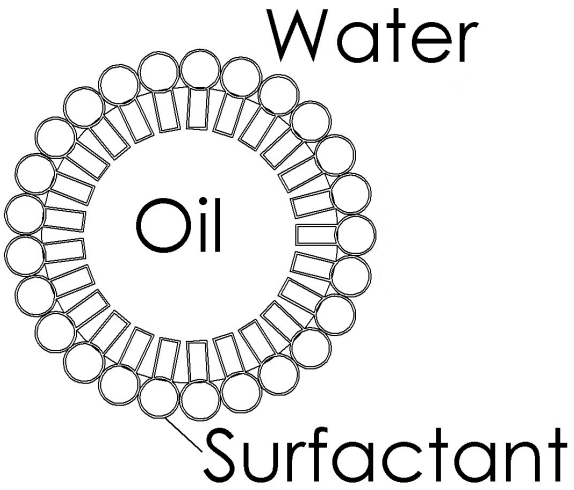

Figure 2.8: Droplet in equilibrium encased by a monolayer of surfactant.

shown in Figure 2.9. The front of the droplet becomes free of surfactant leaving the front of the droplet with normal interfacial tension whereas the rear of the droplet becomes surfactant-rich so the interfacial tension is severely reduced. This creates a gradient in the interfacial tension between the front and rear of the droplet. This exerts an opposing force to the direction of travel of the droplet caused by the surfactant trying to transport around the droplet by diffusion to equalise the surface tension gradient. An equilibrium state is reached when the diffusive force of the surfactant around the droplet interface is matched by the opposing force of the flow sweeping the surfactant around to the droplet base. The force of the attraction of surfactant along the interfacial tension gradient is known as the Marangoni force (Agble and Mendes-Tatsis [2000]). The accumulation of surfactant molecules at the rear of the droplet creates a surfactant cap in which the mobility of the interface is reduced. This increases the drag coefficient of the droplet lowering the terminal velocity in relation to a droplet with completely uninhibited internal circulation.

Due to the decrease in mobility of the interface caused by this rigid cap of surfactant at the rear of the droplet, the internal circulation within the droplet is disrupted. Horton et al. [1965] performed experiments to visualise the internal circulation of a fluid flowing upwards past a droplet at a low Reynolds number. It was found that at initiation the centres of the recirculating eddies were positioned halfway down the droplet. However as 'impurities' accumulated at the interface the circulatory patterns changed and the internal velocity slowed. The centre points of the internal eddies were shifted towards the front of the droplet by an increasing displacement with increasing exposure for impurities to accumulate at the interface.

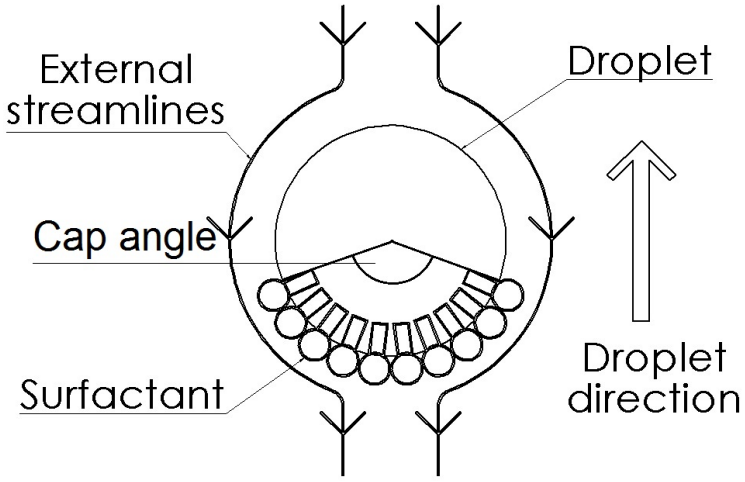

Figure 2.9: Droplet with surfactant at the interface within a flow. Reproduced from Lotfi et al. [2014].

An important finding for the proposed research was that as the circulation zones shrink and move towards the front of the droplet, the streamlines flowing past the rear of the droplet detach from the interface. This affects the surface area of the droplet available for surfactant to adsorb to.

Harper [1982] proposed a solution for the shift of the centre point location for the internal vortices within a droplet in the presence of a surfactant cap:

$$\Delta Z \approx 4\sqrt{2}\Delta W \approx \frac{\sqrt{2}(2\mu_c + 3\mu_d)r\Delta C_D}{3\sqrt{3}\mu_c C_D}, \tag{2.10}$$

where ΔZ is the shift of the centre point in the direction opposite to that of the external flow, ΔW is perpendicular to ΔZ towards the edge of the droplet, ΔC_D is the difference is the drag coefficient between a droplet rising in a pure solution with no surfactant and the drag coefficient for the droplet with the stagnant cap, μ_c and μ_d are the dynamic viscosities of the continuous and disperse phases respectively, and r is the droplet radius.

This theoretical model was compared to the experimental data gathered by Horton et al. [1965] and it showed that while the initial direction of displacement (ΔW and ΔZ) was correct the magnitude was not, leaving this area open for future improvement.

There has been theoretical work performed on the effects of surfactant on a rising bubble. Harper et al. [1967] models how the motion of a bubble containing a small amount of contaminant, and so possessing a surface tension gradient, is only slightly different for a bubble with no contaminant that possesses uniform surface

tension. For a bubble rising in a pure solution there is a surface tension gradient around the interface, but it is too low to slow down the internal circulation of the bubble.

The drag coefficient is developed for droplets in Harper [1982] which gives the drag coefficient, C_D, for a droplet with a cap angle as shown in Figure 2.9, θ, as

$$C_D = \frac{8}{Re(\mu_c + \mu_d)} \left(2\mu_c + 3\mu_d + \frac{4\mu_c \theta^3}{3\pi} \right), \tag{2.11}$$

where Re is the Reynolds number for a droplet rising through a continuous phase, μ_c is the dynamic viscosity of the continuous phase, and μ_d is the dynamic viscosity of the droplet.

Palaparthi et al. [2006] presents theory and experiments focused on the stagnant cap of bubbles rising through a surfactant-rich solution. The experiments performed show the effects of the bulk concentration of surfactant on the drag coefficient of a bubble rising through an aqueous solution. It was found that for low concentrations of surfactant, as will be used in the experiments proposed in this work, that the drag coefficient lay in-between a bubble with no surfactant at the interface and a bubble with a completely immobile interface. This demonstrates an intermediate regime which corresponds to, and proves the existence of, a stagnant rigid region at the rear of the droplet. This agreed well with the numerical results produced that showed an increase in surfactant accumulating at the rear of the droplet as well as demonstrating the presence of a stagnant region at the rear of the droplet. However these results required modelling of the adsorption and transportation kinetics along with surfactant specific parameters.

This work was based on the physical properties associated with bubbles. Converting from bubbles to droplets adds another degree of complexity. The work of Palaparthi et al. [2006] demonstrated the need to understand the processes associated with adsorption along with the adsorption specific parameters related to surfactants.

2.3 Adsorption and diffusion

The process of surfactant molecules adhering to an interface is called adsorption. Adsorption can occur through two different mechanisms; a diffusion only model, or a mixed diffusion-kinetic model. The diffusion only model makes the assumption that surfactant molecules diffuse through the aqueous phase straight to the interface with no barriers against adsorption, whereas the mixed diffusion-kinetic model accounts

for intermolecular forces and other potential effects that affect the rate of adsorption to the interface.

2.3.1 Diffusion only model

Diffusion is the process of molecules moving along a concentration gradient from areas of high concentration to areas of low concentration. A concentration gradient will exist if a soluble substance is not equally dispersed throughout the phase in which it is present. The rate at which molecules transport through a fluid by diffusion is known as the diffusive flux. This diffusive flux, J, is given by Flicks first law (Cussler [2009])

$$J = -D\frac{\delta c}{\delta x}, \tag{2.12}$$

where D is the diffusion coefficient, c is the concentration, and x is the distance. The diffusion coefficient can be given by the Stokes-Einstein equation as

$$D = \frac{k_B T}{6\pi\mu r_s}, \tag{2.13}$$

where k_B is the Boltzmann constant, T is the temperature, μ is the dynamic viscosity of the phase in which the surfactant is dispersed, and r_s is the effective radius of a surfactant molecule.

This diffusion coefficient, D, can be used to calculate the thickness of the layer across which diffusion occurs, δ, over time period, τ, (Alvarez et al. [2010]). This is given by

$$\delta = \sqrt{D\tau}. \tag{2.14}$$

Equations to account for the diffusion to an interface and back into the bulk were combined to give the Ward and Tordai equation to calculate the surfactant surface excess, Γ, in relation to time, t (Ward and Tordai [1946]). This is given as

$$\Gamma(t) = 2c_0\sqrt{\frac{Dt}{\pi}} - 2\sqrt{\frac{D}{\pi}}\int_0^{\sqrt{t}} c_s d(\sqrt{t-\tau}), \tag{2.15}$$

where c_0 is the concentration of the surfactant in the bulk solution, c_s is the concentration of the surfactant in the sub-layer of the interface, D is the diffusion coefficient, and τ is a dummy variable of integration (Eastoe and Dalton [2000]).

The surface excess at an interface is the difference in the volume of surfactant at a unit area of the interface compared to the volume of surfactant at an identical

area deep within the bulk of the solution, on the assumption that the surfactant is evenly dispersed throughout the solution (Mitropoulos [2008]).

This surface excess, Γ, can be linked to the concentration, c, of the surfactant in the bulk solution and the interfacial tension, γ, using the Gibbs adsorption isotherm (Sherman [1968]),

$$\Gamma = -\frac{1}{RT}\frac{d\gamma}{d\ln c}, \tag{2.16}$$

where R is the ideal gas constant, T is the temperature, and c is the concentration.

The Gibbs isotherm model assumes that, for both fluids, the concentration is constant from the bulk of the fluid right up to the interface. It does not take into account any surfactant concentration gradients that occur in the vicinity of the interface (Borwanker and Wasan [1988]).

Fresh, surfactant-rich solution is brought into contact with a droplet rising through a solution by advection. This is taken into account by the Péclet number, Pe, (Clift et al. [1978])

$$Pe = \frac{2Ur}{D}, \tag{2.17}$$

where r is the characteristic length (for a droplet of radius r), U is the flow velocity, and D is the diffusion coefficient. The Péclet number is a ratio of the advective transport rate to the diffusive transport rate.

Harper [1974] presents numerical work with the aim of modelling the rear stagnation point of a bubble rising in a surfactant solution and its effect on the drag of the bubble. The author shows the boundary thickness of the diffusion layer, δ, to be in the order of

$$\delta = rPe^{-\frac{1}{2}}, \tag{2.18}$$

where r is the radius of the bubble, and Pe is the Péclet number. The author concludes that although the drag coefficient does increase when a stagnation region appears at the rear of the droplet, this increase is very small and so would not be easily measurable in the proposed experiments.

Harper [1972] describes in more depth the diffusion layer thickness for the case of weak surfactants, stating the diffusion boundary layer thickness, δ, as

$$\delta = \sqrt{\frac{4r^2}{6Pe}}, \tag{2.19}$$

where r is the droplet radius, and Pe is the Péclet number.

2.3.2 Mixed diffusion-kinetic model

The mixed diffusion-kinetic model consists of this same diffusion of the surfactant molecules through the aqueous phase, but at the interface there is a barrier to adsorption. This barrier against adsorption could be caused by different factors (Eastoe and Dalton [2000]). The first of these is a potential energy barrier. As a greater volume of surfactant adsorbs to an interface, the interfacial pressure increases and so, in order to adsorb, incoming molecules require a high enough activation energy to break this barrier. This energy barrier would include any electrostatic charges held by the molecules and any interaction between the adsorbed molecules.

A second barrier to adsorption would be the orientation of the molecule. The hydrophobic tail section of the molecule is soluble in the oil phase of a multiphase solution, and so if the molecule approaches with the hydrophilic head towards the interface it may desorb back into the bulk rather than reorientating to adsorb. The tail of a surfactant molecule with a long hydrophobic tail may get tangled. These molecules also have a tendency to desorb rather than gain the correct orientation (Eastoe and Dalton [2000]).

The location of surfactant molecules already on the interface could also pose an obstacle to adsorption. If there is a molecule already in a position on the interface that a new molecule would ideally adsorb to, then this molecule would desorb back to the bulk solution.

The final barrier occurs when the concentration of surfactant is above the CMC point. Molecules that have clumped together in a micelle have a very slow break-up rate and so are not available for adsorption at the interface.

The simplest solution to take into account this additional activation energy for adsorption was to retain the diffusion model but adjust the diffusion coefficient to take into account the activation energy (Eastoe and Dalton [2000]). If the activation energy, ϵ_a, for the surfactant is known, a new diffusion coefficient, D^*, can be calculated as

$$D^* = De^{-\epsilon_a/RT}, \tag{2.20}$$

where R is the ideal gas constant, and T is the temperature.

Adsorption isotherms were developed to relate the concentration of the surfactant in the bulk solution, c, to the quantity of surfactant adsorbed, Γ. In 1803 William Henry developed an adsorption isotherm (Eastoe and Dalton [2000])

$$\Gamma = K_H c, \tag{2.21}$$

in which K_H is an experimentally determined constant based on the volume of surfactant required to reach the equilibrium state. It is linear and so will only be valid for very low levels of bulk surfactant concentration where there is no interaction between surfactant molecules and no barriers against adsorption due to the changing state at the interface (Limousin et al. [2007]).

The most often used adsorption model is the Langmuir isotherm. This is a non-linear technique in which it is assumed that only a monolayer of surfactant is adsorbed to the interface. It takes into account the location of surfactant on the interface, assuming every location on the interface is equivalent, as well as assuming that there is no interaction between the surfactant molecules that have already adsorbed to the interface. The Langmuir isotherm for the quantity of surfactant adsorbed, Γ, is given by (Foo and Hameed [2010])

$$\Gamma = \Gamma_\infty \left(\frac{K_L c}{1 + K_L c} \right) , \tag{2.22}$$

where Γ_∞ is the maximum adsorbable volume of surfactant, c is the concentration, and K_L is the Langmuir equilibrium adsorption constant.

The Langmuir isotherm was developed by equating the rate of change of the surfactant at the interface due to adsorption to the rate of change of surfactant at the interface due to desorption. The rate of change of surfactant at the interface due to adsorption is given by

$$\frac{d\Gamma}{dt} = k_a c \Gamma_\infty \left(1 - \frac{\Gamma}{\Gamma_\infty} \right) , \tag{2.23}$$

where k_a is an adsorption constant associated with the surfactant, c is the concentration, Γ_∞ is the maximum adsorbable volume of surfactant, Γ is the volume of surfactant adsorbed, and t is the time. This equation shows a relationship between the rate of change of surfactant at the interface to the concentration of the surfactant in the bulk solution, and the proportion of the volume already adsorbed to the total adsorbable volume.

The rate of change of surfactant at the interface due to desorption is a function of the volume of surfactant at the interface and is given by

$$\frac{d\Gamma}{dt} = k_d \Gamma, \tag{2.24}$$

where k_d is a desorption constant associated with the surfactant, Γ is the volume of surfactant adsorbed, and t is the time.

Equating Equation 2.23 and Equation 2.24 gives the Langmuir isotherm in

Equation 2.22 in which the equilibrium adsorption constant, K_L, is given by

$$K_L = \frac{k_a}{k_d}. \tag{2.25}$$

Frumkin developed an isotherm based on the Langmuir adsorption isotherm to take into account the intermolecular forces. The Frumkin adsorption isotherm (Dukhin et al. [1995]) is given by

$$\gamma = \gamma_0 - RT\Gamma_\infty \left[\ln\left(1 - \frac{\Gamma}{\Gamma_\infty}\right) + a' \left(\frac{\Gamma}{\Gamma_\infty}\right)^2 \right], \tag{2.26}$$

where γ is the interfacial tension, γ_0 is the interfacial tension with no surfactant present, a' is the intermolecular forces due to the interaction between adsorbed molecules, R is the ideal gas constant, T is the temperature, Γ is the quantity of surfactant adsorbed, and Γ_{max} is the maximum surfactant adsorption at infinite dilution. This adsorption isotherm was successfully implemented to match theoretical work to experiments by Palaparthi et al. [2006]. However Dukhin et al. [1995] discusses how it is not an easy isotherm to use as, while the Gibbs adsorption isotherm (2.16) can be used to relate the concentration to surface excess, there is no such relation between concentration and interfacial tension.

Although other adsorption isotherms have been developed, the isotherms discussed here are the isotherms most often used to model surfactant adsorption and show the progression of the development of the adsorption problem. These adsorption isotherms only apply to a steady-state system where the rates of adsorption and desorption are in equilibrium. They also require parameters of the surfactant to be known; such as the free energy of adsorption, the constants associated with adsorption, or even the quantity required to form a monolayer at the interface. The chemical used as a surfactant in the proposed experiments is most commonly used as a tracer dye and so there is no information in the literature for any of these values.

The proposed experiments of passing a droplet through a fluid to observe adsorption means that fresh surfactant-rich solution would always be present at the interface. This means that an equilibrium state would be very hard to identify. These factors potentially make applying any of these adsorption isotherms extremely difficult.

2.4 Experiments involving Rhodamine-6G

Rhodamine-6G has been used as an adsorbate in experiments in the past. Annadurai et al. [2001] performed experiments to investigate the adsorption of Rhodamine-

6G to the surface of activated carbon. This was done by measuring the mass of the activated carbon to find the amount of adsorption for different concentrations of Rhodamine-6G infused in an aqueous solution. It was found that as the concentration of Rhodamine-6G in the bulk phase increased, so did the quantity of Rhodamine-6G adsorbed to the surface of the activated carbon. However, there reached a point where a further increase of the bulk concentration led to no further increase in the volume adsorbed to the interface. The concentration at which there is no further increase in adsorption can be related to the CMC point of the Rhodamine-6G. The adsorption isotherms generated in this research show a good match for the Langmuir isotherm model. However it demonstrates how the adsorption constant is different for changes in the variables. A match for the Langmuir adsorption isotherm model for Rhodamine-6G was also achieved by experimental work done by Ren et al. [2014] showing that this is a valid adsorption model for use with the surfactant to be used in the proposed experiments.

The research of Annadurai et al. [2001] also showed that an increase in the temperature leads to more Rhodamine-6G being adsorbed to the interface. Increasing the pH of the solution led to a decrease of the volume of Rhodamine-6G adsorbed to the interface. This demonstrates the importance of maintaining constant environmental parameters throughout the proposed experiments.

Experiments were also performed by Annadurai et al. [2001] to investigate how the quantity of Rhodamine-6G adsorbed to the interface changed over a time period. It was found that there was a steady increase in the quantity of Rhodamine-6G adsorbed up until a critical time after which the quantity did not change. This critical time was found to be the same for all parameters tested. However these measurements were made every five minutes for sixty minutes and so the spatial resolution between data points is limited leaving large gaps of uncertainty.

Other work has been performed that investigates the adsorption of Rhodamine-6G to a solid interface. Martínez et al. [2004] used the fluorescence properties of Rhodamine-6G to observe the adsorption of Rhodamine-6G to a solid clay interface. The author showed that this is a valid technique to measure the adsorption of Rhodamine-6G, however no values are presented to link this adsorption to any adsorption isotherms.

2.5 Measurement techniques

There are two main types of measurement techniques used in fluid dynamics: intrusive techniques and optical techniques. Intrusive techniques are those in which sen-

sors are inserted into a flow to take readings, whereas optical techniques take readings from a distance. This experiment is focused on the interface of an oil droplet, so intrusive probes are not appropriate as disruption to the interface caused by the probes is undesirable. To this effect two different optical techniques were identified that allow measurements to be taken from a distance; laser-induced fluorescence to explore the interface and wake of the droplet, and particle image velocimetry to explore the effects on the internal circulation within the droplet.

2.5.1 Laser-induced fluorescence

Laser-induced fluorescence (LIF) is the process of using a laser to excite molecules within the flow and so obtain information on the flow structure (Miles [2012]). This technique has been used for a long time and can be used to explore very low numbers of molecules (Kinsey [1977]). With a careful selection of a fluorescent surfactant it is possible to detect the surfactant concentration around a droplet with high accuracy. However LIF only works for the fluid phase that it is dispersed in. It does not give any indication as to any of the properties of the phase in which it is not dispersed. Furthermore, LIF does not give any measurements of the flow velocity patterns of the fluids, and so would be an inappropriate technique for measuring the internal circulation within the oil droplet.

2.5.2 Particle image velocimetry

A non-invasive technique (Johnson [1998]) designed for measuring velocity profiles is particle image velocimetry (PIV) (Adrian and Westerwell [2011]). In PIV the flow is seeded with tracer particles and illuminated with a light source (Gharib and Dabiri [2012]). Images are taken with a short known separation time to give instantaneous velocity profiles measured by the displacement of the tracer particles (Raffel et al. [1998]). The light source can be the same as the one used for LIF, as PIV uses reflected light rather than fluoresced light. The fluoresced light can be filtered out to ensure that only light reflected by the particles is measured and analysed.

A potential issue with PIV is that the tracer particles could interact with the interface, potentially interfering with the adsorption dynamics at the interface and masking the effects linked to adsorption of surfactant. To this effect, LIF and PIV will be performed independently from each other to ensure accurate LIF data. For the PIV measurements, the concentration of reflective seeding particles was kept low to reduce unnecessary interaction of the particles at the interface.

2.6 Summary

This project brings together different disciplines of research; the fluid dynamics of a droplet rising through a solution, the chemistry behind surfactants and how they operate, the process of adsorption, and the mass transfer at the interface of a droplet.

The theory describing how spherical objects move in a flow has been well established, so it was important to identify the flow regime to be able to give an in-depth look at the case specific to this research. The flow regime was identified to be a laminar flow with no flow separation from the droplet. However the introduction of a stagnant cap at the rear of the droplet has been shown to detach the flow around the stagnant part of the droplet, effectively reducing the surface area for surfactant to adsorb to.

A droplet rising within a flow has internal circulation caused by the flow accelerating the interface of the droplet around to the base and back up the centre. This effect can increase the terminal velocity of the droplet by up to 1.5 times. However with the introduction of surfactant forming a stagnant cap at the rear of the droplet, this velocity is inhibited and the terminal velocity of the droplet is reduced to be in line with Stoke's law.

Surfactants are molecules that interact with both an oil phase and an aqueous phase so are in equilibrium at an interface. They lower the interfacial tension between two phases. Surfactants adhere to an interface through the process of adsorption and are transported through the bulk by diffusion. Adsorption can either be modelled by a diffusion-only model or by a mixed kinetic-diffusion model in which there is a barrier to adsorption at the interface.

The issue with adsorption isotherms is that they require interfacial properties of the surfactant to be known. The chemical used in the proposed research, Rhodamine-6G, is most often used as a tracer dye with the surfactant properties overlooked and so none of the required values are known. There have been experiments performed that show that the Langmuir adsorption isotherm is appropriate in the case of Rhodamine-6G, but the values differ between experimental parameters and so could not be extracted for this research.

There have been theoretical models developed for the steady-state case of a droplet rising through surfactant, but very little has been done on the development of the stagnant cap in relation to time. There have been experiments performed that observe the shift in the centre positions of the recirculation eddies within a droplet with surfactant present at the interface. However there is very little agreement with an existing theoretical model.

Experiments that visualise the formation of the surfactant cap behind a droplet in a flow are yet to be performed in order to observe the internal circulation within the droplet as well as the surfactant cap at the interface. This project will aim to link the size of the surfactant cap with the size of the eddies within the droplet. This will be done for Rhodamine-6G — a chemical which is often used for a different purpose and so very little is understood about the effect it has on an interface.

Chapter 3

Experimental setup

An experiment was designed that allowed for both LIF and PIV to be performed to explore the formation and development of a stagnant, surfactant cap at the rear of the droplet and the effect this stagnant cap has on any internal circulation within the droplet.

This chapter presents the experimental setup along with how the setup was changed between the two different measurement techniques.

3.1 General experimental procedure

The experiment designed to explore the entrapment of surfactant behind a droplet consisted of a droplet of oil being released at the base of a tank and rising through an aqueous solution containing surfactant as shown in Figure 3.1. The aqueous solution consisted of a mixture of 96% glycerol and 4% deionised water. This ratio was used to index match the aqueous solution with the oil, giving the solution a high viscosity. This viscosity kept the rising speed of the droplet low ensuring laminar flow as well as assisting in the capture of higher resolution photographs.

A weak fluorescent surfactant was used. This fluorescence allowed the use of a laser sheet and camera to visualise the droplets as they passed through the tank. The camera was positioned perpendicularly to the laser sheet to reduce optical distortion. Photographs were taken at a range of positions with a fixed separation to track the development of the stagnant cap and accumulation of surfactant behind the droplet as it rose through the tank. An 8mm diameter stainless steel rod was used to stir the solution between each droplet to keep the concentration consistent throughout the tank.

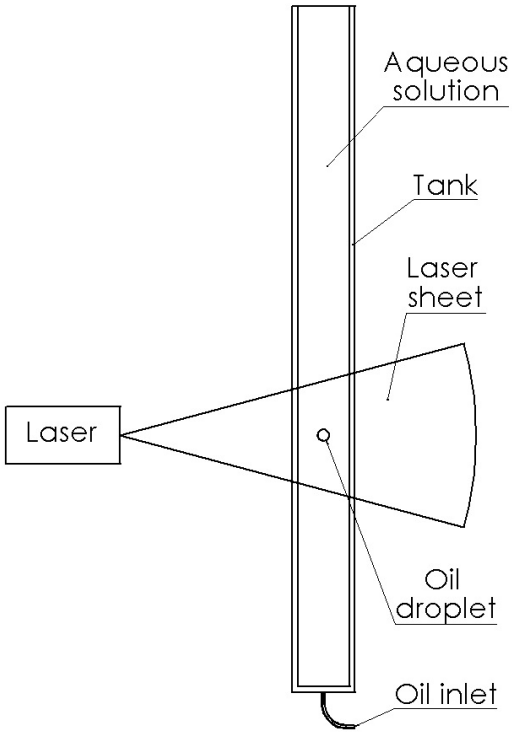

Figure 3.1: Experimental setup showing key constituent parts of the experiment.

3.2 Tank design

The tank was designed with a rectangular cross-section so as to eliminate any optical distortion. This enabled the laser beam to be projected through the side wall with the camera positioned perpendicularly to the tank and laser sheet. This setup is demonstrated by the plan view shown in Figure 3.2. The tank dimensions were 45mm by 40mm with the oil injection nozzle placed 15mm from the front face of the tank and 15mm from the left hand wall.

The tank was 680mm tall and held 1l of aqueous solution. The tank was manufactured from 10mm thick transparent Perspex. The rear face of the tank was blacked out to provide a blank screen for the experiments and to block any ambient light coming through from the rear of the tank. Perspex has a refractive index of 1.49 (Budwig [1994], Stöhr et al. [2003]).

The tank was attached to the experimental rig using a vertical supporting beam along which the tank was moved to adjust the height in the tank at which each photograph was captured. For the main experimental series the positions for each height were separated by 50mm, reduced from a distance of 57mm used in

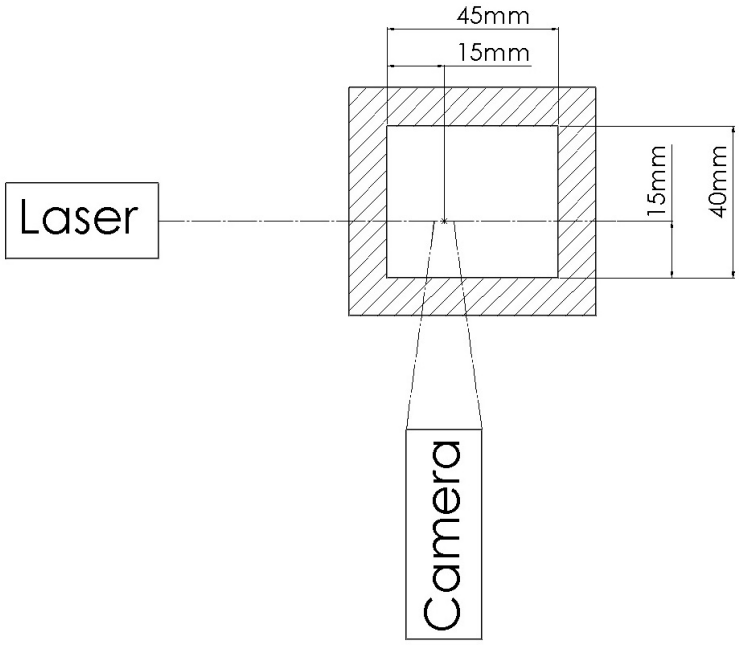

Figure 3.2: Horizontal cross-section of experimental tank showing laser and camera positioning with dimensions.

the preliminary experimental series. An added position in the main experimental series ensured the same height coverage as in the preliminary experimental series but with improved spatial accuracy. The height reference number and associated experiment height measured from the base of the tank for the main experimental series are shown in Table 3.1.

3.2.1 Droplet insertion

The injection nozzle was positioned 15mm from the front and side walls of the tank as shown in Figure 3.2. This reduced the effect of light intensity being lost from passing through surplus solution containing Rhodamine-6G. The end of the nozzle was raised 5mm from the base of the tank to prevent the droplet from interacting with the tank floor. The oil was injected using a 1ml syringe and was pumped through 140mm of 0.020in diameter piping through the base of the tank. The syringe was manually operated with an attempt to keep the droplet size consistent.

Following the preliminary experimental series, an Aladdin programmable syringe pump from World Precision Instruments was used to attempt to achieve a constant, repeatable droplet size for later experiments. However the maximum

Table 3.1: The heights at which measurements were taken for the main experimental series. Height measured from the base of the tank to the lower edge of the image.

Position number	Height in tank (mm)
1	10
2	60
3	110
4	160
5	210
6	260
7	310
8	360
9	410
10	460
11	510

pumping rate of 53.07ml/hr was insufficient to produce droplets approaching a similar diameter used in the preliminary experimental series and so manual injection was used throughout.

3.2.2 Cleaning and maintenance

It was important to consider the potential for contamination of the experiment by external sources. Potential sources of contamination were identified as:

- Cross-contamination from previous experiments: The remnants of solutions from previous experiments within the tank being mixed with a solution of different surfactant concentration would cause the surfactant concentration in the tank to be changed. This highlights the need to thoroughly clean the tank between experiments to remove any traces of previous surfactant.

- Contamination through maintenance and cleaning: Whilst cleaning the tank was necessary, it was a potential source of contamination. Cleaning products contain strong surfactants so any trace left in the tank could affect the results of the experiments. Because of this, no cleaning agents were used. The tank was cleaned using deionised water by repeatedly filling the tank with the water and thoroughly agitating until clean.

- Contaminants in the air: All fluids were stored in air-tight containers while not in use. These containers were cleaned in the same manner as the tank after each use. The period of time any solution remained in the tank was kept

to a minimum with a layer of oil on the surface to provide a barrier against the air.

3.3 Oil

Mineral oil purchased from Acros Organics with a designated use for spectroscopy was used, with properties given in Table 3.2. The transparency of the mineral oil made it a good choice for visualisation as a negligible amount of light was lost passing through the droplet allowing visualisation of the entire droplet interface.

Table 3.2: Mineral oil specifications (Acros Organics).

Density (15°C)	$827 - 862 \text{kg/m}^3$
Refractive index (20°C, 589nm)	1.4620 - 1.4730
Viscosity (20°C)	$33 - 42 \text{mm}^2/\text{s}$

3.4 Aqueous solution

A major problem of using laser sheets in the visualisation of multiphase flows is the differing refractive properties of the two phases. The solution to this problem was to use a mixture for the aqueous continuous phase that had the same refractive index as the dispersed phase. This section will discuss the properties of the fluids used to create this mixture and the technique used for index matching.

3.4.1 Glycerol

Glycerol is commonly used in experiments combined with water to make an aqueous phase (Palaparthi et al. [2006], Maxworthy et al. [1996]). In these experiments the glycerol used was Glycerol Tech from ReAgent with a relative density of 1.26 (ReAgent). Glycerol is soluble with water with a refractive index of 1.474 at 20°C (Hoyt [1934]). Glycerol has a high viscosity of 1410mPa.s at 20°C (Segur and Oberstar [1951]), which assisted in keeping the rising velocity of the droplet low and giving laminar flow. The colourless appearance of glycerol makes it ideal for use with a laser sheet.

3.4.2 Deionised Water

Deionised water was used for these experiments. Mains water contains impurities and chemicals which would impact the results of the experiments. Deionised water

has the majority of these impurities removed and so has a minimal impact on the experiments. The viscosity of water at 25°C is 0.893mPa.s (Lide and Kehiaian [1994]) and the refractive index of water is 1.33 at 20°C (Daimon and Masumura [2007]).

3.4.3 Index matching

The mineral oil used has a different refractive index to any appropriate fluid that could be used for the aqueous phase. Whilst this would not be a problem if each interface was perpendicular to the laser sheet, it becomes an issue when the interface is curved; as for the droplets generated in this experiment. Curved interfaces cause the laser light passing the droplet interface to be refracted by different angles, causing the laser sheet to disperse and, more significantly, not pass through the droplet in a straight line. With the refractive indices of the oil and aqueous phases matched, the angle of incidence of the laser sheet equalled the angle of refraction at the interface and so the laser sheet passed through the droplet with no dispersion.

The method used to achieve index matching between the two phases was to create a mixture for the aqueous phase. This was done by mixing two aqueous fluids with refractive indices less than and greater than the refractive index of the oil. The two fluids selected were glycerol and deionised water. The setup used to achieve the index matching is demonstrated in Figure 3.3, with the apparatus shown in Figure 3.4. A laser beam is directed perpendicularly through a perspex tank with two compartments, each filled with a different phase. The phases are separated by an internal wall at an angle to force different angles of incidence and refraction. The laser beam is refracted differently according to the refractive indices of the phases and so can be matched by changing the properties of one phase. This is similar to the method used in Budwig [1994].

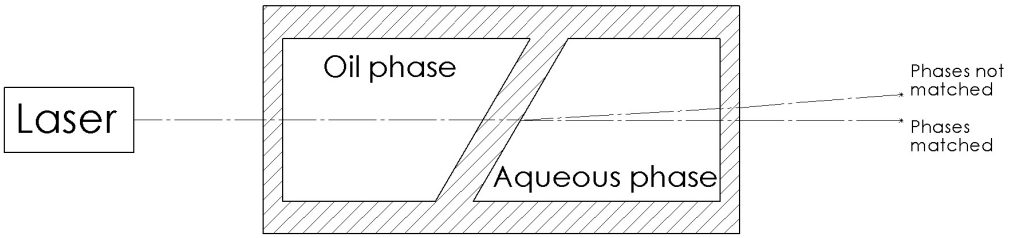

Figure 3.3: Plan view of index matching process.

Index matching was achieved by firstly marking the end point of the laser beam passed through the tank when both compartments were filled with oil. This

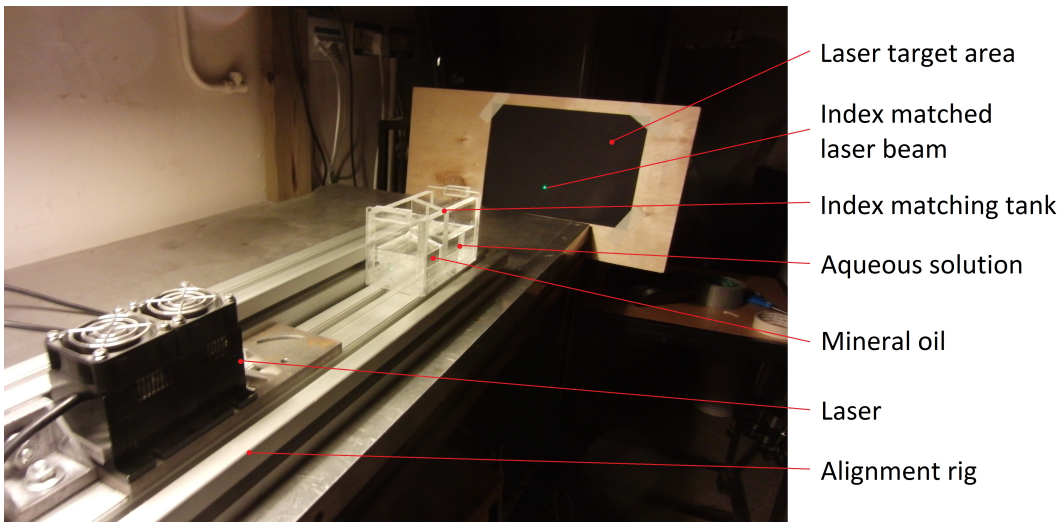

Figure 3.4: Experimental rig used to achieve index matching.

gave a marker for when index matching had been achieved. From here, one side of the tank remained filled with the mineral oil and the other side was filled with a known volume of glycerol. Water was mixed in with the glycerol until the path of the laser beam matched the original path. The water-glycerol ratio found to achieve index matching was 4% water and 96% glycerol. This gave a refractive index of 1.468 at 20°C (Hoyt [1934]) which falls in the range of the refractive index of the mineral oil given in Table 3.2.

3.5 Rhodamine-6G

Rhodamine-6G is classed as a weak cationic surfactant (Paul et al. [2011], Lopez Arbeloa et al.). Rhodamine-6G has fluorescent properties so it can be used to visualise the concentration of surfactant around the interface of an oil droplet. The Rhodamine-6G molecules absorb light at one wavelength and emit light at a different wavelength. Rhodamine-6G has very low levels of photo-degradation when exposed to laser light (Rigler et al. [1979]) making it appropriate to use with a continuous wave laser where the Rhodamine-6G would be exposed to the laser light for long time periods. The fluorescence allows the use of a filter to remove any light not associated with the concentration of surfactant. Values for the wavelength of light absorbed and emitted by Rhodamine-6G along with the molecular weight are given in Table 3.3 provided by Sabnis [2010].

The size of a Rhodamine-6G molecule could have an impact on the experiments based on the surface area it covers. The largest surface area a Rhodamine-

Table 3.3: Rhodamine-6G specifications given by Sabnis [2010].

Molecular weight	479.02
Absorption (λ_{max})	528nm
Emission (λ_{max})	551nm

6G molecule could occupy is approximately 8Å by 16Å (Mubarekyan and Santore [1998]), where $1\text{Å} = 1 \times 10^{-10}\text{m}$, giving a Rhodamine-6G molecule an approximate maximum cross-sectional area of 1.28nm^2.

Before 2000 there appeared to be little agreement on the diffusion coefficient of Rhodamine-6G in water. The values reported in the literature ranged from $(2.8 \pm 0.3) \times 10^{-10}\text{m}^2\text{s}^{-1}$ (Magde et al. [1974], Rigler et al. [1979]) through to $4.0 \times 10^{-10}\text{m}^2\text{s}^{-1}$ (Jones et al. [1996]). With such a wide range of values it would be very difficult to calculate the diffusion coefficient for the aqueous mixture used in these experiments. However, since 2000, a wide range of experiments have been done to measure the diffusion coefficient of Rhodamine-6G in water using multiple techniques. These experiments returned values of $(4.0 \pm 0.3) \times 10^{-10}\text{m}^2\text{s}^{-1}$ (Gendron et al. [2008]), $(4.14 \pm 0.01) \times 10^{-10}\text{m}^2\text{s}^{-1}$ (Culbertson et al. [2002]), $(4.14 \pm 0.05) \times 10^{-10}\text{m}^2\text{s}^{-1}$ (Müller et al. [2008]), and $4.26 \times 10^{-10}\text{m}^2\text{s}^{-1}$ (Petrášek and Schwille [2008]). These new values are all relatively similar so the median Rhodamine-6G diffusion coefficient of $(4.14 \pm 0.14) \times 10^{-10}\text{m}^2\text{s}^{-1}$ at 20°C was used in this study.

3.5.1 Surfactant solution

The Rhodamine-6G used was obtained from Sigma-Aldrich in powder form. A base concentration was created by mixing a 1g/l solution of Rhodamine-6G in deionised water. This solution was stored in a dark cupboard to eliminate the possibility of photodegradation. This Rhodamine-6G solution was mixed with the water-glycerol solution to give aqueous solutions with different Rhodamine-6G concentrations. Each volume of Rhodamine-6G is dispersed throughout a 1l aqueous mix. The concentrations used in the main experimental series are presented in Table 3.4 along with the initial volume of Rhodamine-6G converted to the number of molecules per mm^3 of solution.

3.6 Laser

A continuous wave, 500mW green laser with a wavelength of 532nm was used. This was very close to the absorption wavelength required by the Rhodamine-6G to

Table 3.4: Volume of Rhodamine-6G dilute solution combined with 1l of water-glycerol and conversion to concentration and the number of molecules per mm^3 in main experimental series.

Volume of Rhodamine-6G dilute solution at 1g/l (ml) = Concentration (mg/l)	Concentration (mol/l)	Number of Rhodamine-6G molecules per mm^3
1.00	2.09×10^{-6}	1.257×10^{12}
0.80	1.67×10^{-6}	1.006×10^{12}
0.60	1.25×10^{-6}	7.543×10^{11}
0.50	1.05×10^{-6}	6.286×10^{11}
0.40	8.36×10^{-7}	5.029×10^{11}
0.30	6.27×10^{-7}	3.771×10^{11}
0.20	4.18×10^{-7}	2.514×10^{11}
0.10	2.09×10^{-7}	1.257×10^{11}
0.08	1.67×10^{-7}	1.006×10^{11}
0.06	1.25×10^{-7}	7.543×10^{10}
0.05	1.05×10^{-7}	6.286×10^{10}
0.04	8.36×10^{-8}	5.029×10^{10}
0.03	6.27×10^{-8}	3.771×10^{10}
0.02	4.18×10^{-8}	2.514×10^{10}
0.01	2.09×10^{-8}	1.257×10^{10}

achieve good fluorescence. Fine tuning of the laser alignment for each droplet as the droplet passed through the capture window was achieved by the constant presence of the laser sheet. A laser sheet was created by passing the laser beam through light sheet optics. This generated a wide laser sheet with a noticeable bulge across the laser sheet width. An even laser sheet width of 1mm was obtained by passing the laser sheet generated by the optics through a 1mm wide slit. The exit aperture of the laser was set 210mm from the tank with the slit positioned 40mm from the tank. This enabled manipulation of the tank without disturbing the laser configuration. The laser ensemble module had a small degree freedom of movement around the vertical axis to allow fine tuning of the experiment alignment at each height.

3.7 LIF setup

The surfactant distribution profile of Rhodamine-6G around the interface and in the wake of a droplet can be calculated from a single image. This differs from the requirements of PIV experiments for capturing the internal circulation within the droplet which requires a string of images at a high frame rate. Therefore the aim

for the LIF experiments was to capture high resolution images. The experimental setup used for the LIF experiments is shown in Figure 3.5 and shows the use of a Nikon digital SLR (Nikon D5000) camera to capture high resolution photographs. The captured images have a field of view of 2,848 pixels by 4,288 pixels. The use of a combination of a macro lens and extension rings gave a high level of magnification with good resolution. The long length of the target area of the image gave the opportunity to fine tune the laser alignment for each droplet before each photograph was captured.

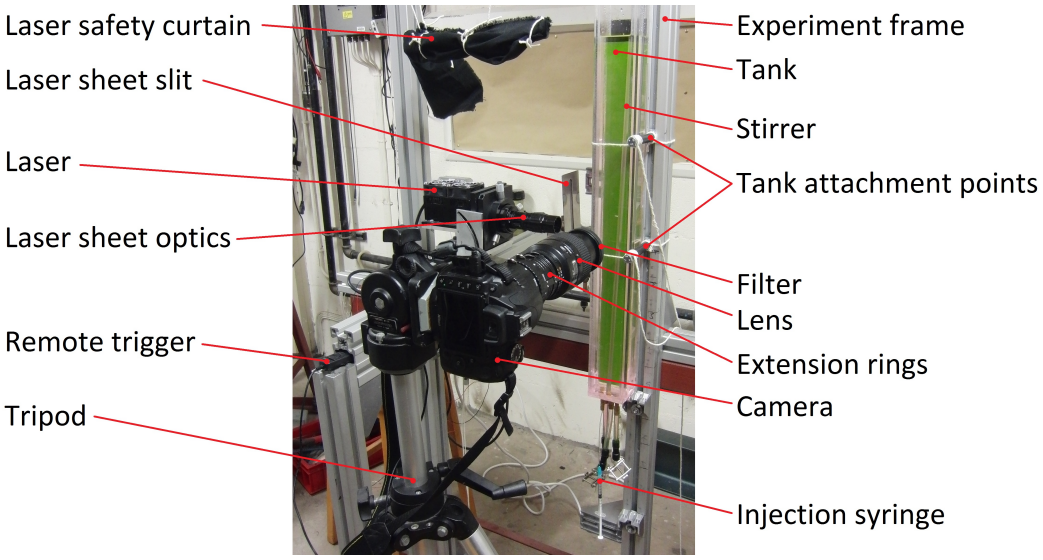

Figure 3.5: Experimental setup showing components for LIF experiments.

With such a high level of magnification, small vibrations or disturbances could interfere with the image. One source of these disruptions was identified as human interaction when activating the shutter. To eliminate this vibration an external trigger (Nikon MC-DC2) was used.

As LIF data is a measure of light intensity, there was the potential for ambient light to affect the results. To reduce this effect, experiments were performed in a darkened room. The laser had a warm-up period for the power to stabilise to reduce the variation in the laser beam power.

3.7.1 Camera settings

The lens used was a Nikon AF Micro Nikkor with a focal length of 105mm. Further magnification was achieved using extension rings. Extension rings increase the distance between the camera and the lens and so reduce the minimum focusing dis-

tance. This enabled the camera to focus on smaller areas magnifying the target area. The main experimental series used 70mm of extension rings allowing higher image resolution than the 65mm of extension rings used in the preliminary experimental series. The trade-off of using extension rings was the reduction in the quantity of light that reached the camera; the longer the extension ring, the less light reached the camera sensor. This could be compensated for by decreasing the aperture, increasing the ISO speed, or increasing the exposure time. Each of these has its merits and practical implications:

- Aperture setting: The aperture f-stop value controls the amount of light passing through the camera lens. It also controls the depth of field of the image. The lower the f-stop value, the larger the aperture gets, increasing the volume of light that reaches the camera sensor. However, the higher the f-stop value the greater the depth of field of the image. Choosing the correct f-stop value is a trade-off between the volume of light and the depth of field of the image. Due to the complexity of this relationship in regards to LIF calibration and the requirement to fine tune the position of the laser for each droplet, it was decided to fix the f-stop value at f/11 for all LIF experiments.

- ISO speed: This is a measure of how sensitive the camera is to light. As the ISO speed increases the noise associated with the image also increases. Whilst a low ISO speed is desirable, higher ISO speeds can be used to increase the exposure without changing the exposure time.

- Exposure time: Also known as the shutter speed. This is a measure of how long the sensor of the camera is open to incoming light. This value is measured in seconds and for the Nikon D5000 ranges from 30 seconds to 1/4000th of a second. The shorter the exposure time the less light reaches the sensor. As the droplet was moving, shorter exposure times were preferred as they led to less blurring in the image.

The aperture size, ISO speed, and exposure time are all interlinked so each image setup is a combination of these three settings. Fixing the aperture left two settings to be varied to achieve suitable results, and reduced the complexity of the LIF calibration as there were fewer variables to consider. The ISO speeds and exposure times used for the main experimental series are given in Table 3.5.

Table 3.5: ISO speeds and exposure times used in main LIF experimental series.

Rhodamine-6G concentration (mg/l)	ISO speed	Exposure time (1/E)
1.00	640	500
0.80	800	500
0.60	800	500
0.50	1000	500
0.40	1000	500
0.30	1600	500
0.20	2000	500
0.10	3200	500
0.08	2000	320
0.06	3200	250
0.05	3200	250
0.04	3200	250
0.03	3200	160
0.02	3200	160
0.01	3200	100

3.7.2 LIF filter

The final component needed to complete the LIF setup was a filter to block out all light not fluoresced by the Rhodamine-6G. This removed the majority of ambient light and reflected laser light, ensuring clearer, more accurate LIF data. The filter used for LIF experiments was an orange filter provided by Dantec Dynamics that only allows through light greater than 550nm in wavelength. The wavelength emitted by Rhodamine-6G is 551nm.

3.8 PIV setup

For the PIV experiments a high frame rate was required in order to capture images of the droplet with low displacement between frames for PIV vector field analysis to be successful. The camera used for the PIV experiments was a Grasshopper3 manufactured by PointGrey. This is a black and white camera controlled by the computer via a USB3 connection with the capability to achieve 90 frames per second. The camera has a field of view of 2,048 pixels by 2,048 pixels. The PIV setup is shown in Figure 3.6.

The maximum frame rate achieved in these experiments, due to the limitations of the computer controller was 80Hz with images recorded over a 3 second duration as the droplet moved through the field of view. All of the camera settings

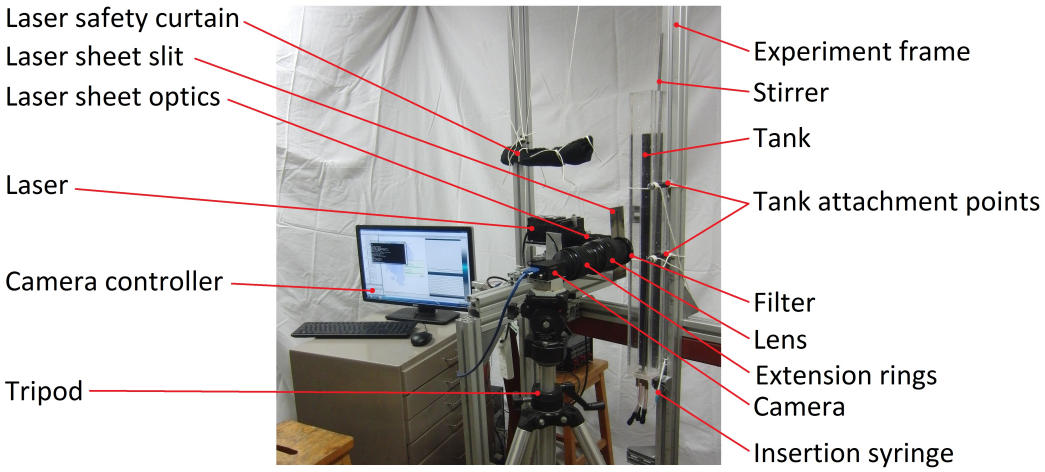

Figure 3.6: Experimental setup showing components for PIV experiments.

were kept constant for each Rhodamine-6G concentration except for the shutter speed which varied as lower Rhodamine-6G concentrations allowed more reflected light to reach the camera sensor allowing the shutter speed to be reduced.

The shutter speeds for each Rhodamine-6G concentration are given in Table 3.6. These were the speeds requested of the camera by the computer. However the camera processed a marginally different value. The same discrepancy occurred with the camera gain. The gain controls the amplification of light reaching the sensor, with a higher gain value leading to higher background noise. The requested and received values for the shutter speed and gain are given in Table 3.7.

Whilst the shutter speeds used are very close to the values requested, the gain values are significantly lower. However as the gain of the camera contributes to the signal noise, the lower gain values lead to less noise in the images.

The same Nikon AF Micro Nikkor 105mm lens was used with the aperture f-stop value set to f/11. The lens was connected to the camera via a C-mount bracket with 70mm of extension rings.

3.8.1 PIV filter

PIV data involves the measurement of light reflected from particles in the flow. Therefore the only light of interest was that reflected by the particles from the 532nm wavelength green laser. However the Rhodamine-6G was fluorescing light so a bandwidth filter was used to eliminate all unwanted light. A high performance green filter supplied by Dantec Dynamics was used that only allowed through light

Table 3.6: Shutter speeds used in PIV experiments for each concentration.

Rhodamine-6G concentration (mg/l)	Shutter speed requested by computer (ms)
1.00	3
0.80	3
0.60	3
0.50	3
0.40	3
0.30	2
0.20	3
0.10	3
0.08	2
0.06	2
0.05	2
0.04	2
0.03	2
0.02	2
0.01	2
0.00	2

Table 3.7: Camera settings requested by the computer along with those achieved for the PIV experiments.

Shutter speed (ms)		Gain (dB)	
Requested	Achieved	Requested	Achieved
2.00	1.998	2.00	1.584
3.00	3.002	2.00	1.584

of wavelengths 527nm and 532nm.

3.8.2 Tracer particles

The particles used to seed the oil droplet for PIV experiments were silver coated, hollow glass spheres, provided by Dantec Dynamics. These particles were 10μm in diameter. The particles were premixed with the mineral oil at a concentration of less than 0.05g/50ml and thoroughly mixed with a magnetic stirrer. However it was found that the concentration of particles varied noticeably between individual droplets due to the separation of the particles from the oil when held in the syringe for differing periods of time between droplet insertions.

3.9 Averaging

The results for both LIF and PIV experiments were averaged over multiple repeated data points to reduce the impact of any anomalous results and achieve reliable results. For the main LIF experimental series averaging occurred over a minimum of twenty droplets.

For the PIV experiments, each data point only needed two photographs to generate an instantaneous vector field. However due to the nature of the experimental setup used for PIV, strings of images were automatically captured. This meant that the droplet could be averaged over its corresponding string of vector fields. For each height of each concentration a minimum of six droplets were captured for further averaging to increase reliability.

3.10 Summary

This chapter has described the development of the experimental setup and procedures used to explore the entrapment of surfactant in the wake behind a rising oil droplet. The experimental apparatus was developed to take into consideration the requirements of the measurement techniques. This included the need for transparent tank walls, as well as the avoidance of curved walls that would introduce optical distortion. Different methods of droplet insertion were experimented with and a user operated syringe was identified as the most appropriate injection method. The aqueous phase was index matched to avoid any optical distortion at the droplet interface.

The two experimental techniques required a different setup of camera system, with LIF aiming for single, high-quality photographs, whereas PIV experiments required strings of relatively high-speed images. Appropriate cameras were identified along with suitable magnification apparatus and lens selection. The final stage was to select specific camera settings for the different concentrations of surfactant used.

Each of these areas came together to give a good range of data for both LIF and PIV experiments, with enough data gathered to average out any anomalous results and to perform calibration to process quantitative results.

Chapter 4

Calibration

To produce quantitative results for the volume of surfactant held behind a droplet, calibration techniques were developed to reduce the impact of any experimental irregularities and to provide a link between the light intensity captured by the photographs and the concentration of surfactant. The production of quantitative results allows each experiment to be compared to experiments with different camera settings.

Different parameters were considered in order to calibrate these experiments. These included laser and laser sheet irregularities, rising velocity of the droplet, and the relationship between different strengths of surfactant concentration to the intensity recorded by the camera.

This chapter explores the effects caused by different components of the experiment to develop necessary calibration techniques and protocols. Initially the laser module was investigated to identify the ways in which the components affected the experiment. The second area explored was the rising velocity of the droplet and how this was affected by different concentrations of Rhodamine-6G. The relationship between the pixel separation and millimetres was calculated for both LIF and PIV experiments. Finally the relationship between the light intensities recorded by the camera and the concentration of Rhodamine-6G was explored to produce quantitative data.

The main concern for the PIV experiments was the potential effect of the reflective tracer particles on the interface of the droplet. If the tracer particles interacted with the interface, the effects of the adsorption of the Rhodamine-6G may be affected, leading to inconsistencies between the LIF and PIV data.

Each of these factors was investigated and appropriate calibration methods were developed to limit the effect of any undesirable properties and to relate exper-

imentally specific values to quantitative data.

4.1 Laser calibration

There were different properties associated with the laser module that potentially influenced the experimental data. These issues were divided into three categories: the consistency of the laser sheet, the interaction of the laser light with the Rhodamine-6G, and the stability of the laser power. This section explores the effects of each of these categories and how the system was calibrated to account for them.

4.1.1 Laser sheet consistency

Imperfections in the laser sheet optics caused the power of the laser sheet to vary across its height in the field of view. Figure 4.1(a) shows how the intensity of the laser sheet light recorded by the camera varied over the height of the image for different concentrations of Rhodamine-6G. The line of measurement was an averaged pixel intensity over a 20 pixel wide strip down the centre of the field of view. As the intensity of a solution containing no surfactant is greater than zero, it shows that there is a baseline noise level associated with the settings of the camera. The three lines corresponding to solutions containing surfactant show that the intensity had a small increase moving downwards from the top of the image. The maximum intensity is achieved between pixels 1500 - 3500, with a sharp decrease from pixel 1500 towards the base of the image. This was caused by the laser sheet optics not forming an even laser sheet so a lower laser power was achieved at the lower end of the image with a peak laser power being achieved at around a pixel height of 3500. There were also distinctive peaks and troughs across the height of the image, an example highlighted by the red box in Figure 4.1(a). The tank walls were kept clear of air bubbles so these shadowy streaks in the image were associated with impurities in the perspex walls of the tank.

Figure 4.1(b) shows the absolute intensities of the intensity values recorded across over the sheet height normalised against the concentration relating to each line after the background intensities were subtracted. It would be expected that each of these lines collapse as the intensities recorded should be a function of the concentration. Figure 4.1(b) shows that the intensity for the line corresponding to the Rhodamine-6G concentration of 0.50mg/l obtains higher values over the strongest part of the laser sheet but the degradation at the lower end matches that of the intensity line relating to a concentration of 1.00mg/l. The line corresponding to a concentration of 0.10mg/l is a relatively good match with the concentration of

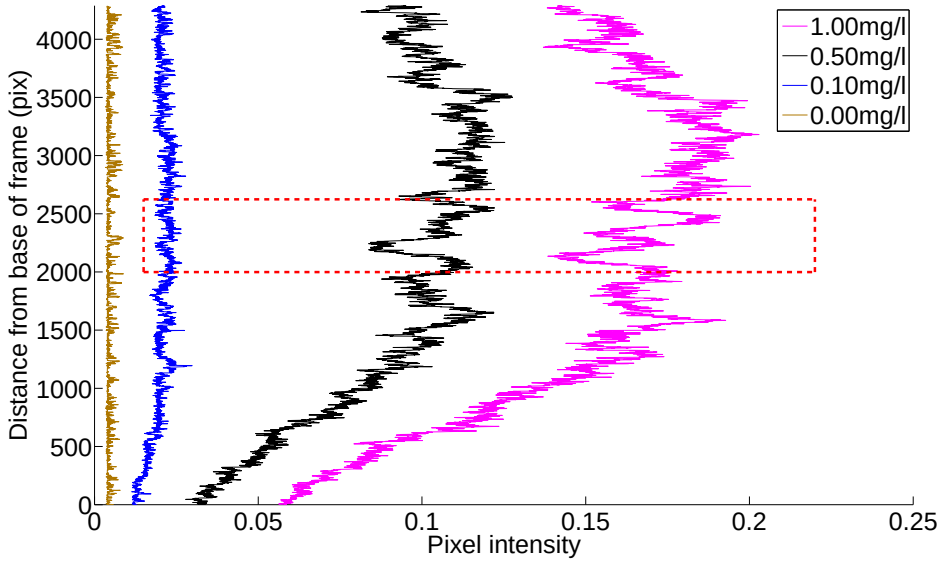

(a) Absolute intensities,

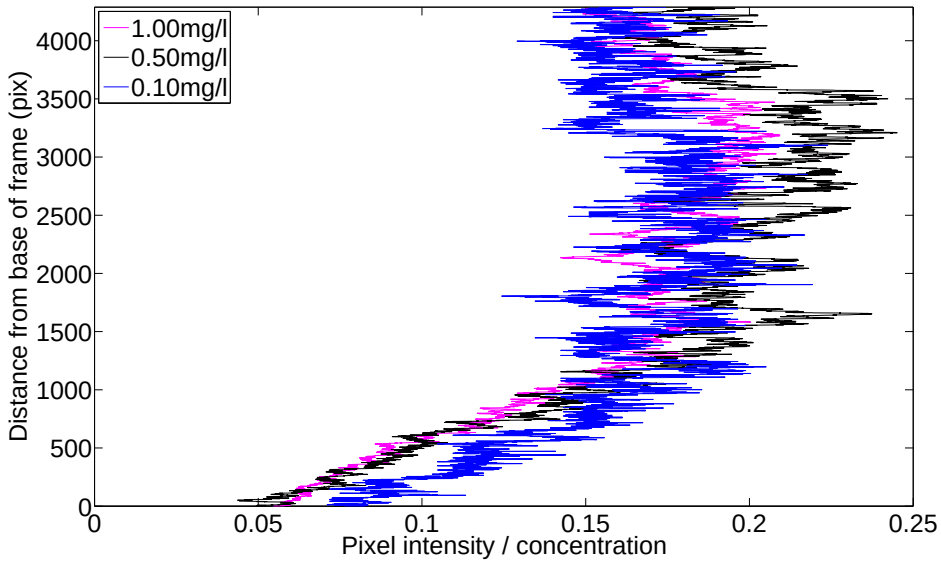

(b) Intensities normalised by concentration.

Figure 4.1: Variation in intensity over the length of the light sheet measured in pixels from the base of the image for different concentrations. ISO speed: 1600, exposure time: 1/500s.

1.00mg/l although at the lower end of the image the values are higher than the other concentrations. These inconsistencies could be due to fluctuations in the laser power or minute changes in the positioning of the camera in relation to the laser sheet between data points.

To reduce these effects each experimental image was normalised against the background laser sheet pattern in the horizontal direction. This was achieved by capturing the photograph containing the droplet, immediately followed by a photograph of the same target area but with no droplet present. This ensured that each image could be normalised against an image with the same pattern of shadowy streaks and same degree of laser light intensity.

The best quality photographs were captured in the region of the image with the strongest intensity of laser sheet. As the laser light intensity significantly decreased towards the base of the image, the droplet photographs were captured in the upper two thirds of the field of view. The lower section of the field of view was used to fine-tune the laser sheet alignment with the centre line of the droplet as the position of this centre line varied slightly between droplets.

4.1.2 Attenuation due to Rhodamine-6G

A limiting factor for the concentration range of the Rhodamine-6G was the volume of light lost through the absorption of laser light to the Rhodamine-6G molecules as shown in Figure 4.2(a). This shows the average pixel intensities for a strip measured across the width of the target image for different surfactant concentrations. Stronger concentrations of Rhodamine-6G meant a larger density of molecules for the laser light to absorb to. This left less laser light for absorption further across the width of the laser sheet. As there was less laser light being absorbed by the molecules further across the laser sheet, a lesser quantity of light was emitted by the Rhodamine-6G molecules leading to diminishing levels of light intensity recorded by the camera as the width across the laser sheet increased.

The strongest Rhodamine-6G concentration of 2.00mg/l has a reduction of approximately 45% of the light intensity as the laser sheet passes through the frame. This percentage drops down to approximately 40% for 1.50mg/l, 35% for 1.00mg/l, and 25% for 0.50mg/l. To avoid excessive light intensity being lost through the reduction of fluoresced light due to the concentration of Rhodamine-6G, the maximum surfactant concentration used for these experiments was 1.00mg/l of Rhodamine-6G.

Towards the lower end of the concentration range, very little light is lost throughout the width of the image. A Rhodamine-6G concentration of 0.01mg/l has a small but distinct difference to an aqueous solution containing no surfac-

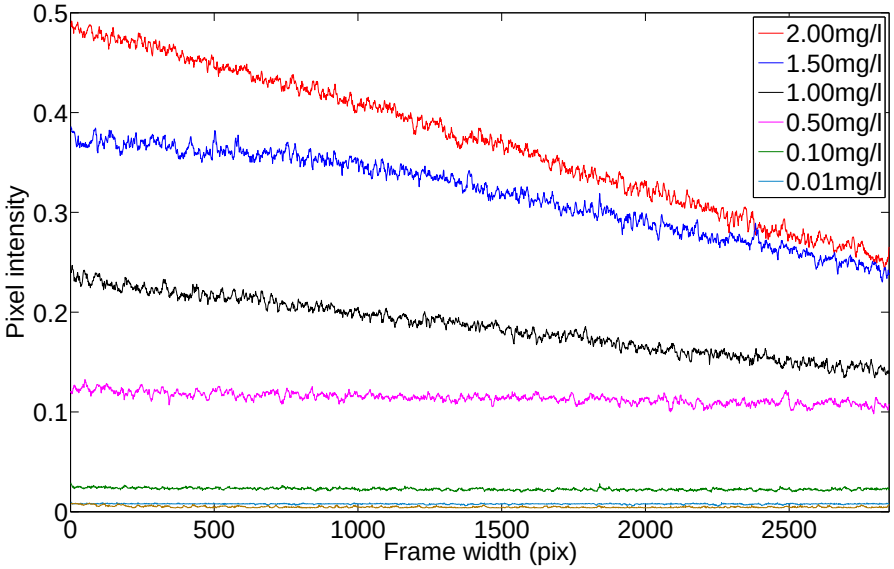

(a) Absolute intensities,

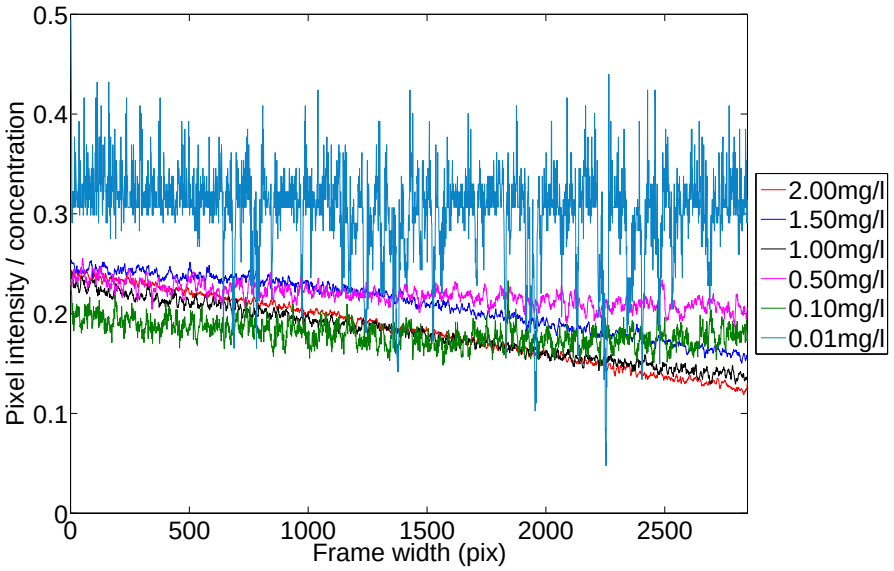

(b) Intensities normalised by concentration.

Figure 4.2: Attenuation of laser light intensity due to Rhodamine-6G. ISO speed: 1600, exposure time: 1/500s.

tant. Therefore the lowest concentration used for these experiments was 0.01mg/l of Rhodamine-6G.

The effects of subtracting the background intensity from the curves in Figure 4.2(a) and normalising against the bulk concentration are shown in Figure 4.2(b). Ideally each of these curves would have collapsed and be perfectly horizontal to show that the light intensity recorded by the camera only relies on the bulk concentration and that no light intensity is lost as the laser light passes through the Rhodamine-6G. However it is observed that strongest concentrations lose intensity across the width of the image in relation to the concentrations of 0.10mg/l and 0.50mg/l. It was also observed that the normalised profile for a concentration of 0.01mg/l of Rhodamine-6G has significantly higher normalised intensity values as well as a very high level of noise. This shows the large influence the background noise has on very low concentrations that have similar intensity values to the background noise.

This effect of the reduction of light intensity recorded by the camera across the width of the image was reduced by normalising the droplet images against a blank background image in the vertical direction. Combined with the change in laser sheet strength across the height of the image (discussed in Section 4.1.1) led to a normalisation formula given by

$$D_{ij} = \frac{A_{ij}}{B_{ij}}, \tag{4.1}$$

where D_{ij} is the normalised pixel matrix, A_{ij} is a pixel matrix of the light intensities relating to an image containing a droplet, B_{ij} is the same pixel matrix but corresponding to a blank image. i and j are the height and width coordinates of the pixels within the matrices. This normalises each individual pixel of the image with relation to the fluctuations of the laser sheet in the vertical direction and the attenuation caused by the Rhodamine-6G in the horizontal direction, as each pixel is normalised against a corresponding pixel with the same level of laser sheet power and same level of Rhodamine-6G attenuation.

4.1.3 Laser power stability

The stability of the laser power was important as the fluorescence emitted by Rhodamine-6G molecules is a function of the laser light absorbed by the molecules. The lesser the power from the laser, the less fluoresced light is emitted. If the laser beam fluctuates in power the light intensities recorded by the camera also fluctuates between droplets so droplets cannot be directly compared.

The stability of the laser beam was tested using a PM30 optical power meter

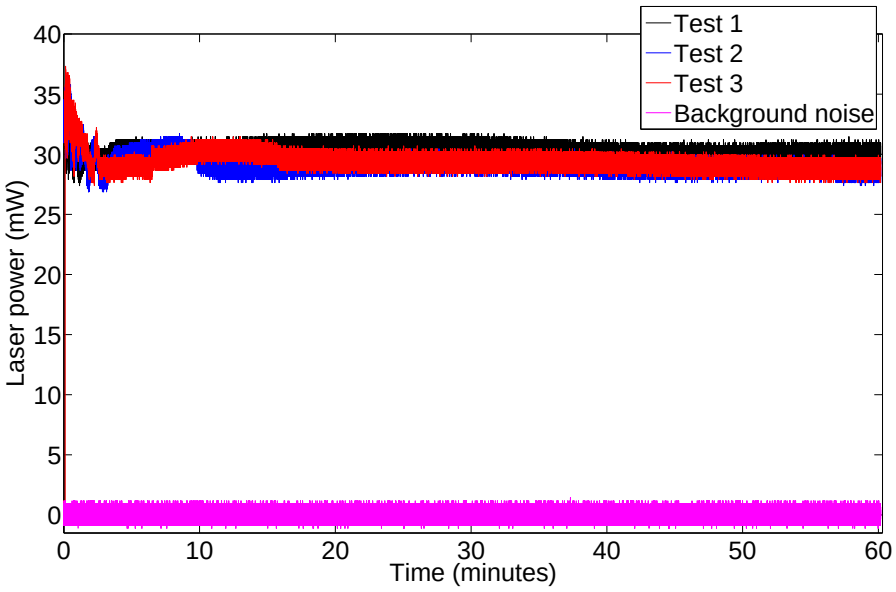

Figure 4.3: Laser power over 60 minutes along with background noise given by the data logger.

from Thorlabs to record the laser sheet power over a period of 60 minutes. A National Instruments data logger was used to record the analogue signal produced by the power meter. The laser power was measured 30 times a second in a darkened room with no ambient lighting to interfere with the readings and was repeated a total of three times. The laser power was recorded from the moment of laser initiation, with the laser having not been used for 12 hours prior to each experiment. This captured the laser warm-up period, tested whether the laser power stabilised over time, and how long the laser should be left to warm up before experiments. The raw data for the three laser power calibration tests are shown in Figure 4.3, along with the noise recorded by the data logger with the laser turned off.

Immediately after initiation the laser power reaches a peak before oscillating down to a steady power of approximately 30mW. The laser power in Test 1 significantly fluctuates for approximately 5 minutes before settling down. In Test 2 the laser power fluctuates for around 12 minutes, and in Test 3 it fluctuates for around 16 minutes after being switched on. Therefore, a minimum of a 60 minute warm-up period for the laser was used before experiments commenced.

The noise recorded by the data logger fluctuated over a range of 2.5mW in each test. This masked the behaviour of the laser power after the warm-up period. A moving average was applied to these curves to reduce the noise and reveal any variations of the laser power after the warm-up period.

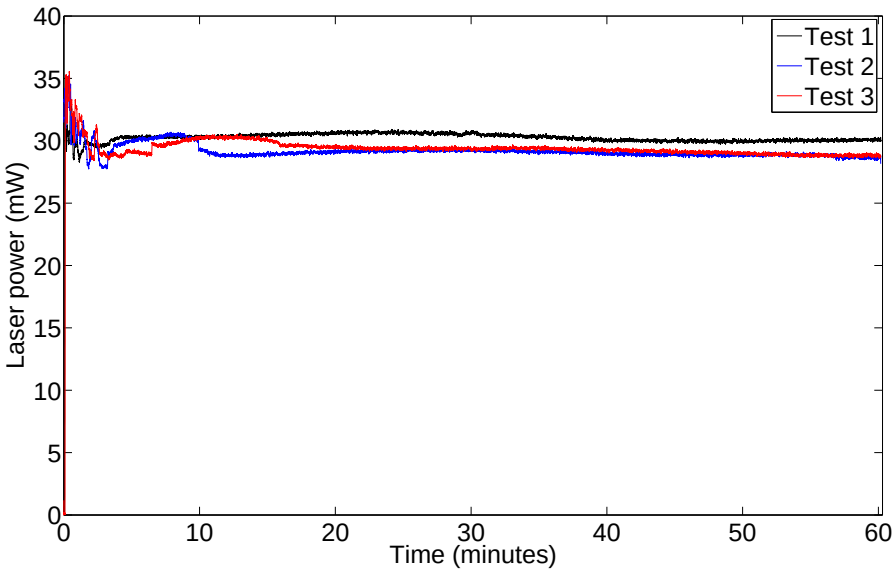

Figure 4.4: Smoothed laser power over 60 minutes.

Figure 4.4 shows the smoothed laser power calibration curves from Figure 4.3. It reveals that the laser power is inconsistent over time and individual experiments. For each test the laser power settled at a different base power with Test 1 significantly higher than Tests 2 and 3. This base power fluctuated over the course of the tests, and so a consistent power was unlikely across the experiments.

To reduce this effect, an image containing a droplet was normalised against an image of the same area with no droplet present with a scale factor to give the solution of the bulk an intensity of 1. This was achieved by calculating a scale factor, α, to relate the background intensities. α was calculated using

$$\alpha = \frac{\sum_{i,j}(A_{ij} - \bar{c})}{\sum_{i,j}(B_{ij} - \bar{c})}, \tag{4.2}$$

where i and j were not equal to the location of the droplet and any associated adsorption effects. α was introduced into Equation 4.1 to account for the laser stability giving

$$D_{ij} = \frac{A_{ij}}{\alpha B_{ij}}. \tag{4.3}$$

4.2 Droplet velocity measurements

The main factor that affected the rising velocity of the droplet was the radius; as larger droplets have a larger rising velocity. A second consideration was the behaviour that the droplet exhibits as it rises. As discussed in Section 2.1 a droplet can either rise as a solid particle with a rigid interface, or as a fluid droplet with a fully mobile interface. Droplets with completely mobile interfaces rise with a greater velocity than those exhibiting a solid behaviour as discussed in Section 2.1.4.

The third consideration was whether a change in the concentration of Rhodamine-6G within the aqueous phase would affect the rising velocity of the droplets, as the circulation of the interface may be disrupted by the adsorption of surfactant. Stronger levels of surfactant could cause greater disruption and so have a larger effect on the rising velocity.

To explore this, an experiment was performed to measure the rising velocity of droplets with different radii for different concentrations of Rhodamine-6G. The time taken for droplets to rise through 500mm of fluid was recorded with the radius extracted from a photograph of the droplet. The rising velocity was calculated and compared for three different strengths of Rhodamine-6G as shown in Figure 4.5. This graph shows that the range of concentrations of surfactant used in these experiments had no effect on the rising velocity of the droplet. Calculated for comparison with this data were solutions for the terminal rising velocity taken from literature as discussed in Section 2.1. The solid green lines show the limits for the theoretical rising velocity for a droplet with a completely mobile interface. The dashed black lines correspond to the limits for a theoretical solution of Stokes law for a solid sphere, where the interface is completely immobile, rising through the fluid. Both of these solutions were functions of the density difference and the viscosities of the oil and aqueous phases, with the limits calculated using the minimum and maximum density and viscosity data for the mineral oil at $20°C$. Comparison with the experimental data showed a good match for a droplet rising as a solid particle. This gave a model to calculate the droplet rising velocity for use as a parameter in the experiments.

4.2.1 Pixel slippage

The choice of exposure time potentially had an effect on the data, due to blurring caused by the distance travelled by the droplet while the shutter was open. The longer the shutter was open, the further through the frame a droplet of any size would move, leading to a larger pixel slippage. This creates blurring leading to a

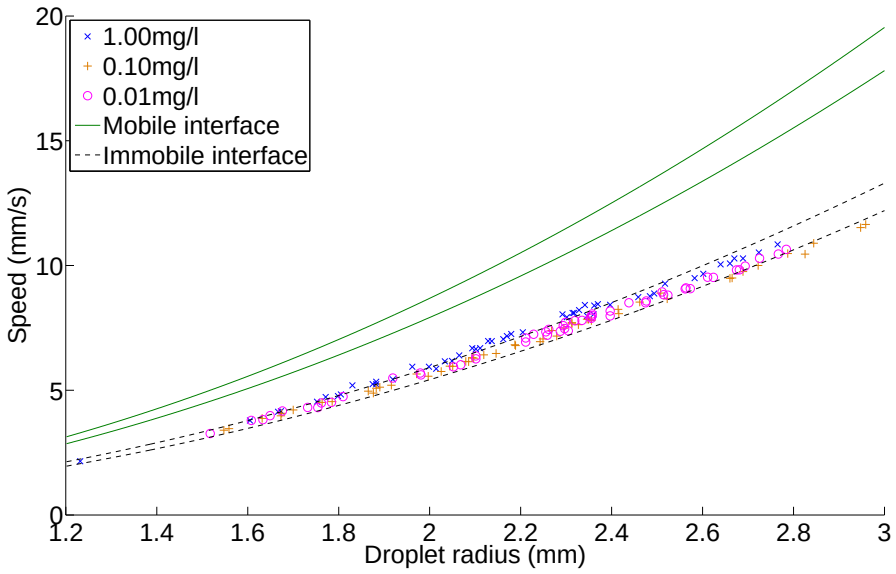

Figure 4.5: Rising speed of droplets for different radii and concentrations along with theoretical terminal velocities for droplets with a fully mobile and immobile interface calculated using the minimum and maximum density and viscosity data for mineral oil provided by the literature.

loss of quality in the image.

To measure this, the minimum, maximum, and an intermediate rising velocity were used to calculate the pixel slippage over the available range of exposure times. These calculated pixel slippage values are presented in Figure 4.6 and show that the shorter the exposure time the less slippage there is. Larger droplets have a larger pixel slippage at longer exposure times but converge with smaller droplet sizes as the exposure time shortens.

The shortest exposure time used in the experiments of 1/500s shows that the maximum sized droplet has a pixel slippage of 7.9 pixels which equates to 0.023mm, whereas the minimum sized droplet had a pixel slippage of 1.5 pixels, equating to 0.004mm. The longest exposure time used in the experiments of 1/100s had a pixel slippage for the largest radii droplet of 39.3 pixels and 7.3 pixels for the smallest droplet, equating to 0.116mm and 0.022mm respectively (pixel to millimetre conversion demonstrated in Section 4.3.1). Efforts were made to try to keep the exposure time as short as possible, although, as the largest droplet size measured in Figure 4.6 was the maximum achieved droplet size for the droplet insertion method used, it was unlikely droplets would often achieve this radii and so the exposure time of 1/100s was set as the longest exposure time that was used in the experiments

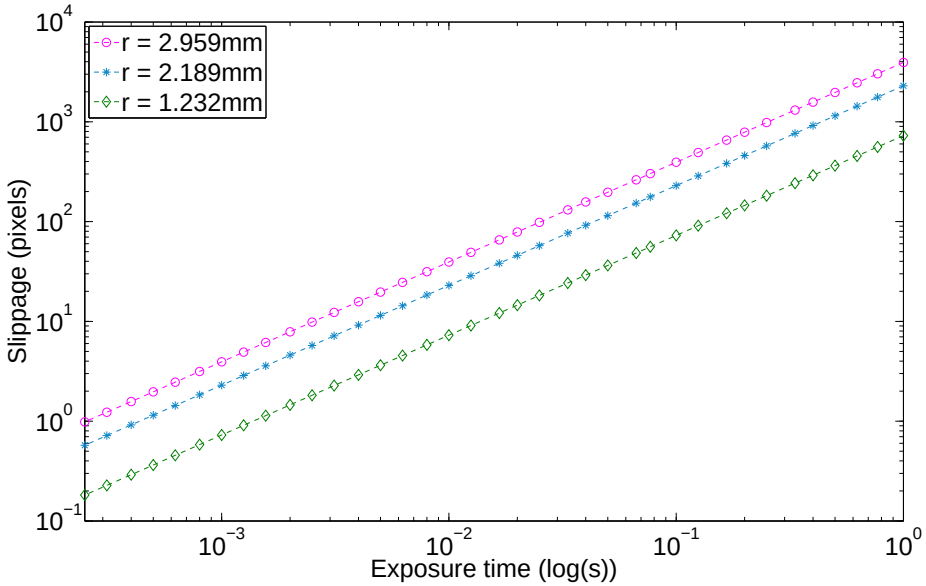

Figure 4.6: Pixel slippage over different exposure times for droplets with differing radii.

with an average slippage of less than one tenth of a millimetre.

4.3 LIF experiments calibration

To extract quantitative results from these experiments, the recorded values needed to be converted to standard units of measurement. For the LIF experiments there were two areas that needed to be explored. The first of these was to convert pixel length to millimetres. The second area was to relate camera intensity readings to the number of molecules per pixel in order to be used for comparison with experiments with different camera settings.

4.3.1 Length calibration

The aim of the length calibration was to calculate the number of pixels in a millimetre. This enabled the calculation of a droplet radius, surfactant layer thickness, and droplet wake radius from a photograph. This calibration was achieved by creating a calibration sheet consisting of black dots with a diameter of 1mm printed on a white background with separation between the droplet centres of 2mm. This was mounted on a rigid plate, inserted into the fluid, and photographed. From this image the size and distance between the black dots could be calculated to give the number of pix-

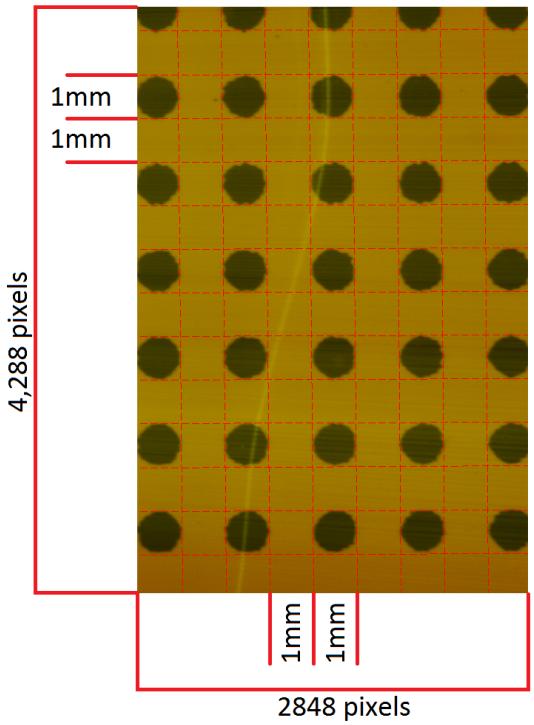

Figure 4.7: Process for pixel to millimetre conversion for LIF experiments.

els per millimetre. As high accuracy printing was not possible, averages were taken over a large range of dots to give 338 pix/mm. This photograph with calibration measurements is demonstrated in Figure 4.7.

4.3.2 Intensity calibration

This section explores the relationship between the different strengths of Rhodamine-6G and the light intensity recorded by the camera. This relationship enabled a conversion from light intensity per pixel to the number of Rhodamine-6G molecules per pixel. This section will also explore the effect of the different camera settings on the intensities recorded by the camera before individual calibration curves for each bulk concentration of Rhodamine-6G are produced.

Camera settings

The camera settings used for each experiment had an impact on the intensity recorded by the camera as well as contributing to the background noise associated with the camera sensor. Figure 4.8 shows the effect of increasing the ISO speed on the average pixel intensity for different concentrations of Rhodamine-6G taken

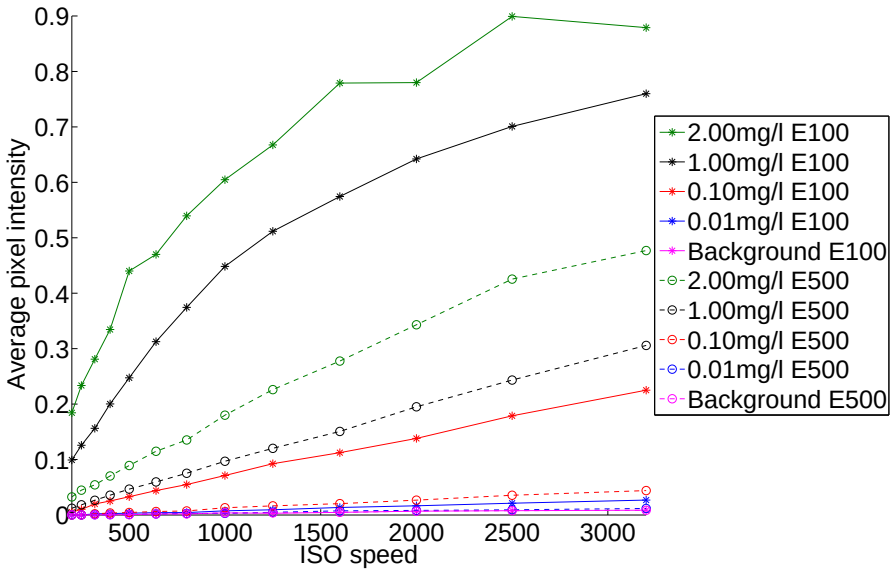

Figure 4.8: Effects of ISO speed on intensity and background noise for different exposure times measured as (1/E)s.

from the main experiments. The exposure times shown were for the maximum and minimum exposure times used in the experiments. The background noise associated with both of these exposure times is also shown.

For the higher concentration at the longer exposure time (E100), as the ISO speed increases the initial intensity increase is large. However as the ISO speed increases the intensity increase is slower. This is due to the camera sensor getting close to its maximum saturation at an intensity value of 1. This curvature is visible for Rhodamine-6G concentrations of 2.00mg/l and 1.00mg/l. Lower concentrations have a much more linear profile. This indicates that longer exposure times should only be used for lower concentrations of Rhodamine-6G in which it is unlikely to have strong enough peak concentrations to reach the upper limit of the camera sensor sensitivity.

The shorter exposure time (E500) shows a linear profile for all of the concentrations except for 2.00mg/l of Rhodamine-6G. This concentration starts with a linear increase before slightly flattening off at the higher end of the ISO speed spectrum. This indicates the existence of a point where an increase in concentration would not lead to an increase of intensity. Therefore experiments that contained a high level of Rhodamine-6G were performed using low ISO speeds. As stronger concentrations would have higher peak concentrations of Rhodamine-6G, the maximum

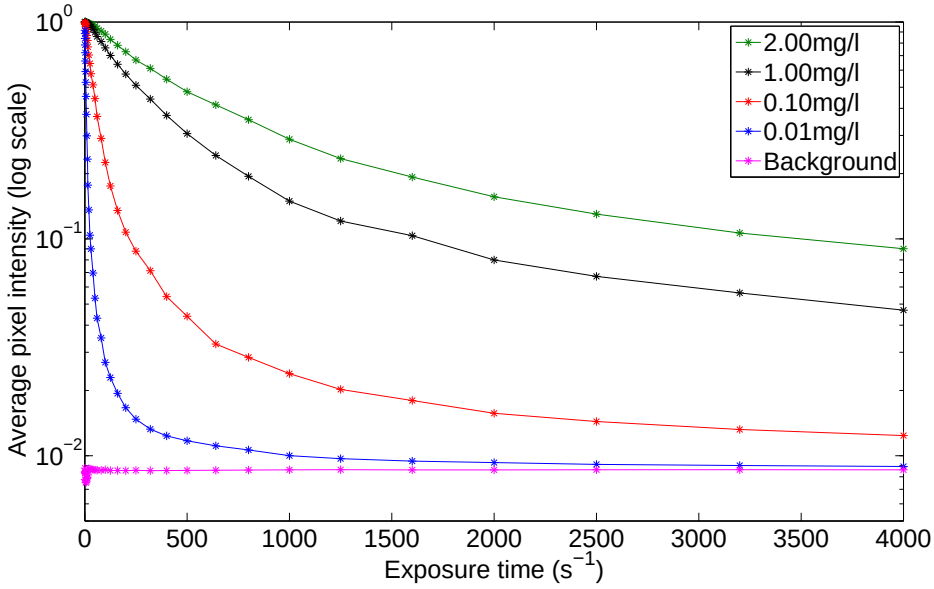

Figure 4.9: Effects of exposure time on intensity and background noise. ISO speed: 3200.

concentration of Rhodamine-6G that was used as the initial bulk concentration was 1.00mg/l to minimise potential loss of detail. The background intensity recorded by the camera sensor increases with the ISO speed but gives similar values for both exposure times, indicating that the background noise of the camera sensor was constituted mainly of noise attributed to the ISO speed.

Figure 4.9 shows the relationship between the average pixel intensity and the exposure time. As the exposure time decreases the intensity recorded by the camera sensor also decreases. This was to be expected as the shutter stays open for a shorter period of time. However, each of the concentrations has a different rate of decay. For the ISO speed of 3200 the strongest concentration of 2.00mg/l of Rhodamine-6G has a continuous decrease over the entire range of exposure times, with a sharper decrease at longer exposure times. However for a Rhodamine-6G concentration of 0.01mg/l, there was a very sharp initial decrease before the intensity converges to the intensity of the background noise. For lower concentrations there was a careful selection of the camera exposure time to ensure a clear intensity resolution. The background noise remained constant throughout the range of exposure times.

Due to these results and the inability to predict the camera settings for each concentration, a library of calibration files was constructed for each concentration, each ISO speed, and each exposure time. This ensured that for every bulk Rhodamine-6G concentration, the calibration data for concentrations used in pre-

vious experiments existed for the correct camera settings.

Background noise

Background noise was caused by a combination of ambient light and the camera settings selected for each experiment. A method was developed to remove the background noise from the data. This was done by finding the average background noise for each camera setting by capturing a set of calibration images with the laser switched off. This measured the background noise associated with each combination of camera settings. From here the average pixel intensity was calculated across the entire image for the experiments with corresponding camera settings. The averaged background noise was subtracted from each pixel for each calibration image and experimental image. This process was combined with Equation 4.3 developed for the laser calibration to give

$$D_{ij} = \frac{A_{ij} - \bar{c}}{\alpha(B_{ij} - \bar{c})}, \tag{4.4}$$

where $\bar{c}$ is an averaged value for background noise given by

$$\bar{c} = \frac{1}{i \times j} \sum_{i,j} C_{ij}, \tag{4.5}$$

in which C_{ij} is an array of the intensities captured for the background noise, with i and j the pixel coordinates.

Concentration strengths

As well as the calibration measurements for each concentration of the experiment, calibration measurements for a concentration of zero were captured at the lower end of the spectrum with an extension at the higher end of the concentration range to deal with any increase in surfactant levels during the experiments. The first stage to achieve the intensity calibration was to convert the number of Rhodamine-6G molecules per millimetre squared to the number of molecules per pixel. This was achieved using the length calibration values obtained in Section 4.3.1 combined with the calculated value for the number of molecules per mm^3 from Section 3.5.1. The captured images were two-dimensional with a depth of 1mm due to the thickness of the laser sheet. Therefore each pixel is a measurement of the light intensity over a depth of 1mm.

A complete list of the calibration concentrations used in the main experimental series along with the conversion to the number of molecules per pixel is given in

Table 4.1.

Table 4.1: Number of Rhodamine-6G molecules per pixel for calibration concentrations in the main experimental series.

Rhodamine-6G concentration (mg/l)	Number of Rhodamine-6G molecules per pixel
0	0
0.01	1.10×10^5
0.02	2.20×10^5
0.03	3.30×10^5
0.04	4.40×10^5
0.05	5.50×10^5
0.06	6.60×10^5
0.08	8.81×10^5
0.10	1.10×10^6
0.20	2.20×10^6
0.30	3.30×10^6
0.40	4.40×10^6
0.50	5.50×10^6
0.60	6.60×10^6
0.80	8.81×10^6
1.00	1.10×10^7
1.50	1.65×10^7
2.00	2.20×10^7

Calibration curves

For each Rhodamine-6G concentration tested, the relevant calibration files for the camera settings used were selected from the calibration library to produce calibration curves. Values from Table 4.1 were used to convert the concentrations from mg/l of Rhodamine-6G to the number of Rhodamine-6G molecules per pixel which were then compared to the average pixel intensity for the camera settings relevant to the experiment.

The same camera settings were used for experiments involving different bulk surfactant concentrations producing duplicated raw calibrations curves as shown in Figure 4.10.

Each of the curves follows a general increasing trend, as expected from an increase in concentration of Rhodamine-6G. However due to the fluctuations in the laser power there are undesired peaks leading to points where one intensity could have two different concentrations. These calibration curves needed to be smoothed

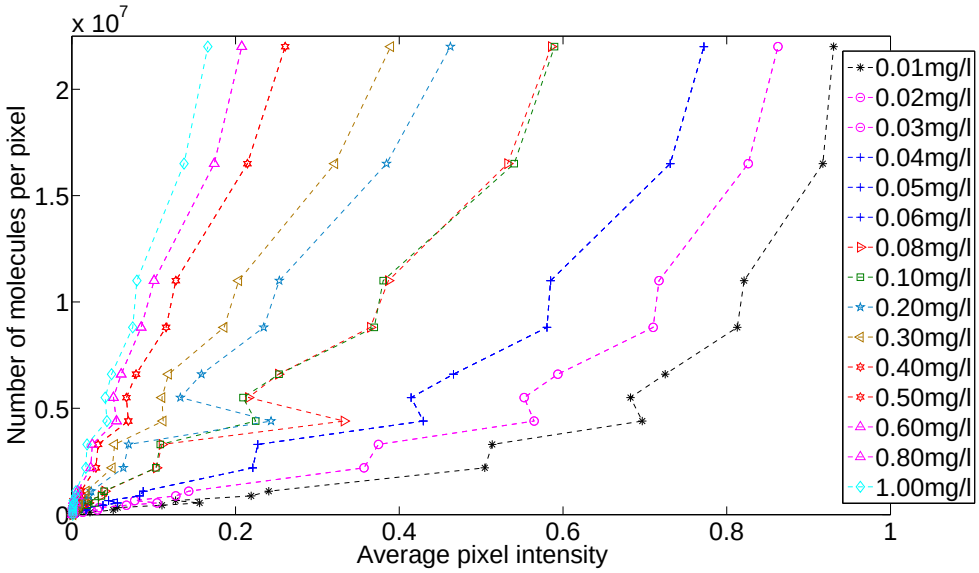

Figure 4.10: Raw calibration curves based on the camera settings for the main experimental series.

to give monotonically increasing curves. The only known point was at a surfactant concentration of 0.00mg/l as there is no Rhodamine-6G to fluoresce and so a change in laser power would not affect this reading. Due to this, the data point for 0.00mg/l of Rhodamine-6G was heavily weighted, and monotonically increasing curves were fitted to the rest of the data points as shown in Figure 4.11. A comparison to the raw data points show a successful fit for the data.

The final stage was to normalise these calibration curves against the calibration value for the bulk concentration to give a bulk concentration equal to 1. This gave a unique calibration curve for each different bulk concentration as shown in Figure 4.12, enabling interpolation and extrapolation of the intensity of a pixel in an image to the corresponding number of molecules of Rhodamine-6G at that pixel.

4.4 PIV experiments calibration

The vector fields produced by the PIV analysis were calculated using the commercial software package DynamicStudio v4.10 from Dantec Dynamics. This software required a length calibration to relate the pixel size to millimetres. Also considered here was whether the reflective particles interacted with the interface and affected the surfactant adsorption process.

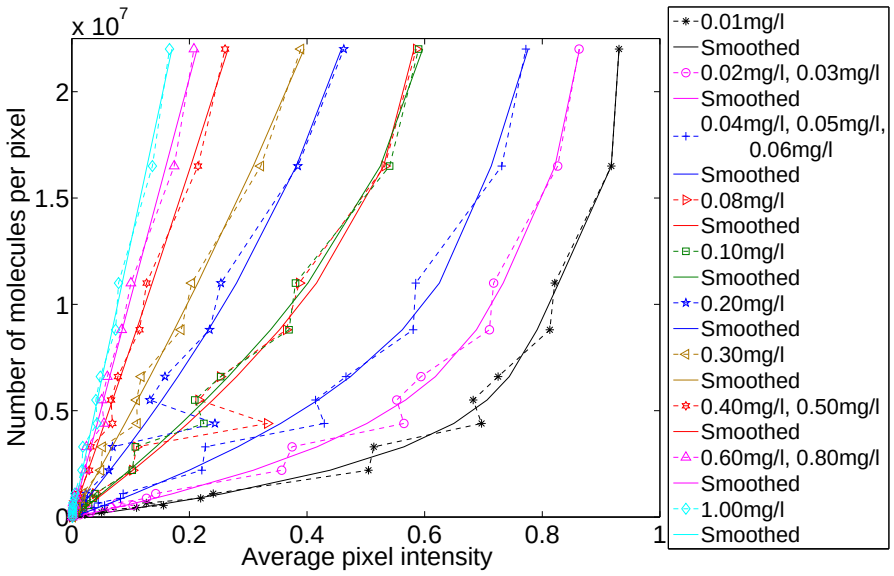

Figure 4.11: Smoothed calibration curves for main experimental series.

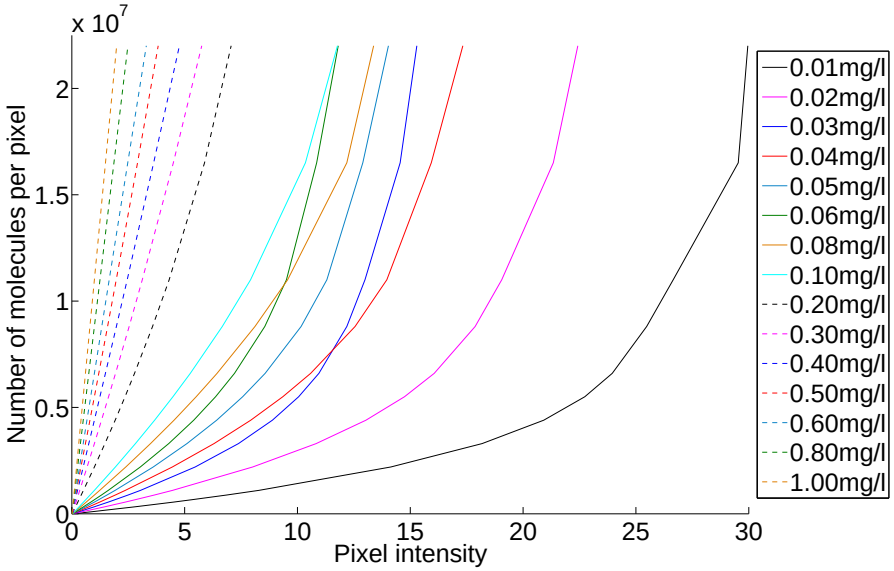

Figure 4.12: Normalised calibration curves for each concentration in main experimental series.

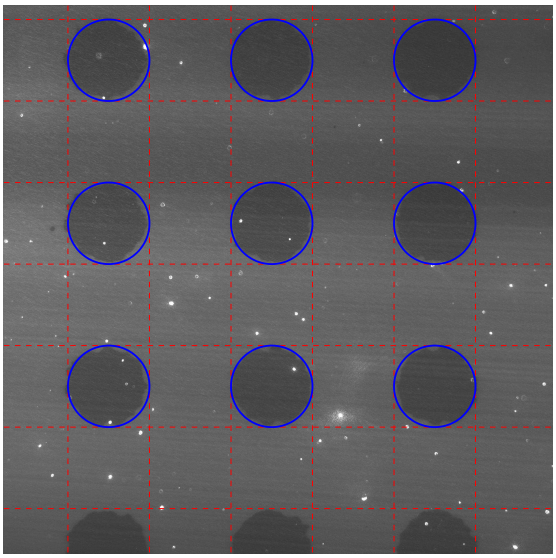

Figure 4.13: Process for calibrating the pixel length for PIV experiments for the shortest focal length.

4.4.1 Length calibration

This was the same process as performed for LIF, however a different camera was used and so the measurements were different. The camera used for PIV had a square field of view measuring 2,048 pixels by 2,048 pixels. It was found that the depth of field for the camera used for PIV experiments was more sensitive than the camera used for LIF and so the focal length had to be changed throughout an experiment. Three different focal lengths were used for the PIV experiments and had to be calibrated.

Figure 4.13 shows the process used to calibrate the number of pixels in a millimetre for the shortest focal length used for the PIV. The same calibration plate was used as for the LIF experiments, with measurements averaged over multiple points to account for inaccuracies in the manufacturing of the calibration plate. The commercial software imputed these values and converted them to scale factors. The conversion from pixels to millimetres for each focal length along with the corresponding scale factor are given in Table 4.2.

4.4.2 Effects of particles on LIF measurements

To test whether the reflective particles used for the PIV had an effect on the adsorption dynamics at the interface and therefore the results, droplets from the PIV experiment containing tracer particles were photographed using the LIF filter to

Table 4.2: Scale factors associated with different focal lengths in the PIV experiments.

Lens focal length	Pixels per millimetre	Scale factor
0.33m	304.5	0.5905
0.34m	290.5	0.6205
0.35m	276.5	0.6505

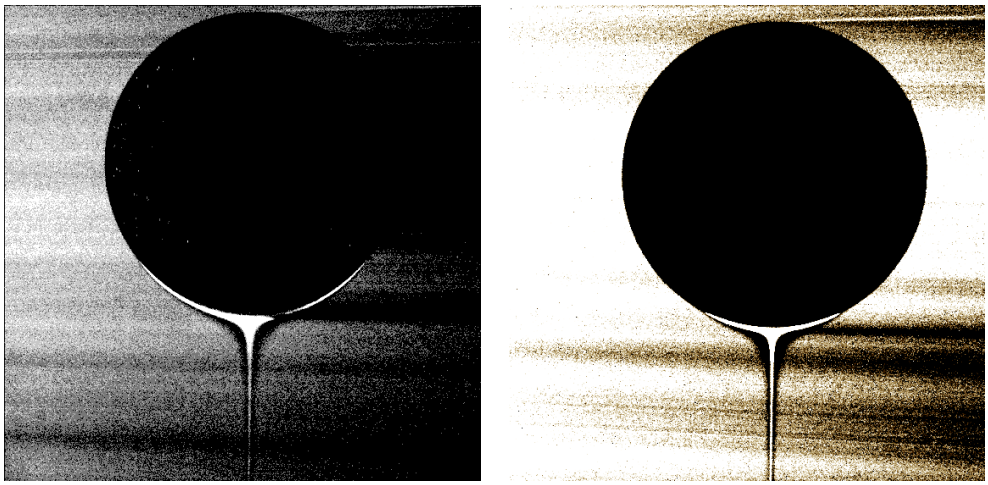

(a) Droplet with reflective tracer particles from PIV exerimental setup,

(b) Droplet without particles from LIF experimental setup.

Figure 4.14: A comparison of LIF for droplets as captured by cameras used for PIV and LIF experiments respectively. Rhodamine-6G concentration of 1.00mg/l. Height from base of tank: 460mm.

block out the reflected light from the particles. Although intensity calibration had not been performed, the images could be qualitatively measured and compared with a droplet from the LIF experiments with the same concentration and position in the tank. Figure 4.14 shows an example of the results gained using the LIF filter for the PIV and LIF experiment setups respectively. The only difference between the two images was the camera used to photograph the droplet and the presence of tracer particles in Figure 4.14(a).

Figure 4.14 compares droplets of an approximately equal size. It shows the existence of a bright cap at the rear of the droplet in both images. This shows that adsorption of Rhodamine-6G is not being prevented due to the presence of the reflective particles interacting with the interface. The surfactant caps are of a similar size and shape and so the reflective particles do not have an overriding contribution to the adsorption process at the interface.

4.5 Summary

This chapter has looked at the calibration techniques and procedures that were performed in order to produce accurate quantitative results. Deficiencies of the experimental setup were considered along with methods to correct these deficiencies. The first issue was caused by the laser. The laser was a key part of the experiment, being the source of light to produce fluorescence for the LIF and reflections for the PIV. It was found that the profile of the laser sheet over the field of view was not consistent, in part due to the laser sheet optics and in part due to the different strengths of Rhodamine-6G absorbing the laser light in differing quantities as it passed through the width of the image. The final issue with the laser was that the power fluctuated with time. Each of these issues was addressed to produce a normalisation process to apply to each image to reduce these effects.

Factors that had the potential to affect the rising velocity of the droplet were considered, as the radius of the droplet was a potential variable in the experiments. It was shown that changes in concentration did not affect the rising speed of the droplets which moved through the fluid with a profile of a droplet rising as a rigid sphere. The effects of the droplet radius and exposure times on the blurring of an image were explored and found to be minimal for the selected camera settings.

The main calibration process was to relate measured intensities of light at each pixel to the number of molecules of Rhodamine-6G. A large library of calibration data was gathered to ensure that data existed for any combination of camera settings. These camera settings were used to produce unique calibration curves for each strength of Rhodamine-6G. Smoothing techniques had to be applied to the calibration curves used for the main experiments to ensure that they were monotonically increasing so that there were no points of duplicated intensity.

Calibration was performed on both LIF and PIV experiments to allow the conversion between number of pixels and millimetres. Finally there was a comparison of LIF images obtained using the PIV and LIF experimental setups to show the validity between the experiments when reflective particles were added to the PIV droplets.

Chapter 5

Raw data and analysis

This chapter looks at the raw data gathered in the experiments and how the data were processed. It begins with an example of the data obtained by LIF to observe the fundamental challenges faced with the analysis of this data. From here the analysis begins with the normalisation of the data to reduce the effects of any irregularities introduced by the experimental setup as described in Section 4.1. The normalised data values were converted to quantitative values for comparison with other experiments and theory. Each stage will include a discussion as to the pitfalls that were overcome along with any equations and methods used.

The second part of the chapter looks at the PIV data, the software used to calculate the vector fields, and the techniques used to average and further process these vector fields.

5.1 LIF raw data

This section gives an example of the raw data obtained from the main LIF experiments. This gives an understanding of the challenges and pitfalls associated with dealing with large quantities of this data. The data give an insight into the mechanisms which are described along with the aims of the data processing.

5.1.1 Data quantity

As discussed in Section 3.9, to ensure the accuracy of the data and to reduce the effects of any anomalies, multiple droplets were photographed for each concentration and height. For the main experimental series, eleven positions in the tank were photographed for fifteen different concentrations. A minimum of twenty droplets were captured at each height for each concentration. This gave a total of 3,306 data

points to be processed with each data point consisting of a photograph containing a droplet and a background photograph to normalise against.

A calibration library was created to accompany these data points to cover the full potential range of variable parameters as these were not known in advance. The calibration library consisted of 9,139 data points.

This large quantity of data needed to be processed, and it was important that this was an automated approach as it was not feasible to process each data point individually.

5.1.2 Raw LIF result

Changes were made between the preliminary experimental series shown in Appendix A and main experimental series to increase the resolution of the droplet by magnifying it further, and to decrease the distance between photographs to enhance the spatial resolution of the data. The position of the first image was raised by 10mm, as the droplet released in Figure A.3(a) shows deformation at the rear as it had not had time to stabilise after release from the injection nozzle. Figure 5.1 shows the effects of these changes. The first position after the release of the droplet is shown in Figure 5.1(a). There is a dark shadow forming at the rear of the droplet. In Figure 5.1(b) this shadow has developed into a dark wake with a bright surfactant cap at the rear of the droplet. Figure 5.1(c) show the beginning of a bright tail forming within the dark wake, which grows and stabilises in Figures 5.1(d) onwards.

Figure 5.1 demonstrates that the rear of a droplet passes through different stages as it rises through a surfactant-rich solution. The first stage, shown in Figure 5.2, occurs at the lower end of the tank shortly after the release of the droplet. This stage consists of Rhodamine-6G molecules, dispersed in the aqueous solution, adsorbing to the interface of the droplet. This process is made apparent by a dark surfactant-depleted zone that develops at the rear of the droplet. Ideally, at the release of the droplet there would be no surfactant on the interface. However, during the creation of the droplet it expands out of the injection nozzle and the interface is exposed to surfactant solution and adsorption occurs before its release. This could affect the duration of this first stage, as once a sufficient volume of Rhodamine-6G molecules adsorb to the interface they are swept around to the base of the droplet where they accumulate forming a bright surfactant-rich cap, as shown in Figure 5.3. Adsorption is continually occurring at the forward facing part of the droplet as indicated by the presence of a dark, surfactant-depleted wake behind the droplet. This is the second stage.

The third and final stage of the development of the droplet is the creation of a

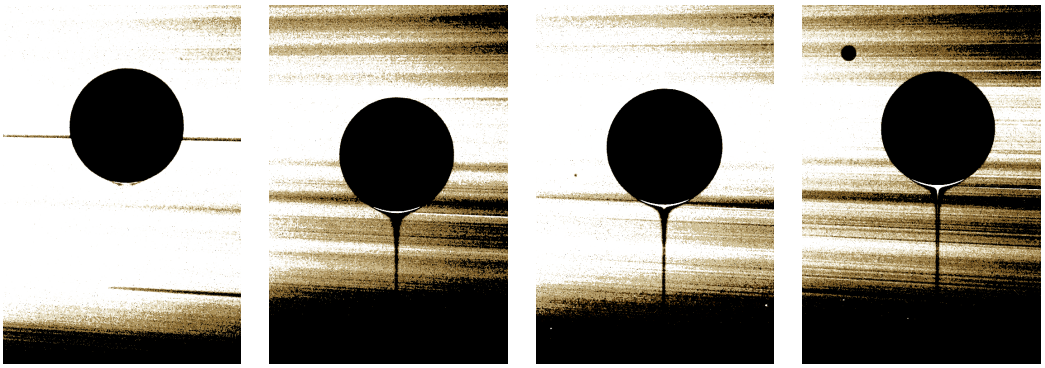

(a) Height = 10mm, (b) Height = 60mm, (c) Height = 110mm, (d) Height = 160mm,

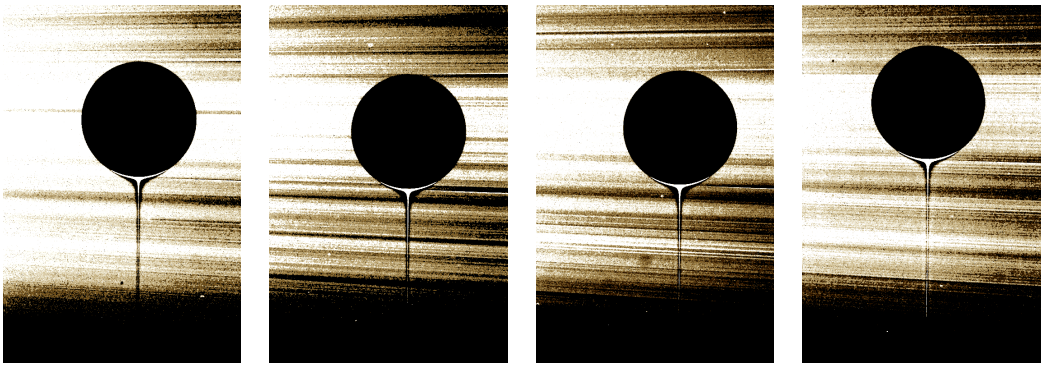

(e) Height = 210mm, (f) Height = 260mm, (g) Height = 310mm, (h) Height = 360mm,

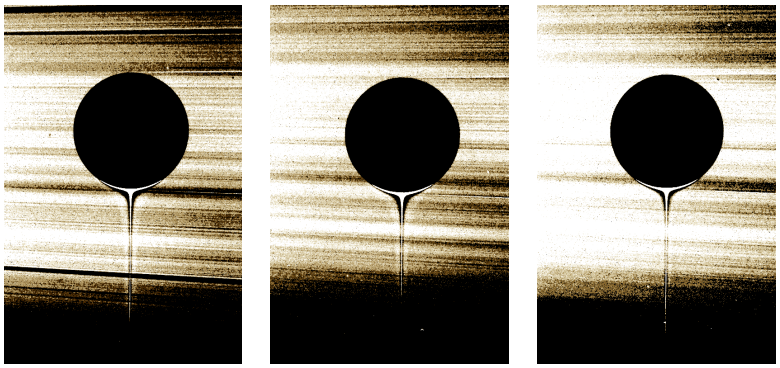

(i) Height = 410mm, (j) Height = 460mm, (k) Height = 510mm.

Figure 5.1: Examples of droplets at different heights from the base of the tank in the main experimental series for a Rhodamine-6G concentration of 0.50mg/l. Photographs edited for clarity.

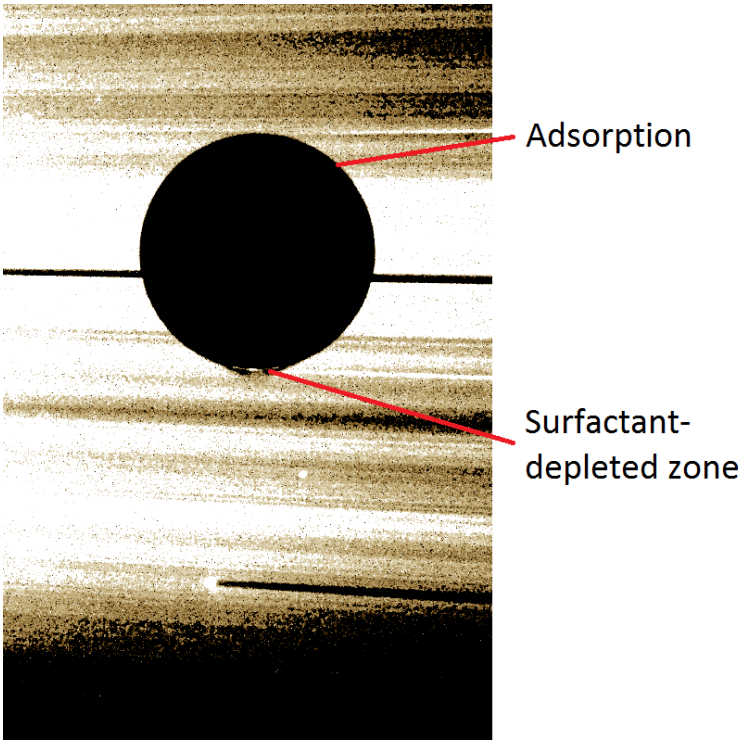

Figure 5.2: First stage of droplet wake development.

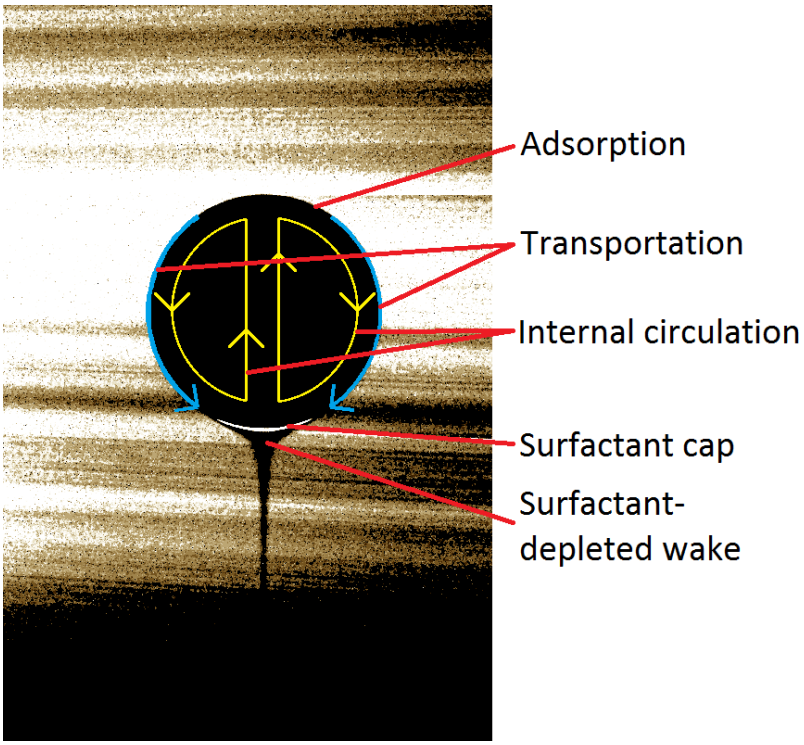

Figure 5.3: Second stage of droplet wake development.

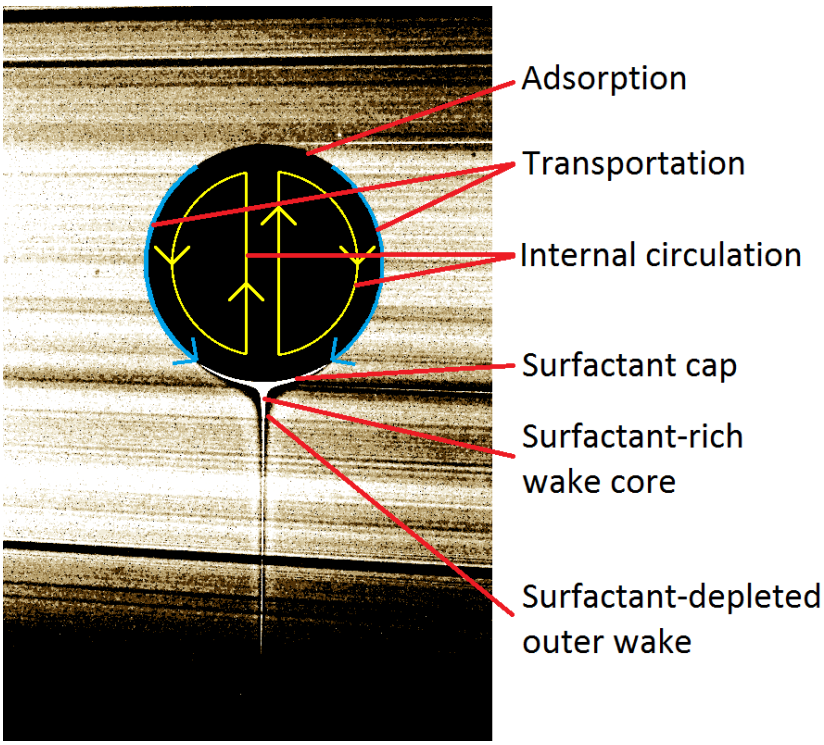

Figure 5.4: Third stage of droplet wake development.

core, surfactant-rich wake within the dark, surfactant-depleted wake. This is demonstrated in Figure 5.4, and is caused by the surfactant cap behind the droplet reaching a surfactant saturation level. This is caused by the Rhodamine-6G molecules that are continually adsorbed to the front of the droplet being swept around to the surfactant cap at the rear. The surfactant cap reaches a level at which no more Rhodamine-6G can be held at the interface behind the droplet so the Rhodamine-6G gets swept back into the flow. The volume of surfactant being swept back into the flow is initially small, but increases until it is comparable to the volume being adsorbed at the front of the droplet.

5.1.3 LIF processing objectives

The initial visual examination of the data assisted in the identification of objectives for the LIF data processing and analysis. These objectives were identified as:

- Image normalisation: To reduce the effects of irregularities within the images.
- Quantifying the size and volume of the surfactant cap: To see how the size of the surfactant cap grows over the height of the tank, along with the volume

of Rhodamine-6G molecules held behind the droplet.

- Droplet averaging: To develop a technique to average over droplets of different radii and to assess the validity of such a process.
- Comparison of the surfactant cap development over different surfactant concentrations: To compare the effects of different surfactant strengths on the size and formation of the surfactant cap.

5.2 LIF processing

The main aim for the LIF processing was to produce quantitative data for comparison with theoretical models and other experiments. To do this irregularities had to be accounted for before relating experiment specific values to standard units of measurement. An objective for the LIF processing was to produce averaged profiles of the surfactant distribution around droplets for each height and bulk solution surfactant concentration. This task was split into two sections, firstly to calculate the concentration of Rhodamine-6G at each point on the interface in terms of the quantity of Rhodamine-6G molecules, and to secondly calculate the angle and volume of the visible surfactant cap.

This section follows the processing methods and techniques applied to a single droplet to extract quantitative data, from the normalisation process, through to conversion to standard units of measurement, through to the extraction of meaningful data. Finally the validity of averaging the data over different droplet radii was explored.

5.2.1 Droplet identification

The first stage of processing the LIF data was to locate the droplet within each image. An attempt was made to automate this process based on the light intensity of the oil droplet being significantly lower than the intensity of the bulk fluid. However, as discussed in Section 4.1.1, the intensity at the bottom edge of the field of view was of a significantly lower intensity, similar to the intensity of the oil droplet. This often caused the location of the droplet to be missed.

The solution to this was to manually cycle through the photographs selecting a point within each droplet. By working outwards from this point, Matlab R2013b from MathWorks was used to locate the edge of the droplet and therefore the centre point and radius of the droplet. This was achieved using the difference in light intensity between the oil droplet and the bulk solution. It was found that the

droplets were not perfectly circular. They were stretched slightly along the vertical axis which meant that circular profiles could not be applied to the droplets. Cycling through the droplet images in this fashion additionally allowed a visual validation for every data point ensuring all droplets were within the target area, in focus, and correctly aligned with the laser sheet.

5.2.2 Image normalisation

Normalisation of the images took place to reduce the effects of any systematic irregularities. These were irregularities associated with shadows caused by the laser sheet passing through defects in the tank walls, as well as fluctuations in the laser power over the height of the laser sheet (as discussed in Section 4.1).

Normalisation was achieved by capturing the target area with the droplet present and capturing exactly the same area but without the droplet. The light intensity values were stored in arrays where A is an array of the light intensity values of an image containing the droplet, and B is an array of the light intensity values of a blank image. The intensity values of the normalised image, D, were achieved using

$$D_{ij} = \frac{A_{ij} - \bar{c}}{\alpha(B_{ij} - \bar{c})}, \tag{5.1}$$

where i and j are the coordinates of the arrays, $\bar{c}$ is an averaged value for background noise given by

$$\bar{c} = \frac{1}{i \times j} \sum_{i,j} C_{ij}, \tag{5.2}$$

where C is an array of background intensity values recorded by the camera associated with sensor noise and ambient lighting. α is a scale factor used to correct for the instability in the laser power and is calculated as

$$\alpha = \frac{\sum\limits_{i',j'} (A_{i'j'} - \bar{c})}{\sum\limits_{i',j'} (B_{i'j'} - \bar{c})}, \tag{5.3}$$

where i' and j' are areas corresponding to the array positions of Area X in Figure 5.5. This discounted the effects of intensity changes due to the droplet so that the intensities of the bulk solutions could be matched. These equations are derived in full in Section 4.1.

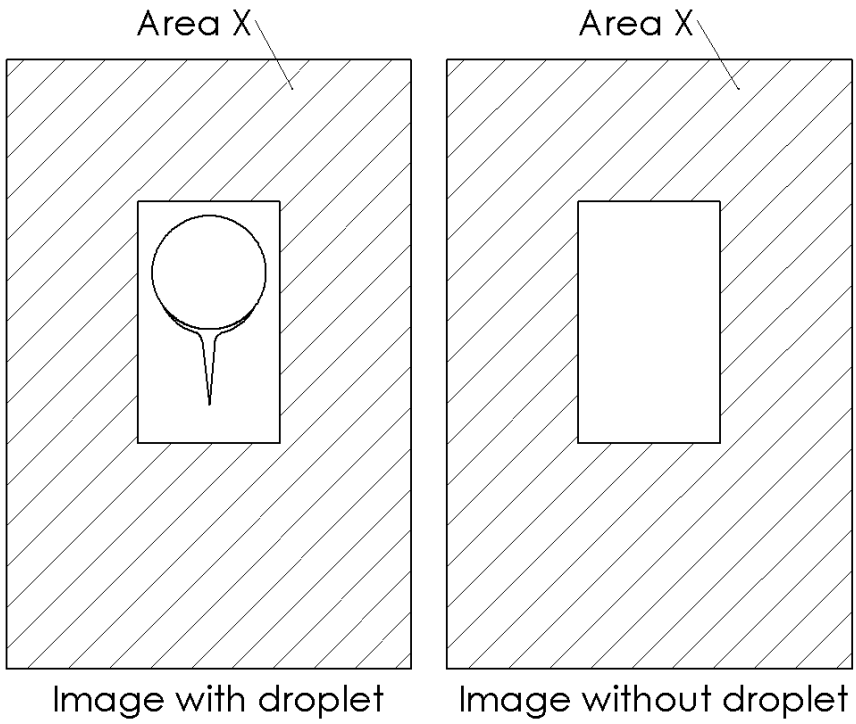

Figure 5.5: Area of images used for calculating α for image normalisation.

5.2.3 Droplet mapping

As circular profiles could not be directly applied to the interface a method was developed to extract data from the interface. This was achieved by measuring the light intensity values radially outwards from the centre of the droplet. The droplet was split into segments and the intensity values were measured outwards from the droplet centre, with a spacing equal to the length of one pixel, for a total length of double the droplet radius. This extended beyond the droplet interface to capture the detail within the wake at the rear of the droplet. The droplets from the main experimental series were split into 6,000 segments with a division of 0.060°. An example of a droplet having been split into segments along with the droplet circumference calculated from an automated process is shown in Figure 5.6.

This method consisted of extracting data using polar coordinates from a Cartesian coordinate based pixel grid, so very few of the desired data points coincided with the array positions of the recorded intensities. Therefore a process was developed to map the intensity points from the rectangular arrays of intensities to the data points along the radial lines. Figure 5.7 demonstrates a radial intensity point, I_{xy}, falling between four known intensity values in an array, I_1 to I_4. The

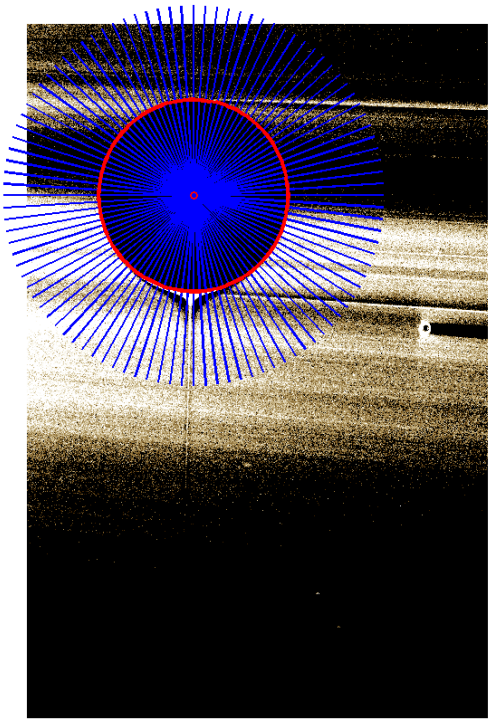

Figure 5.6: Process of dividing the droplet into segments (100 segments shown).

desired intensity was calculated as a function of the four closest intensity values stored at coordinates representing the centres of each pixel. A weight was assigned to each intensity value based on its distance, r, from the desired intensity point, with shorter distances carrying a larger weight and therefore having a larger contribution to the desired intensity value. The equation used to calculate the radial intensities from the closest four known intensities is given by Equation 5.4.

$$I_{xy} = \frac{\frac{I_1}{r_1} + \frac{I_2}{r_2} + \frac{I_3}{r_3} + \frac{I_4}{r_4}}{\frac{1}{r_1} + \frac{1}{r_2} + \frac{1}{r_3} + \frac{1}{r_4}}. \tag{5.4}$$

The intensities along these segment lines were stored in an array working clockwise around from the front of the droplet. This produced a droplet with the interface mapped to a straight line as shown in Figure 5.8. The oil phase constitutes the top half of the image with the droplet interface running in a horizontal line across the centre of the image with the surfactant cap in the centre. The lower half of the image is the aqueous phase with dark semicircles at the base of the image corresponding to where the radial lines overshoot the edge of the image array, as in Figure 5.6.

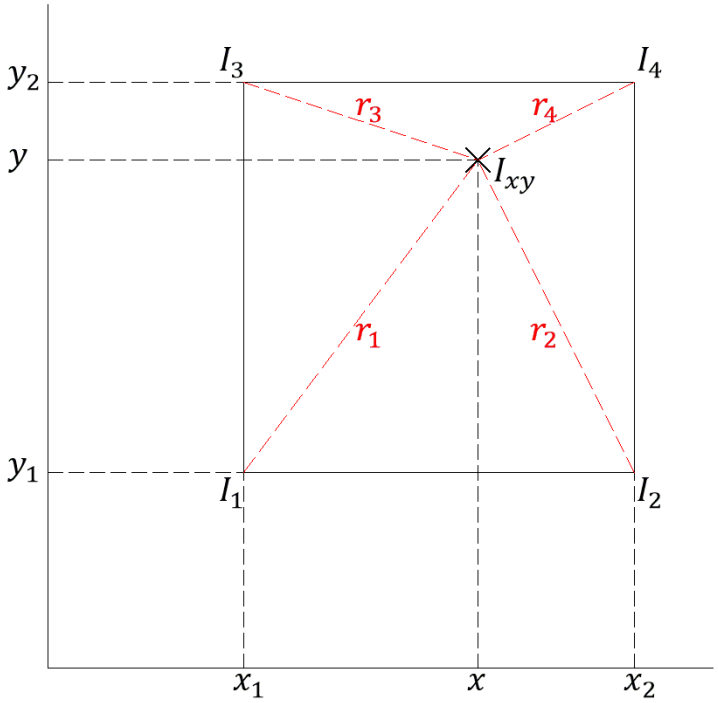

Figure 5.7: Terminology used for calculating point intensity from the nearest four pixels.

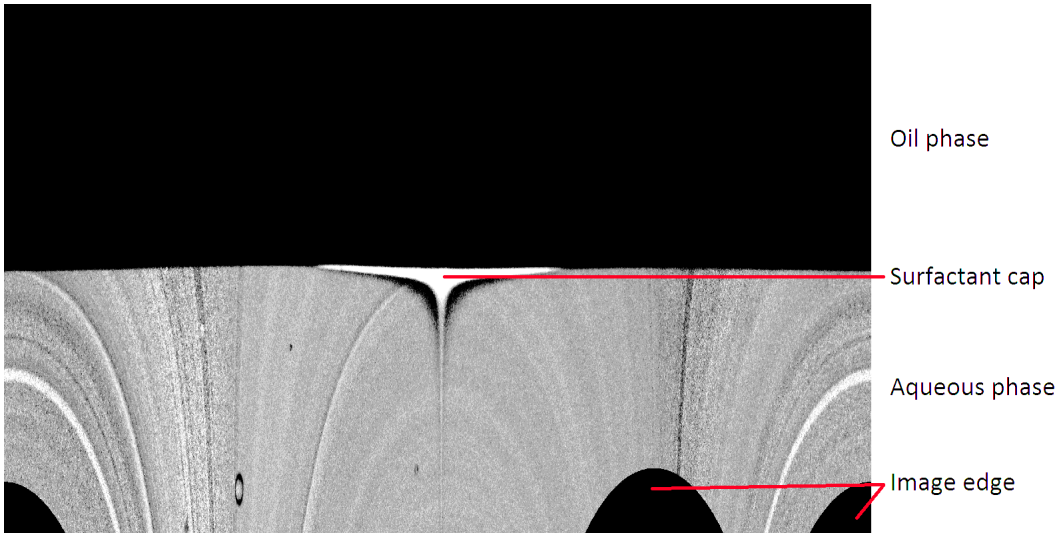

Figure 5.8: An example of linearising a droplet. Rhodamine-6G concentration: 0.50mg/l from preliminary experimental series. Height: 456ml from the base of the tank.

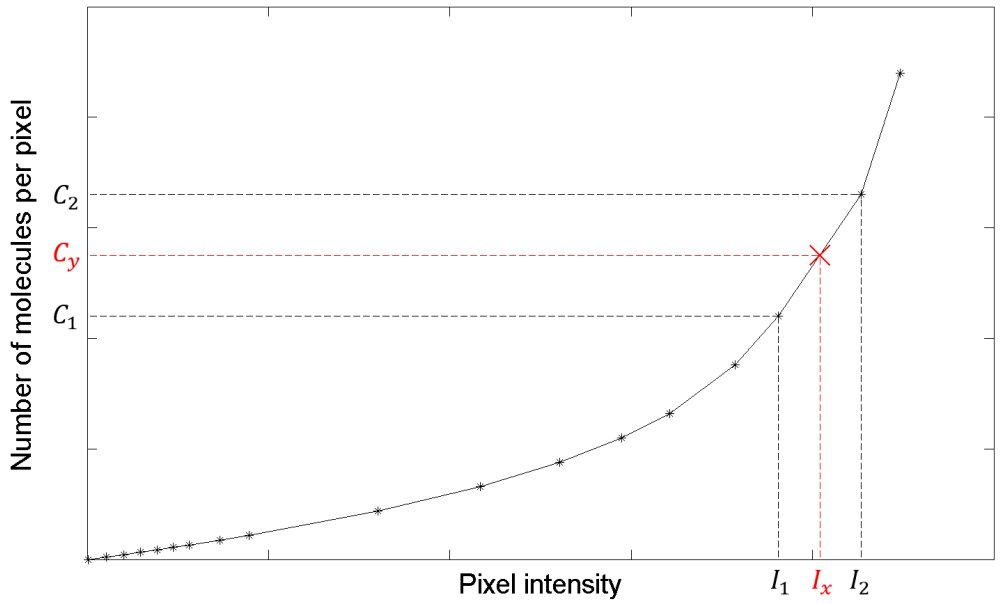

Figure 5.9: Calibration curve showing interpolation process.

5.2.4 Intensity conversion

The intensity readings for each pixel were converted to the number of Rhodamine-6G molecules at this stage in order to calculate the volume of molecules held in the surfactant cap. Two different processes were used for the conversion; interpolation when the intensity fell within the range of calibration data gathered, and extrapolation when the intensity was greater than the highest concentration measured for the calibration data. This mainly happened for the higher bulk concentrations of Rhodamine-6G.

Using the intensity calibration curves produced in Section 4.3.2 the intensity for each array value was converted to the number of Rhodamine-6G molecules at that position. This was achieved by locating the closest intensity points located in the calibration library above and below the value of intensity for conversion. A linear relationship was assumed between these points as for low concentrations with a large difference in intensity there was a high density of known points, whereas for higher concentrations there was a smaller change in intensity. The ratio of the distance between intensity values was used to calculate the concentration of Rhodamine-6G molecules. A calibration curve with this process is shown in Figure 5.9, with Equation 5.5 used to interpolate the concentrations.

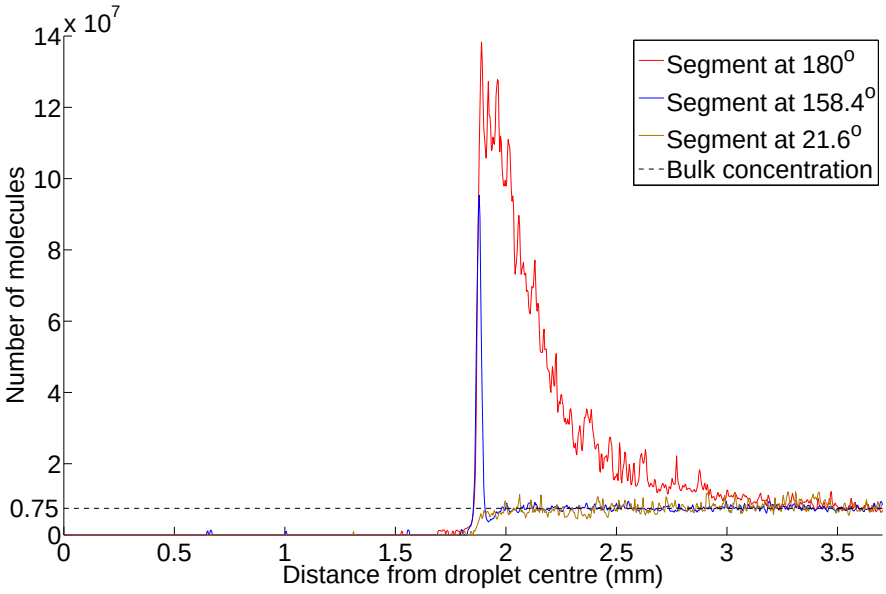

Figure 5.10: Concentration profiles of segments passing through different angles. All angles measured from the front of the droplet.

$$C_y = C_1 + (C_2 - C_1)\frac{(I_x - I_1)}{(I_2 - I_1)}, \tag{5.5}$$

where C_y is the desired concentration, C_1 and C_2 are known concentrations from the calibration library relating to intensities I_1 and I_2, and I_x is the intensity value from the array to be converted.

Equation 5.5 was also used to extrapolate data for intensity values that fell above the measured range. For the main experimental series the linear profiles between the two highest known concentration points, and between the highest and third highest known concentration points were averaged to produce a linear profile which was extended outwards.

5.2.5 Concentration profiles

Figure 5.10 shows concentration profiles along three different segments measured radially outwards from the centre of a droplet taken from the preliminary experimental series. Each segment represents an angle step of 0.072° which is measured clockwise from the front of the droplet. The positions of these example segments are shown in Figure 5.11. The yellow line shows an example of the concentration profile from the adsorption zone at an angle of 21.6° from the front of the droplet. At this angle accumulation of surfactant is not expected so there should be a instantaneous

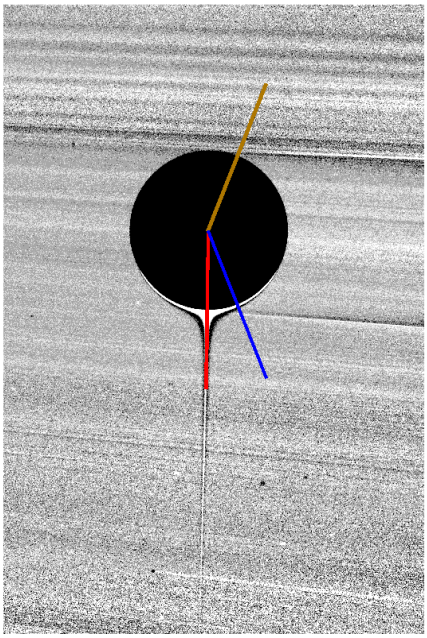

Figure 5.11: Position of example segments shown in Figure 5.10.

transition from zero concentration at the oil droplet interface to the concentration of the bulk solution. Figure 5.10 shows this to be the case, although the transition zone between the concentrations of the oil droplet and the bulk solution was not instantaneous. This was due to the laser sheet thickness covering a 1mm depth of the curved droplet interface so a gradual increase from the concentration of the oil droplet to the concentration of the bulk solution is seen. Although the concentration of the bulk fluid was relatively constant, there was still noise from pixel to pixel. This issue had to be taken into account for further processing.

The blue line in Figure 5.10 corresponds to a segment that passes through the edge of the surfactant cap but not the wake. At the transition zone between the edge of the droplet and the bulk solution a peak concentration of 12.8 times that of the bulk concentration appears. This was used to quantify the accumulation of Rhodamine-6G molecules in the surfactant cap behind the droplet. This blue line proceeds to drop down to a trough with a concentration of 0.49 times the concentration of the bulk solution before returning to the concentration of the bulk solution. This surfactant-depleted trough shows the presence of a surfactant-depleted layer situated behind the surfactant cap. This surfactant-depleted layer confirmed that adsorption was ongoing at the forward facing part of the droplet.

The final segment example, given by the red line, passes through the very rear of the droplet. It passes through the surfactant core wake trailing behind the

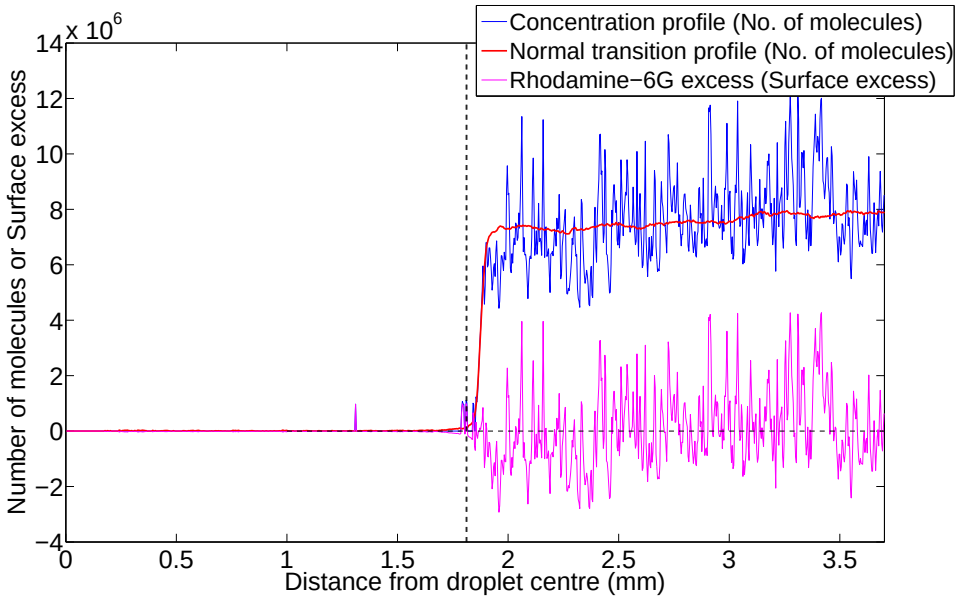

Figure 5.12: Effects of subtracting the normal concentration profile from a segment at 21.6° from the front of the droplet.

droplet. This segment reaches a peak concentration of 18.5 times the concentration of the bulk solution at the interface, before decreasing back down to the bulk concentration. The concentration in this segment takes longer to decrease to that of the bulk solution, with no surfactant-depleted trough. This is related to the volume of surfactant leaving the surfactant cap being dispersed back into the bulk solution.

An observation of Figure 5.10 revealed that the transition zones for each segment did not begin at the same distance from the centre of the droplet. An exploration of a range of segments at the front of the droplet revealed that the increase in concentration in the transition zone followed the same gradient, but the start of the transition zone varied with angle. The starting position of the transition zone was symmetrical around the vertical axis of the droplet therefore the discrepancy in the starting location was related to the fact that the droplet was not completely spherical.

Concentration profiles from the front of the droplet where no surfactant cap was present were averaged and subtracted from all of the concentration profiles around the droplet. This concentration profile at the front of the droplet shows the normal behaviour at the interface. Subtracting this behaviour left concentration values related to just the build-up of surfactant in the surfactant cap.

Figure 5.12 demonstrates a concentration profile at the front of the droplet where there is no expected build-up of Rhodamine-6G. The blue line is the original

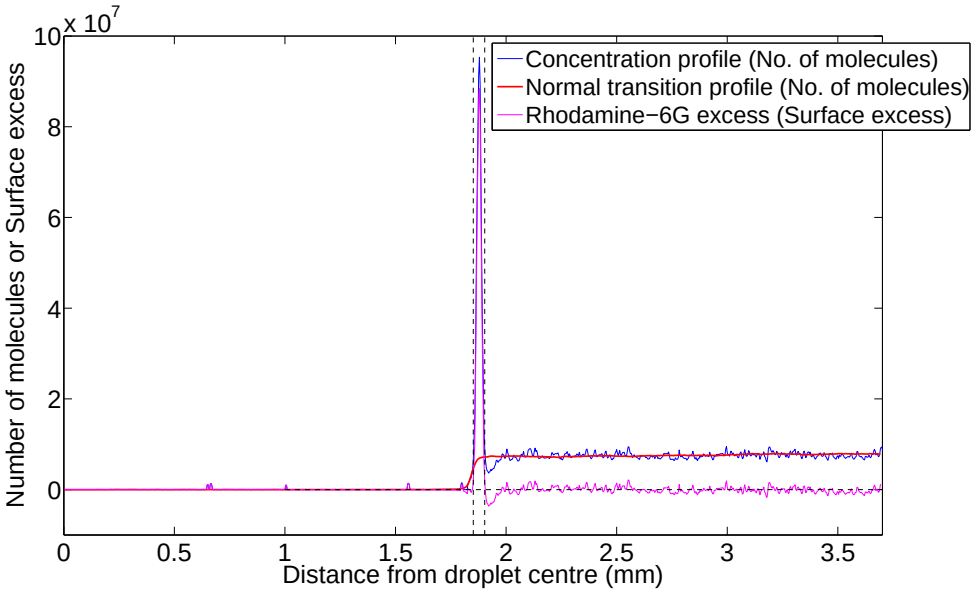

Figure 5.13: Effects of subtracting the normal concentration profile from a segment passing through the surfactant cap at 158.4° from the front of the droplet.

concentration profile at an angle of 21.6° from the front of the droplet, as shown by the yellow line in Figure 5.10. The red line is the average concentration profile as averaged around the front of the droplet where no Rhodamine-6G build-up is expected, and therefore is the expected normal behaviour of the interface. The magenta line is this normal interface behaviour subtracted from the concentration profile. This result shows the quantity of excess Rhodamine-6G at the interface. For this segment, the result shows a fluctuation of the original noise around zero, and so there is no build-up of Rhodamine-6G for this segment. The vertical black dashed lines show the start and finish locations of the Rhodamine-6G layer based at the droplet interface. For this segment, as shown by the magenta line, there is no excess and so the Rhodamine-6G layer thickness is zero.

The blue line in Figure 5.13 shows a segment passing through the surfactant cap without the influence of the wake. This profile corresponds to the blue profile in Figure 5.10 at an angle of 158.4° from the front of the droplet. The red line is the normal interface behaviour and is subtracted from the concentration profile to give the magenta line to show the concentration excess at the interface. This profile shows a sharp peak in the excess Rhodamine-6G, reaching a maximum pixel concentration of 8.84×10^7 molecules of Rhodamine-6G above the normal expected behaviour. It then drops down to a trough before returning to the behaviour of the bulk solution. This trough shows a Rhodamine-6G depleted layer of a concentration lower than

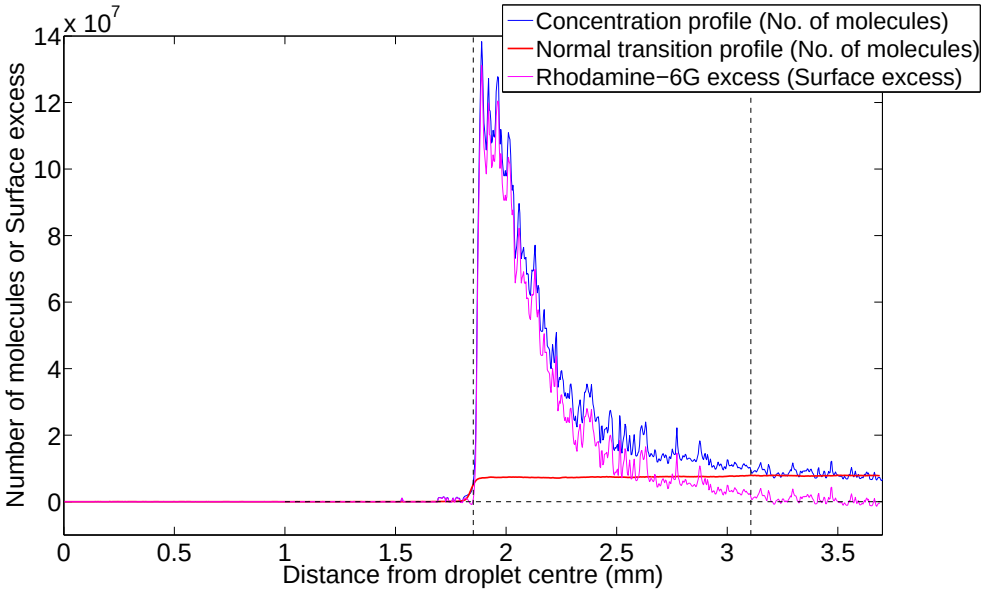

Figure 5.14: Effects of subtracting the normal concentration profile from a segment at the rear of the droplet.

the expected concentration at that point. The vertical black dashed lines show the start and finishing positions of the surfactant excess layer and gave a quantifiable layer thickness of 0.051mm.

The final surfactant profile, given by the red profile in Figure 5.10, has the normal interface behaviour subtracted in Figure 5.14. The original profile given by the blue line has the normal interface behaviour subtracted to produce the magenta line. This profile passes through the very rear of the droplet and shows a large distance of excess Rhodamine-6G as marked by the vertical black dashed lines. This is due to the segment passing through the wake of the droplet, giving the core surfactant-rich wake a length of 1.26mm.

The start points for the surfactant excess layer around the droplet should follow the circumference of the droplet in Figure 5.8, whereas the finish point points should follow the outside edge of the surfactant cap and surfactant-rich wake. This result is shown in Figure 5.15.

Figure 5.15 shows that around the front of the droplet where there is no build-up of Rhodamine-6G the result varies. This is due to the noise of the data causing variations. However, when a surfactant cap is detected the data smooths out and both edges of the surfactant cap are successfully located.

Integrating the surfactant excess curves between these two positions of the start and end of the transition zone gave the total number of Rhodamine-6G molecules

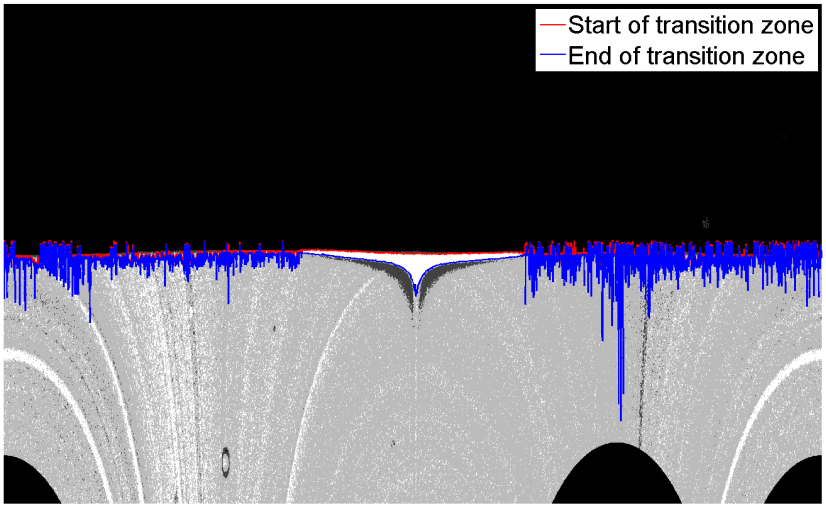

Figure 5.15: Calculated thickness of the transition zone around a droplet.

held at the interface for each 0.072° segment of the droplet. This surfactant volume profile is plotted around the droplet to give the profile in Figure 5.16.

Figure 5.16 shows the surfactant volume profile around the droplet with the angle measured from the front of the droplet. Around the front of the droplet there is a negligible volume of surfactant. Towards the rear of the droplet at the position relating to the surfactant cap, the volume of surfactant increases steadily until the very rear of the droplet where a sharp peak is reached. This peak relates to the large quantity of surfactant within the surfactant-rich part of the wake.

The vertical red dashed lines show the angles at which the volume of surfactant noticeably increases from the very low level of Rhodamine-6G around the front of the droplet. For the preliminary experimental series, presented in Appendix A, an indication of the volume of surfactant held behind the droplet was achieved by integrating this curve between these two angles.

For the main experimental series these surfactant distribution profiles were extrapolated around the surface of the droplet to obtain the total volume of surfactant held behind the 3-dimensional droplet. To achieve this the thickness of the laser sheet had to be taken into account as close to the poles of the droplet the entire cross-sectional area of the droplet and wake was illuminated, whereas around the widest part of the droplet only a small fraction of the interface was illuminated. The volume of each segment of the surfactant distribution profile was summed around

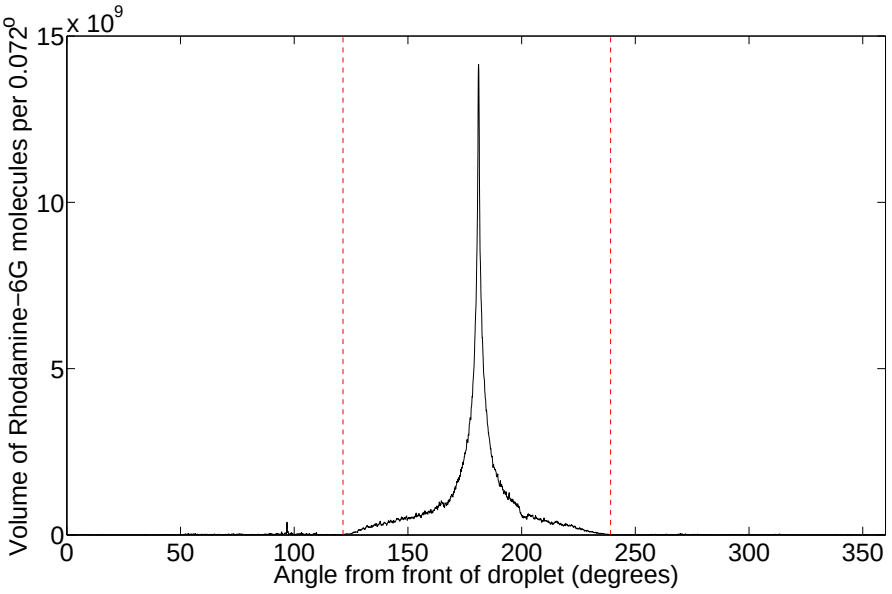

Figure 5.16: Surfactant distribution profile showing the volume of Rhodamine-6G held within each 0.072° segment of the droplet. Angle measured from the front of the droplet.

the vertical axis of the droplet. This required the distance of the segment location from the vertical axis of the droplet to be known.

Figure 5.17 shows the cameras perspective of the droplet. The volume at point p is separated from the vertical axis of the droplet by a distance, r, of

$$r = R \sin \theta, \tag{5.6}$$

where R is the radius of the droplet, and θ is the angle from the front of the droplet as for the surfactant distribution profiles.

If the radius at point p is less than the half of the thickness of the laser sheet then the entire volume of the surfactant for a horizontal plane through that point is illuminated by the laser sheet and recorded by the camera. This is demonstrated in Figure 5.18 which shows a plan view of the cross-sectional area of the droplet with the laser sheet passing through the droplet centre with thickness, t. The radius of the segment, r, is half of the width of the laser sheet so all of the surfactant at the droplet interface around the 3-dimensional droplet is illuminated. This scenario occurs at the front and rear of the droplet including the surfactant-rich wake.

However, if the segment of interest has a radius, r, from the vertical axis of the droplet larger than half of the thickness of the laser sheet then a scale factor

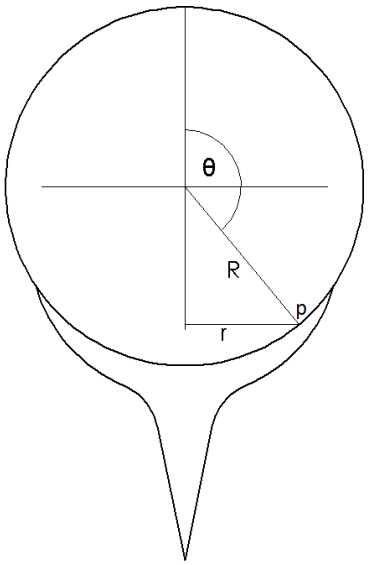

Figure 5.17: Camera perspective of droplet with notation for calculating volume of surfactant held behind a 3-dimensional droplet.

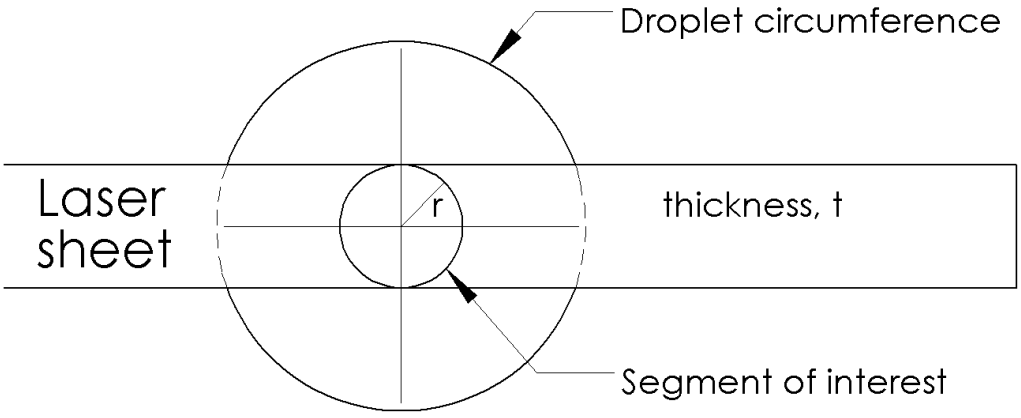

Figure 5.18: Plan view for a segment radius less than the width of the laser sheet with notations for calculating the volume of Rhodamine-6G around a 3-dimensional droplet.

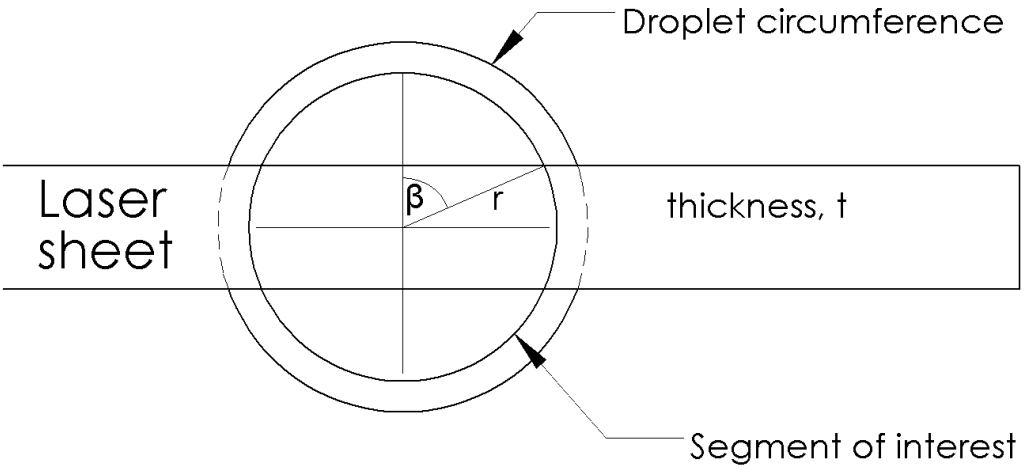

Figure 5.19: Plan view for a segment radius greater than the width of the laser sheet with notations for calculating the volume of Rhodamine-6G around a 3-dimensional droplet.

needs to be calculated to extrapolate the total volume of Rhodamine-6G around the droplet at that angle. An example of this scenario is demonstrated by the plan view of the droplet with the laser sheet of thickness t passing through the droplet centre in Figure 5.19.

To calculate the scale factor the length of the arc represented by angle β needed to be calculated for normalisation against the thickness of the laser sheet. This angle was given by

$$\beta = \cos^{-1} \frac{t}{2r}. \tag{5.7}$$

This gave a scale factor, S, for the volume of each segment of the surfactant distribution profile of

$$S = 1 + \frac{2R\sin\theta}{t} \cos^{-1}\left(\frac{t}{2R\sin\theta}\right), \tag{5.8}$$

where R is the radius of the droplet, t is the thickness of the laser sheet, and θ is the segment angle from the front of the droplet.

This process was repeated for each droplet at each height of each concentration. This allowed a comparison of surfactant volume and associated surfactant cap size across different concentrations, as well as allowing the development of the surfactant cap behind a droplet to be tracked as the droplets rose through the tank.

5.3 PIV raw data

The PIV experiments consisted of a different camera setup than used for LIF. The PIV camera was selected to take relatively high speed images and was controlled by software manually activated on the computer. This led to less accuracy in the timing of the camera activation, so images were taken for a three second period to ensure the droplet's capture.

This section discusses the volume of data produced for PIV along with how this volume was reduced to a manageable level. An example of the raw data is displayed along with a discussion of the data and how this impacted the analysis.

5.3.1 Data quantity

The data gathered for each individual droplet consisted of a three second burst of images at a rate of 80Hz. This produced 240 images for each droplet. A minimum of six droplets were captured for each height of each concentration, with 1,444 droplets being photographed in total. This led to 346,560 photographs being captured. Most of these photographs were blank having been captured before and after the droplet moved through the field of view. To reduce the quantity of images all photographs in which the droplet was not entirely in the frame were identified and removed. This left 27,948 images to be processed.

5.3.2 Raw PIV result

An example of the data produced by the PIV experiments is displayed in Figure 5.20. This shows a relatively densely seeded droplet in a bulk concentration solution containing 0.03mg/l of Rhodamine-6G at a height of 110mm from the base of the tank, and shows the droplet rising through the field of view. Due to the high density of seeding particles, features of the internal circulation can be determined. The main observable features are the circulation regions mirrored around the central vertical axis of the droplet. This is caused by the fluid at the droplet interface being pushed around to the rear of the droplet and recirculating up the centre. This created a velocity gradient across the fluid of the droplet and internal eddies were formed. At the rear of the droplet a bright cap of reflective particles appears to accumulate potentially indicating the presence of a stagnant region at the rear of the droplet.

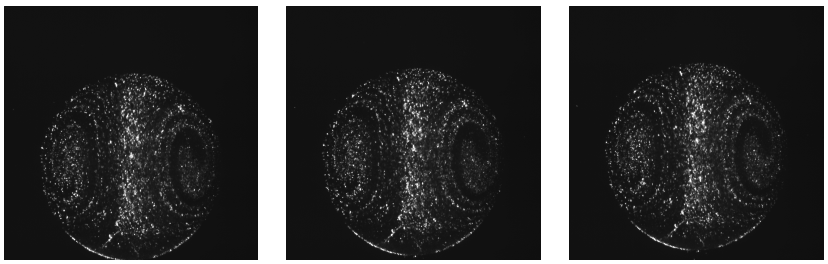

(a) Image 1, (b) Image 2, (c) Image 3,

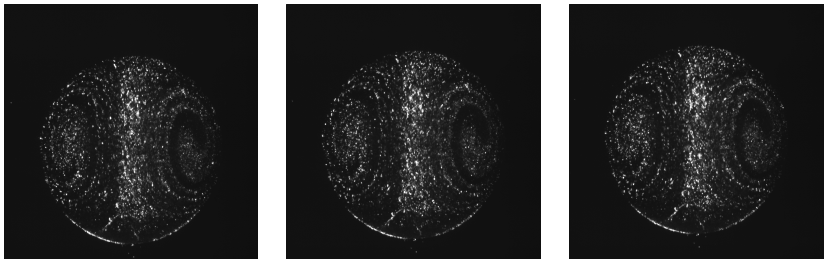

(d) Image 4, (e) Image 5, (f) Image 6,

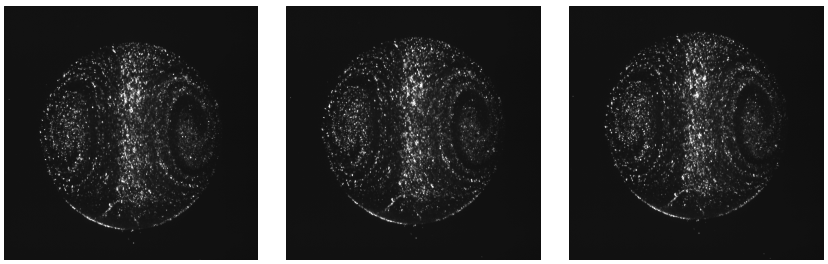

(g) Image 7, (h) Image 8, (i) Image 9,

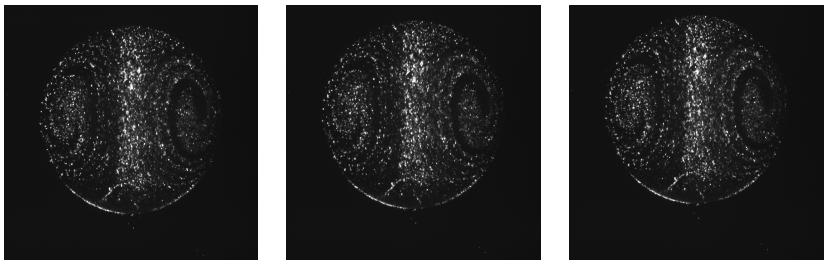

(j) Image 10, (k) Image 11, (l) Image 12,

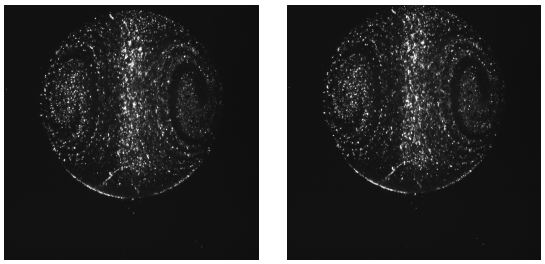

(m) Image 13, (n) Image 14.

Figure 5.20: Example of raw PIV data with a high density of reflective tracer particles with a Rhodamine-6G concentration of 0.03mg/l. Height from the base of the tank: 110mm.

5.3.3 PIV processing objectives

The aim for the PIV processing was to produce an angle for the stagnant cap that could be used for comparison with the surfactant cap angle generated by the LIF processing. Processing objectives to produce this angle from the raw data were identified as:

- Individual droplet averaging: The data shown for a single droplet, shown in Figure 5.20, can be used to produce a string of vector fields relating to a single droplet. Averaging over these vector fields reduces any irregularities introduced by the vector field calculations. This process requires shifting the droplets from each image so that they all overlap in order for the related vectors in each vector field to be averaged.

- Changing the frame of reference: In the raw data the droplet is rising upwards through the fluid. The rising speed of the droplet needed to be determined and subtracted from the vector fields to give a frame of reference of a stationary droplet. This enables better visualisation of the internal circulation.

- Calculating the tangential velocity profile around the droplet: By calculating the velocity normal to the interface, regions of the droplet with no circulation could be detected and related to the position of the stagnant cap at the rear of the droplet.

- Droplet averaging at each height: The stagnant cap angle for each droplet at each height needed to be compared to validate averaging over droplets with different sized radius.

- Comparison of the stagnant cap development over different surfactant concentrations: The effects of the different bulk concentrations of Rhodamine-6G needed to be compared to explore the effects of different surfactant strengths on the formation of the stagnant cap.

5.4 PIV processing

In Figure 5.20, as for all image sets, the droplet is moving upwards through the images. This created two problems. The first problem was that in order to average the droplets over the individual image set, the droplets needed to have the same location within the frame in order to be able to average corresponding points. The second issue was that as the droplet was moving up through the image all of the

reflective particles had a velocity in the vertical direction. This masked the effects of the internal circulation and so a method was developed to convert the frame of reference to that of a stationary droplet with the fluid flowing from the top of the image downwards, rather than having the droplet rising upwards through a stationary fluid.

This section describes the processing methods applied to a set of raw data images; the calculation of instantaneous vector fields, averaging the individual strings of images, and extracting quantitative results for the development of a stagnant cap at the rear of the droplet. Finally a comparison between different images at the same concentrations and heights tests the validity of averaging droplets with different radii.

5.4.1 Vector field calculation

A commercially available software package was used to calculate the instantaneous vector fields for each string of images. The software used was DynamicStudio v4.10 obtained from Dantec Dynamics. A vector field measures the displacement of the tracer particles, and so each vector field calculation is a combination of a pair of images. Each string of images was imported into the software and analysed in pairs (image 1 with image 2, image 2 with image 3, image 3 with image 4 etc). This produced $n - 1$ vector fields where n is the total number of images in the string.

The software offered different techniques to analyse PIV signals. The method chosen to analyse this data was adaptive PIV. Adaptive PIV splits the image into interrogation areas before iteratively adjusting the individual size and shape of each interrogation area to find the best adaptation. The interrogation areas are adjusted based on the density of the seeding particles and the flow gradients (Dantec Dynamics [2013], Wieneke and Pfeiffer [2010]).

The analysis required the setup of the interrogation area grid. The step size of the grid had to be specified along with the maximum and minimum limits of the individual interrogation areas. The grid step size specifies the distance between interrogation areas with a smaller step size leading to a larger number of more densely packed interrogation areas. The selection of this value was a trade-off between a higher resolution of calculated vectors which was very computationally intensive, and a lower resolution but less computationally intensive result. The maximum interrogation area size is the size applied to all interrogation areas used for the first iteration of the vector field calculation. A large size was chosen for these calculations, as larger droplets had a high rising velocity and so a large displacement of the internal tracer particles. From here the interrogation areas are iteratively reduced

Table 5.1: Values used for the setup of the PIV interrogation area grid.

	Width (pixels)	Height (pixels)
Grid step size	16	16
Maximum interrogation area size	512	512
Minimum interrogation area size	32	32

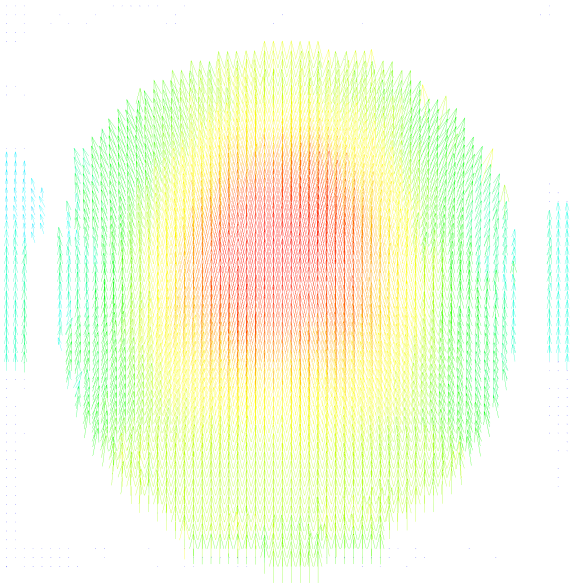

Figure 5.21: Example of a vector field generated by DynamicStudio v4.10.

to find the optimum size without going beneath the minimum specified interrogation area size. The smaller the minimum value, the more iterations are performed, leading to an increase in the computational resources used. The values for these three parameters are given in Table 5.1.

A vector field calculated between two images is shown in Figure 5.21 with blue vectors having a small velocity through to the red vectors having a high velocity. The highest velocities occur within the centre of the droplet. There are no particles in the bulk fluid and so very few vectors are outside the droplet. All of the vectors have a positive magnitude in the vertical direction showing that the rising speed of the droplet is the main contributor towards the length of the vectors. The original dimensions of each image were 2,048 pixels by 2,048 pixels. The process of the vector analysis converted these to arrays of 127 by 127 vectors.

Errors associated with PIV

There was a potential for errors to be introduced into the PIV analysis. These errors could be introduced either through the experimental procedure or through the analysis process. This section will look at some of the potential sources of error identified.

The quantity of tracer particles within the oil droplet was one potential error source. An insufficient volume of particles within the oil droplet created areas with no particles present. This meant that the PIV software could not detect any particles to perform calculations on, so a velocity of zero was returned. This effect mainly happened around the edge of the droplet which was the area of interest in these experiments. However, if there were too many particles within the droplet then the particles adsorbed to the interface. This had the potential to affect the adsorption dynamics of the Rhodamine-6G. The effect of particles adsorbing to the interface is demonstrated by the raw PIV data presented in Figure 5.20. As discussed in Section 4.4.2 this does not visually affect the adsorption of Rhodamine-6G but effects could be detected after analysis and comparison with other droplets.

The process of calculating the vector fields also introduced error into the system. Due to the grid size selected for the PIV analysis, the effective data set was decreased from 2,048 pixels by 2,048 pixels to a 127 by 127 array of vectors. This effectively lowered the resolution of the data so that the droplet interface had a smaller effective size and a lot of detail at the interface was lost.

The PIV system used for these experiments produced a 2-dimensional result. The analysis does not take into account the velocity of particles moving through the laser sheet along the z-axis towards the camera. Any particles moving in the third dimension could affect the readings given by the PIV analysis. This could have a large effect as the width of the laser sheet was 1mm compared to the minimum achieved diameter of a droplet at 2.8mm.

These various factors needed to be considered during analysis, with droplets possessing the same parameter values compared for inconsistencies before being averaged.

5.4.2 Individual droplet averaging

To average the vector maps over the string of images relating to a single droplet, the shift of the droplet between frames had to be calculated. This was done by manually locating the droplets in two of the frames from the raw data image string with the droplets separated by a large distance. The shift between individual frames

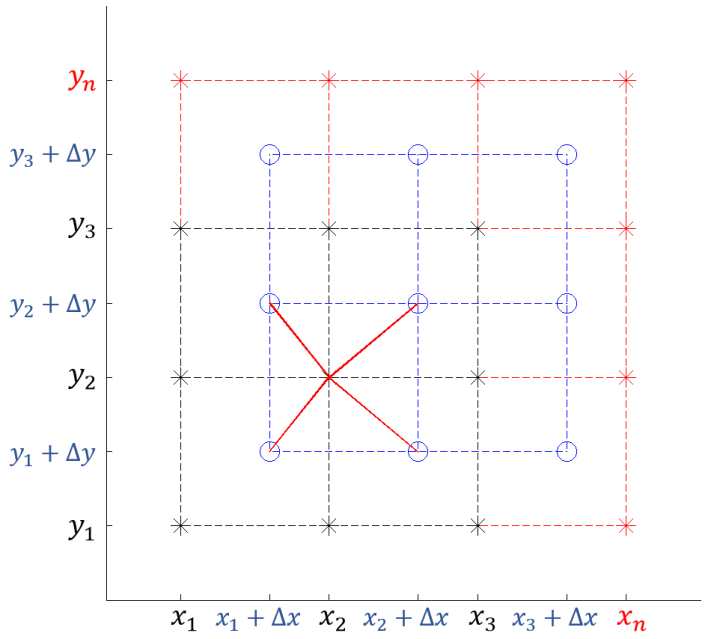

Figure 5.22: Effects of the droplet shift between frames on the vector fields.

was calculated by dividing the total shift by the number of separating frames giving the average shift between frames in both the vertical and horizontal directions. The time difference between the frames was then used to calculate the rising speed of the droplet.

Following this process, each individual vector field in the string of vector fields was shifted so that the droplet overlapped in each frame. Due to the loss of resolution from the conversion of the raw images to the vector fields these offset values were not rounded numbers. This meant that none of the vector fields shared the same coordinate system, as shown in Figure 5.22.

The black grid in Figure 5.22 represents the first vector field in the string with the blue grid corresponding to a vector field with an offset of Δx and Δy. This produced different locations for each of the new vectors, that did not match the position coordinates of the first set of vectors, preventing averaging. This was dealt with by extending the vector field of the base vectors by one location in the x-direction and y-direction (the red points). This created a vector field that encompassed the offset of the vector field. The offset vector field was then mapped to the coordinates of the original vector field. Using the process described in Section 5.2.3, each point was a function of the closest four offset values. For example (x_2, y_2) was a function of $(x_1 + \Delta x, y_1 + \Delta y)$, $(x_2 + \Delta x, y_1 + \Delta y)$, $(x_1 + \Delta x, y_2 + \Delta y)$, and

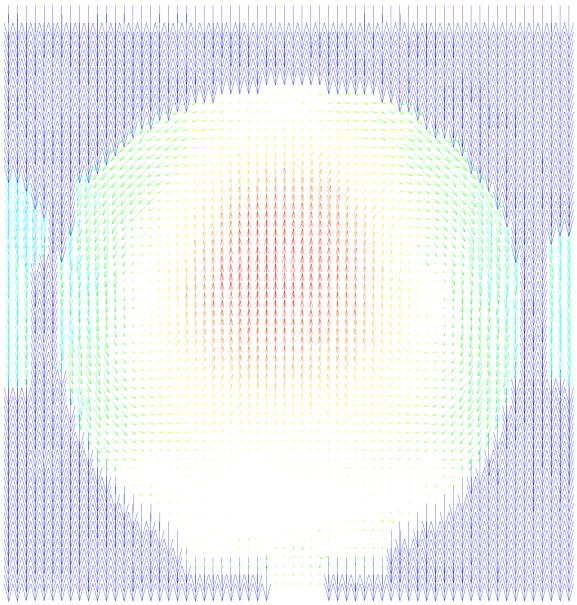

Figure 5.23: Example of a vector field generated by DynamicStudio v4.10 with the droplet rising velocity subtracted from each vector.

$(x_2 + \Delta x, y_2 + \Delta y)$ with the inverse distance from (x_2, y_2) to the offset values used as a weighting function.

With this mapping complete the vectors were summed and averaged over the entire string of vector fields.

5.4.3 Frame of reference

The frame of reference for the raw data images was of the droplet rising through a stationary fluid. However, the overriding contributor towards the vector fields was the rising speed of the droplet, which gave all of the vectors a large positive magnitude in the direction that the droplet was moving. The frame of reference needed to be changed so that the droplet was stationary with the continuous phase flowing past it. This was achieved by subtracting the rising velocity of the droplet from y-component of every vector. This process was performed on the vector field example in Figure 5.21 within the DynamicStudio v4.10 software to produce the vector field shown in Figure 5.23.

There were no reflective particles in the bulk solution, so the majority of vectors within the continuous phase initially registered with zero velocity. When the

rising velocity of the droplet was subtracted from these vectors, they all registered unrealistically as a length corresponding to the negative rising velocity instead of following the expected streamlines. Due to this, the initial calculated vector fields were exported to Matlab R2013b prior to this process so that these vectors could be removed. Figure 5.23 shows two recirculation zones within the droplet mirrored around the vertical axis. The fluid of the droplet is accelerated in the direction of the flow from the front of the droplet towards the rear before recirculating back up the centre where the largest vectors within the droplet were achieved. There was a stagnation point at the front of the droplet as was to be expected. The rear of the droplet shows a large area with extremely low velocities. This area corresponds to the stagnant cap and was potentially related to the surfactant cap visible in the LIF experiments.

5.4.4 Tangential velocity profile

As the stagnant area at the rear of the droplet was potentially related to the size of the surfactant cap measured in LIF experiments, the angle of this stagnant cap was measured. This was done by measuring the tangential velocity profile around the interface of the droplet. This gave the velocity normal to the interface of the droplet so disregarded the movement of particles to or from the droplet interior. From this tangential velocity profile the point at which the fluid at the interface became stagnant was located. To calculate the tangential velocity profile the centre of the droplet within the vector field had to be located and the droplet radius had to be calculated. Due to the inherent error of the loss of resolution between the original images and the calculated vector fields, the droplets were assumed to be circular and a circular profile was applied to the interface. The tangential velocity was measured at 96% of the droplets radius so as to not be affected by the bulk solution with zero velocity or areas close to the droplets interface that lacked particles. The circular profile for the velocity close to the interface was split into 400 points with the velocity on the profile calculated in the same way as the LIF intensities as shown in Figure 5.7 and Equation 5.4, in which a rectangular array of values was mapped to a curved interface.

An example of the tangential velocity profile corresponding to Figure 5.23 is shown in Figure 5.24. The red line shows the velocity profile measured from a single vector field whereas the black line corresponds to the velocity profile around a droplet averaged over the string of vector fields for the same droplet. The line for the velocity profile around a droplet calculated from a single vector field shows a relatively large amount of noise as well as a large dip in velocity at 267.3° where the velocity should

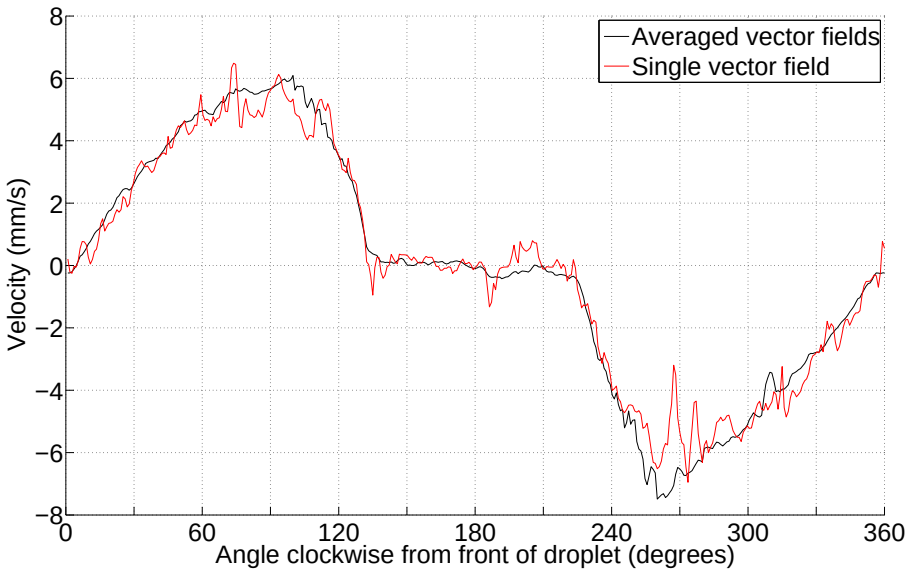

Figure 5.24: Velocity around the edge of a droplet at 96% of the radius calculated over an averaged string of vector fields and from a single vector field.

be at its maximum. The line corresponding to the velocity profile averaged over the string of vector fields shows good agreement with the shape of the profile for a single vector field. However, the fluctuations were decreased giving a smoother profile. This profile shows a good symmetry of shape around the vertical axis of the droplet. There is a small area of very low velocity at 0° that corresponds to the stagnation point at the front of the droplet. The velocity increases moving downwards towards the rear of the droplet with one side reaching a maximum velocity of 6.09mm/s at an angle of 99.9° from the front of the droplet, whilst the other side reaches a maximum velocity magnitude of 7.49mm/s at an angle of 260.1° from the front of the droplet. At the rear of the droplet there is a large zone of very little velocity. This zone covers an angle of approximately 90° and is symmetrical about the rear of the droplet. This corresponds to the stagnant cap at the rear of the droplet.

Figure 5.25 shows a comparison of the tangential velocity around the droplet measured over different distances from the droplet interface. For the profiles measured at the droplet radius and at 99% of the droplet radius, velocity values register as zero when they should be the profiles largest velocities. This happened due to particles not being detected at the corresponding points within the droplet. This also impacts the measurements at 98% of the radius and 97% of the radius. To eliminate this effect the velocity was measured at 96% of the droplet radius. Each of the profiles measured in Figure 5.25 drops down to the low velocity of the stagnant

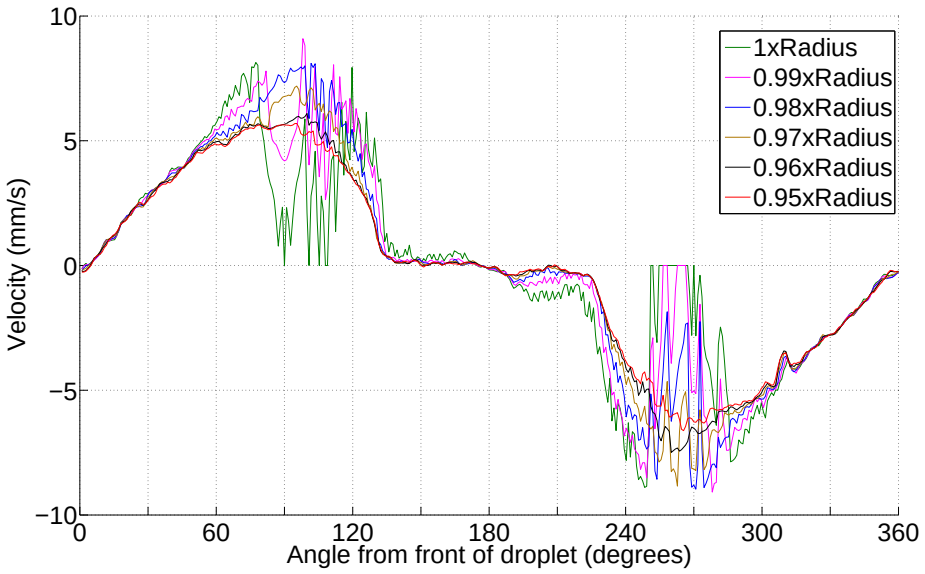

Figure 5.25: Comparison of the velocity profiles measured at different distances from the droplet interface.

cap at the same angle. Measuring the velocity profile at 96% of the droplet radius did not affect the measurement for calculating the angle of the stagnant cap.

By calculating the tangential velocity profile for droplets at different positions in the tank the growth of the stagnant cap as the droplet rises through the tank was explored. With multiple droplets measured for each concentration, this angle was compared for droplets of different radii to see how the size of the droplet affected the size of the stagnant cap and to validate averaging over droplets of different sizes.

5.5 Summary

In this chapter successful processing techniques were developed to analyse both the LIF and PIV data. The data sets for the LIF experiments and PIV experiments had to be processed in different ways. Both data sets consisted of extremely large volumes of data and so the processing methods had to be automated. The LIF process was focused on extracting quantitative data relating to the formation of the surfactant cap, and the volume of surfactant held behind the droplet from single images, whereas the PIV data consisted of strings of images from which velocity information was extracted to measure the size of the stagnant cap at the rear of the droplet.

The processes developed to analyse the LIF data enabled the extraction of

data from experiments that used different camera settings and so could not be directly compared. The process started by normalising the images to reduce the effects of any irregularities caused by the fluctuations of the light intensity throughout the image. From here each of the droplets were visually inspected to ensure the accuracy of the data. The centre coordinates and radius of the droplets were calculated using the difference in light intensity between the darkness of the oil droplet and the intensity of the bulk solution. Due to droplet stretch, a circular profile could not be applied to the interface so the droplet was divided into segments along which the light intensity was measured radially outwards from the droplet centre. The pixel values were converted from light intensity to the number of Rhodamine-6G molecules at each pixel.

Measuring the concentration profiles at different stages around the droplet revealed three different types. The first occurred around the front of the droplet and showed that there was a transition zone at the interface between the oil droplet and the concentration of the bulk solution due to the thickness of the laser sheet capturing the curvature of the droplet. The second profile passed through the surfactant cap and showed the accumulation of Rhodamine-6G molecules in a peak at the interface. The concentration profile dipped down beneath the bulk concentration showing the existence of a surfactant-depleted layer behind the surfactant cap before increasing back to the intensity of the bulk solution. The third profile passed directly through the rear of the droplet and showed the strongest concentration of Rhodamine-6G molecules at the interface, before a gradual decline down to the intensity of the bulk solution. Subtracting the profile generated at the front of the droplet gave values for the concentration excess stored in the surfactant cap. However, due to droplet stretch, the start of the transition zone had to be located in each profile before the subtraction could occur.

From these profiles the thickness of the stagnant cap could be calculated with the area integrated to give the total volume of Rhodamine-6G molecules held in the surfactant cap for each segment. These volumes were plotted as a surfactant profile around the droplet from which the angle of the visible surfactant cap could be extracted.

The PIV analysis involved analysing a string of images for each data point. The string of images was divided into pairs and a commercial PIV software package was used to compute the vector fields for image pairs. The vector fields corresponding to a single droplet were combined to reduce the effects of errors introduced through the experiments and vector field calculations.

The tangential velocity profile around the droplet was calculated which gave

angles for where the maximum velocity was obtained, as well as the location of a stagnant area at the rear of the droplet. The angle for the stagnant area was extracted for comparison against the visual surfactant cap angle from the LIF experiments.

Chapter 6

LIF Results

This chapter presents an analysis of the results obtained from the LIF experiments. The initial part of the chapter compares measurements extracted from the LIF data to theoretical values calculated from the literature. This validates the physical mechanisms at work in the experiments. This is followed by an in-depth analysis of the LIF data.

The development of the droplet as it rises through the tank was examined by investigating how the volume of Rhodamine-6G molecules held behind the droplet increases as the droplet rises, before investigating how the surfactant cap angle changes as the droplet rises through the tank. Each separate surfactant concentration was examined for both the volume of Rhodamine-6G molecules held in the surfactant cap and the surfactant cap angle. This allowed an investigation of the effects of different radius sizes on the results, before a comparison between the different concentrations occurred for both the volume of surfactant held in the surfactant cap and the surfactant cap angle.

6.1 Theoretical results

To validate whether these experiments operated as expected, values extracted from the data were directly compared to theoretical values obtained from the literature. First the Reynolds number was calculated to confirm the flow regime that was assumed to occur for the experiments. This was followed by a comparison of the diameter of the surfactant-depleted wake to theoretical values for the diffusion layer thickness. This involved calculating the effective radius of a Rhodamine-6G molecule along with the diffusion coefficient of the Rhodamine-6G in the aqueous solution.

6.1.1 Reynolds number

The Reynolds number is used to classify the flow regime as discussed in Section 2.1.2. For these experiments all of the droplets had a diameter between 2mm and 6mm giving the droplet rising velocity to be between 1.4mm/s and 13.3mm/s. The Reynolds number range was calculated to be between 0.005 to 0.16. This gave the system a Reynolds number much less than 1, therefore the flow regime of the experiments consisted of laminar flow with no flow separation from the droplet.

6.1.2 Droplet wake diameter

To explore how well the observed surfactant-depleted wake diameter compared with the theoretical solution some parameters relating to the Rhodamine-6G had to be calculated. The surfactant-depleted wake of a droplet is caused by the adsorption of Rhodamine-6G to the interface. To estimate the theoretical size of this wake it was assumed that the adsorption was diffusion controlled with no barrier against adsorption. This enabled the use of the Stokes-Einstein equation for diffusion (as discussed in Section 2.3.1). The Stokes-Einstein equation calculates the diffusion coefficient, D, of the Rhodamine-6G dispersed throughout the aqueous solution as a function of the temperature, T, dynamic viscosity, μ, and the hydrated radius, r_s, of the Rhodamine-6G molecules (Gendron et al. [2008]). By assuming the Rhodamine-6G molecule to be spherical, and with a low Reynolds number, the diffusion coefficient is given by (Cussler [2009])

$$D = \frac{k_B T}{6\pi\mu r_s}, \tag{6.1}$$

where k_B is the Boltzmann constant.

By using the diffusion coefficient of Rhodamine-6G in water as $4.14\times10^{-10}\mathrm{m}^2\mathrm{s}^{-1}$ at 20°C (Section 3.5), the effective radius of a Rhodamine-6G molecule was calculated, by rearranging Equation 6.1, as 5.18×10^{-10}m. This gives the Rhodamine-6G molecule a maximum cross-sectional area of $0.843\mathrm{nm}^2$ at its widest point. This differs to the value obtained from literature due to the assumption that the molecule is spherical.

This effective radius was used to calculate the diffusion coefficient of the Rhodamine-6G in the aqueous solution used in these experiments at the temperature at which the experiments were performed. This gave a diffusion coefficient of $7.8\times10^{-13}\mathrm{m}^2\mathrm{s}^{-1}$.

With this diffusion coefficient it was possible to calculate the diffusion layer thickness, δ, around the droplet. This was done using

$$\delta = \sqrt{\frac{d^2}{6Pe}}, \tag{6.2}$$

where d is the droplet diameter, and Pe is the Péclet number given by

$$Pe = \frac{2Ur}{D}, \tag{6.3}$$

where D is the diffusion coefficient, r is the radius of the droplet, and U is the rising velocity of the droplet given by

$$U = \frac{2\Delta\rho}{9\mu} g r^2, \tag{6.4}$$

where $\Delta\rho$ is the density difference between the two fluid phases, μ is the dynamic viscosity of the aqueous phase, g is the acceleration due to gravity, and r is the droplet radius.

Equation 6.2 was used to calculate the theoretical thickness of the diffusion layer thickness over the range of droplet sizes. The total volume of the diffusion depleted layer was calculated by summing the diffusion layer thickness around the widest part of the droplet. Assuming no desorption of Rhodamine-6G from the surfactant cap back into the bulk, this volume can be equated to the radius of the surfactant depleted wake by

$$2\pi R\delta = \pi r^2, \tag{6.5}$$

where R is the radius of the droplet, δ is the thickness of the surfactant depleted layer at the widest part of the droplet, and r is the radius of the surfactant depleted wake.

For a droplet in an aqueous solution of 0.50mg/l of Rhodamine-6G, the wake diameter was measure to be 64 pixels, which converted to a radius of 0.095mm. The droplet radius was 834 pixels, which converted to a radius of 2.44mm. This gave the droplet a rising velocity of 8.4mm/s.

Equation 6.2 was used to produce a diffusion layer thickness of 2.75×10^{-3}mm giving a final wake radius of 0.037mm.

The result extracted from the experiment gives a surfactant-depleted wake radius 2.5 times larger than the theoretical value. This is relatively accurate for an approximation with the assumptions that have been made, and validates that the physical mechanisms occurring in the experiment are as expected.

6.2 Main experimental series results

The main experimental series was performed with an extra height and shorter distances between the heights compared to the preliminary experimental series, shown in Appendix A, in order to increase the spatial resolution. As observed in the preliminary experimental series, at a height of 0mm at the base of the tank, there is a negligible volume of Rhodamine-6G held in the surfactant cap with the angle of the cap very close to zero degrees. This can be used to supplement the data gathered in the main experimental series, in which the first data point was taken at an offset of 10mm from the droplets point of release. The main experimental series were performed with an average ambient temperature of 11°C, lower than that used in the preliminary experimental series. Greater care was also taken in the laser sheet alignment to ensure the widest point of the droplet and surfactant-rich wake were captured.

The first relationship explored was how the volume of Rhodamine-6G held in the surfactant cap changed over the height of the tank for all of the concentrations tested before moving on to investigate the angle of the surfactant cap at each height for each concentration. Averaged surfactant distribution profiles are presented before a comparison of the surfactant cap volumes and angles across the range of concentrations occurs.

6.2.1 Individual concentration surfactant cap volume

The total volume of Rhodamine-6G held within the surfactant cap and wake was calculated and normalised against the volume of the droplet. This was done to account for the droplets having different radii. For each concentration the individual droplet results for each height are presented along with a curve fitted through the data set at each height. This allowed a comparison of the individual results along with the trend of how the droplet radius affects the volume of Rhodamine-6G held behind the droplet.

Figure 6.1 presents the result for the experiment relating to a surfactant bulk concentration of 0.01mg/l of Rhodamine-6G. It shows that as the droplets increase in height a greater volume of Rhodamine-6G is stored behind the droplet per unit volume. It also shows that for all heights in the tank except for a height of 10mm from the base of the tank that smaller droplets contain a higher volume of Rhodamine-6G per unit volume. At the lowest height of 10mm from the base of the tank the range of the spread of data points was larger than at other heights. This indicates a degree of uncertainty in the result at this lowest height. Therefore

the results from this lowest height were treated with caution. This irregularity at the lowest height occurs due to the levels of background noise in the surfactant distribution profiles obscuring any increased surfactant levels.

Similar effects are seen for all other concentrations and are shown in Appendix B. The curves fitted through the data points show a linear relationship between the log-log scales of the droplet radius against the number of Rhodamine-6G molecules per unit volume. This linear relationship gave a slope of between -1 and -6 with the average being approximately -3. This demonstrates that the volume of surfactant held behind the droplet is proportional to the volume of the droplet.

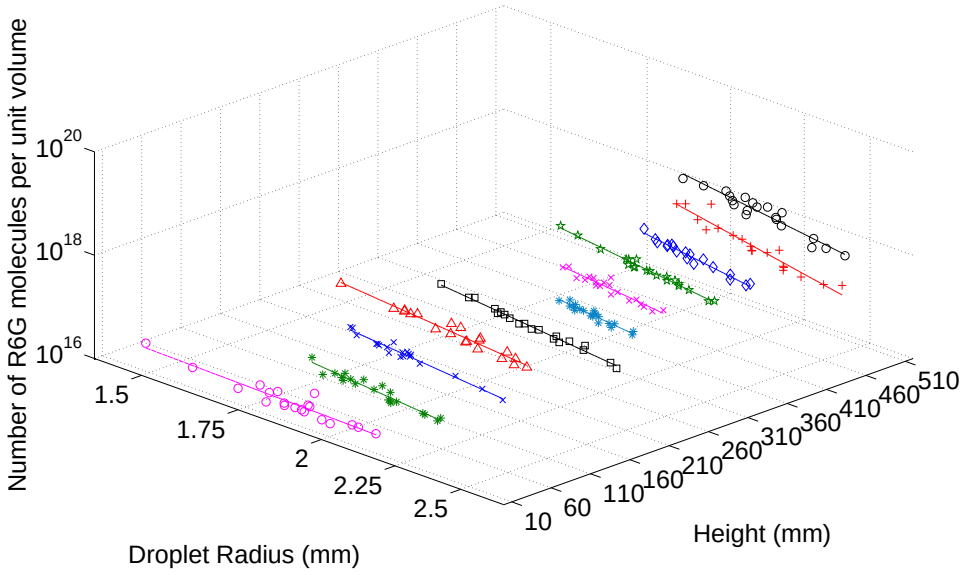

(a) 3-dimensional visualisation,

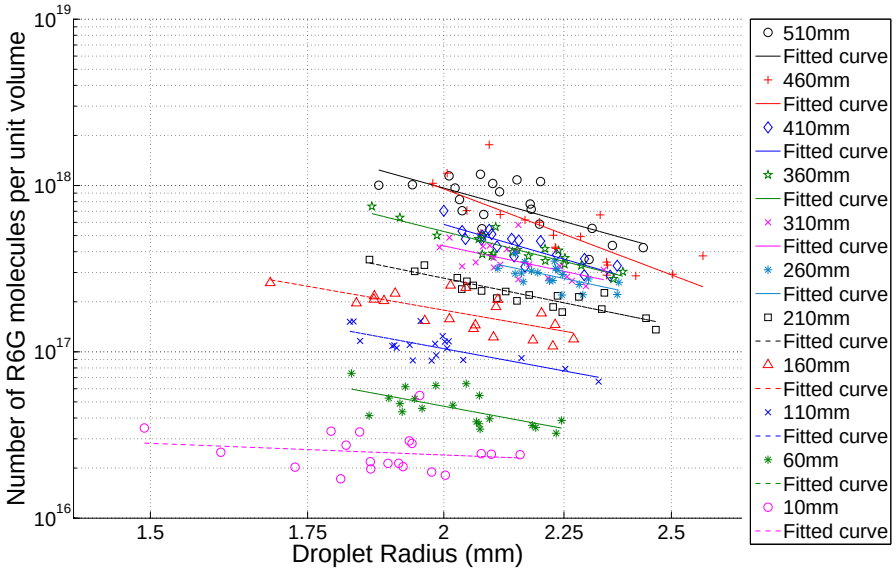

(b) Volume of Rhodamine-6G against droplet radius for different heights in tank.

Figure 6.1: Development of the Rhodamine-6G volume stored within the surfactant cap as it rises through the tank for different droplet radii in the main experimental series. Rhodamine-6G concentration of 0.01mg/l.

6.2.2 Individual concentration surfactant cap angle

The angle of the surfactant cap was calculated over the visible region of the surfactant increase measured from the surfactant distribution profiles. Calculating the size of the surfactant cap allowed a comparison with the stagnant cap angle obtained from PIV to allow a relationship between the two techniques to be explored. Initially the data range for each concentration was explored individually before averaging the results for a comparison between concentration strengths. This allowed an exploration of the effects of differing radii on the size of the surfactant cap.

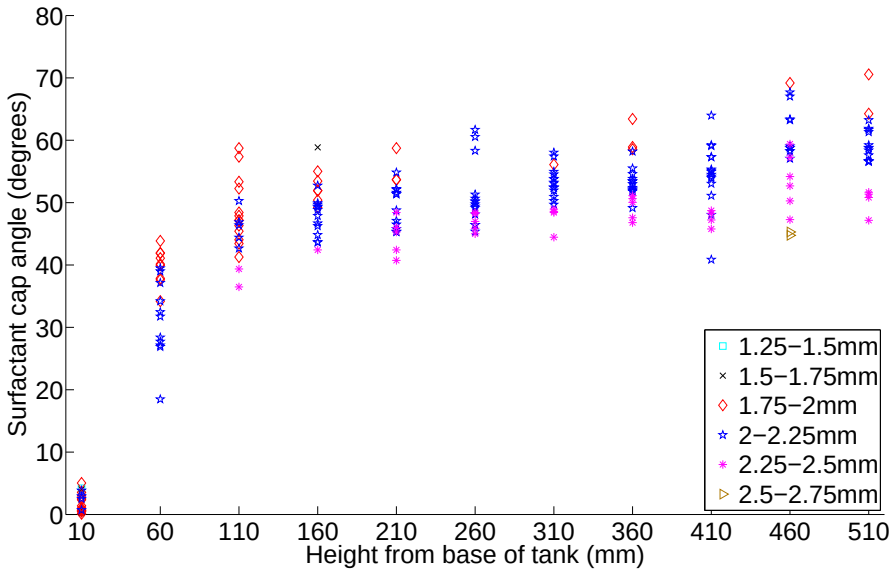

Figure 6.2: Development of the surfactant cap angle over the height of the tank for different droplet radii in the main experimental series. Rhodamine-6G concentration of 0.01mg/l.

Figure 6.2 shows the size of the surfactant cap angle for each individual data point, measured for each height of each concentration. It shows that there is a large initial increase in the surfactant cap angle before flattening off over the upper end of the tank.

Figure 6.2 shows that there is overlap between the data points for droplets of different radii. However it was observed that in general droplets with a smaller radius possess a larger cap angle. The agreement between stagnant cap angles at each height was better than in the preliminary experimental series shown in Appendix A. This reinforces that the improvements to the experimental setup improved the quality of the results in the main experimental series. The other

concentrations show the same trend and are presented in Appendix C.

It would be expected that the cap angle for droplets of different radii would not be overlapping. Reasons for the overlapping results were identified as errors introduced in the experimental stage of photographing the droplets and in the image processing stage. Errors can be introduced in the experimental stage through the misalignment of the laser sheet with the centre line of the droplet. If there is a small degree of misalignment then the widest point of the droplet and the droplet wake would not be captured, leading to an underestimate of the surfactant cap angle.

Image processing errors can be introduced due to the noise of the surfactant distribution profile at a zero level. A high level of noise could lead to errors in determining the position of the surfactant cap zone and therefore an error in calculating the angle of the surfactant cap.

6.2.3 Averaged surfactant distribution profiles

The surfactant distribution profiles of the data points were averaged at each height for each concentration to produce an averaged surfactant distribution profile. This averaged out the noise in the surfactant distribution profiles providing smoother more reliable results.

These averaged surfactant distribution profiles were used to calculate the average volume of Rhodamine-6G held in the surfactant cap and the average surfactant cap angle for each height of each concentration. They could also potentially be used for a comparison with the tangential velocity profiles calculated around the droplet from the PIV data.

Figure 6.3 shows how the averaged surfactant distribution profile develops over the height of the tank for a Rhodamine-6G concentration of 0.01mg/l. It shows that as the droplets height in the tank increases so does the volume of Rhodamine-6G held within the surfactant cap with a sharp peak occurring at the later heights at 180° relating to the surfactant-rich tail that develops behind the droplet.

Appendix D presents these averaged surfactant distribution profiles for all other concentrations of Rhodamine-6G tested. They show the same trends of an increasing volume of surfactant towards the higher end of the tank in the majority of cases. However, due to the stronger concentrations and the camera settings used, the distinction between the intensities of the droplet and the bulk solution was more pronounced leading to a reduction of noise within the profiles. It was also observed that the maximum cap angle remains relatively consistent over the upper heights in the tank for each concentration.

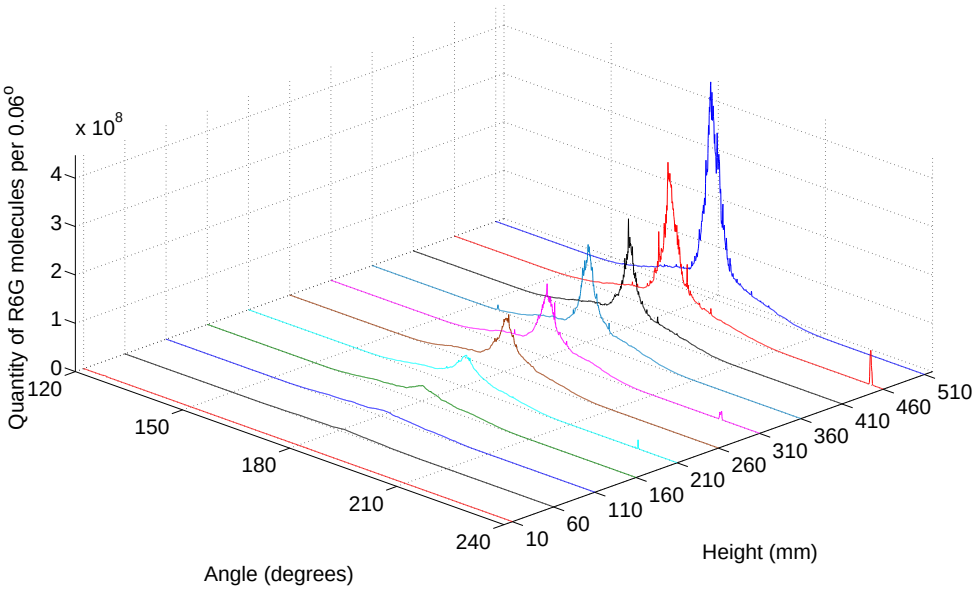

Figure 6.3: Averaged surfactant distribution profiles for a Rhodamine-6G concentration of 0.01mg/l at different heights from the base of the tank. Angle measured from the front of the droplet.

6.2.4 Concentration comparison

Figure 6.1 and Figures B.1-B.14 in Appendix B showed the reliance of the quantity of Rhodamine-6G held behind a droplet on the volume of the droplet. Therefore the droplet volume was used to normalise the averaged data for all bulk concentrations and heights in the tank. Figure 6.4 presents how the averaged volume of Rhodamine-6G held behind the droplet relies on the concentration of the bulk solution and the height of the droplet in the tank when normalised against the quantity of Rhodamine-6G molecules held within a droplets volume of the bulk solution.

Figure 6.5 shows the dependence of the volume of Rhodamine-6G gathered behind the droplet on the bulk concentration and the height in the tank respectively for when the accumulated volume is normalised against the volume of Rhodamine-6G in a droplets volume of the bulk solution. Figure 6.5(a) shows how the normalised volume at each height is affected by the bulk surfactant concentration. All of the heights follow the same trend with the larger heights carrying a higher volume of Rhodamine-6G. It confirms that at the lower end of the tank there is a larger increase in the volume between heights than at the higher end of the tank. This shows that the rate of entrapment slows as the droplet rises through the tank. This is related to the droplet nearing its surfactant saturation level where the volume of surfactant

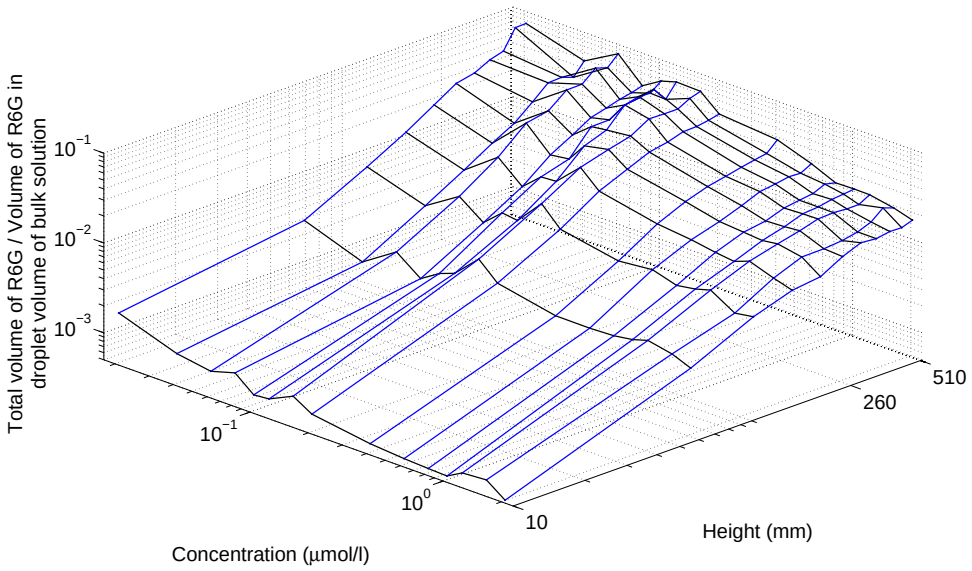

Figure 6.4: 3-dimensional visualisation of how the bulk concentration and the height from the base of the tank affects the volume of Rhodamine-6G held behind the droplet normalised against the number of Rhodamine-6G molecules held within a droplets volume of bulk solution.

adsorbing to the droplet is similar to the volume being swept from the surfactant cap back into the bulk solution.

Figure 6.5(a) also shows that as the concentration of the bulk solution increases, the normalised volume decreases for all heights. This shows that droplets rising in weaker bulk surfactant concentrations obtain a higher proportion of surfactant in relation to the concentration of surfactant distributed throughout the bulk solution demonstrating a better efficiency than at higher bulk concentrations.

Figure 6.5(b) shows how the normalised volume increases as the height in the tank increases. All of the bulk surfactant concentrations show an increase in the volume of surfactant over the height of the tank. However the results for the higher bulk surfactant concentrations possess a lower volume of surfactant. Despite this, all of these curves are closely packed indicating that the relationship between the quantity of surfactant gathered with the volume of the droplet is relatively strong.

The relationship between the volume of surfactant held behind a droplet and the quantity of surfactant required to form a monolayer around the droplet was also explored. This was done to explore the quantity of Rhodamine-6G that could be held behind the droplet in relation to the volume of Rhodamine-6G that would adsorb to the interface in an ideal, equilibrium condition. The dependence of

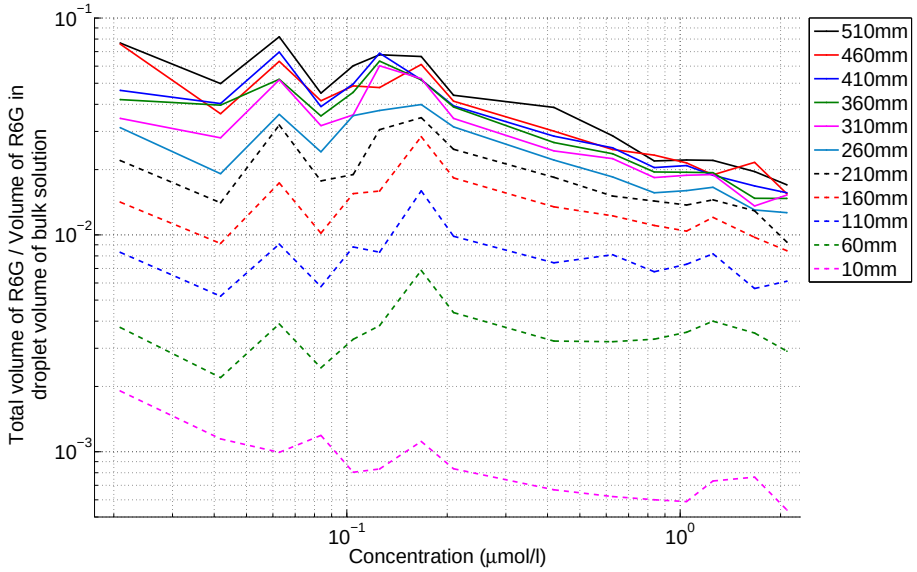

(a) Normalised volume of Rhodamine-6G per droplet against bulk surfactant concentrations for different heights,

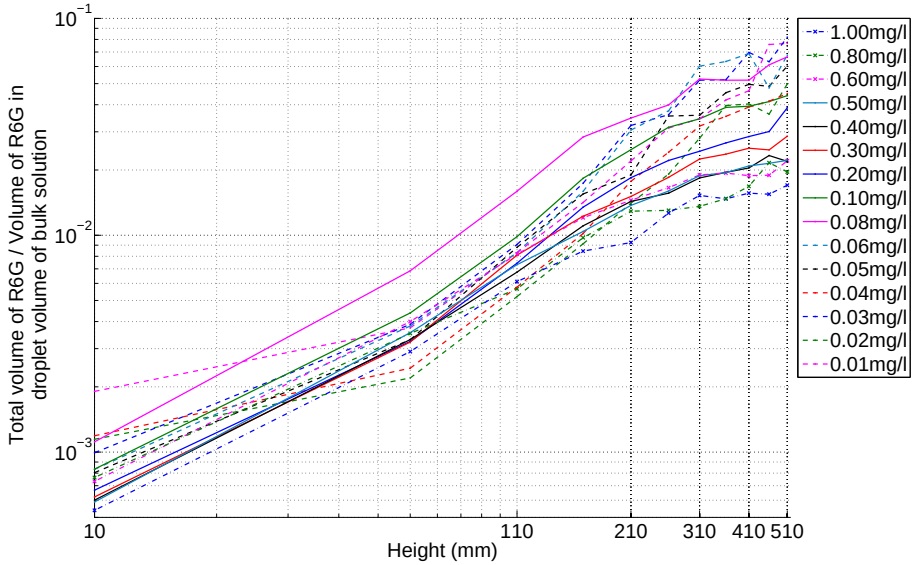

(b) Normalised volume of Rhodamine-6G per droplet against height in tank for different bulk concentrations

Figure 6.5: Total volume of Rhodamine-6G held behind a droplet normalised against the volume of Rhodamine-6G held within a droplets volume within the bulk solution.

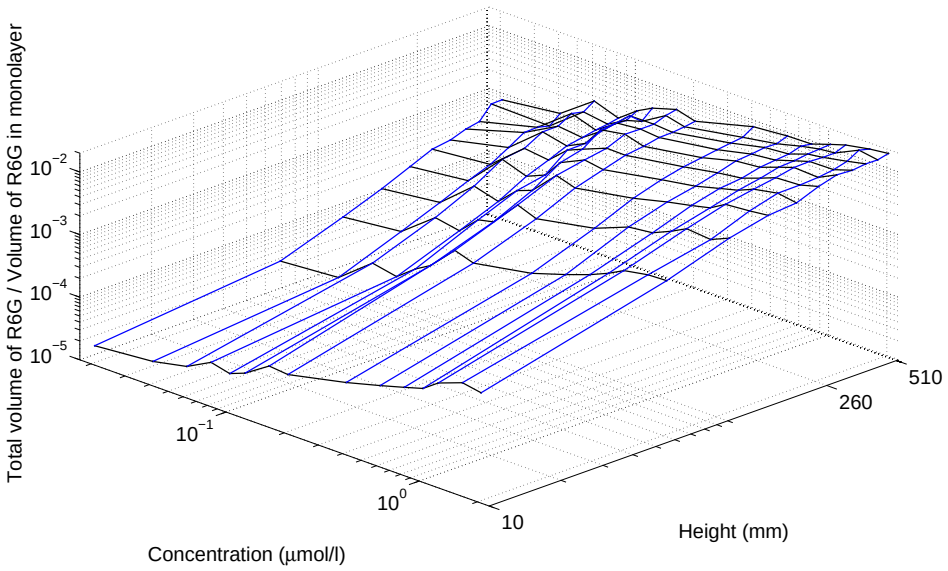

Figure 6.6: 3-dimensional visualisation of how the bulk concentration and the height from the base of the tank affects the volume of Rhodamine-6G held behind the droplet normalised by the number of Rhodamine-6G molecules required to form a monolayer around the droplet.

the volume held behind the droplet normalised by the quantity of Rhodamine-6G needed to form a monolayer on the bulk surfactant concentration and the height from the base of the tank is presented in Figure 6.6.

Figure 6.7(a) presents how the bulk concentration affects this normalised volume for different heights of the droplet in the tank. This shows an increase in the volume of surfactant gathered as the concentration of the bulk solution increases unlike Figure 6.5(a), although it again shows that larger heights have a greater quantity of surfactant with a large rate of increase at the lower end of the tank.

Figure 6.7(b) shows the dependence on height for the volume of Rhodamine-6G held behind the droplet normalised against the quantity required to form a monolayer. The curves for each bulk concentration grow over the height of the tank. However the rate of increase at the top of the tank slows as the droplet approaches the surfactant saturation level. These curves are spread over a larger range than the equivalent curves in Figure 6.5(b) with the stronger concentrations holding a larger volume of surfactant. The quantity of Rhodamine-6G required to form a monolayer is a function of the surface area of the droplet (r^2) whereas the volume of the droplet relies on r^3. The differences between Figures 6.7(b) and 6.5(b) highlight the dependence of the droplet volume on the quantity of surfactant

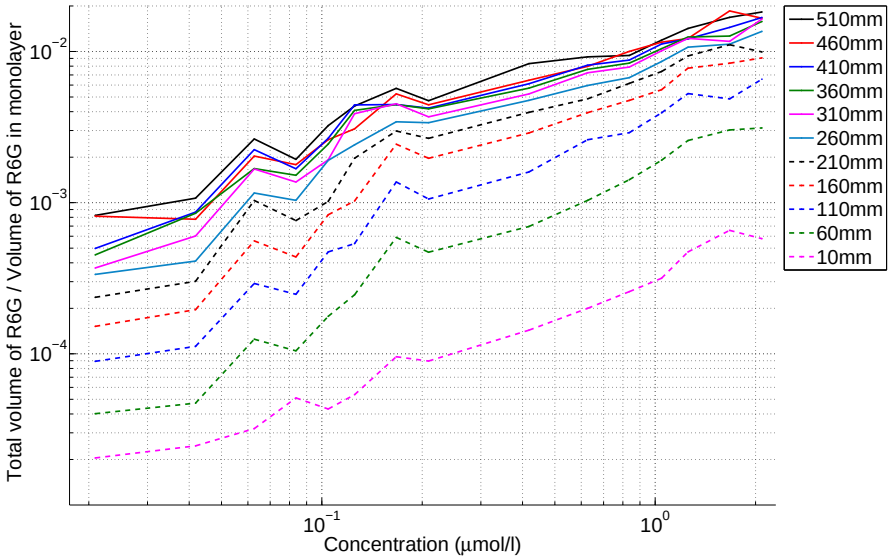

(a) Normalised volume of Rhodamine-6G per droplet against bulk surfactant concentrations for different heights,

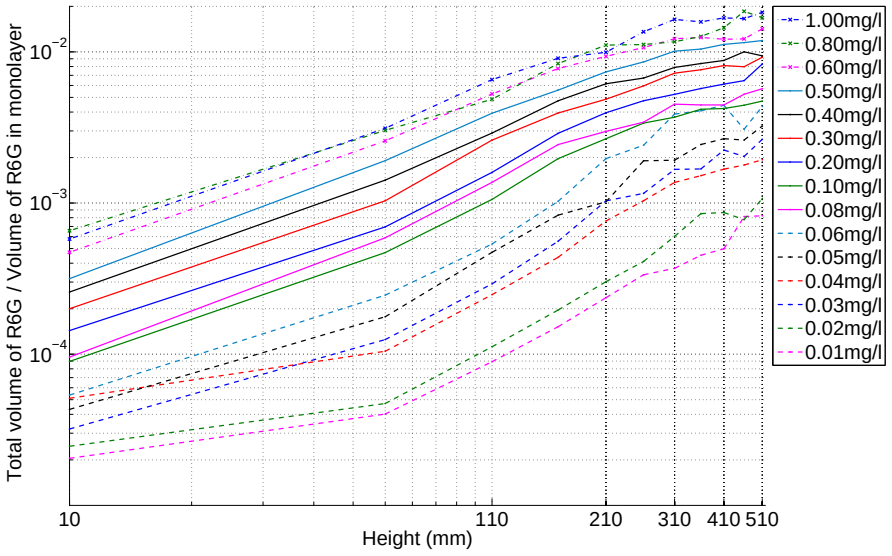

(b) Normalised volume of Rhodamine-6G per droplet against height in tank for different bulk concentrations

Figure 6.7: Total volume of Rhodamine-6G held behind a droplet normalised against the volume of Rhodamine-6G required for a monolayer.

gathered over the height of the tank.

From Figures 6.7(b) and 6.5(b) the relationship between the height in the tank and the volume can be measured as there is a linear increase over the initial part of the tank. As discussed in Section 6.2.1 the readings for the initial height should be treated with caution and so this height was not included in these measurements. The slope of the curve for the first half of the tank was calculated between 1.0 and 1.6 with the lower concentrations having larger rates of increase.

Figure 6.7 shows that the volume of surfactant held behind the droplet is far less than the volume required to form a monolayer around the droplet. As Rhodamine-6G is a weak surfactant, it takes a low amount of energy to remove the molecules from the interface. This could potentially contribute to the fact that the volume of the surfactant cap is lower than the volume of Rhodamine-6G required to form a monolayer. The quantity required to form a monolayer was most likely overestimated as it was assumed that ideal molecule packing at the interface occurred over the entire surface area of the droplet. In reality interactions between the surfactant molecules would increase the spacing between the individual molecules leading to a lower volume of Rhodamine-6G required to form a monolayer.

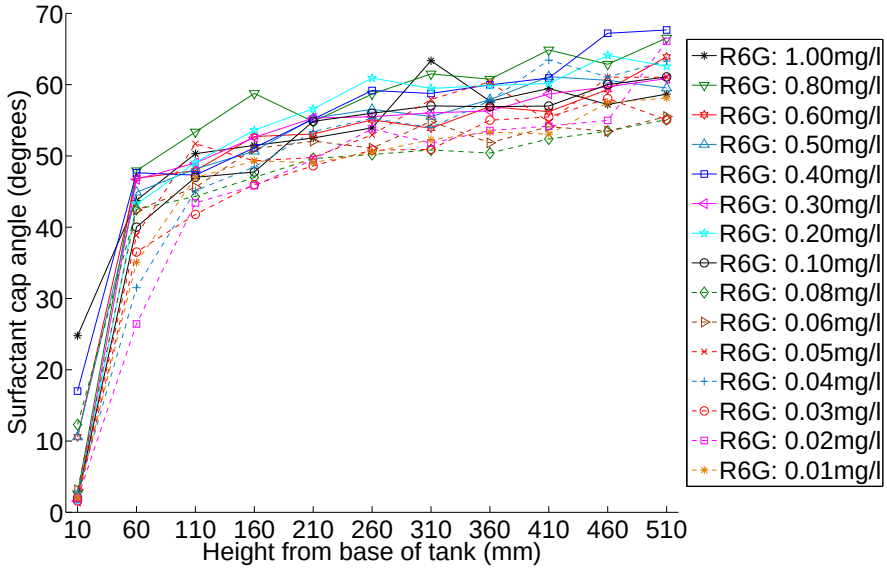

Figure 6.8: Comparison of the development of the angle of the surfactant cap over the height of the tank for all concentrations in the main experimental series.

The development of the surfactant cap angle as the droplet rises through the tank was compared for all Rhodamine-6G concentrations in Figure 6.8.

Figure 6.8 shows that for all concentrations the initial increase in surfactant cap angle is large. However the surfactant cap angle of all of the concentrations grow at approximately the same rate with a lot of overlap between each concentration profile. The angle profile for some of the concentrations fluctuates unexpectedly. These fluctuations are most likely due to the surfactant cap angle being averaged over droplets of different radii, as droplets with a smaller radius were shown to possess a larger cap angle. There is no clear order between the different concentrations implying that the averaged surfactant cap angle is more heavily influenced by the size of the droplet rather than the volume of surfactant within the surfactant cap. This implies that the size of the surfactant cap for each individual droplet is more heavily influenced by the flow speed past the droplet than by the accumulation of surfactant in the surfactant cap.

6.3 Summary

This chapter has presented the LIF results obtained from the main experimental series. The Reynolds number was calculated along with a comparison of the surfactant-depleted wake that forms behind the droplet obtained from experimental and theoretical data. This confirmed that the adsorption mechanisms were operating as expected within the experiment.

The surfactant cap volume for every droplet for each concentration was calculated and compared for each height to show a dependence on the quantity of Rhodamine-6G molecules in the surfactant cap on the volume of the droplet. These produced averaged profiles that were used to compare how the volume of Rhodamine-6G held behind a droplet developed over the height of the tank for different bulk concentrations along with the affects of the different bulk concentrations at different heights. This showed that as the height in the tank increased the volume of the surfactant cap also increased. At the lower end of the tank there was a maximum rate of increase of height to the power of 1.6 achieved for lower concentrations through to a minimum of height to the power of 1.0 achieved at higher concentrations. However at the higher end of the tank this increase levelled off as the droplets approached a surfactant saturation level where the volume of Rhodamine-6G adsorbing to the interface is approximately equal to the volume being swept back into the flow.

The surfactant cap angle shows an initial sharp increase over the lower end of

the tank before levelling off and remaining approximately constant. The same rates of increase were observed for all of the concentrations. However droplets with a smaller radius tended to have larger surfactant cap angles than the bigger droplets.

Chapter 7

PIV results

In this chapter the effects of surfactant on the internal circulation of an oil droplet as measured by PIV were investigated. The effect of changing the concentration of Rhodamine-6G dispersed throughout the bulk solution was explored with the aim of investigating the rate at which a stagnant cap at the rear of the droplet grows in size at different concentrations. The size of the stagnant cap was measured by calculating the tangential velocity around the droplet at 96% of the droplet's radius, and the stagnant cap was defined as the area of zero velocity at the rear of the droplet.

The results for individual droplets at each separate concentration are presented. This shows how the cap angle develops over individual droplets at increasing heights from the base of the tank. The droplets were divided into radius size bands to explore the effect of the radius on the size of the stagnant cap. This also allowed anomalous results to be identified and extracted before averaging the results over the remaining droplets.

The average results for each concentration are presented, and a relationship between the size of the stagnant cap and the surfactant concentration was investigated.

7.1 Maximum tangential velocity

The tangential velocity was measured around each droplet at 96% of the droplet radius, as discussed in Section 5.4.4, to give a tangential velocity profile of the internal circulation within the droplet. This allowed the stagnant region that formed at the rear of the droplet to be quantified, and the maximum velocity of the droplet fluid around the interface to be measured. Calculating this maximum tangential

velocity validates the processing methods applied to the PIV data, confirms the presence of internal circulation within the droplet, and allows a comparison of all of the data points to show consistency between different experimental droplets.

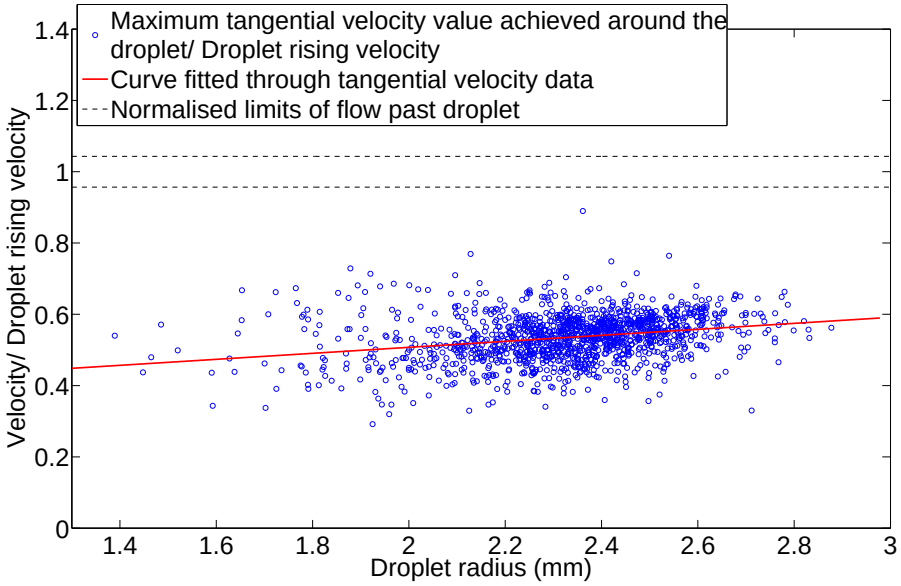

Figure 7.1: Maximum tangential velocity value achieved around the droplet at 96% of the droplet's radius compared with the limits of the theoretical rising velocity of the droplet for all Rhodamine-6G concentrations.

Figure 7.1 shows a comparison of the maximum tangential velocity achieved close to the interface of every droplet normalised by the theoretical droplet rising velocity at each concentration measured in the PIV experiments. The black dashed lines show the upper and lower limits of the normalised theoretical rising velocity of the droplet calculated using Equation 2.5 for a rigid sphere in a flow. This equation was shown to model the case for a fluid droplet rising through a surfactant solution in Section 4.2.

The maximum tangential velocity achieved at a point around a droplet was calculated from the average maximum velocity from both hemispheres of the droplet to reduce the effects of any irregularities. The solid red line shows a curve fitted through all of the data points to show the rate at which the value for the maximum tangential velocity achieved around the interface increases with the droplet radius.

The maximum value of the tangential velocity values around the interface increase as the radius of the droplet increases as would be expected. However this maximum tangential velocity value for each droplet is lower than the theoretical velocity of the flow past the droplet.

This lower tangential velocity value in comparison to the theoretical flow velocity past the droplet was caused by the stagnant cap reducing the mobility of the interface as well as the velocity gradient across the radius of the droplet. This velocity gradient is due to the flow past the droplet being the driving factor for the internal flow. As these maximum tangential velocity values were measured at 96% of the droplet radius they have a lower velocity than the expected velocity at the interface. The lower rate of change in the maximum tangential velocity implies that the majority of velocity is lost close to the interface (4% of a larger radius covers a larger distance than 4% of a smaller radius).

Although all of the data points follow the same trend, there is a relatively large range between the maximum and minimum recorded velocity values over the radius range making it difficult to determine a relationship between the maximum value of the tangential velocity around the droplet and the droplet rising velocity. Figure 7.1 shows the success of the processing techniques but also demonstrates the range of the fluctuations in the results introduced by the PIV analysis. Figure 7.1 also shows potential anomalous results in the form of droplets with a velocity greatly different from other droplets at the same radius. These anomalies could be caused by a lack of tracer particles within the droplet giving incorrect velocity readings.

7.2 Internal droplet streamlines

This section describes the internal circulation patterns observed within the droplets. Examples are presented for each height and each concentration of surfactant to validate the assumption of internal circulation within the droplet and the success of the vector field calculations performed by the commercial software package DynamicStudio v4.10 from Dantec Dynamics.

Figures 7.2 and E.1-E.14 in Appendix E present examples of contour plots showing the velocity levels within the droplets calculated from the vector fields, along with the internal streamlines with a frame of reference of a stationary droplet. The vector fields obtained from DynamicStudio v4.10 were post-processed to subtract the rising velocity of the droplet and to exclude all vectors falling outside the outer circumference of the droplet.

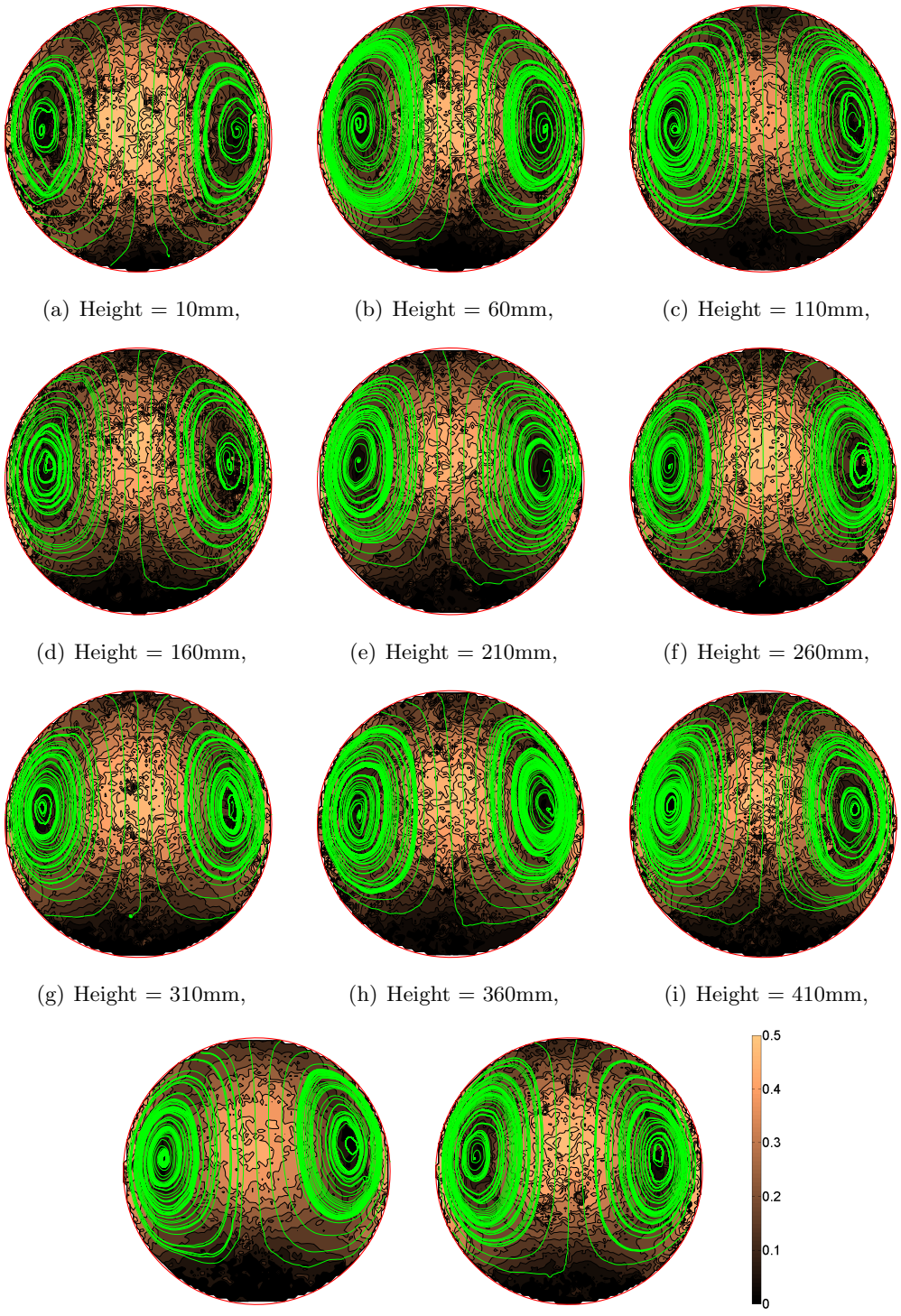

(a) Height = 10mm, (b) Height = 60mm, (c) Height = 110mm,

(d) Height = 160mm, (e) Height = 210mm, (f) Height = 260mm,

(g) Height = 310mm, (h) Height = 360mm, (i) Height = 410mm,

(j) Height = 460mm, (k) Height = 510mm.

Figure 7.2: Contour plots calculated from the vector fields superimposed with the internal streamlines (green lines) of the droplet (red outline) rising through the tank at different heights for a Rhodamine-6G concentration of 0.01mg/l. Internal velocities normalised against droplet rising speed.

Figure 7.2 shows the contour plots calculated from the computer vector fields vector fields along with associated streamlines for a Rhodamine-6G concentration of 0.01mg/l. The contour plots and associated streamlines for the Rhodamine-6G concentrations of 0.02mg/l to 1.00mg/l are presented in Appendix E. These streamlines show that the droplets exhibit internal circulation. It shows the success of using particle image velocimetry as a non-intrusive optical measurement technique to visualise the internal circulation within a droplet. The internal circulation follows the patterns as discussed in the literature in Section 2.1.4. However, as demonstrated in Section 4.2 the velocity of each droplet is in line with the velocity of a droplet rising as a solid sphere. This demonstrates that there is interference at the rear of the droplet that provides drag and reduces the terminal velocity of the droplet. This drag occurs due to the formation of a stagnant cap at the rear of the droplet which disrupts the internal circulation. The existence of this stagnant cap is confirmed by the areas of very low velocity at the rear of the droplets.

7.3 Individual concentration stagnant cap angles

The stagnant cap angle of every droplet was compared to explore the validity of averaging over the data set for each concentration. The tangential velocity profile was used to calculate the angle of the stagnant cap at the rear of the droplet, measured as the area of very low velocity. This angle where the velocity was close to zero corresponds to the stagnant cap zone caused by the build-up of surfactant at the rear of the droplet. The results for each concentration are shown in Figures 7.3 and F.1-F.14 in Appendix F, and show the development of the cap angle over the height of the tank. The droplets were divided into different bands based on the droplet radius to explore how the droplet size affects the results.

Figures 7.3 and F.1-F.14 were visually inspected to identify any outlying results. Due to the inherent inaccuracies associated with PIV measurements (as discussed in Section 5.4.1), any obvious outliers were treated as anomalous results and were excluded from the averaging process.

Figure 7.3 shows the results for the individual droplets for a concentration of 0.01mg/l of Rhodamine-6G. Over the lower end of the tank there is an increase in the stagnant cap size of the droplets. This growth rate flattens off at around 110mm from the base of the tank and there appears to be a constant stagnant cap angle over the remainder of the tank. The results for droplets with different radii overlap. The height of 460mm from the base of the tank shows that the size of the droplet could potentially impact the size of the stagnant cap. At this height

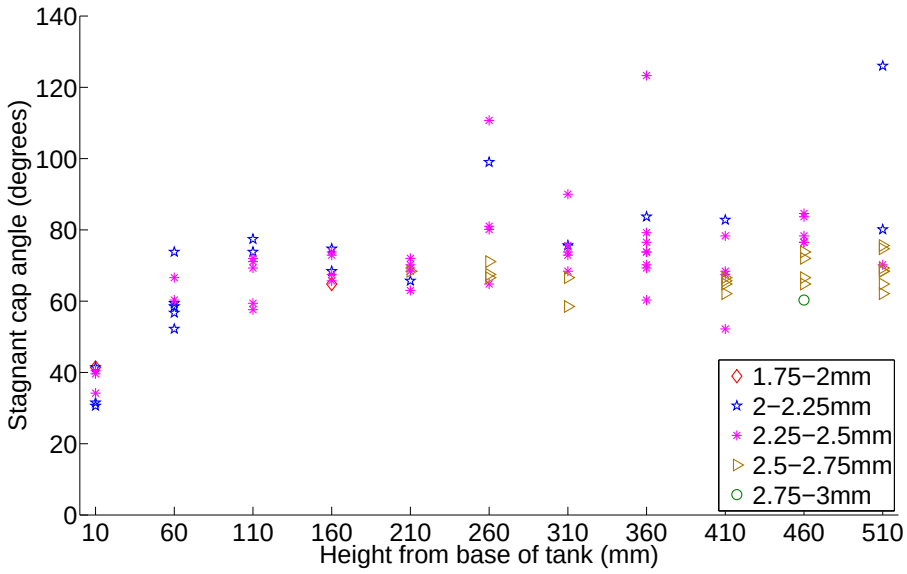

Figure 7.3: Development of the stagnant cap angle over the height of the tank for different droplet radii. Rhodamine-6G concentration of 0.01mg/l.

the droplet in the largest radius band of 2.75-3mm has the smallest stagnant cap angle size, the droplets with a radius between 2.5mm and 2.75mm have slightly larger stagnant cap angle size, and the smallest droplets measured at that height with radii between 2.25mm and 2.5mm have the largest stagnant cap angle sizes. However, the data presented here does not have the resolution or repeatability to draw a firm conclusion.

Figures F.1-F.14 in Appendix F show the stagnant cap angles for all of the droplets over the range of concentrations.

7.4 Averaged tangential velocity profiles

The droplets for each height of each concentration were averaged. This averaging was achieved by averaging the tangential velocity profiles calculated around the droplet at 96% of the droplet radius. The profiles for each height were compared at each measured concentration of Rhodamine-6G to explore the effects of the averaging process as well as how the stagnant cap angle grows over the height of the tank.

Figures 7.4 and G.1-G.14 in Appendix G show the results of the averaging process from the weakest Rhodamine-6G concentration through to the strongest Rhodamine-6G concentration. As shown in Section 5.4.4 the size of the stagnant cap angle is independent of the tangential velocity achieved around the front of

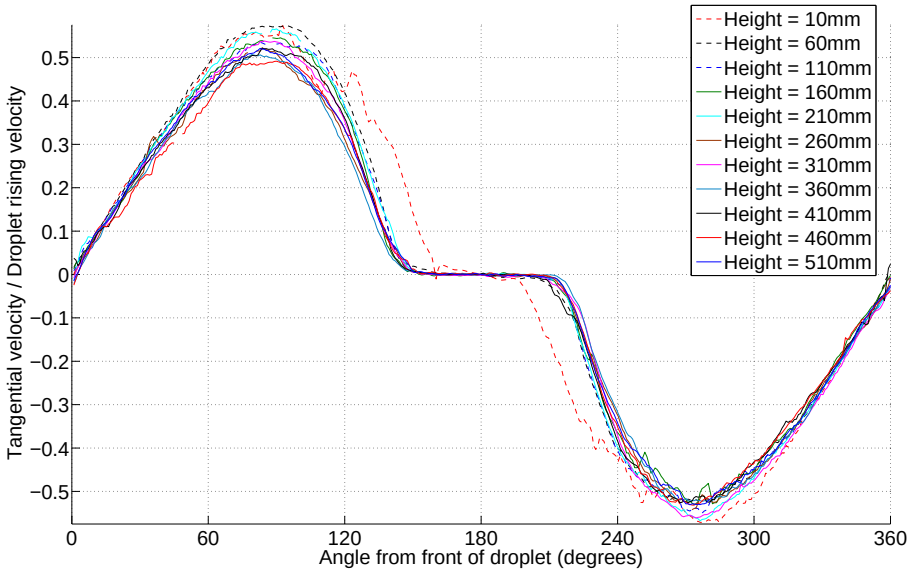

Figure 7.4: Averaged tangential velocity profiles around a droplet for a Rhodamine-6G concentration of 0.01mg/l at different heights from the base of the tank.

the droplet, so the magnitude of the velocity for each profile can be ignored. The averaging process was successful as all of the profiles show flat sections of zero velocity at the rear of the droplet from approximately 150-210 degrees, except for the Rhodamine-6G concentration of 0.08mg/l presented in Figure G.6. At this concentration the profiles at heights of 410mm and 510mm from the base of the tank show undulations around the zero velocity expected in the stagnant cap zone. However these two profiles pass through zero velocity at the very rear of the droplet showing that the subtraction of the droplet rising velocity from the calculated vectors was successful.

For all of the concentrations shown in Figures 7.4 and G.1-G.14 the tangential velocity profile for the lowest measured height, given by the dashed red line, show a far smaller zone of low velocity, as expected. Each of the heights at the higher end of the tank show very little difference in the stagnant cap angle. These graphs also confirm that the tangential velocity profiles around the droplet are mirrored around the vertical axis of the droplet, as expected.

7.5 Concentration comparison

The averaged stagnant cap angles were calculated from Figures 7.4 and G.1-G.14 and plotted for each concentration to compare the effects of surfactant concentration

on the size of the stagnant cap that forms at the rear of the droplet and how the cap angle develops over the height of the tank. This result is given in Figure 7.5.

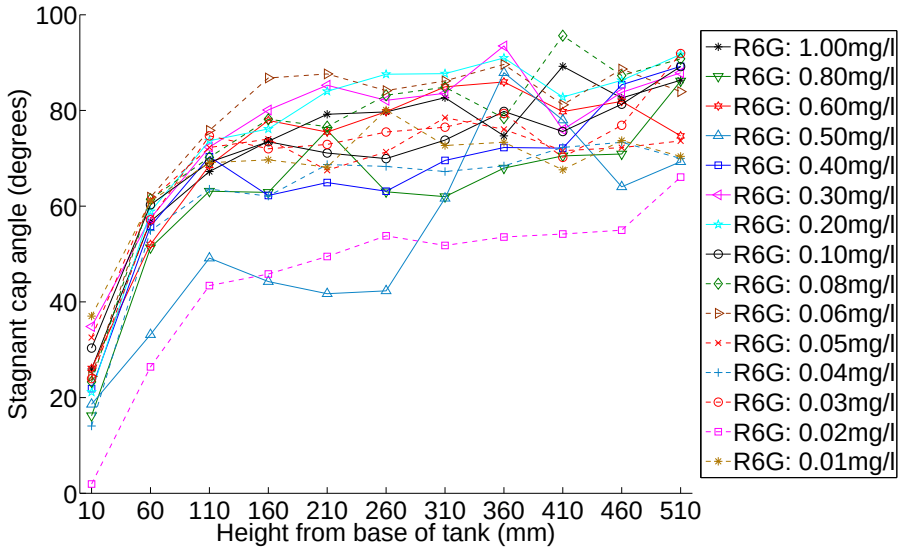

Figure 7.5: Comparison of the development of the angle of the stagnant cap that forms at the rear of a rising droplet of oil over the height of the tank for all concentrations of Rhodamine-6G.

The general trend of the data in Figure 7.5 shows a drastic increase in the size of the stagnant cap angle up to a height of 160mm from the base of the tank, at which point the curves flatten off. Each of the concentrations follow the same shape except for the concentration of 0.50mg/l of Rhodamine-6G. However there is no clear relation between the surfactant concentration and the size of the stagnant cap as each of the curves overlaps and are not arranged in order corresponding to surfactant strength.

Figure 7.5 shows how inconsistencies introduced in the PIV vector field analysis propagates through to have a large impact on these final results. Examples of this occur for a surfactant concentration of 1.00mg/l of Rhodamine-6G which consists of a smooth curve as expected until a height of 360mm from the base of the tank where the cap angle sharply decreases before rising to a sharp peak at 410mm and finally returning to expected values (as would be expected from a smooth curve) at 460mm. Similar irregularities are seen for the majority of Rhodamine-6G concentrations causing a large overlap between each concentration with some of the lower concentrations showing larger cap angles than stronger concentrations. A surfactant concentration of 0.06mg/l of Rhodamine-6G has the largest cap angles from 60mm

from the base of the tank to 210mm. Some of the higher concentrations show lower cap angles than weaker concentrations. Rhodamine-6G concentrations of 0.80mg/l and 0.40mg/l have some of the lowest cap angles throughout the height of the tank.

Two concentrations stand out as having different characteristics from the other concentrations. The surfactant concentration of 0.02mg/l of Rhodamine-6G shows the expected profile shape but with stagnant cap angles significantly lower than all other concentrations. The curve relating to a Rhodamine-6G concentration of 0.50mg/l shows an odd result in which the cap angle decreases from 110mmm from the base of the tank to 260mm before an abnormally large increase to a peak at 360mm followed by a drastic decrease. This concentration does not follow the same shape as any of the other concentrations and so is most likely an anomalous result.

The fluctuations in the results could occur from many different sources. One of the main areas for the introduction of error is through the process of calculating the PIV vector fields, as discussed in Section 5.4.1. The second source could be through the inconsistencies in droplet sizes captured throughout the experiments. As observed in Section 7.3, in general, smaller droplets possess larger cap angles. Therefore as each concentration possessed a different quantity of droplets with different radii then the results would be skewed. Further sources of error could be due to errors introduced in the experiments. If the laser sheet was marginally out of alignment with the centre line of the droplet then stationary particles on the interface around the sides of the droplet could have been captured masking the internal circulation around the droplets centre plane. The thickness of the laser sheet could be a source of error as the ratio of the width of the laser sheet to the diameter of the droplets was quite large. This could cause particles moving through the laser sheet in the third dimension to have been captured and analysed, so contributing to unrealistic results as the PIV analysis only calculates two-dimensional vector fields.

However despite these inconsistencies Figure 7.5 shows that the stagnant cap at the rear of the droplet initially increases from the point of droplet release. This rate of increase slows down until the stagnant cap angle maintains an approximately steady angle.

7.6 Summary

In this chapter the data obtained from the PIV experiments was analysed and compared to show the success of the use of PIV to measure the developing stagnant cap at the rear of a rising droplet of oil. Initially the maximum tangential velocity

around all of the droplets at 96% of the droplet radius was compared to validate the results from all of the individual droplets. This showed that larger droplets possess a larger maximum tangential velocity. However the spread of the data highlighted that the generation of the instantaneous vector fields introduced a degree of uncertainty into the data.

From here the streamlines within the droplet were calculated and plotted to confirm the presence of internal circulation within the droplet. This demonstrated the success of the PIV technique and showed a stagnant cap to grow at the rear of the droplet. The presence of this cap increased the droplet drag causing it to rise with the terminal velocity of a solid sphere rising through an aqueous solution.

The cap angles for each droplet were calculated and compared to show how the stagnant cap size developed over the height of the tank. It gave an opportunity to identify anomalous results as well as showing the potential for the size of the droplet to have an impact on the angle of the stagnant cap.

With the anomalous results removed, the remaining tangential velocity profiles were averaged and plotted for each concentration to show how the profile of velocity around the droplet develops over the height of the tank. The stagnant cap zones at the rear of the droplet were measured and plotted for each concentration to allow for a comparison of the effects of concentration on the size of the stagnant cap.

This comparison showed that at the lower end of the tank there was a drastic increase in the size of the stagnant cap for all concentrations. This increase levelled off towards the upper end of the tank, although, due to a variety of factors these results exhibited large fluctuations. These average cap angles for each concentration are compared with the profiles of the surfactant cap angles measured by LIF in Chapter 6 to explore the relationship between the LIF and PIV techniques.

Chapter 8

Comparing LIF and PIV results

The aim of this chapter is to investigate the relationship between the visible surfactant cap angle obtained by LIF and the stagnant cap angle obtained by PIV to enable the surfactant cap angle to be calculated when only the stagnant cap angle measured by PIV is known. This would allow this work to be developed in the future using non-fluorescent surfactants of different strengths.

This chapter initially presents a visual comparison of the surfactant distribution profile and the tangential velocity profile around the droplet. From here a comparison of the surfactant cap angle against the stagnant cap size for each of the surfactant concentrations over the height of the tank explores whether a relationship exists.

8.1 Profile comparison

The profile for the distribution of surfactant held around the interface of a rising droplet of oil obtained from the LIF experiments can be compared to the tangential velocity profile obtained from the PIV experiments to provide a direct visual comparison between the two techniques.

The profiles obtained from the LIF and PIV data were plotted around the interface of a spherical droplet for each height and concentration in Figures 8.1 and H.1-H.14 in Appendix H. The droplet interface represents a zero value for the excess surfactant volume and the tangential velocity. The blue line shows the LIF data for the profile of the distribution of surfactant around the interface with the blue angle representing the calculated surfactant cap angle. The red line shows the tangential velocity profile obtained from the PIV data with the red angle representing the calculated stagnant cap angle. Lines outside of the droplet interface represent a

positive value of either surfactant volume or tangential velocity.

The surfactant cap from the LIF data occurs when the surfactant level at the rear of the droplet rises above zero. However for the PIV data showing the tangential velocity, the stagnant cap is measured from where the velocity is zero, so where the profile meets the droplet interface. For the PIV data the magnitude of the tangential velocity was plotted. This allowed a visual qualitative comparison between the two measurement techniques. It would be expected that where the presence of the LIF surfactant cap should lead to an area of zero tangential velocity.

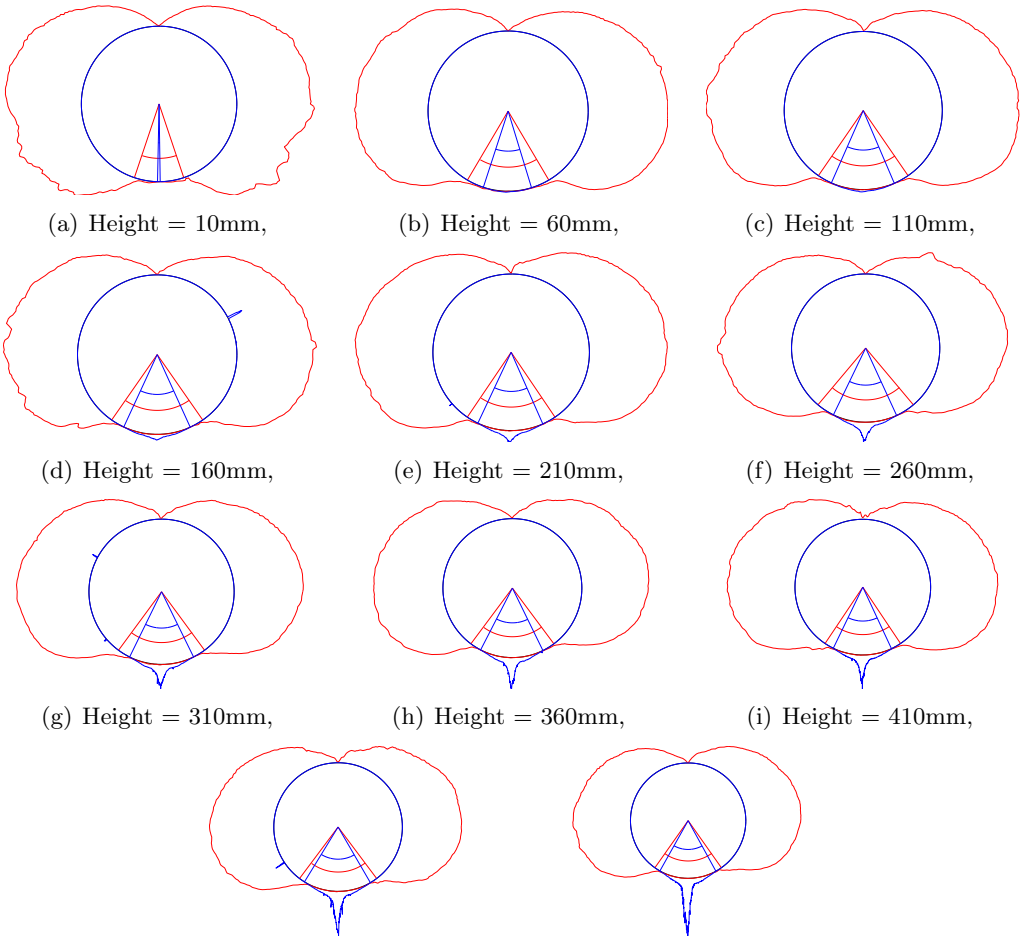

(a) Height = 10mm, (b) Height = 60mm, (c) Height = 110mm,

(d) Height = 160mm, (e) Height = 210mm, (f) Height = 260mm,

(g) Height = 310mm, (h) Height = 360mm, (i) Height = 410mm,

(j) Height = 460mm, (k) Height = 510mm.

Figure 8.1: Averaged LIF surfactant distribution profile (blue) compared with the averaged PIV tangential velocity profile (red) over the height of the tank for a Rhodamine-6G concentration of 0.01mg/l.

Each of the profiles for Rhodamine-6G concentrations from 0.02mg/l to 1.00mg/l are presented in Appendix H and show the success of the processing methods. The profiles for the LIF data and the PIV data are relatively symmetrical around the vertical axis of the droplet as expected. For each concentration the LIF data shows the progression from very little surfactant stored behind the interface at the rear of the droplet to a high volume of surfactant occurring behind the droplet, with a peak at the very rear of the droplet corresponding to the droplet wake. The PIV data show the presence of a stagnation point at the front of the droplet. The velocity increases moving down the sides of the droplet before a region of very low velocity signifying the presence of a stagnant cap at the rear of the droplet. This stagnant cap zone at the rear of the droplet increases over the height of the tank for each concentration.

8.2 Concentration comparison

The angle size of the surfactant cap measured by LIF as it developed over the height of the tank was compared to the angle size of the stagnant cap obtained by PIV. Each of the individual concentrations are presented in Figures 8.2-8.16 along with the associated error bars. These error bars show the range of the maximum and minimum surfactant or stagnant cap size of all droplets calculated at each height. In Figure 8.13 for a surfactant concentration of 0.50mg/l of Rhodamine-6G the result obtained for this concentration from the preliminary LIF experiments is also shown.

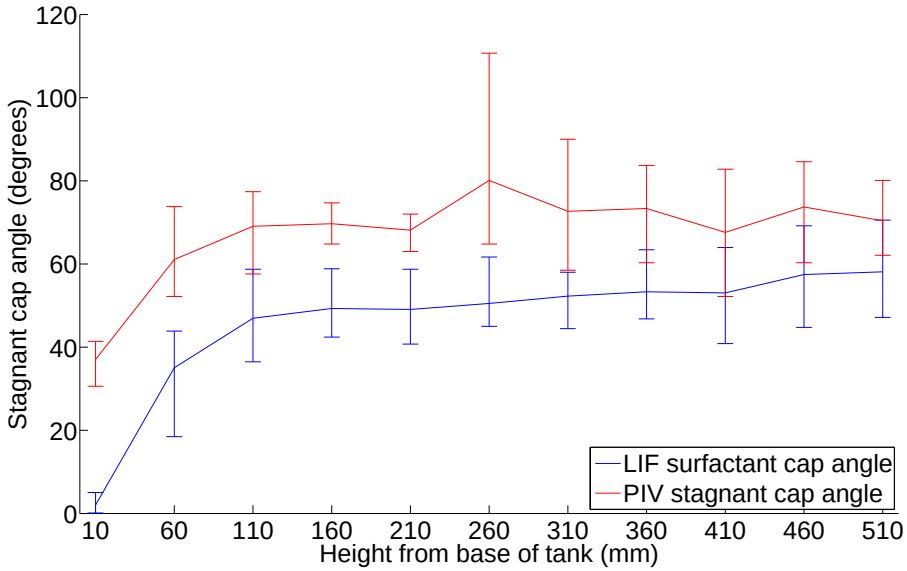

Figure 8.2: LIF surfactant cap angle (blue line) compared with the PIV stagnant cap angle (red line) over the height of the tank for a Rhodamine-6G concentration of 0.01mg/l.

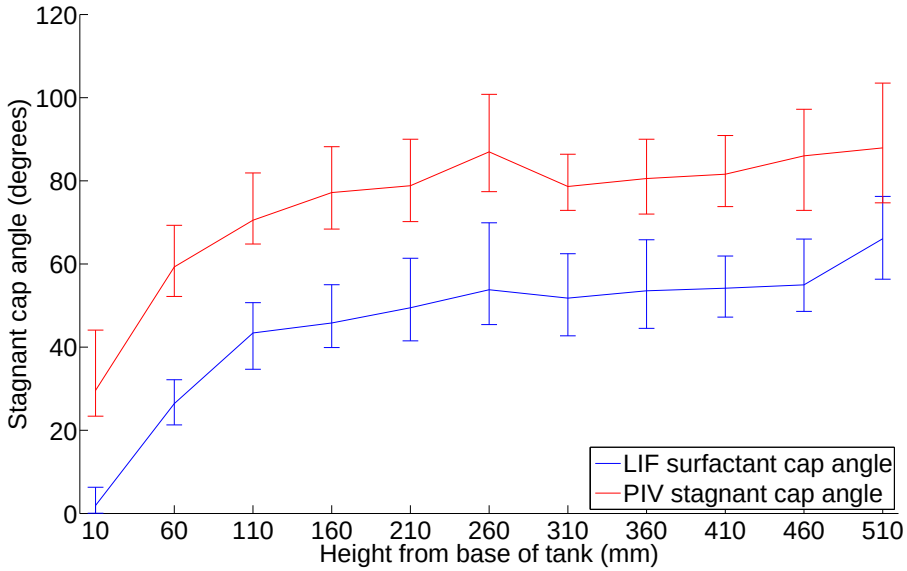

Figure 8.3: LIF surfactant cap angle (blue line) compared with the PIV stagnant cap angle (red line) over the height of the tank for a Rhodamine-6G concentration of 0.02mg/l.

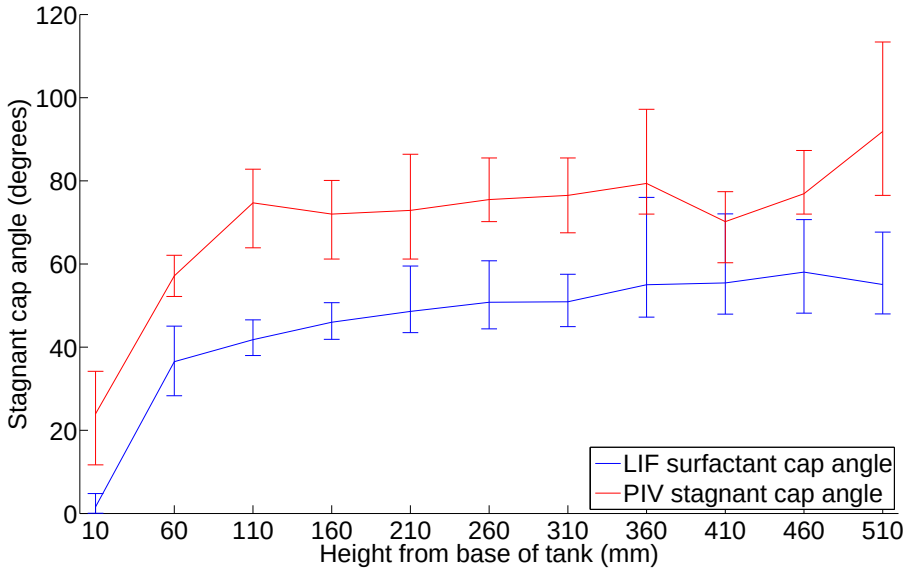

Figure 8.4: LIF surfactant cap angle (blue line) compared with the PIV stagnant cap angle (red line) over the height of the tank for a Rhodamine-6G concentration of 0.03mg/l.

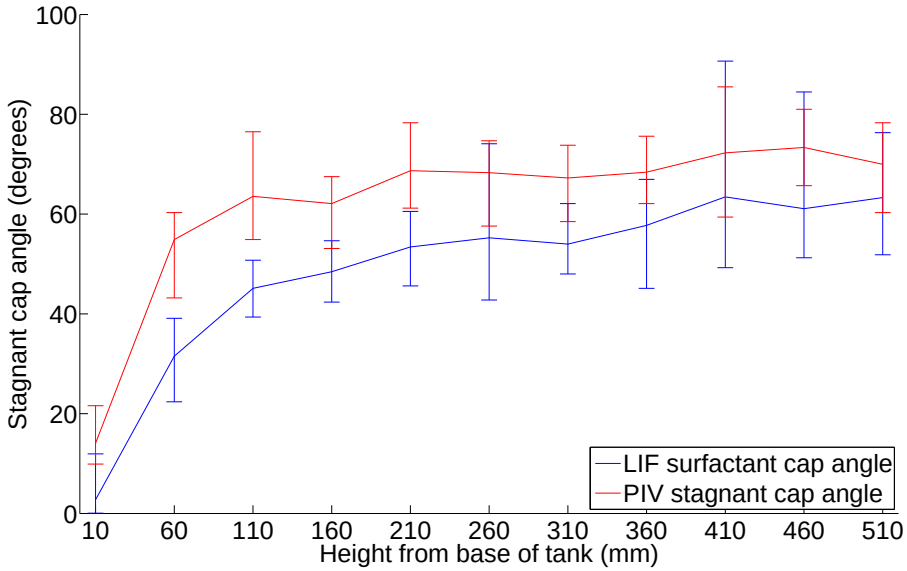

Figure 8.5: LIF surfactant cap angle (blue line) compared with the PIV stagnant cap angle (red line) over the height of the tank for a Rhodamine-6G concentration of 0.04mg/l.

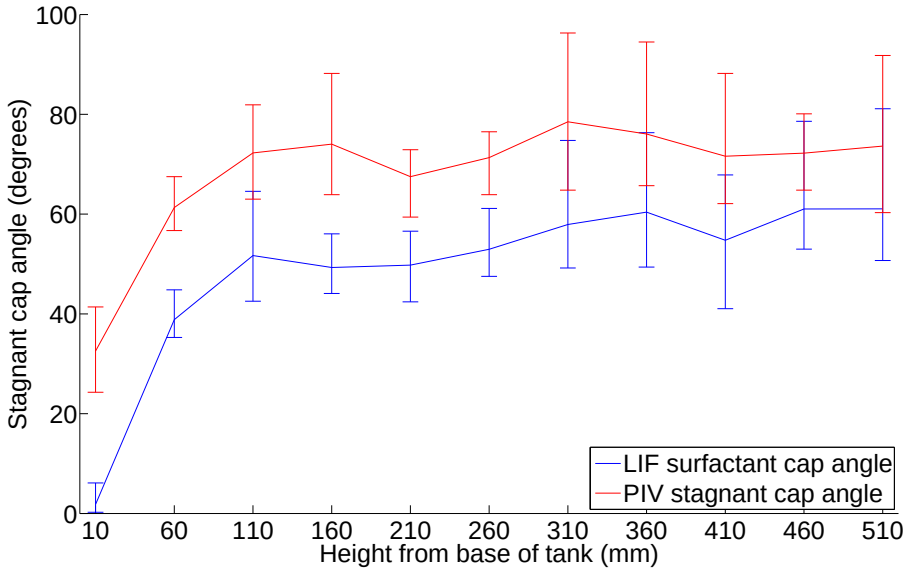

Figure 8.6: LIF surfactant cap angle (blue line) compared with the PIV stagnant cap angle (red line) over the height of the tank for a Rhodamine-6G concentration of 0.05mg/l.

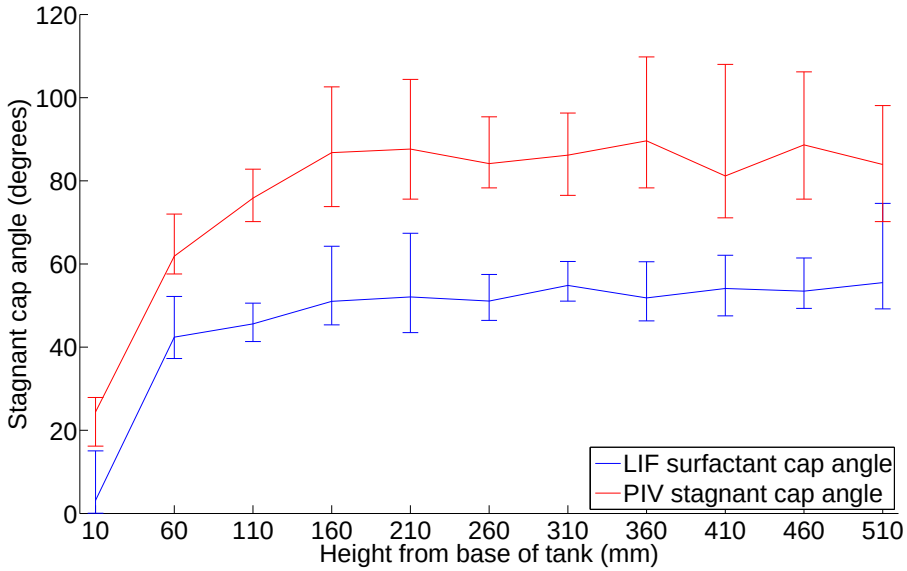

Figure 8.7: LIF surfactant cap angle (blue line) compared with the PIV stagnant cap angle (red line) over the height of the tank for a Rhodamine-6G concentration of 0.06mg/l.

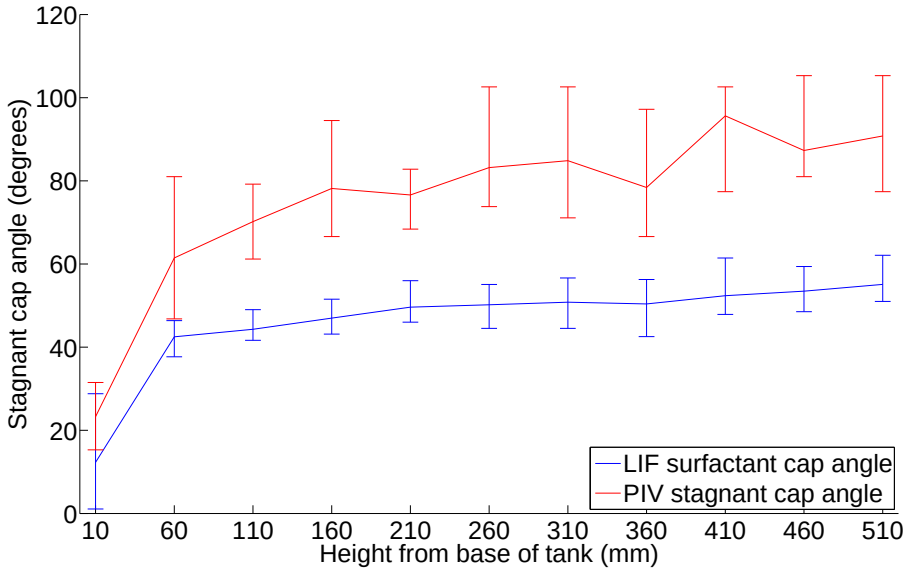

Figure 8.8: LIF surfactant cap angle (blue line) compared with the PIV stagnant cap angle (red line) over the height of the tank for a Rhodamine-6G concentration of 0.08mg/l.

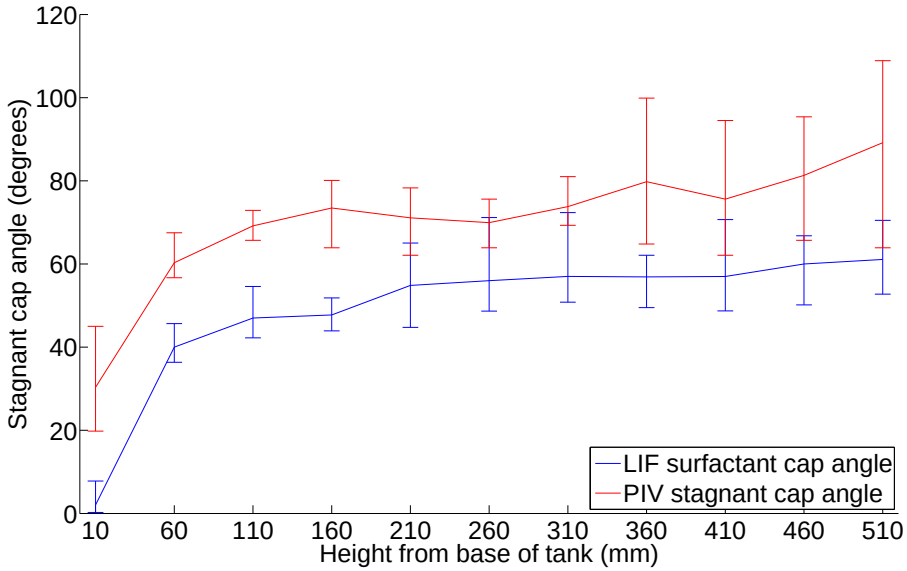

Figure 8.9: LIF surfactant cap angle (blue line) compared with the PIV stagnant cap angle (red line) over the height of the tank for a Rhodamine-6G concentration of 0.10mg/l.

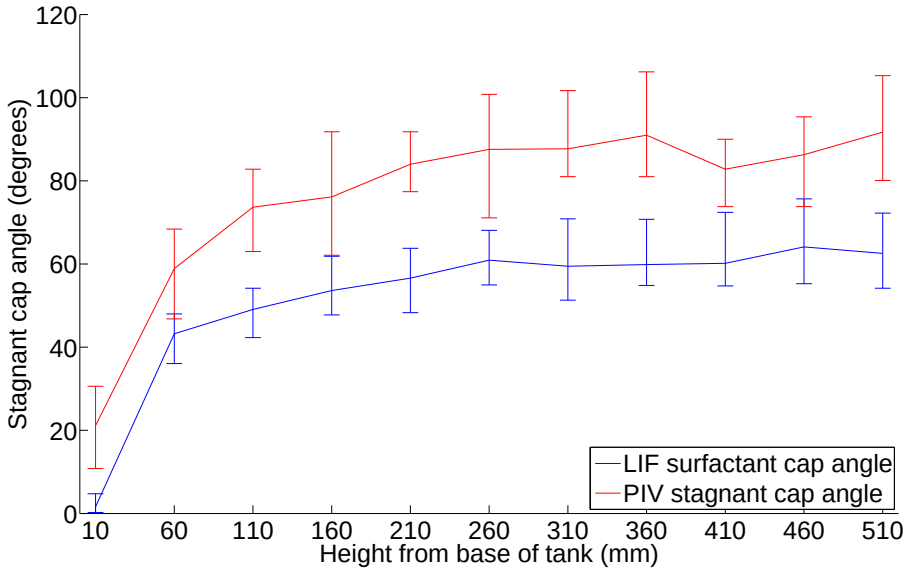

Figure 8.10: LIF surfactant cap angle (blue line) compared with the PIV stagnant cap angle (red line) over the height of the tank for a Rhodamine-6G concentration of 0.20mg/l.

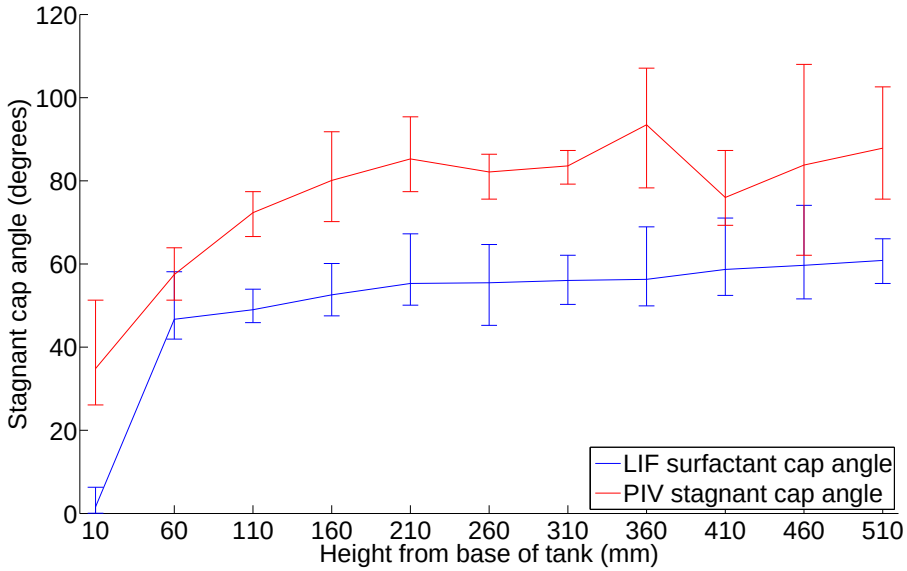

Figure 8.11: LIF surfactant cap angle (blue line) compared with the PIV stagnant cap angle (red line) over the height of the tank for a Rhodamine-6G concentration of 0.30mg/l.

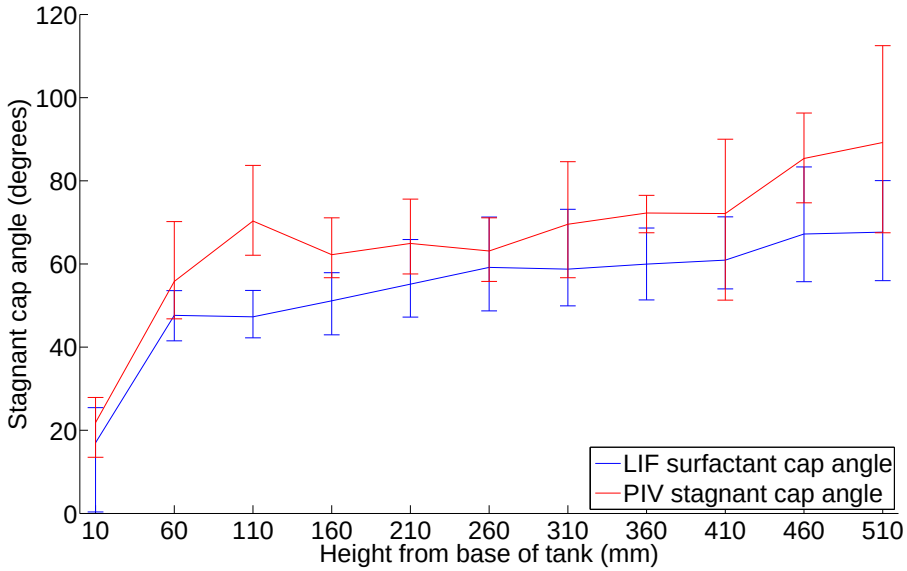

Figure 8.12: LIF surfactant cap angle (blue line) compared with the PIV stagnant cap angle (red line) over the height of the tank for a Rhodamine-6G concentration of 0.40mg/l.

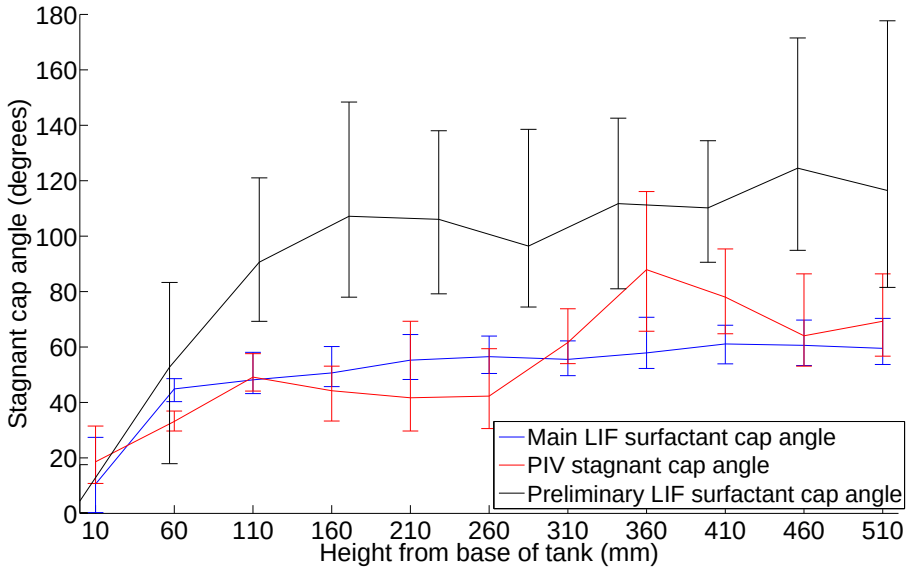

Figure 8.13: LIF surfactant cap angle from main experimental series (blue line) compared with surfactant cap angle from preliminary experimental series (black line) and the PIV stagnant cap angle (red line) over the height of the tank for a Rhodamine-6G concentration of 0.50mg/l.

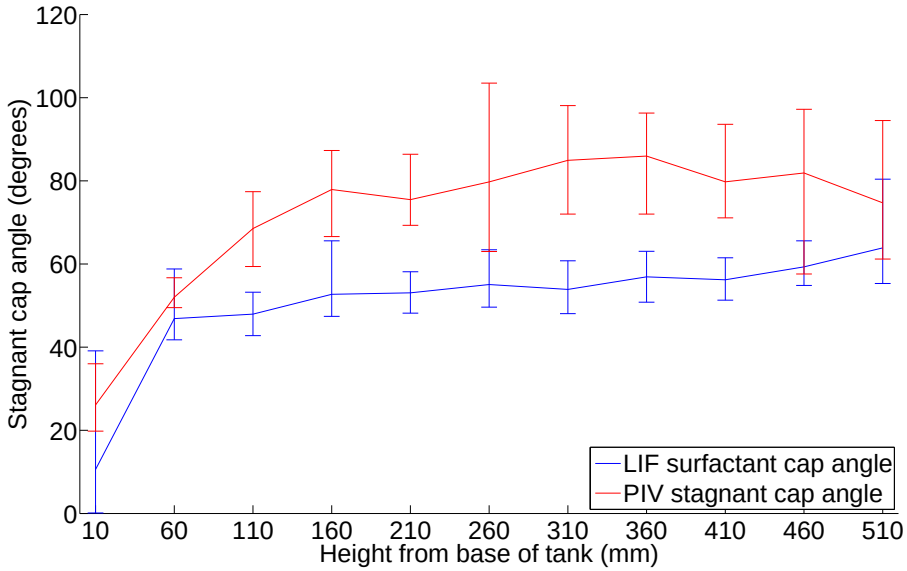

Figure 8.14: LIF surfactant cap angle (blue line) compared with the PIV stagnant cap angle (red line) over the height of the tank for a Rhodamine-6G concentration of 0.60mg/l.

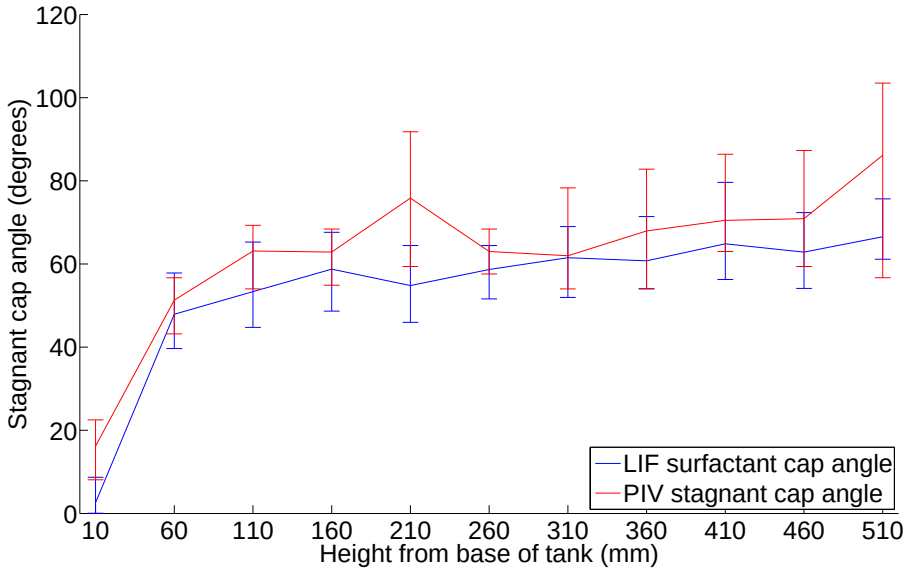

Figure 8.15: LIF surfactant cap angle (blue line) compared with the PIV stagnant cap angle (red line) over the height of the tank for a Rhodamine-6G concentration of 0.80mg/l.

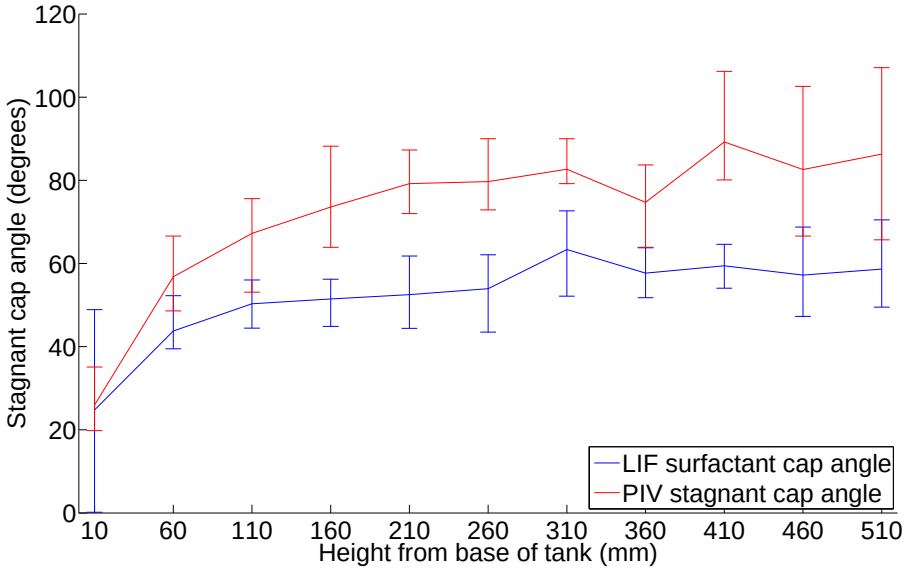

Figure 8.16: LIF surfactant cap angle (blue line) compared with the PIV stagnant cap angle (red line) over the height of the tank for a Rhodamine-6G concentration of 1.00mg/l.

The comparisons between the techniques shown in Figures 8.2-8.16 show that both techniques give lines of the same shape. However, the stagnant cap angle obtained from the PIV experiments tends to have a larger angle than the visible surfactant cap angle obtained by the LIF. The only case of the PIV result having a smaller angle than the LIF result occurs at a Rhodamine-6G concentration of 0.50mg/l, where the PIV stagnant cap angle curve exhibits an abnormal shape in comparison with all other concentrations.

The difference in the stagnant cap angle calculated by the PIV experiments, and the surfactant cap angle calculated by the LIF experiments, was calculated for each concentration and averaged over the height of the tank. The averaged angle difference for each concentration is shown in Table 8.1.

Table 8.1: Difference between the stagnant cap angle measured by PIV and the visible surfactant cap angle measured by LIF, averaged over the height of the tank.

Rhodamine-6G concentration (mg/l)	Angle difference (degrees)
0.01	21.4
0.02	28.7
0.03	24.7
0.04	13.4
0.05	19.2
0.06	30.2
0.08	29.3
0.10	21.3
0.20	24.5
0.30	25.9
0.40	12.3
0.50	2.6
0.60	21.0
0.80	8.8
1.00	20.4

Table 8.1 confirms that in all cases the stagnant cap angle measured by the PIV experiments is larger than the visible surfactant cap angle measured by the LIF experiments. In most cases the PIV experiments give a cap angle 19-30 degrees larger than the cap angle measured by the LIF experiments. For a Rhodamine-6G concentration of 0.50mg/l the averaged angle difference is far smaller as the LIF result gave a larger cap angle at the lower end of the tank, as shown in Figure 8.13. Rhodamine-6G concentrations of 0.4mg/l and 0.8mg/l also gave relatively low averaged angles. Figures 8.12 and 8.15 show a close agreement between

the two sets of data for the concentrations of 0.4mg/l and 0.8mg/l respectively. However, on average there is a substantial observable difference between the results obtained from the two measurement techniques.

There are two potential reasons for the discrepancies between the data produced by the LIF and PIV experiments. The first of these is due to the fluorescence properties of the Rhodamine-6G, whereas the second reason is due to obstruction of the adsorption dynamics of the system by the tracer particles used for the PIV experiments.

A single layer of Rhodamine-6G molecules does not emit enough light to be detected by the camera. However layers of surfactant not detected by the camera would still contribute to the size of the surfactant cap increasing the disruption of the internal circulation within the droplet. The LIF results correspond to only the size of the visible surfactant cap and therefore underestimate the true size of the surfactant cap angle.

As discussed in Section 4.4.2 the tracer particles used for the PIV experiments could affect the adsorption dynamics of the Rhodamine-6G adsorbing to the interface. As Rhodamine-6G is classed as a weak surfactant the interaction with the interface is weak and so the adsorption dynamics are more prone to disruption from external sources. If the tracer particles adhere to the interface inside the droplet they would be swept around to the rear by the flow past the droplet which causes the internal circulation. The accumulation of tracer particles at the interface around the rear of the droplet could contribute to a stagnant cap independent of the effects of the Rhodamine-6G.

The tracer particles used had a radius of 5.00×10^{-6}m in comparison to the effective radius of a Rhodamine-6G molecule at 5.18×10^{-10}m. As the radius of the tracer particle is many orders of magnitude larger, a small amount of tracer particles adhering to the interface could have a large effect on the size of the stagnant region at the rear of the droplet in comparison to the volume of Rhodamine-6G. This could cause a larger cap angle than when a droplet contains no tracer particles.

This effect of the tracer particles adhering to the interface was observed in the raw photographs captured during the experiments. Figures 8.17-8.19 show examples taken from the raw data set that show the tracer particles adhering to the interface.

Figure 8.17 shows an example from a surfactant concentration of 0.01mg/l of Rhodamine-6G. It shows the first and last frames of the droplet photographed to create one set of instantaneous vector fields. A layer of particles can be observed in these frames at the rear of the droplet extending up the sides following the circular shape of the droplet interface and forming a cap. This implies that there is a

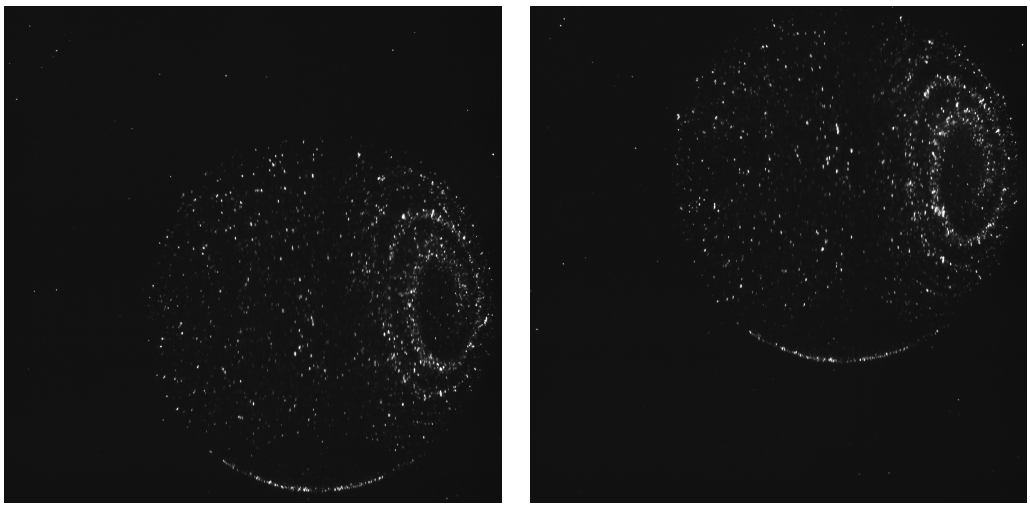

(a) Frame number 1, (b) Frame number 12,

Figure 8.17: Raw PIV photographs showing tracer particles positioned at the interface. First and last frames used for a string of vector fields separated by 0.1375s captured at a height of 260mm from the base of the tank. Rhodamine-6G concentration of 0.01mg/l.

stagnant cap formed from the tracer particles used for PIV at the interface at the rear of the droplet, contributing to an increased angle of the stagnant cap.

The same observations can be made for different concentrations and heights (Figures 8.18 and 8.19).

8.3 Summary

This chapter showed a comparison of the data obtained from the LIF technique from Chapter 6 with the data obtained from the PIV technique from Chapter 7. The averaged profiles for the distribution of surfactant around the droplet measured by LIF were compared to averaged profiles for the tangential velocity around the droplet measured by PIV for each height of each concentration. These profiles showed that both sets of data were symmetrical around the vertical axis of the droplet and showed the existence of an external surfactant cap caused by a build-up of Rhodamine-6G, in conjunction with an internal stagnant zone at the rear of the droplet. This confirmed that these two techniques are valid measurement techniques to determine the behaviour of a droplet rising through a surfactant-rich solution.

The LIF surfactant cap angle was compared to the PIV stagnant cap angle for each of the concentrations of Rhodamine-6G. This comparison showed that, in

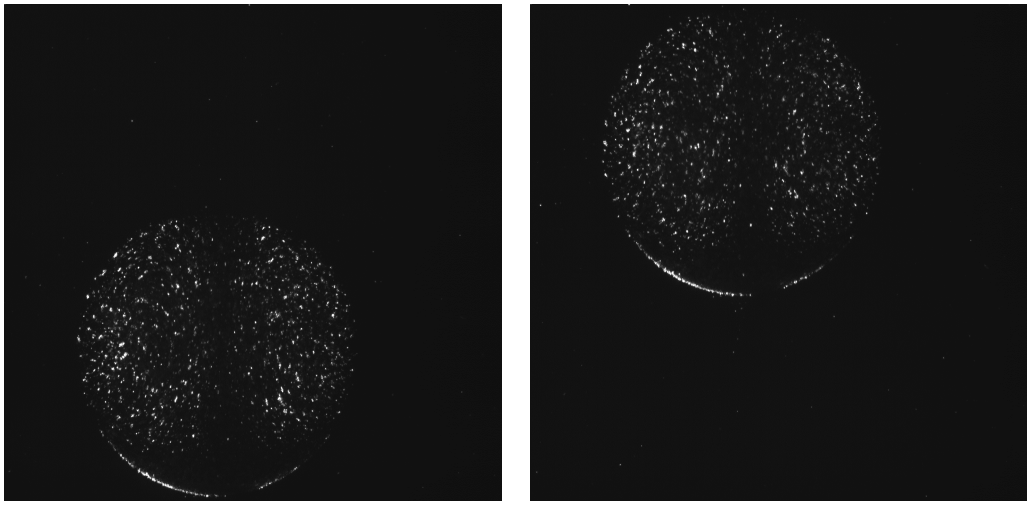

(a) Frame number 1, (b) Frame number 29,

Figure 8.18: Raw PIV photographs showing tracer particles positioned at the interface. First and last frames used for a string of vector fields separated by 0.35s captured at a height of 510mm from the base of the tank. Rhodamine-6G concentration of 0.10mg/l.

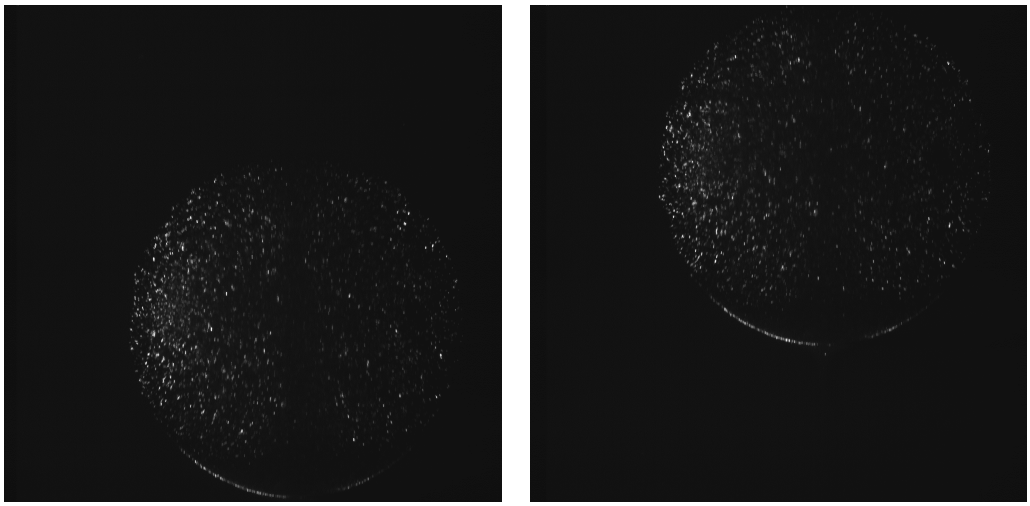

(a) Frame number 1, (b) Frame number 16,

Figure 8.19: Raw PIV photographs showing tracer particles positioned at the interface. First and last frames used for a string of vector fields separated by 0.1875s captured at a height of 410mm from the base of the tank. Rhodamine-6G concentration of 1.00mg/l.

general, the PIV experiments produced a larger stagnant cap angle than the LIF surfactant cap angle, although the curves followed the same shape. This discrepancy could be due to the LIF data showing a smaller angle than actually exists as very thin layers of Rhodamine-6G do not emit enough light to be registered by the camera, or it could be due to the tracer particles used for the PIV accumulating at the rear of the droplet and increasing the stagnant cap angle. The effects of the tracer particles used for PIV at the interface of an oil droplet in a flow need to be explored in order for the relationship between the surfactant cap angle and the stagnant cap angle to be developed.

Chapter 9

Conclusions & further work

9.1 Conclusions

The main finding of this work is that a weak surfactant, with a low interfacial concentration, can be extracted from the medium in which it is dispersed, to the rear of an immiscible droplet possessing a different density. Where strong surfactants gather at the interface due to strong interfacial attraction forces, the majority of the weak surfactant accumulates at, and is carried in, the wake of the droplet instead.

The aim of this project was to explore the effects of surfactant on the development of the wake behind a rising droplet of oil and on the internal circulation within the droplet. These aims were achieved using a fluorescent surfactant in order to perform laser-induced fluorescence, in which a laser sheet was used to visualise the entrainment of the surfactant at the rear of the droplet. This visualisation enabled the capture of images that showed the formation of a surfactant-rich cap at the rear of the droplet at different heights of the tank. These images were processed to calculate the size of the surfactant cap and the volume of surfactant held within it.

As very few surfactants are fluorescent, this technique to explore the effects of surfactant on a droplet in a flow is not widely applicable. Therefore it was desirable to link the size of the surfactant cap to a measurable property related to the droplet that was not dependent on the optical properties of the surfactant. This was achieved by exploring the internal circulation within the droplet by seeding the oil droplet with tracer particles. Particle image velocimetry was used to calculate the instantaneous vector fields for the droplets at each height in the tank. These vector fields were used to calculate the tangential velocity close to the interface of the droplet. The tangential velocity profiles showed an area of very low velocity at

the rear of the droplet that could be linked to the size of the visible surfactant cap measured by the LIF.

The project was divided into separate objectives. The first of these was to identify and understand the physical phenomena that would occur in the proposed experiments. This included identifying the flow regime of the system as laminar with no flow detachment from the droplet, exploring how surfactants functioned and their effects on the interface between two immiscible fluids, and the process of mass transfer due to adsorption. Values obtained from the experiment matched up reasonably well with theoretical values when assumptions were made. This confirmed the validity of the methods used in this work.

An experiment was designed in which a droplet of oil was released from the base of a tank to rise through an aqueous solution containing surfactant. Water was mixed with glycerol to give an aqueous solution with a high viscosity with Rhodamine-6G used as a fluorescent surfactant. The height of the tank was divided into equally spaced positions at which the oil droplet was photographed. A laser was used to optimise the fluorescent properties of the surfactant for the LIF experiments and to illuminate the tracer particles in the PIV experiments.

Calibration techniques were developed to reduce the impact of experimental inconsistencies and to relate the brightness of each pixel in the photograph to the concentration of Rhodamine-6G at each point. Experiments were also performed to measure the terminal rising velocity of the droplets. It was found that, due to the presence of surfactant at the interface, the terminal velocity was reduced to match that of a sphere with a completely rigid interface within a flow.

The raw data, in the form of photographs, had to be processed to extract quantitative results. For the LIF experiments the images were processed to extract the size of the visible surfactant cap and the volume of Rhodamine-6G stored within the surfactant cap. The images captured for the PIV data were initially processed by a commercial software package to calculate the instantaneous vector fields of the droplets. These vector fields were post-processed to calculate the tangential velocity close to the interface of the droplet. An area of low velocity at the rear of the droplet signified the presence of a stagnant region relating to the formation of the surfactant cap caused by the accumulation of surfactant.

The LIF results showed that the surfactant was swept around to the rear of the droplet where it accumulated in a surfactant-rich cap before being swept back into the flow. As the droplet moved through the tank the volume of surfactant held behind the droplet increased. It was observed that the higher the concentration of surfactant dispersed throughout the bulk solution, the greater the quantity of

surfactant held behind the droplet. However when the volume of Rhodamine-6G held behind the droplet was normalised by the volume of Rhodamine-6G within a droplet volume of the bulk solution it was found that the ratio of the volume of the surfactant cap to the volume in the droplet decreased as the concentration of the bulk solution increased. Normalising by the quantity of Rhodamine-6G held by a droplet's volume of the bulk solution caused the curves for the height in the tank against the normalised volume to collapse, showing a good dependency on the volume. In log scale these curves showed linear behaviour over the lower section of the tank before the rate of adsorption slowed towards the upper end of the tank. This decrease in the adsorption rate occurred due to the droplets approaching a surfactant saturation level where the rate of adsorption at the front of the droplet would equal the rate at which the surfactant is swept from the rear of the droplet back into the flow.

There was no discernible difference between the angle range of the surfactant cap for different concentrations of Rhodamine-6G.

The PIV data revealed the formation of a stagnant zone at the rear of the droplet as it rose through the tank. There was a large stagnant angle increase over the initial section of the tank before the stagnant cap angle became relatively constant. As with the surfactant cap angle obtained from the LIF data, there was no obvious difference between the stagnant cap angle over the range of Rhodamine-6G concentrations.

The surfactant cap angle obtained from the LIF was compared to the stagnant cap angle obtained from the PIV. There was a good agreement between the shape of the curves for the development of the surfactant and stagnant caps, however the results for the PIV experiments consistently showed a larger angle. This was potentially due to the presence of the tracer particles necessary for PIV interfering with the effects of the surfactant.

Despite these inconsistencies this project has shown that both the LIF and PIV techniques were successful in non-intrusively studying the entrapment of surfactant behind a rising droplet of oil. This work has presented a base on which work in the future can expand upon.

9.2 Practical applications

This work could be utilised for applications that require control of chemicals in a system. One potential use would be for the removal of surfactant-like substances that adsorb to an interface. Passing droplets of an immiscible fluid through a solution

containing a surfactant-like chemical would speed the process of chemical removal compared to waiting for separation to occur naturally as the chemical would adsorb to the interface of the droplet and be transported to the surface. However there would be design considerations as it was shown that the droplet size, surfactant concentration, and height in the tank all affected the results.

The requirements of the speed of separation against efficiency would need to be considered as it was shown that, per unit volume of the droplet, smaller droplets held a higher volume of surfactant. However, larger droplets have a larger surface area for surfactant to adhere to and so carry a larger volume of surfactant with each droplet.

The height of the tank is an important consideration based on the concentration of the surfactant. Stronger concentrations gather a larger volume and reach the surfactant saturation point earlier than weaker concentrations so a shorter tank would be desired. It would be inefficient to have a tank height greater than the height required to reach the surfactant saturation level.

9.3 Further work

Whilst this work has been successful and has given an insight into this research area, there is a wide range of ways in which it can be improved and extended. These extensions can be split into two sections; experimental work and theoretical work. This section will describe both the experimental and the theoretical aspects for furthering this work.

9.3.1 Experimental work

The improvements for the experimental side to this project can be split into different areas. The first area to be discussed is how the experimental setup could be improved to obtain higher quality results with less initial processing being required, as well as discussing how the spatial resolution of the data could be increased. From here ideas of how to progress the exploration into the effects of different parameters will be explored.

Experimental setup

The first area that could be improved upon is to develop a system to create large droplets of a consistent diameter. While attempts were made in this work to produce equal sized droplets, a method was not successfully developed that could produce

droplets of a large enough size. Initially droplets on a macro-scale should be produced in order to compare to this work. Having a constant radius would achieve a constant surface area for the surfactant to adsorb to, as well as ensuring a constant rising speed of the droplet. Fixing the rising speed ensures that the diffusion layer thickness would be the same for all droplets and so adsorption of surfactant to the droplet would be consistent across the experiments.

There is the potential to redesign the experimental rig used for these experiments. It is preferable to have a stationary droplet within a tank with the aqueous phase flowing past it. With a flow past a stationary droplet the spatial resolution could be improved. Instead of capturing images at set length intervals, the droplet images could be captured continuously or at smaller time intervals, which would improve the spatial resolution of the current experiments. This would lead to a better understanding and improved accuracy of the mechanisms operating on the droplet.

The effect of a stationary droplet within a flow could be achieved in different ways. The first idea is to fix the position of the camera and laser and have the tank moving, as in this project. However, the tank would be mounted on a traverse which could be controlled so that the droplet is always within the field of view of the camera. The advantages of this method would be that the initial acceleration of the droplet could be easily accounted for. The disadvantages would be that accelerating the tank would cause inertial effects within the fluid, potentially disrupting the flow regime. Also, unless the tank is perfectly manufactured and the orientation of the traverse is extremely precise there could be alignment and focusing issues between the droplet and the camera. Alternatively the tank could remain fixed with the laser and camera mounted on a traverse. This would remove the risk of inertial effects within the fluid. However, a high level of precision would still be required to achieve perfect alignment and focusing of the camera.

Another method could be to have the tank, camera, and laser fixed in position. Instead of relying on the buoyancy of the droplet to rise through the tank, a flow could be generated past the droplet. The buoyancy of the droplet would then keep the droplet in the field of view of the camera. This could be achieved by controlling the speed of the flow past the droplet as the rising speed of the droplet would be known. This would enable the camera to be fixed in place in relation to the tank and avoid any risk of loss of focus when the tank was moved. A potential issue would be the insertion of the droplet. The droplet could not be suspended from a syringe tip as this would affect the transport of surfactant around the interface, and as the surfactant lowers the surface tension of the droplet it would probably break

away from the syringe tip. The formation of the droplet could present an issue as the droplet has to accelerate from rest to its terminal rising velocity, requiring fine control of the flow speed. This is a crucial time as there is a large effect early in the droplets lifespan, as observed in these experiments. The added benefit of this system would be that the aqueous fluid could be recirculated, potentially giving the droplet an infinite medium in which to rise through. This could be used to experiment over a longer time period. These improvements were made through the observation of deficiencies that arose at different stages of the current project with a lack of time and resources to explore further.

Further improvements could be made to the experimental setup. The first of these would be to manufacture the tank out of a purer material. In the current experiments due to the level of magnification tiny imperfections within the Perspex tank walls cast shadows. The Perspex also reduced the quantity of laser light that passed through the fluid. With a higher quality material, such as glass, the tank walls could be thinner with fewer imperfections. With no shadow streaks in the image, normalisation images of the exact target area in which the droplet was present would not be needed and the normalisation process could be simplified.

Another improvement to the experimental setup would be to the laser module. Ideally a laser would be used where the power is highly stable over time. This would reduce the need for normalisation of the droplet images, and remove any uncertainty of the results caused by the fluctuations in laser power. Improvements of the laser sheet optics would be desirable in order to create a thinner laser sheet. A thinner laser sheet would pass through a narrower section of the droplet then the results would be less affected by the curvature of the interface in this direction, as well as reducing the effects of tracer particles moving in the third dimension in PIV experiments. It would be desirable to have the laser sheet at a constant power over the entirety of the target area rather than the gradients observed in these experiments. This would further reduce the need for the normalisation process.

With the droplet in a fixed position within the tank it could be possible to use a pulsed laser rather than a continuous laser. This would be possible as, if the droplet size is consistent, fine tuning the alignment of the laser sheet with the centre line of the droplet would not be necessary (as was required in these experiments). By synchronising the camera and laser pulse, images could be captured at peak laser power.

Some work needs to be performed on the selection of tracer particles used for PIV. The experiments presented in this work showed the tracer particles accumulating at the rear of the droplet, potentially affecting how the surfactant interacted

with the interface. Ideally tracer particles would be selected that do not interact with the interface and only show the internal circulation patterns within the droplet.

Experimental parameters

As observed in these experiments the size of the droplet has an impact on the results. The first key aspect to any future work would be to produce droplets of consistent radius. From here a principled exploration of changing the radius of the droplet on the experimental results could be undertaken. As shown in this work, smaller droplets tend to have a lower volume of Rhodamine-6G within the surfactant cap, but the surfactant cap tended to have a larger angle. This was caused by the fact that smaller droplets have a lower surface area at the rear of the droplet for the surfactant to accumulate behind. Smaller droplets also have a lower rising velocity and so less force is imposed by the flow past the droplet on the interface causing larger surfactant cap angles to be achieved.

Other pure fluorescent surfactants should be tested to develop the knowledge on how different surfactants interact. However most surfactants do not have fluorescent properties and so it would be important to test a mix of non-fluorescent and fluorescent surfactants.

Once the effects of a laminar flow regime are fully understood, it would be interesting to introduce a turbulent flow regime by altering the Reynolds number of the system. This would be used to explore how turbulent flow affects the formation of the surfactant cap and the wake behind the droplet.

9.3.2 Theoretical work

The main task for the theoretical work would be to develop a model of the experiment presented in this work. This would involve linking the properties of the surfactant used to the adsorption process at the interface of the droplet. The transportation of the surfactant around the interface of the droplet would need to be modelled, based upon the quantity of surfactant already at the rear of the droplet and the rising speed, and the final desorption process at the rear of the droplet.

Creating an accurate theoretical model would reduce the need for experimental data, as well as allowing more complex geometries and scenarios to be explored that do not have to take account of the requirements associated with the experimental techniques.

Bibliography

Acros Organics. Product specification: Product 12402 mineral oil. URL www.acros.com/printPDFResult.aspx?PageLink=http://10.140.0.33/usas40080/internet/cgi-bin/spec01cl.pgm?Prdnr=12402\&Type=specs. Accessed June 2015.

Ronald J. Adrian and Jerry Westerwell. *Particle Image Velocimetry*. Cambridge University Press, New York, 1st edition, 2011.

D. Agble and M.A. Mendes-Tatsis. The effects of surfactant on interfacial mass transfer in binary liquid-liquid systems. *International Journal of Heat and Mass Transfer*, 43:1025 – 1034, 2000.

Nicolas J. Alvarez, Lynn M. Walker, and Shelley L. Anna. Diffusion-limited adsorption to a spherical geometry: The impact of curvature and competitive time scales. *Physical Review E*, 82:011604–1 – 011604–8, 2010.

Matthieu A. André and Philippe M. Bardet. Interfacial shear stress measurement using high spatial resolution multiphase PIV. *Experiments in Fluids*, 56:132, 2015.

Gurusamy Annadurai, Ruey-Shin Juang, and Duu-Jong Lee. Adsorption of Rhodamine 6G from aqueous solutions on activated carbon. *Journal of Environmental Science and Health, Part A*, 36(5):715 – 725, 2001.

Peter Atkins and Julio de Paula. *Elements of physical chemistry*. Oxford University Press, Oxford, 5th edition, 2009.

M.M. Awad. Two-phase flow. In Salim N. Kazi, editor, *An overview of heat transfer phenomena*, pages 251 – 340. INTECH Open Access Publisher, 2012.

Geoffrey T. Barnes and Ian R. Gentle. *Interfacial science: An introduction*. Oxford University Press, Oxford, 1st edition, 2005.

D. Bhaga and M.E. Weber. Bubbles in viscous liquids: shapes wakes and velocities. *Journal of Fluid Mechanics*, 105:61 – 85, 1981.

Robert D. Blevins. *Flow-induced vibration.* Van Nostrand Reinhold Company, New York, 1st edition, 1977.

W.N. Bond. LXXXII. Bubbles and drops and Stokes' law. *The London, Edinburgh, and Dublin Philosophical Magazine and Journal of Science*, 4(24):889–898, 1927.

R.P. Borwanker and D.T. Wasan. Equilibrium and dynamics of adsorption of surfactants at fluid-fluid interfaces. *Chemical Engineering Science*, 43(6):1323 – 1337, 1988.

R. Budwig. Refractive index matching methods for liquid flow investigations. *Experiments in Fluids*, 17:350–355, 1994.

Tae-Ho Chang and J.N. Chung. The effect of a stagnant surfactant cap on the transport mechanisms of a condensing droplet in a high Reynolds number flow. *Computers & Fluids*, 15(1):1 – 11, 1987.

Roland Clift, John Grace Grace, and Martin E. Weber. *Bubbles, Drops, and Particles.* Dover Publications, New York, 1st edition, 1978.

Clayton T. Crowe, John D. Schwarzkopf, Martin Sommerfeld, and Yutaka Tsuji. *Multiphase Flows with Droplets and Particles.* CRC Press, Boca Raton, 2nd edition, 2012.

B. Cuenot, J. Magnaudet, and B. Spennato. The effects of slightly soluble surfactants on the flow around a spherical bubble. *Journal of Fluid Mechanics*, 339:25 – 53, 1997.

Christopher T. Culbertson, Stephen C. Jacobson, and J. Michael Ramsey. Diffusion coefficient measurements in microfluidic devices. *Talanta*, 56:365–373, 2002.

E.L. Cussler. *Diffusion: Mass Transfer in Fluid Systems.* Cambridge University Press, Cambridge, 3rd edition, 2009.

Masahiko Daimon and Akira Masumura. Measurement of the refractive index of distilled water from the near-infrared region to the ultraviolet region. *Applied Optics*, 46(18):3811 – 3820, 2007.

Dantec Dynamics. *DynamicStudio User's Guide*, 2013.

R. Defay, I. Prigogine, A. Bellemans, and D.H. Everett. *Surface Tension and Adsorption*. Longmans, London, 1 edition, 1966.

Stanislaw S. Dukhin, Günter Kretzschmar, and Reinhard Miller. *Dynamics of Adsorption at Liquid Interfaces: Theory, Experiment, Application*. Studies in Interface Science. Elsevier, 1st edition, 1995.

J. Eastoe and J.S. Dalton. Dynamic surface tension and adsorption mechanisms of surfactants at the air-water interface. *Advances in Colloid and Interface Science*, 85:103 – 144, 2000.

Richard J. Farn. *Chemistry and technology of surfactants*. Blackwell Publishing, Oxford, 1st edition, 2006.

K.Y. Foo and B.H. Hameed. Insights into the modeling of adsorption isotherm systems. *Chemical Engineering Journal*, 156:2 – 10, 2010.

P.-O. Gendron, F. Avaltroni, and K.J. Wilkinson. Diffusion coefficients of several Rhodamine derivatives as determined by pulsed field gradient-nuclear magnetic resonance and fluorescence correlation spectroscopy. *Journal of Fluorescence*, 18: 1093–1101, 2008.

M. Gharib and D. Dabiri. Digital particle image velocimetry. In A.J. Smits and T.T. Lim, editors, *Flow Visualization: Techniques and Examples*, pages 143–166. Imperial College Press, London, 2nd edition, 2012.

William C. Griffin. Classification of surface-active agents by "HLB". *Journal of the Society of Cosmetic Chemists*, 1:311 – 326, 1949.

R.M. Griffith. The effect of surfactants on the terminal velocity of drops and bubbles. *Chemical Engineering Science*, 17:1057 – 1070, 1962.

S. Guido, F. Greco, and M. Villone. Experimental determination of drop shape in slow steady shear flow. *Journal of Colloid and Interface Science*, 219:298 – 309, 1999.

F. Hamdullahpur, M.J. Pegg, and G.D.M. MacKay. A laser-fluorescence technique for turbulent two-phase flow measurements. *International Journal of Multiphase Flow*, 13(3):379 – 385, 1987.

J.F. Harper. The motion of bubbles and drops through liquids. *Advances in Applied Mechanics*, 12:59 – 129, 1972.

J.F. Harper. On spherical bubbles rising steadily in dilute surfactant solutions. *The Quarterly Journal of Mechanics and Applied Mathematics*, 27(1):87 – 100, 1974.

J.F. Harper. Surface activity and bubble motion. *Applied Scientific Research*, 38: 343 – 352, 1982.

J.F. Harper, D.W. Moore, and J.R.A. Pearson. The effect of the variation of surface tension with temperature on the motion of bubbles and drops. *Journal of Fluid Mechanics*, 27(2):361 – 366, 1967.

G.F. Hewitt, G.L. Shires, and Y.V. Polezhaev, editors. *International Encyclopedia of Heat & Mass Transfer*. CRC Press, New York, 1st edition, 1997.

Krister Holmberg, Bo Jönsson, Bengt Kronberg, and Björn Lindman. *Surfactants and polymers in aqueous solution*. John Wily & Sons, Ltd, Chichester, 2nd edition, 2003.

T.J. Horton, T.R. Fritsch, and R.C. Kintner. Experimental determination of circulation velocities inside drops. *The Canadian Journal of Chemical Engineering*, 43 (3):143 – 146, June 1965.

L.F. Hoyt. New table of the refractive index of pure glycerol at $20°C$. *Industrial and Engineering Chemistry*, 26(3):329 – 332, 1934.

Shegen Hu and R.C. Kinter. The fall of single liquid drops through water. *AIChE Journal*, 1(1):42 – 48, 1955.

Richard W. Johnson, editor. *The Handbook of Fluid Dynamics*. CRC Press and Springer-Verlay, 1st edition, 1998.

Michael C. Jones, Ryan D. Nassimbene, Jonathan D. Wolfe, and Nolan V. Frederick. Mixing and dispersion measurements on packed bed flows using a fiberoptic probe array. *Chemical Engineering Science*, 51(7):1009–1021, 1996.

James L. Kinsey. Laser-induced fluorescence. *Annual Review of Physical Chemistry*, 28:349–372, 1977.

Simon Kuhn and Klavs F. Jensen. A pH-sensitive laser-induced fluorescence technique to monitor mass transfer in multiphase flows in microfluidic devices. *Industrial & Engineering Chemistry Research*, 51:8999 – 9006, 2012.

Horace Lamb. *Hydrodynamics*. Cambridge University Press, London, 6th edition, 1932.

Veniamin G. Levich. *Physiochemical Hydrodynamics*. Prentice-Hall, Englewood Cliffs, N.J., 1st edition, 1962.

David R. Lide and Henry V. Kehiaian. *CRC Handbook of Thermophysical and Thermochemical Data*. CRC Press, Boca Raton, 1st edition, 1994.

G. Limousin, J.-P. Gaudet, L. Charlet, S. Szenknect, V. Barthès, and M. Krimissa. Sorption isotherms: A review on physical bases, modeling and measurement. *Applied Geochemistry*, 22:249 – 275, 2007.

Peng Liu and Liuxue Zhang. Adsorption of dyes from aqueous solutions or suspensions with clay nano-adsorbents. *Separation and Purification Technology*, 58:32 – 39, 2007.

F. Lopez Arbeloa, M.J. Tapia Estevez, T. Lopez Arbeloa, and I. Lopez Arbeloa. Spectroscopic study of the adsorption of rhodamine 6G on clay minerals in aqueous suspensions.

M. Lotfi, D. Bastani, V. Ulaganathan, R. Miller, and A. Javadi. Bubble in flow field: A new experimental protocol for investigating dynamic adsorption layers by using capillary pressure tensiometry. *Colloids and Surfaces A: Physicochemical and Engineering Aspects*, 460:369 – 376, 2014.

Douglas Magde, Elliot L. Elson, and Watt W. Webb. Fluorescence correlation spectroscopy. II. an experimental realization. *Biopolymers*, 13:29–61, 1974.

V. Martínez Martínez, F. López Arbeloa, J. Bañuelos Prieto, T. Arbeloa López, and I. López Arbeloa. Characterization of supported solid thin films of Laponite clay. Intercalation of Rhodamine 6G laser dye. *Langmuir*, 20:5709 – 5717, 2004.

T. Maxworthy, C. Gnann, M. Kürten, and F. Durst. Experiments on the rise of air bubbles in clean viscous liquids. *Journal of Fluid Mechanics*, 321:421 – 441, 1996.

James E. McDonald. The shape and aerodynamics of large raindrops. *Journal of Meteorology*, 11:478 – 494, December 1954.

R.B. Miles. Planar imaging of gas phase flows. In A.J. Smits and T.T. Lim, editors, *Flow Visualization: Techniques and Examples*, pages 107–142. Imperial College Press, London, 2nd edition, 2012.

A.Ch. Mitropoulos. What is a surface excess? *Journal of Engineering Science and Technology Review*, 1:1 – 3, 2008.

Ian D. Morrison and Sydney Ross. *Colloidal Dispersions: Suspensions, Emulsions, and Foams*. Wiley-Interscience, New York, 1st edition, 2002.

Ervin Mubarekyan and Maria Santore. Characterization of polystyrene latex surfaces by the adsorption of Rhodamine 6G. *Langmuir*, 14:1597–1603, 1998.

C.B. Müller, A. Loman, V. Pacheco, F. Koberling, D. Willbold, W. Richtering, and J. Enderlein. Precise measurement of diffusion by multi-color dual-focus fluorescence correlation spectroscopy. *EPL*, 83:46001–p1–46001–p5, August 2008.

Drew Myers. *Surfactant science and technology*. VCH publishers, Inc., New York, 1st edition, 1988.

Ravichandra Palaparthi, Demetrios T. Papageorgiou, and Charles Maldarelli. Theory and experiments on the stagnant cap regime in the motion of spherical surfactant-laden bubbles. *Journal of Fluid Mechanics*, 559:1 – 44, 2006.

P.K. Paul, S.A. Hussain, D. Bhattacharjee, and M. Pal. Adsorption of cationic laser dye onto polymer/surfactant complex film. *Chinese Journal of Chemical Physics*, 24(3):348–352, 2011.

Zdeněk Petrášek and Petra Schwille. Precise measurement of diffusion coefficients using scanning fluorescence correlation spectroscopy. *Biophysical Journal*, 94: 1437–1448, February 2008.

Maurice R. Porter. *Handbook of Surfactants*. Blackie Academic & Professional, Glasgow, 1st edition, 1991.

M. Raffel, C. Willert, and J. Kompenhans. *Particle Image Velocimetry: A Practical Guide*. Springer, Berlin, 1st edition, 1998.

ReAgent.

Hui Ren, Dhaval D. Kulkarni, Rajesh Kodiyath, Weinan Xu, Ikjun Choi, and Vladimir V. Tsukruk. Competitive adsorption of Dopamine and Rhodamine 6G on the surface of graphene oxide. *ACS Applied Materials & Interfaces*, 6(4):2459 – 2470, 2014.

R. Rigler, P. Grasselli, and M. Ehrenberg. Fluorescence correlation spectroscopy and application to the study of Brownian motion of biopolymers. *Physica Scripta*, 19: 486–490, 1979.

R.W. Sabnis. *Handbook of biological dyes and stains: Synthesis and industrial applications*. Wiley, Hoboken, New Jersey, 1st edition, 2010.

J.B. Segur and Helen E. Oberstar. Viscosity of glycerol and its aqueous solutions. *Industrial & Engineering Chemistry*, 43(9):2117 – 2120, 1951.

Philip Sherman, editor. *Emulsion Science*. Academic Press, London, 1st edition, 1968.

M. Stöhr, K. Roth, and B. Jähne. Measurement of 3d pore-scale flow in index-matched porous media. *Experiments in Fluids*, 35:159–166, 2003.

Victor L. Streeter, editor. *Handbook of Fluid Dynamics*. McGraw-Hill Book Company, New York, 1st edition, 1961.

D.J. Tritton. *Physical fluid dynamics*. Oxford University Press, Oxford, 2nd edition, 1988.

A.F.H. Ward and L. Tordai. Time-dependence of boundary tensions of solutions I. The role of diffusion in time-effects. *The Journal of Chemical Physics*, 14(7):453 – 461, 1946.

M. Wegener and A.R. Paschedag. The effect of soluble anionic surfactants on rise velocity and mass transfer at single droplets in systems with Marangoni instabilities. *International Journal of Heat and Mass Transfer*, 55(5 – 6):1561 – 1573, 2012.

Bernhard Wieneke and Karsten Pfeiffer. Adaptive PIV with variable interrogation window size and shape. In *15th International Symposium on Applications of Laser Techniques to Fluid Mechanics*, Lisbon, Portugal, July 2010.

Thomas A. Witten and Philip A. Pincus. *Structured fluids: polymers, colloids, surfactants*. Oxford University Press, Oxford, 1st edition, 2010.

Lu Yang, Yanxiang Shu, Milad Abolhasani, and Klavs F. Jensen. Characterization and modeling of multiphase flow in structured microreactors: a post microreactor case study. *Lab on a Chip*, 15:3232 – 3241, 2015.

M.M. Zdravkovich. *Flow Around Circular Cylinders: A Comprehensive Guide Through Flow Phenomena, Experiments, Applications, Mathematical Models, and Computer Simulations. Volume 1: Fundamentals*. Oxford University Press, Oxford, 1st edition, 1997.

Appendix A

Preliminary LIF experiments

A preliminary series of LIF experiments was initially performed to test the validity of using LIF as a technique to visualise the droplet is it rises through a tank of aqueous solution. It also validated the use of Rhodamine-6G as a fluorescent surfactant as well as providing an initial exploration into a suitable range of surfactant concentrations.

This section will initially examine the experimental parameters that were changed between the preliminary and main experimental series along with why these changes occurred. From here the calibration curves specific to the preliminary experimental series are presented to allow the conversion from the light intensity per pixel to the number of Rhodamine-6G molecules held at each pixel.

The data was analysed with lessons on how to improve the experiments for the main experimental series extracted. Finally a comparison between a repeated concentration from the preliminary and main experimental series occurs that shows that the results from the preliminary experimental could not be used to supplement the data from the main experimental series.

A.1 Experimental parameters

The setup for the preliminary experimental series was examined in order to improve the accuracy and quality of the data captured for the main experimental series. This involved improving several aspects of the experimental setup including the number of heights the tank was split into, the number and range of concentrations tested, and the magnification of the droplets. The differences between the two experimental series and the reasons for the differences are discussed in this section.

A.1.1 Tank measurement heights

Initially, for the preliminary experimental series, the height of the tank was split into ten equally spaced positions. Spacers were placed at every 57mm to ensure high accuracy positioning of the tank between the measurement positions. The height from the base of the tank for each measurement position is shown in Table A.1, with the lowest position capturing the droplets release from the injection nozzle. However it was found that in the photographs captured at this first position the droplets had not settled into the spherical shape of the droplet. Therefore for the main experimental series this first position was offset by 10mm. The height between positions was also decreased with an extra height added to improve the spatial resolution over the same overall distance measured in the preliminary experimental series.

Table A.1: The heights at which measurements were taken for the preliminary experimental series. Height measured from the base of the tank to the lower edge of the image.

Position number	Height in tank (mm)
1	0
2	57
3	114
4	171
5	228
6	285
7	342
8	399
9	456
10	513

A.1.2 Surfactant solution

The concentrations used in the preliminary experimental series are given in Table A.2 along with the number of Rhodamine-6G molecules held within each mm^3 of the aqueous solution. Each concentration was halved to find the lowest concentration at which droplets could be identified from the surrounding fluorescence of the bulk solution in the image. With the lowest concentration determined the concentration range was split into even sized spacings to test an increased number of concentrations in the main experimental series.

Table A.2: Volume of Rhodamine-6G dilute solution combined with 1l of water-glycerol and conversion to concentration and number of molecules per mm^3 in preliminary experimental series.

Volume of Rhodamine-6G dilute solution at 1g/l (ml) = Concentration (mg/l)	Number of Rhodamine-6G molecules per mm^3
0.5	6.286×10^{11}
0.25	3.143×10^{11}
0.125	1.571×10^{11}
0.0625	7.857×10^{10}
0.03125	3.929×10^{10}
0.015625	1.964×10^{10}

A.1.3 Camera settings

In the preliminary experimental series an extension ring length of 65mm was used. This allowed more light to reach the camera sensor in comparison to the 70mm extension ring used in the main experimental series. However this led to a lower magnification of the droplet in the target area. Due to different range of concentrations used between the preliminary and main experiments, and as more light reaches the camera sensor in the preliminary experimental series due to the shorter length of extension ring the camera settings used to capture the droplets at each concentration were varied. The ISO speeds and exposure times used for the preliminary experimental series are given in Table A.3.

Table A.3: ISO speeds and exposure times used in preliminary LIF experimental series.

Rhodamine-6G concentration (mg/l)	ISO speed	Exposure time (1/E)
0.5	200	500
0.25	320	500
0.125	640	500
0.0625	1250	500
0.03125	2500	500
0.015625	3200	320

A.1.4 Averaging

Each height for each concentration had twenty droplets photographed in the preliminary experimental series with misaligned droplets and those not completely in the field of view discarded. For each position there were a minimum of ten remaining

droplets to average over to reduce the effects of any anomalous droplets. In the main experimental series to increase the accuracy further, this minimum number of usable droplets was increased to twenty.

A.2 Calibration

Calibration had to be performed on the preliminary experimental series in the same way as the main experimental series in order to relate the values measured by the camera to quantitative results. Due to the different length of the extension ring used, leading to a lower magnification, it was found that one millimetre of the camera field of view consisted of 290 pixels.

A.2.1 Concentration strengths

A range of concentrations used in the experiments along with concentrations both above and below this range were used to compile a calibration library to allow the conversion of intensity to the volume of Rhodamine-6G molecules at each pixel for each camera setting used. The concentrations used for calibration along with the number of Rhodamine-6G molecules per pixel are shown in Table A.4.

Table A.4: Number of Rhodamine-6G molecules per pixel for calibration concentrations in preliminary experimental series.

Rhodamine-6G concentration (mg/l)	Number of Rhodamine-6G molecules per pixel
0	0
0.0078125	1.1678×10^5
0.015625	2.3357×10^5
0.03125	4.6713×10^5
0.0625	9.3427×10^5
0.125	1.8685×10^6
0.25	3.7371×10^6
0.50	7.4741×10^6
1.00	1.4948×10^7
2.00	2.9897×10^7

A.2.2 Calibration curves

Calibration curves were generated for the camera settings shown in Table A.3 for the relevant concentration of Rhodamine-6G. These raw calibration curves are given in Figure A.1.

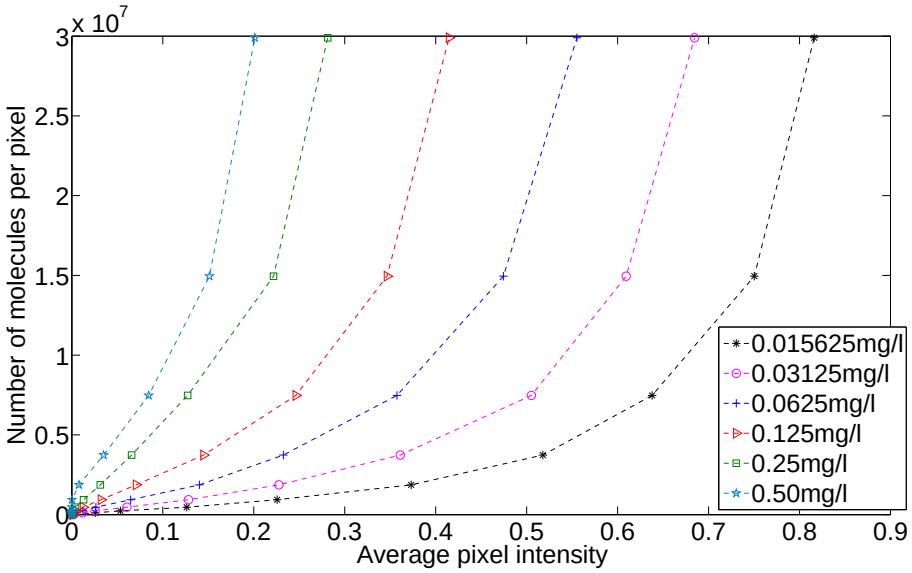

Figure A.1: Raw calibration curves for the preliminary experimental series.

All of these curves were monotonically increasing except for the curve for the camera settings selected for a bulk concentration of 0.50mg/l of Rhodamine-6G. This curve had a small negative fluctuation at a concentration relating to 0.015625mg/l of Rhodamine-6G. As this was such a small concentration in relation to the bulk concentration for this curve, the first data points for this curve were smoothed using a linear fit. The final stage to achieve the calibration curves was to normalise these raw calibration curves against the bulk solution concentration relating to each curve. This equated the bulk solution to a value of one and interpolation allowed the calculation of the number of molecules for intensities falling between the measured points. These final calibration curves for the preliminary experiments are shown in Figure A.2.

A.3 Raw data

The results for the preliminary experimental series were analysed separately from the main experimental series as they were performed at a different temperature. This section presents the results from the preliminary experimental series performed at an ambient temperature of 22.5°C. Initially the results for each individual concentration used in the experiments are displayed. This allowed an exploration of the analysis of individual droplets to investigate how the droplet radius affected the results as well as showing any anomalous results. These anomalous results were removed from

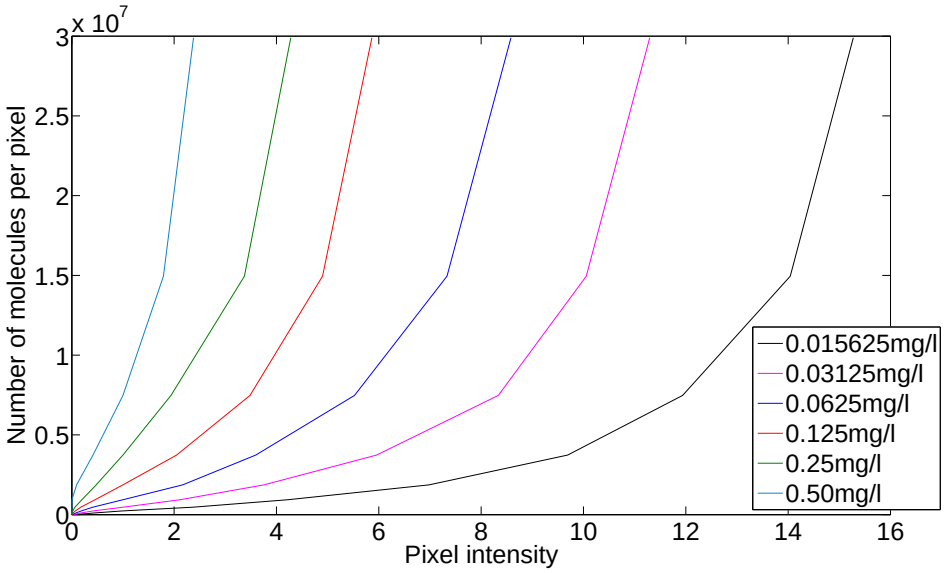

Figure A.2: Normalised calibration curves for each concentration in the preliminary experimental series.

the data set to produce more reliable results when the remaining data points were averaged. This averaging was done to produce averaged surfactant distribution profiles around the droplet different concentrations allowing a comparison with the tangential velocity profiles generated by PIV for the internal circulation within the droplet.

The preliminary experimental series consisted of photographing at least ten droplets for each experiment iteration. This data set consisted of six different concentrations over ten heights, producing a total of 1,105 data points. The calibration library relating to these experiments consisted of 5,291 data points.

Figure A.3 shows the development of a droplet as it rises. This example was for the maximum concentration of Rhodamine-6G tested in the preliminary experimental series at 0.50mg/l of Rhodamine-6G. Figure A.3(a) shows the droplet at the release from the injection nozzle, with a noticeable difference between the darkness of the oil droplet and the fluorescence of the bulk solution. As the droplet begins to rise, in Figure A.3(b), a bright surfactant cap is visible at the base of the droplet with a dark wake trailing behind the droplet. As the droplet rises further, through Figure A.3(c) and Figure A.3(d), the surfactant cap grows and a bright tail begins to develop within the centre of the dark wake. Figure A.3(e) through to Figure A.3(j) shows the growth and stabilisation of this bright tail as the droplet rises through the upper part of the tank.

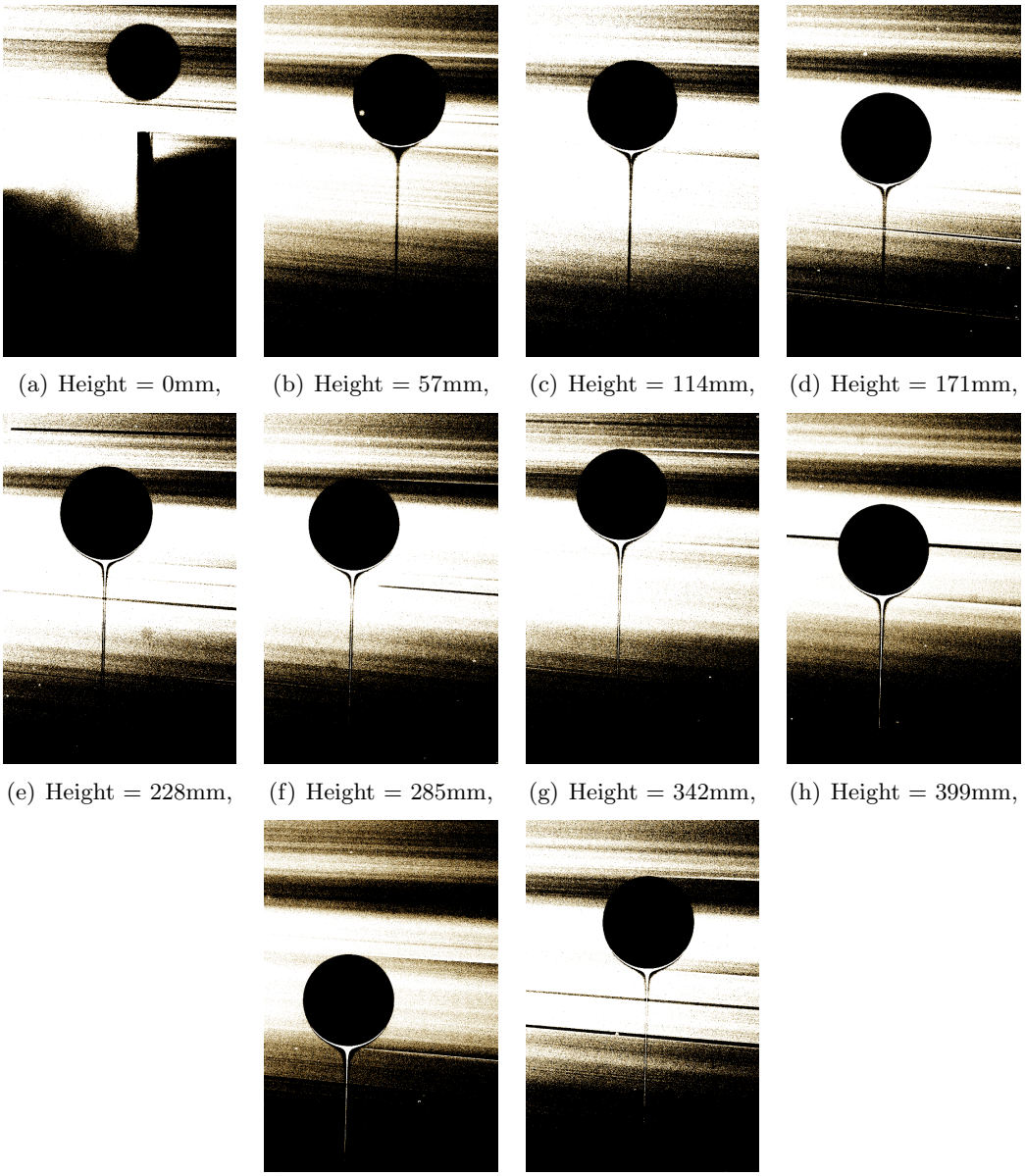

(a) Height = 0mm, (b) Height = 57mm, (c) Height = 114mm, (d) Height = 171mm,

(e) Height = 228mm, (f) Height = 285mm, (g) Height = 342mm, (h) Height = 399mm,

(i) Height = 456mm, (j) Height = 513mm.

Figure A.3: Examples of droplets at different heights from the base of the tank in the preliminary experimental series. Rhodamine-6G concentration of 0.50mg/l. Photographs edited for clarity.

A.4 Results

The data obtained from the preliminary experimental series was processed almost identically to the main experimental series. The only difference was the number of segments that each droplet was split in to. Due to a lower level of magnification, the circumference of each droplet detected in the photographs was smaller and so less segments were required to achieve a resolution of approximately the width of one pixel around the interface. The droplets from the preliminary experimental series were divided into 5,000 segments with an angle between segments of 0.072°.

The processing produced values for each droplet for the volume and angle of the surfactant cap. Each concentration is presented individually for both of these parameters to allow an exploration into how the range of droplet sizes affected the results over the height of the tank along with a validation of the individual results. Anomalous results were identified and removed using the same processes used in the main experimental series. The surfactant distribution profiles for the remaining droplets were averaged before a comparison between concentrations of how the averaged surfactant cap volume and angle developed over the height of the tank.

A.4.1 Surfactant cap volume

The first relationship that was explored was how the volume of Rhodamine-6G molecules held in the surfactant cap behind the droplet developed over the height of the tank for each concentration. Figure A.4 shows how the volume held within the surfactant cap grows over the height of the tank for the lowest preliminary concentration of 0.0156mg/l of Rhodamine-6G. The volume for each droplet at each height was plotted based upon the droplet radius. The range of droplet sizes was split into 0.25mm bands. At the lower heights the volumes are in good agreement. From a height of 342mm the data points begin to become more spread out with overlap between the different bands of radii. At 456mm from the base of the tank there is a single data point, marked by a red circle, far above the others indicating an anomalous result. This had the potential to affect the results in the averaging process and so the droplet linked to this data point was excluded from the averaged results.

Figures A.5-A.9 show the results for the remaining surfactant concentrations. They show that, for all concentrations, as the droplet rises through the tank it accumulates a greater volume of Rhodamine-6G. In general the agreement between data points is high at the base of the tank, although the data points become more

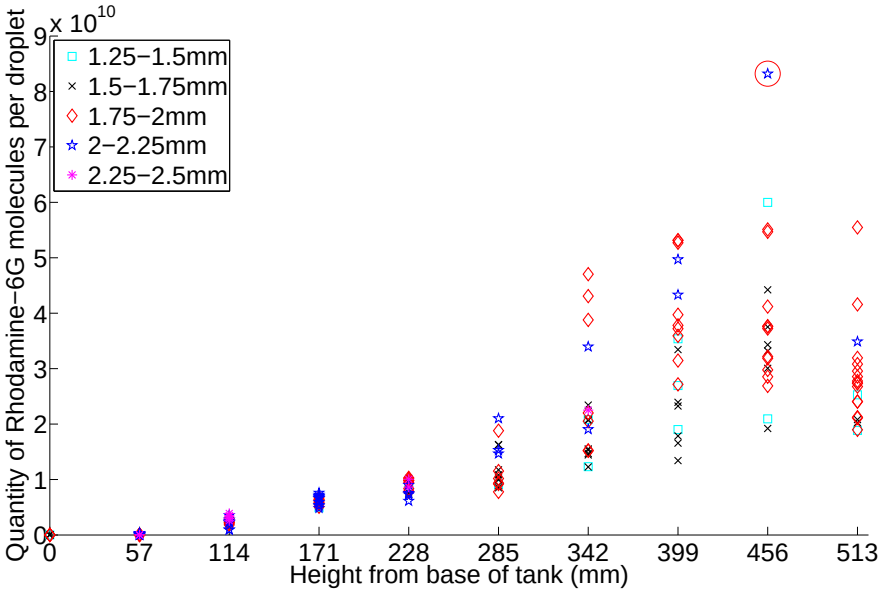

Figure A.4: Development of the Rhodamine-6G volume stored within the surfactant cap as it rises through the tank for different droplet radii in the preliminary experimental series. Rhodamine-6G concentration of 0.0156mg/l. Outliers circled.

spread over the height of the tank. The obvious anomalous data points for each concentration were identified and marked by a red circle. The large spread of data over the larger heights made identifying anomalous results difficult so improving the repeatability of the results was an aim for the main experiments. These fluctuations could be due to imperfections in the experimental setup with the alignment of the laser with the centre line imperfect and so not consistently capturing the volume around the widest part of the droplet and wake.

From Figures A.4-A.9 it was observed that although the data from droplets within different size bands overlapped, in general droplets with a smaller radius contained a lower volume of Rhodamine-6G. This was to be expected as smaller droplets have a lower surface area for the surfactant to accumulate behind.

The range of the data at each height revealed the need for improvements in the experimental setup for the main experimental series in order to produce results with better agreement. The main area identified to be improved was the precision of the alignment of the laser sheet with the centre line of the droplet as, without a high degree of accuracy a large volume of detail within the wake is lost leading to the wide scatter of data points observed here.

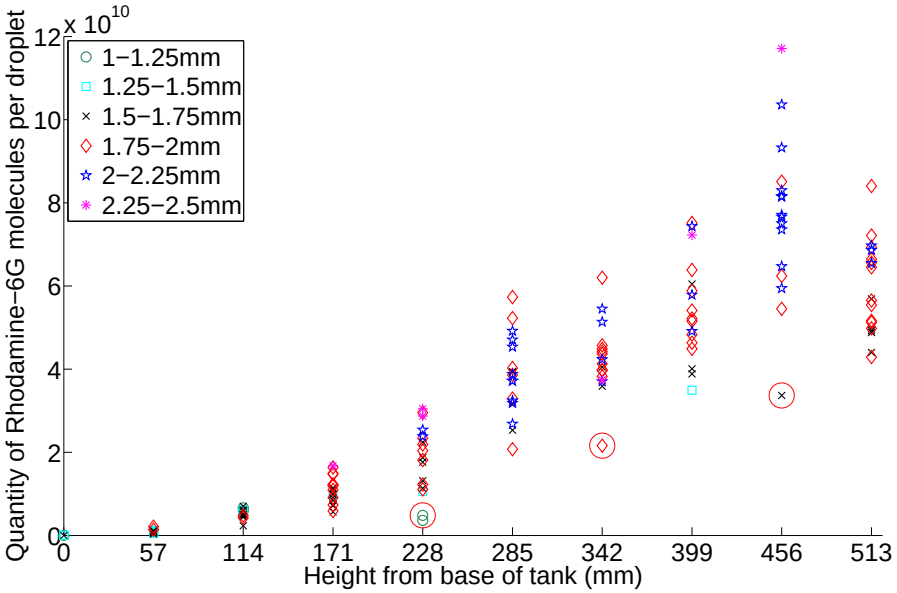

Figure A.5: Development of the Rhodamine-6G volume stored within the surfactant cap as it rises through the tank for different droplet radii in the preliminary experimental series. Rhodamine-6G concentration of 0.0313mg/l. Outliers circled.

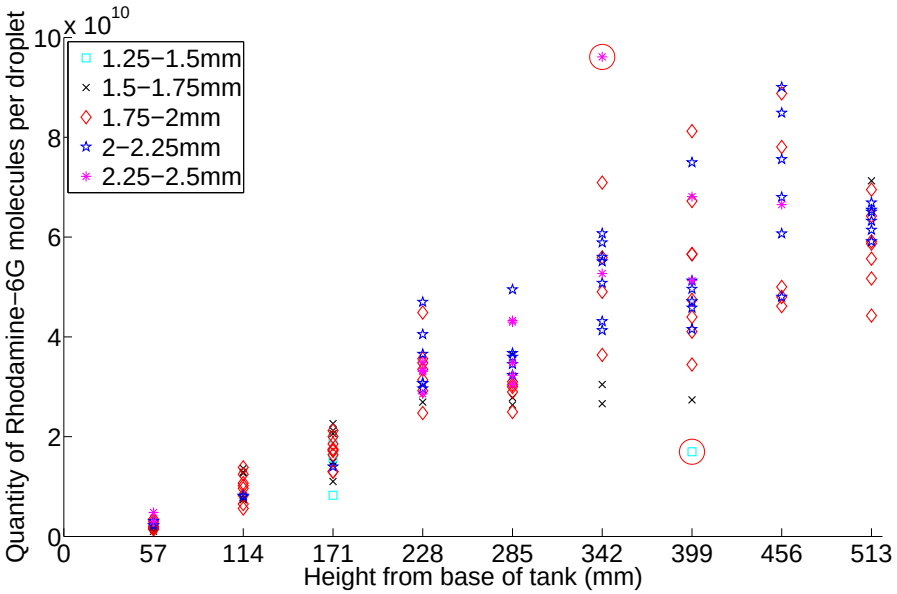

Figure A.6: Development of the Rhodamine-6G volume stored within the surfactant cap as it rises through the tank for different droplet radii in the preliminary experimental series. Rhodamine-6G concentration of 0.0625mg/l. Outliers circled.

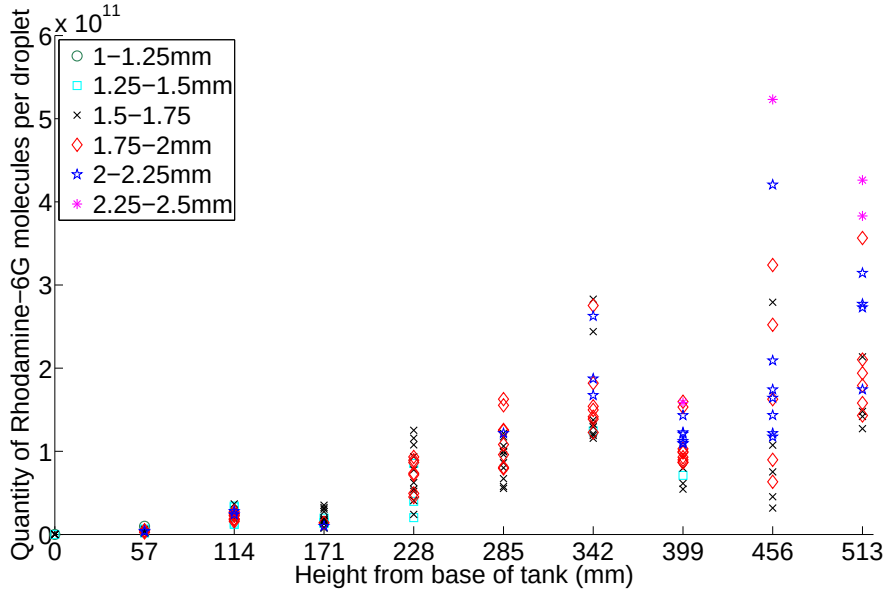

Figure A.7: Development of the Rhodamine-6G volume stored within the surfactant cap as it rises through the tank for different droplet radii in the preliminary experimental series. Rhodamine-6G concentration of 0.125mg/l. No outliers detected.

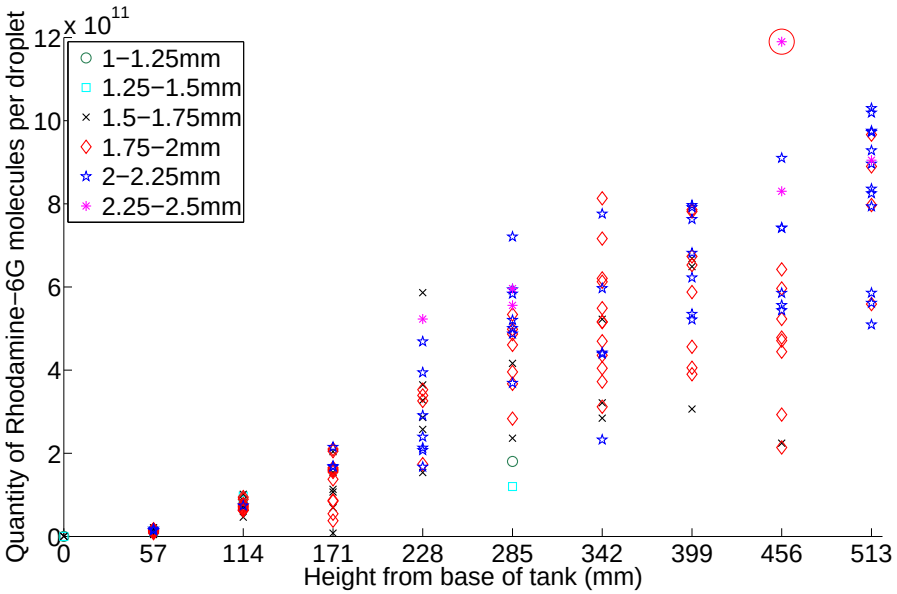

Figure A.8: Development of the Rhodamine-6G volume stored within the surfactant cap as it rises through the tank for different droplet radii in the preliminary experimental series. Rhodamine-6G concentration of 0.25mg/l. Outliers circled.

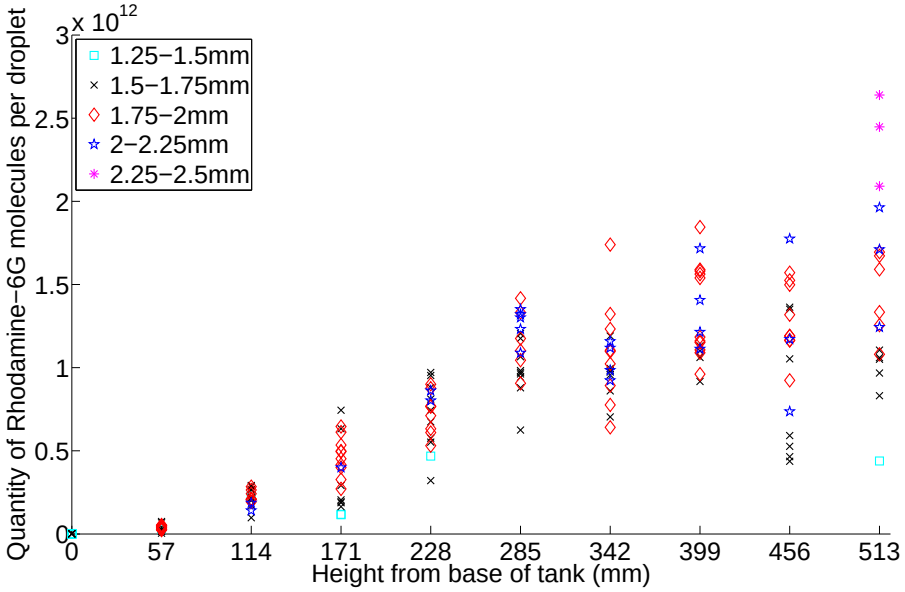

Figure A.9: Development of the Rhodamine-6G volume stored within the surfactant cap as it rises through the tank for different droplet radii in the preliminary experimental series. Rhodamine-6G concentration of 0.50mg/l. No outliers detected.

A.4.2 Surfactant cap angle

The second relationship to be explored was how the angle of the surfactant cap changed over the height of the tank for each concentration. The angle was measured between the two points as specified in Section 5.2.5. This is measured from the surfactant distribution profiles that produced the results for Section A.4.1. Individual concentrations are presented with the droplets divided into size bands covering every 0.25mm radius for a range of radii from 1mm to 3mm.

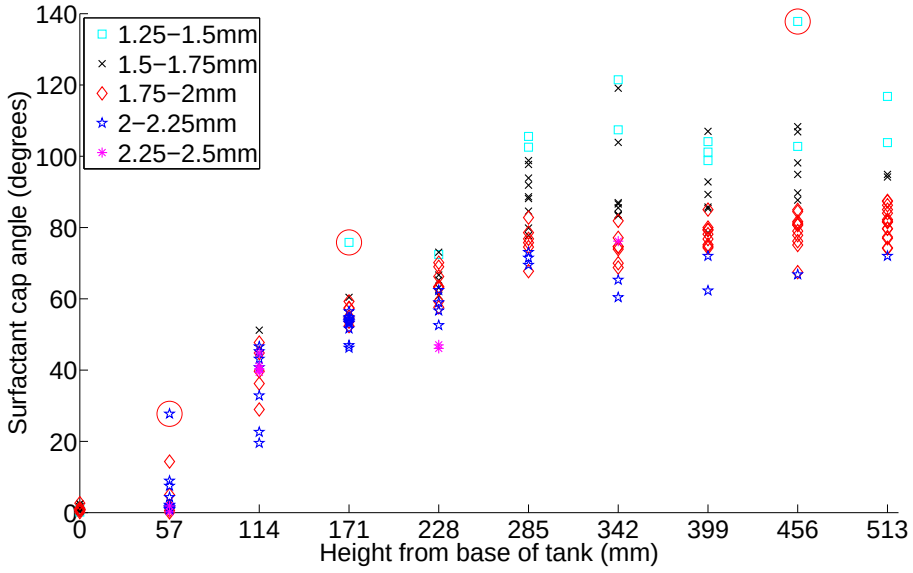

Figure A.10: Development of the surfactant cap angle over the height of the tank for different droplet radii in the preliminary experimental series. Rhodamine-6G concentration of 0.0156mg/l. Outliers circled.

Figure A.10 shows how the surfactant cap angle develops over the height of the tank for a surfactant concentration of 0.0156mg/l of Rhodamine-6G. At the base of the tank there is a good agreement of a very small cap angle. This is to be expected as this data point was obtained immediately after the droplets formation, before the droplet had risen very far and so before enough Rhodamine-6G had adsorbed to the interface to form a stagnant cap. As the droplet rises through the tank there is a fairly even spread of the cap angle over the range of the data points for each height. As with the results for the volume of Rhodamine-6G stored in the surfactant cap, there is an overlap between droplets falling within different radii bands however, in general, the droplets with the smaller sizes have a larger measured surfactant cap angle. These results were consistent over the other concentrations. At a height of

57mm from the base of the tank is a droplet with a radius between 2mm and 2.25mm with a surfactant cap angle far larger than comparable droplets. Also at the height of 456mm there is a single data point falling within the radii band of 1.25mm to 1.5mm that appears to be significantly larger than the other results, indicating two anomalous results.

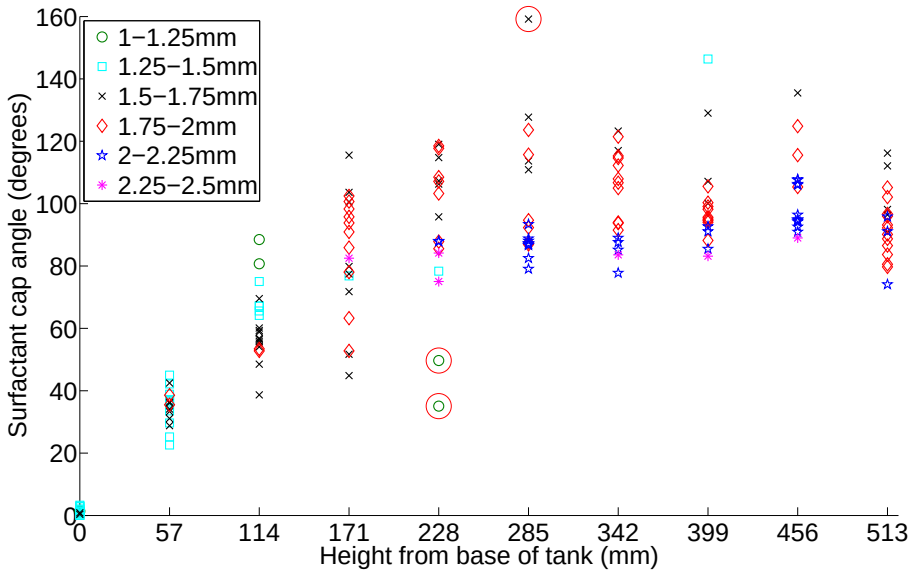

Figure A.11: Development of the surfactant cap angle over the height of the tank for different droplet radii in the preliminary experimental series. Rhodamine-6G concentration of 0.0313mg/l. Outliers circled.

Figures A.11-A.15 show how the surfactant cap angle develops over the height of the tank for the other surfactant concentrations measured in the preliminary experimental series. For all of the concentrations the initial growth of the surfactant cap angle is large before levelling off at the top of the tank. Obvious anomalous results were marked with a red circle on each figure.

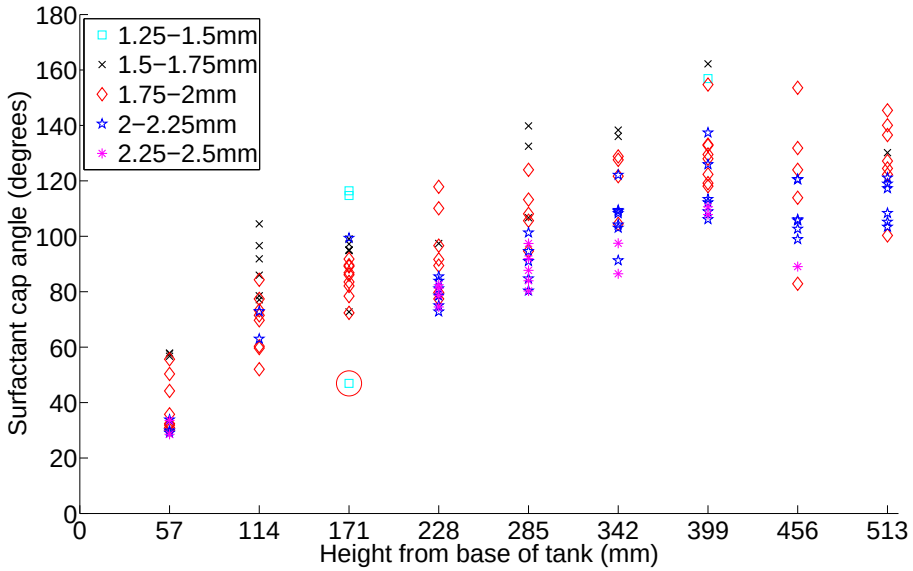

Figure A.12: Development of the surfactant cap angle over the height of the tank for different droplet radii in the preliminary experimental series. Rhodamine-6G concentration of 0.0625mg/l. Outliers circled.

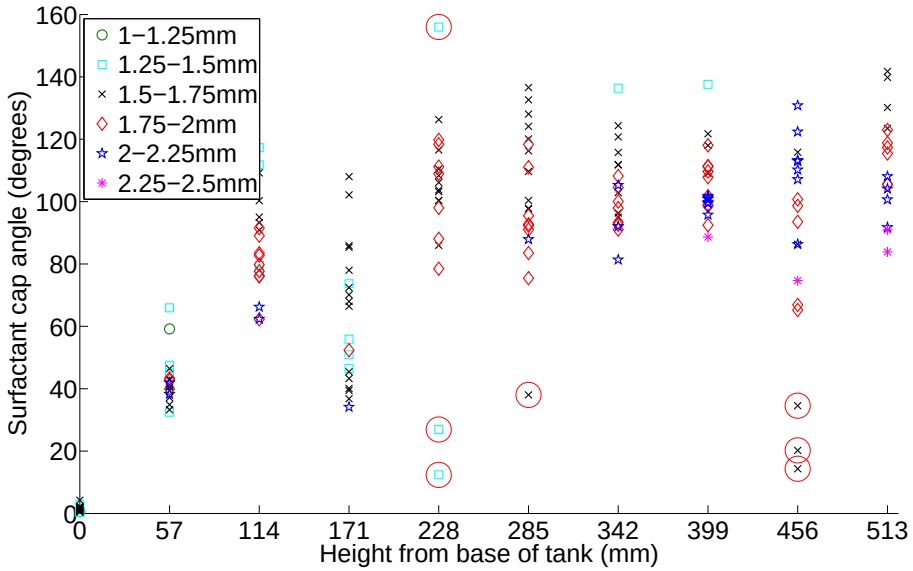

Figure A.13: Development of the surfactant cap angle over the height of the tank for different droplet radii in the preliminary experimental series. Rhodamine-6G concentration of 0.125mg/l. Outliers circled.

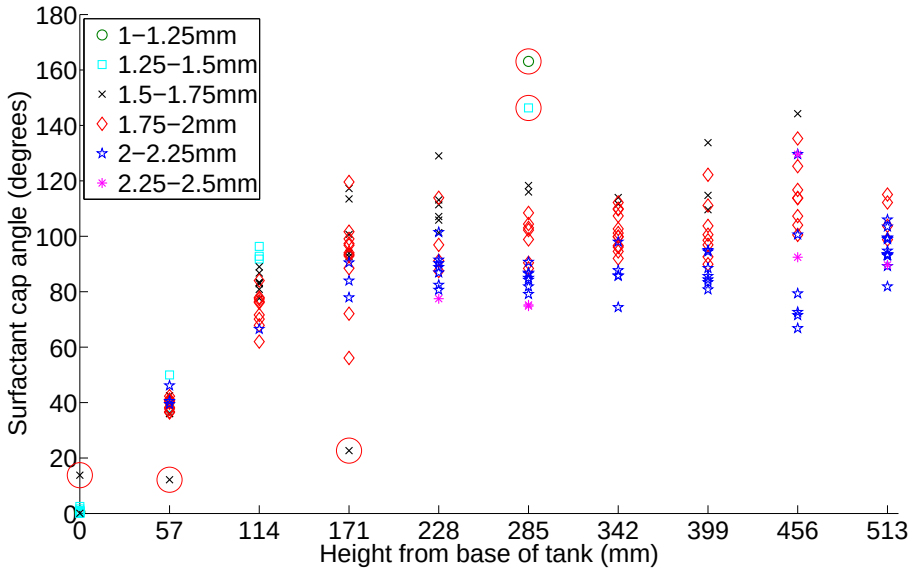

Figure A.14: Development of the surfactant cap angle over the height of the tank for different droplet radii in the preliminary experimental series. Rhodamine-6G concentration of 0.25mg/l. Outliers circled.

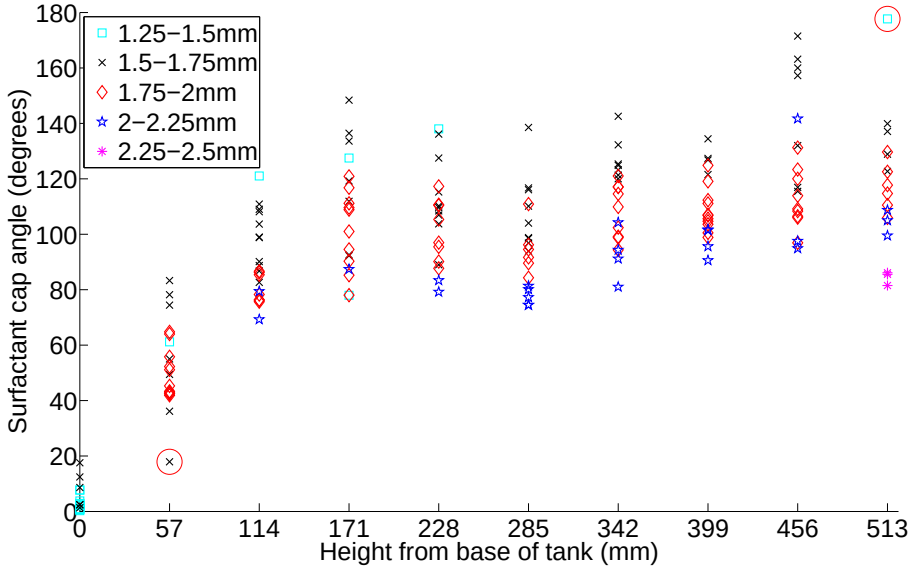

Figure A.15: Development of the surfactant cap angle over the height of the tank for different droplet radii in the preliminary experimental series. Rhodamine-6G concentration of 0.50mg/l. Outliers circled.

A.4.3 Averaged surfactant distribution profiles

Without the anomalous results detected from the surfactant cap volume and surfactant cap angle data in Sections A.4.1 and A.4.2, the remaining surfactant distribution profiles were averaged for each height of each concentration and are shown in Figures A.16-A.21. This allows a visualisation of how the Rhodamine-6G stored in the surfactant cap grows over the height of the tank. The profiles could also be measured and integrated around the visible cap to calculate the averaged surfactant cap angle and volume of Rhodamine-6G stored in the cap.

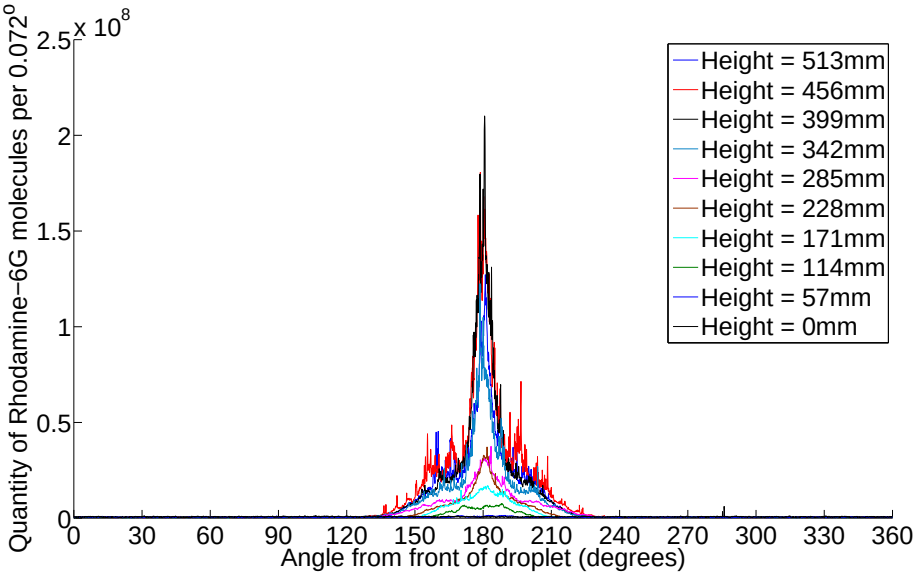

Figure A.16: Averaged surfactant distribution profiles for a Rhodamine-6G concentration of 0.0156mg/l at different heights from the base of the tank.

Figures A.16-A.21 show that smooth growth of the surfactant cap initially exists before a peak at the very rear of the droplet, corresponding to the existence of the surfactant-rich wake. Figure A.16 shows the existence of a significant amount of noise in the profiles from the upper end of the tank for the weakest concentration. For the other concentrations shown in Figures A.17-A.21 this noise is heavily reduced demonstrating the success of the averaging process.

It was observed that initially as the droplet rises through the tank the angle of the surfactant cap increases for each profile. However at the upper end of the tank the profiles are overlapped showing that they all have the same approximate surfactant cap angle.

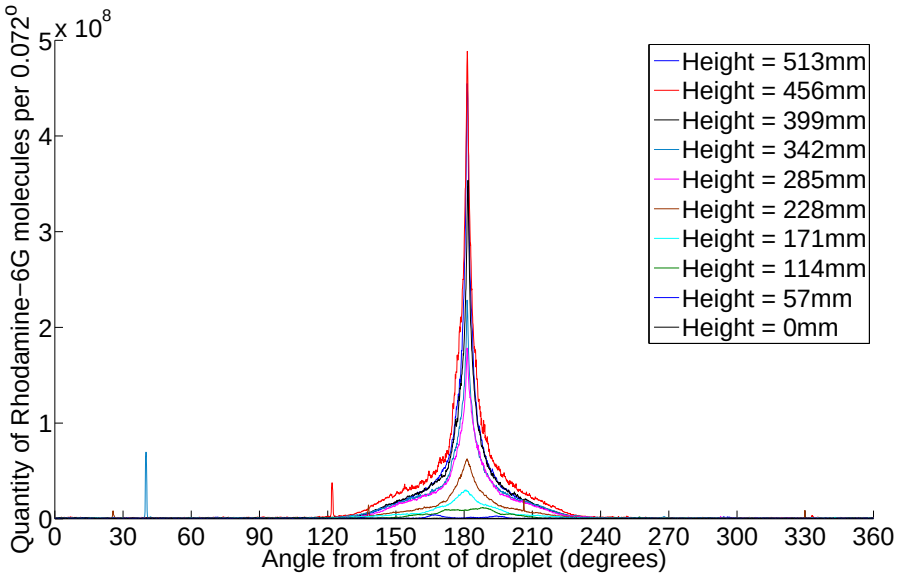

Figure A.17: Averaged surfactant distribution profiles for a Rhodamine-6G concentration of 0.0313mg/l at different heights from the base of the tank.

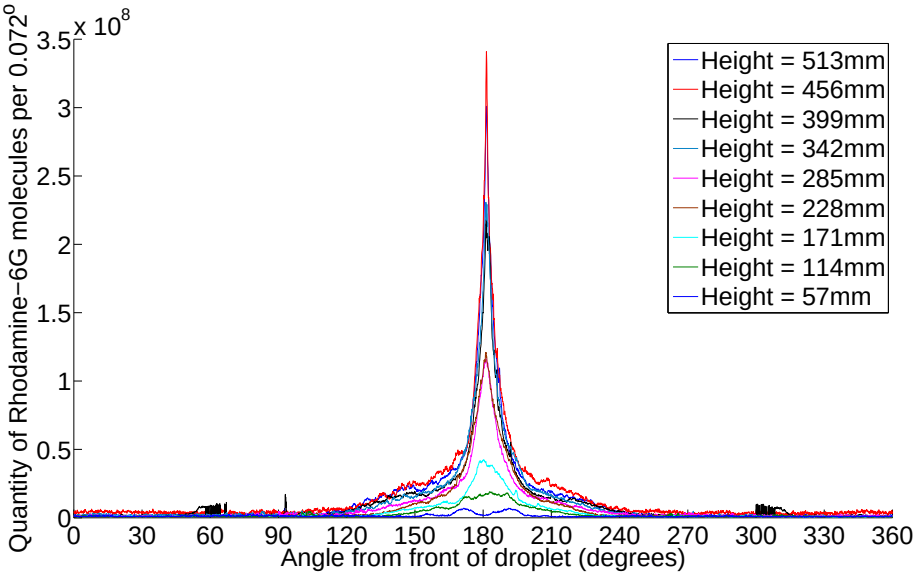

Figure A.18: Averaged surfactant distribution profiles for a Rhodamine-6G concentration of 0.0625mg/l at different heights from the base of the tank.

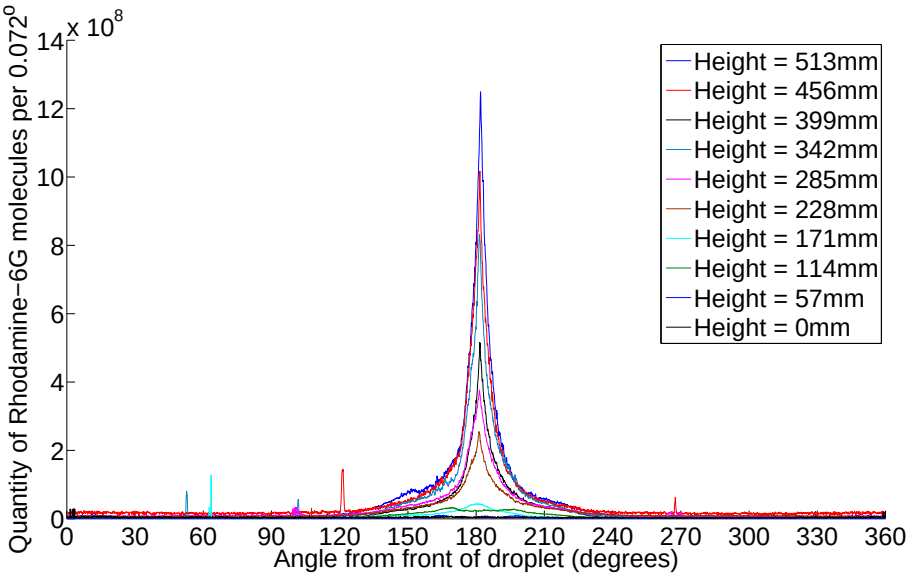

Figure A.19: Averaged surfactant distribution profiles for a Rhodamine-6G concentration of 0.125mg/l at different heights from the base of the tank.

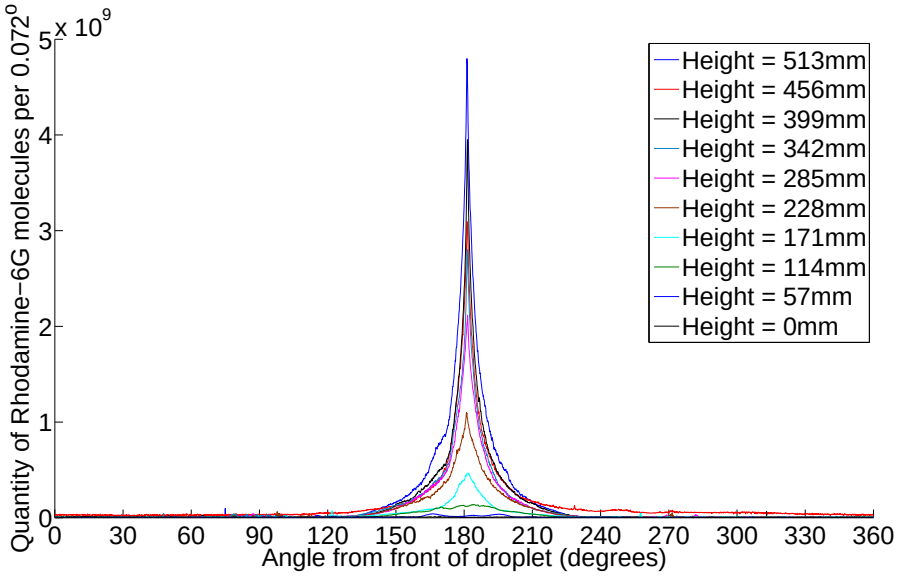

Figure A.20: Averaged surfactant distribution profiles for a Rhodamine-6G concentration of 0.25mg/l at different heights from the base of the tank.

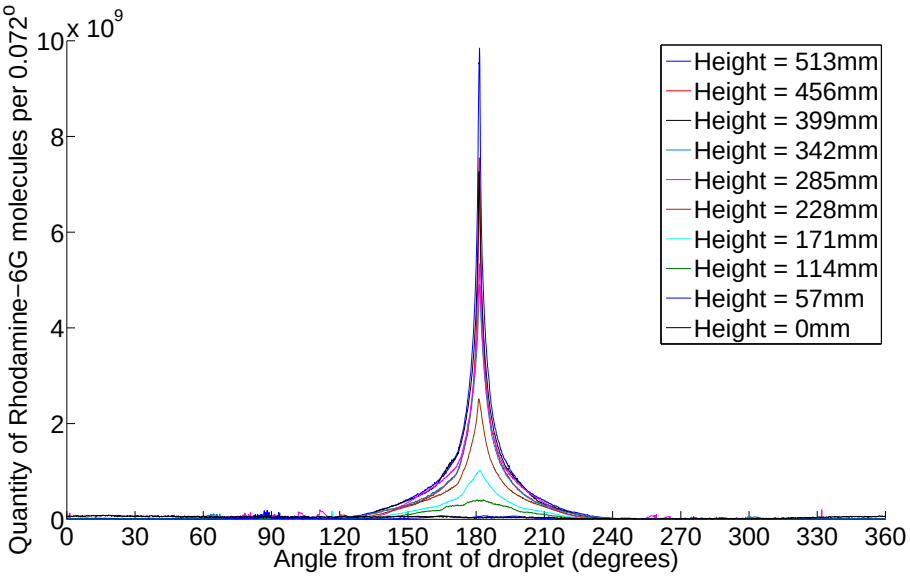

Figure A.21: Averaged surfactant distribution profiles for a Rhodamine-6G concentration of 0.50mg/l at different heights from the base of the tank.

A.4.4 Concentration comparison

The averaged surfactant cap volume for each height of each concentration was plotted to give a comparison of all of the concentrations measured in the preliminary experimental series. This comparison is presented in Figure A.22.

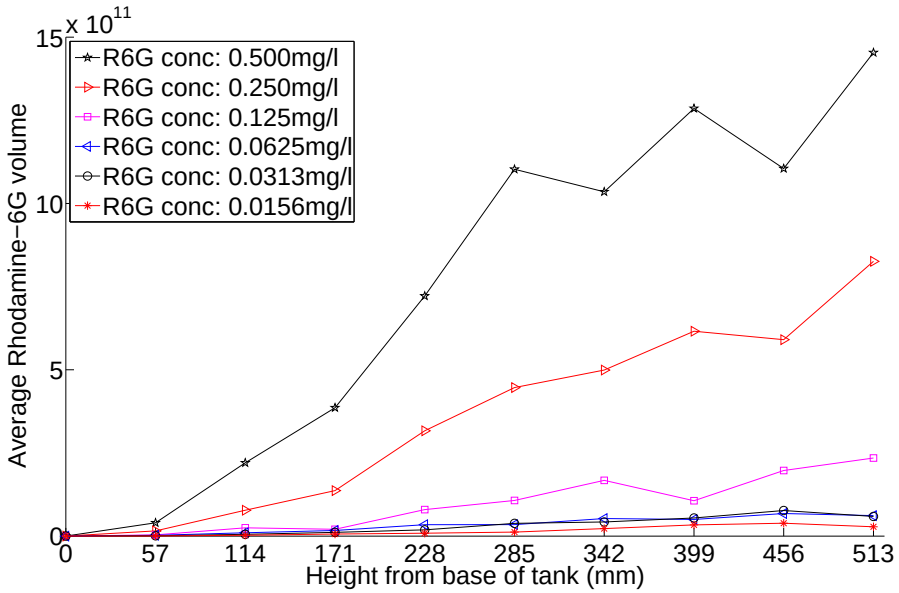

Figure A.22: Comparison of the development of the volume of the surfactant cap over the height of the tank for all concentrations in the preliminary experimental series.

This shows that at a zero height the droplet always posses a negligible volume of Rhodamine-6G. The line from the weakest concentration of Rhodamine-6G has the smallest overall amount of surfactant held behind the droplet as it rises through the tank, with the curve relating to the strongest Rhodamine-6G having the largest volume gain. The curves relating to surfactant concentrations of 0.0625mg/l and 0.0313mg/l of Rhodamine-6G are overlapping. There are also fluctuations in each of the curves. These errors could be due to the surfactant volume values being averaged over different numbers of droplets with differing radii.

The average surfactant cap angle for each height of each concentration was calculated and displayed Figure A.23 to show the effects of different surfactant concentrations on the development of the stagnant cap angle.

This shows that at the base of the tank the surfactant cap angle is zero as was expected. Each of the concentrations has an initial drastic increase in the size of the stagnant cap before levelling off towards the top of the tank. Although the

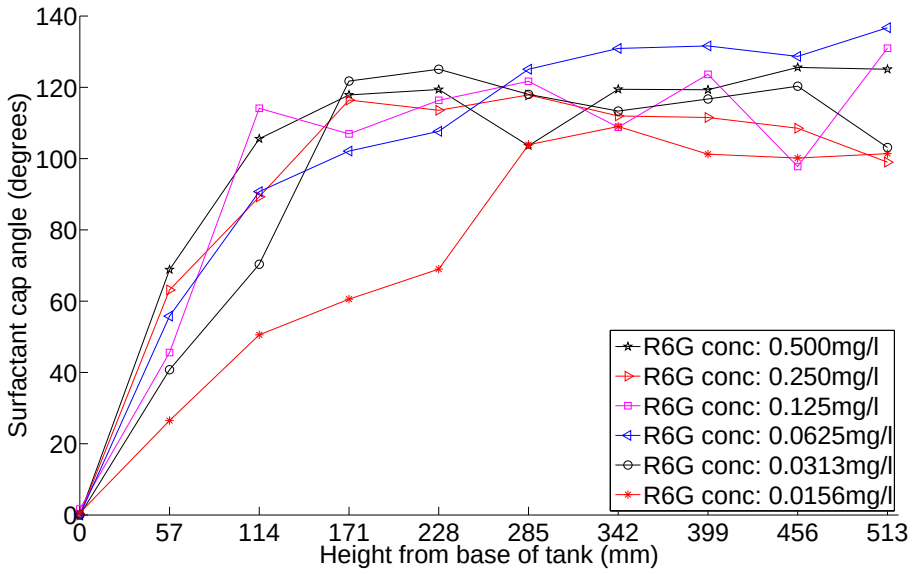

Figure A.23: Comparison of the development of the angle of the surfactant cap over the height of the tank for all concentrations in the preliminary experimental series.

strongest concentration initially has a larger cap angle growth, the droplet with a Rhodamine-6G concentration of 0.0625mg/l possesses the largest surfactant cap angle by the top of the tank.

The weakest concentration has a far slower growth over the first 228mm of the tank but has a surfactant cap of similar size to all other concentrations by the top of the tank. Each of the concentration curves exhibits fluctuations. These fluctuations could be due to the results being averaged over droplets of different sizes, as it was observed that smaller droplets tended to have a larger cap angle size.

A.5 Preliminary and main experiments comparison

This section compares the preliminary experimental series to the main experimental series to observe how changes in the experimental procedure affected the results. This validates whether or not the results from the preliminary experimental series could be used to supplement the main LIF experimental series results for comparison with the PIV data.

Figure A.24 shows a comparison of the averaged profiles for the development of the volume of Rhodamine-6G held behind the droplet as it rises through the tank for a surfactant concentration of 0.50mg/l of Rhodamine-6G. This was the only repeated concentration between the two sets of experiments. The data from the

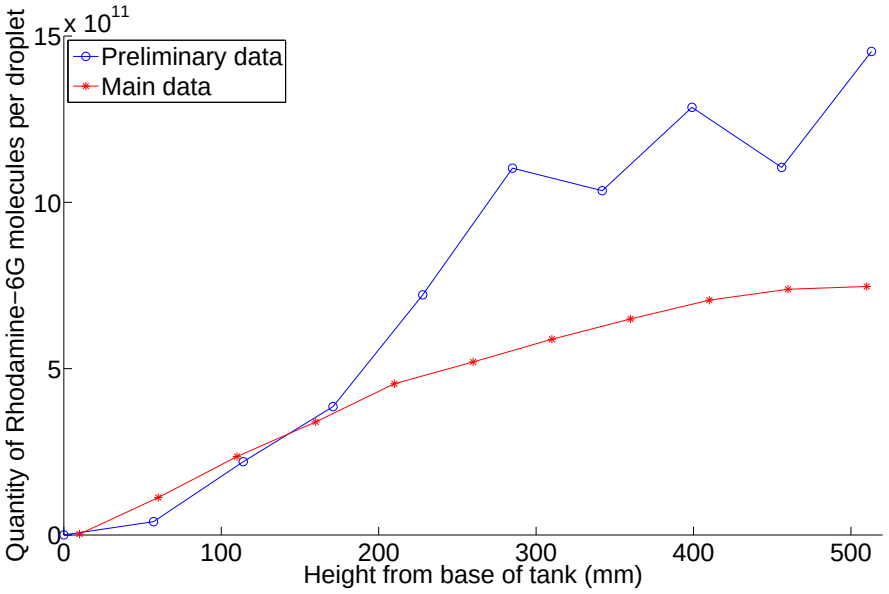

Figure A.24: Comparison of the development of the volume of Rhodamine-6G held in the surfactant cap between preliminary and main experimental series with a Rhodamine-6G concentration of 0.50mg/l.

preliminary experimental series shows an initial exponential increase in the volume of surfactant. The data for the main experimental series shows an initially linear increase before flattening off. This indicates that it is reaching a point where the rate of adsorption of Rhodamine-6G to the interface is similar to the desorption of Rhodamine-6G back into the bulk solution.

The main observation of the comparison between the two data sets is that the maximum volume reached for the preliminary experimental series is almost double that of the main experiments. The main difference between the two experiments was the temperature at which they were performed. The preliminary experimental series was performed at a higher temperature, indicating that a warmer temperature leads to a greater level of adsorption and more Rhodamine-6G being held in the surfactant cap.

Figure A.25 compares the surfactant cap angle between the preliminary and main experimental series. It would be expected that the droplets from the preliminary experiment have a larger cap angle to accommodate the extra Rhodamine-6G levels shown in Figure A.24. This is confirmed by Figure A.25 which shows that in the preliminary experimental series there is a maximum surfactant cap angle double that of the angle reached in the main experiments.

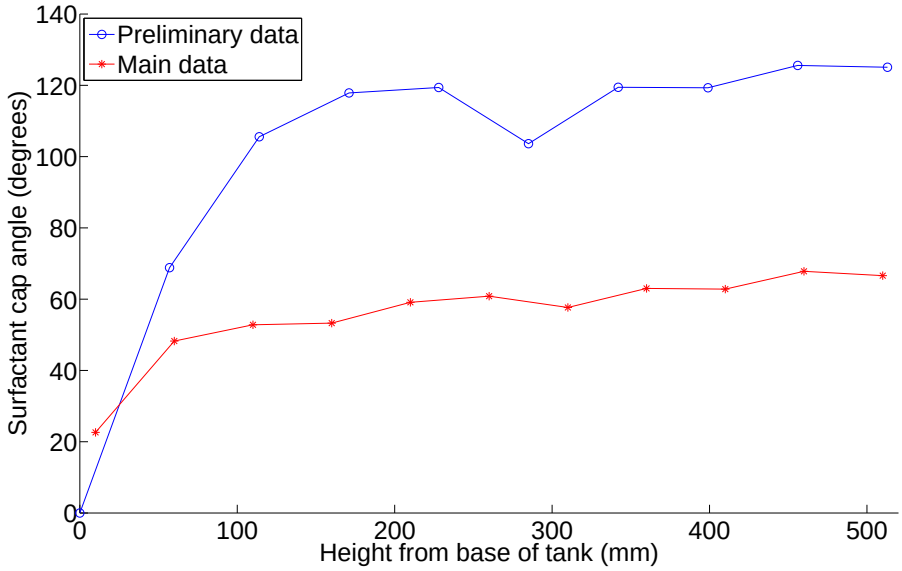

Figure A.25: Comparison of the development of the surfactant cap angle between preliminary and main experimental series with a Rhodamine-6G concentration of 0.50mg/l.

Appendix B

LIF surfactant cap volumes

The effects of the droplet radius and the height in the tank on the volume of Rhodamine-6G held behind the droplet for the concentrations of 0.02mg/l to 1.00mg/l are presented here. The volume for each individual droplet tested is presented with the volume of Rhodamine-6G normalised against the volume of the droplet. Curves are fitted through the data points at each height that show a linear relationship, demonstrating that the quantity of surfactant held behind the droplet is a function of the droplets volume.

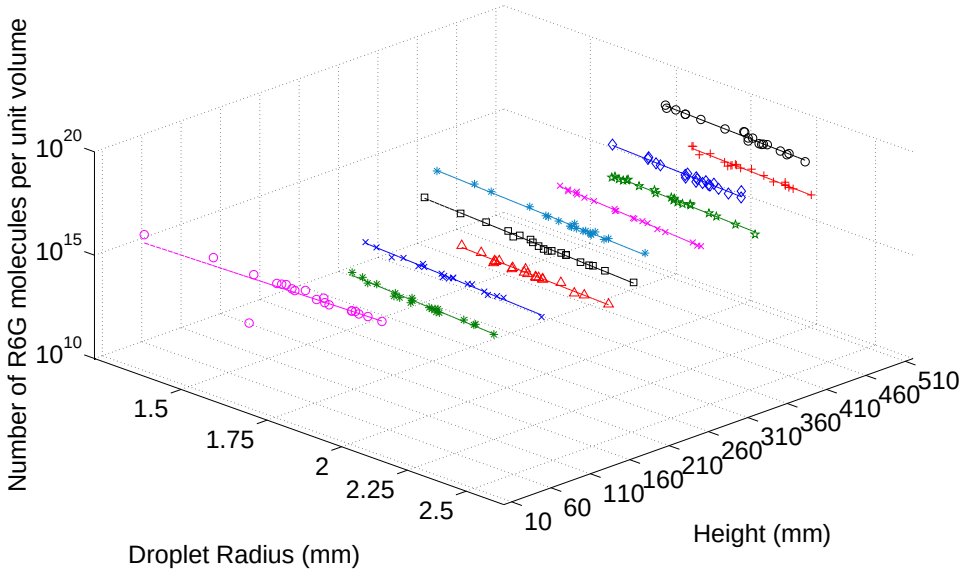

(a) 3-dimensional visualisation,

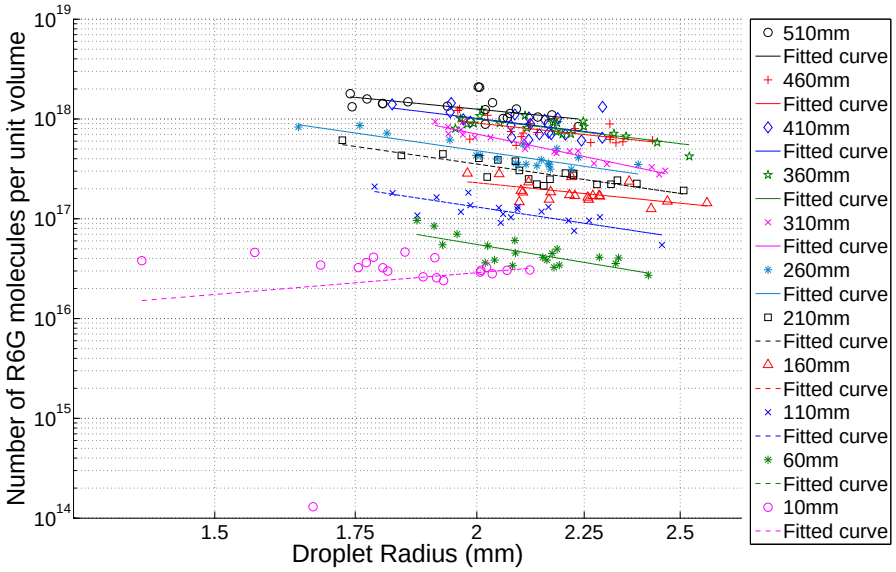

(b) Volume of Rhodamine-6G against droplet radius for different heights in tank.

Figure B.1: Development of the Rhodamine-6G volume stored within the surfactant cap as it rises through the tank for different droplet radii in the main experimental series. Rhodamine-6G concentration of 0.02mg/l.

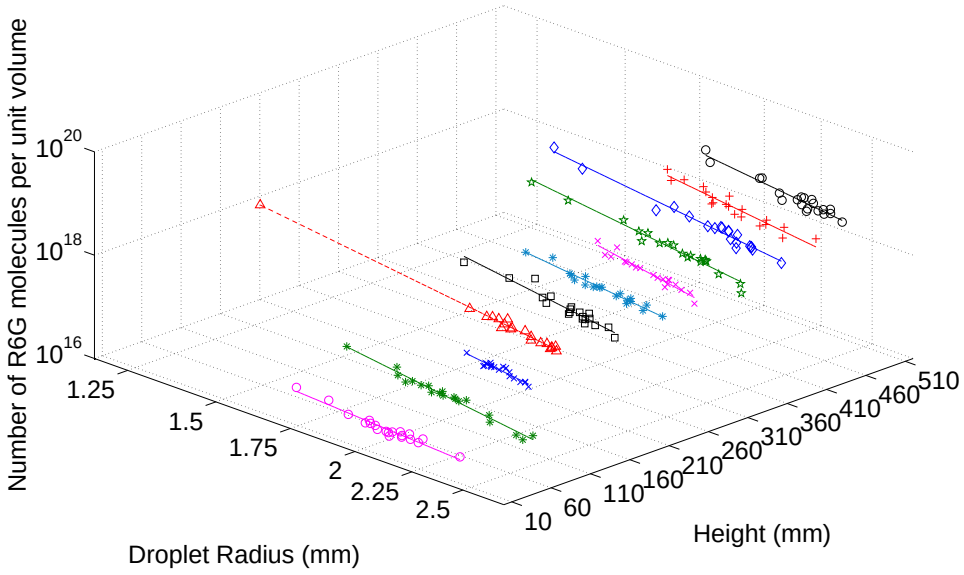

(a) 3-dimensional visualisation,

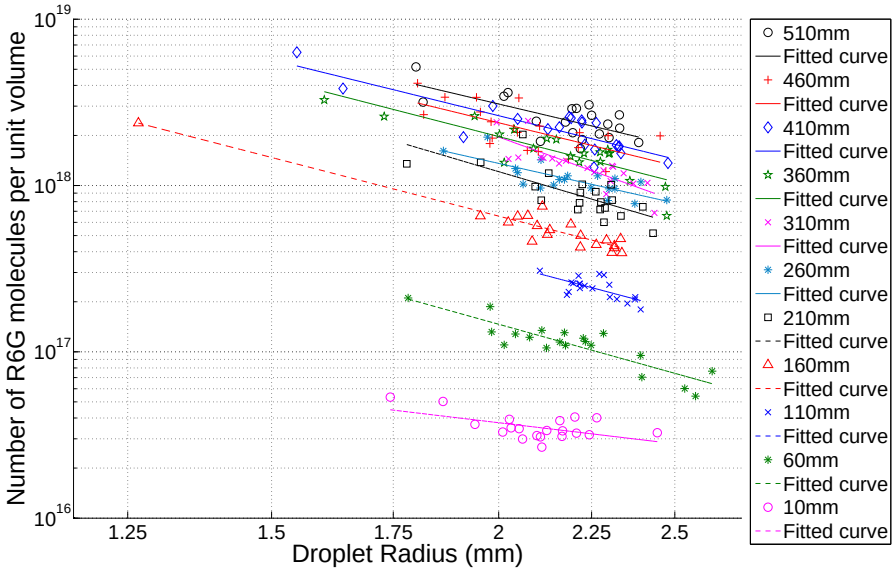

(b) Volume of Rhodamine-6G against droplet radius for different heights in tank.

Figure B.2: Development of the Rhodamine-6G volume stored within the surfactant cap as it rises through the tank for different droplet radii in the main experimental series. Rhodamine-6G concentration of 0.03mg/l.

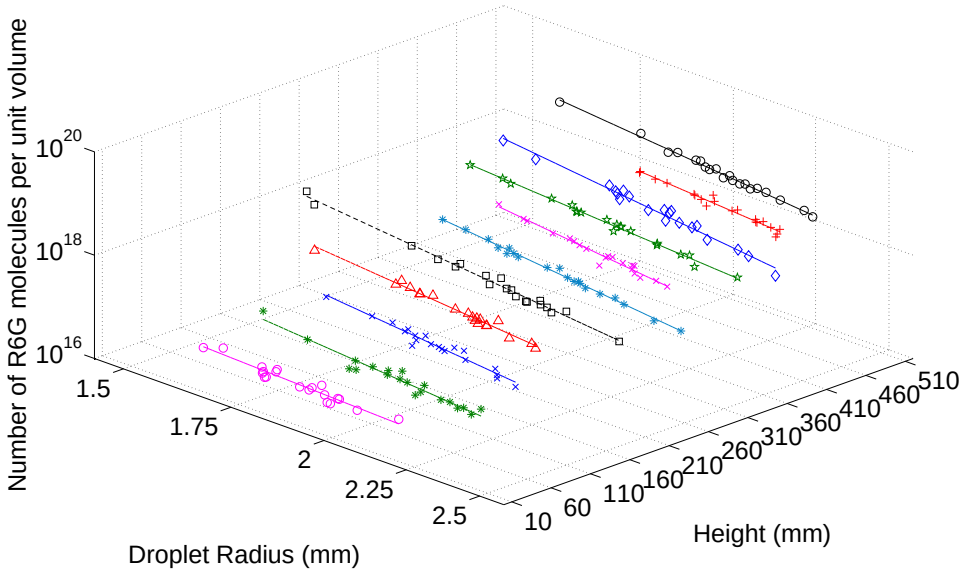

(a) 3-dimensional visualisation,

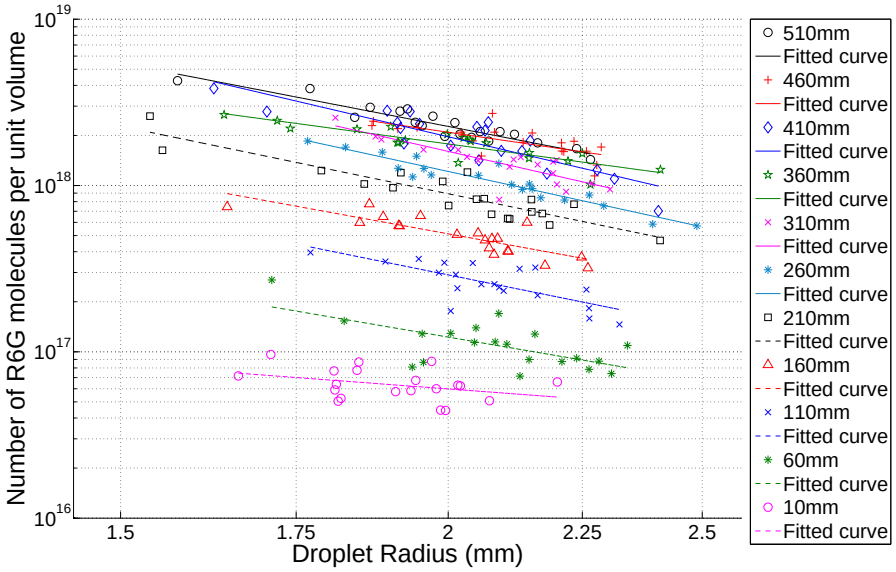

(b) Volume of Rhodamine-6G against droplet radius for different heights in tank.

Figure B.3: Development of the Rhodamine-6G volume stored within the surfactant cap as it rises through the tank for different droplet radii in the main experimental series. Rhodamine-6G concentration of 0.04mg/l.

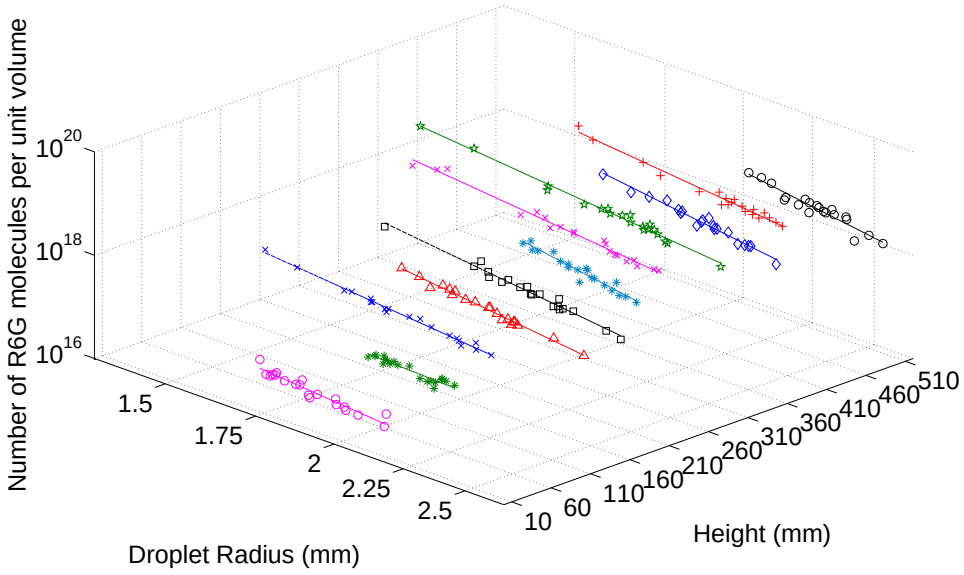

(a) 3-dimensional visualisation,

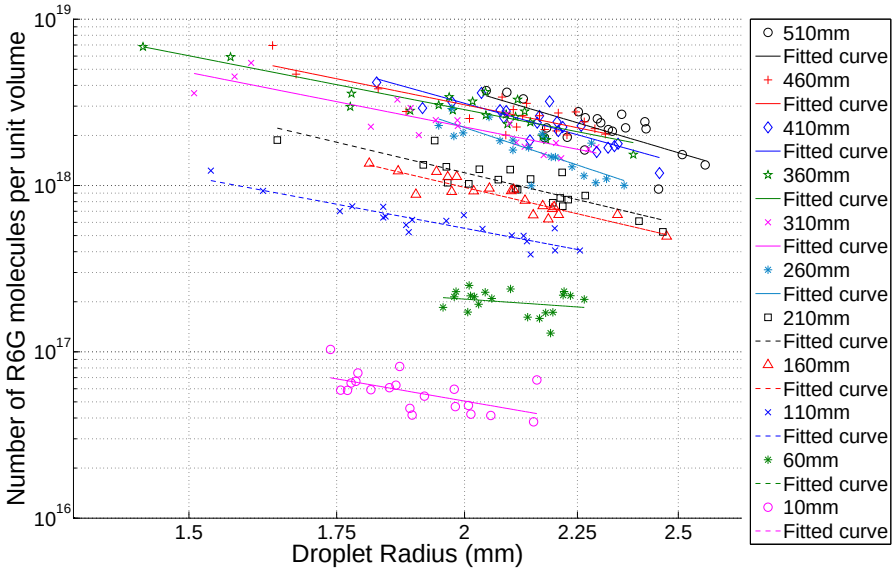

(b) Volume of Rhodamine-6G against droplet radius for different heights in tank.

Figure B.4: Development of the Rhodamine-6G volume stored within the surfactant cap as it rises through the tank for different droplet radii in the main experimental series. Rhodamine-6G concentration of 0.05mg/l.

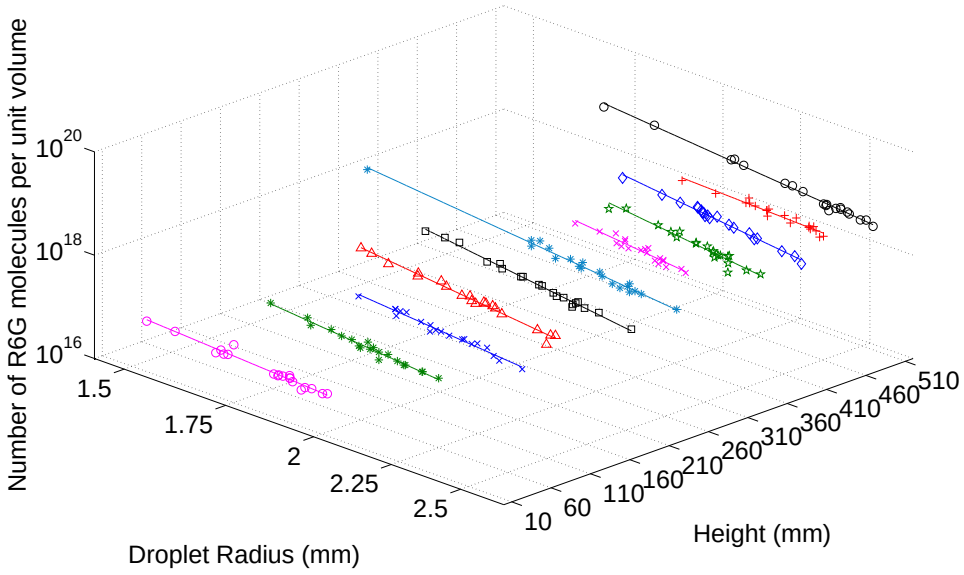

(a) 3-dimensional visualisation,

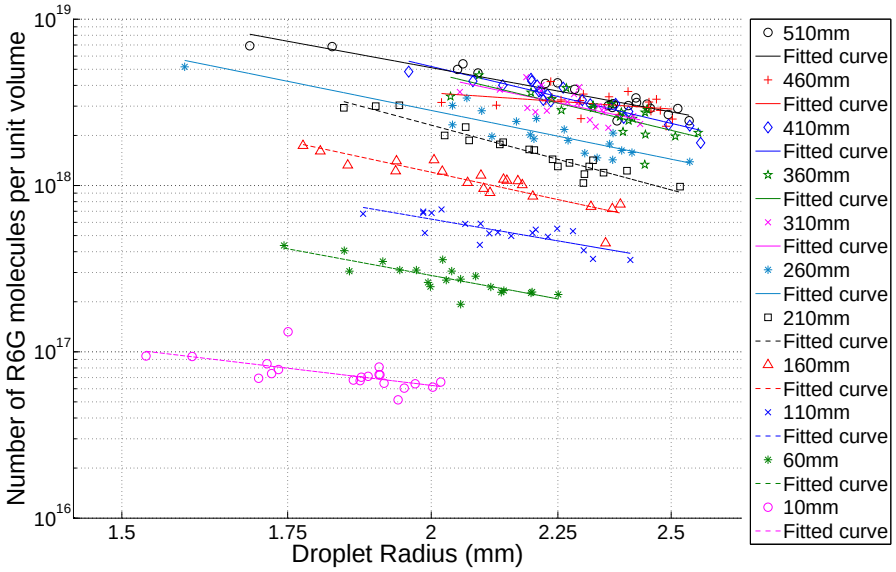

(b) Volume of Rhodamine-6G against droplet radius for different heights in tank.

Figure B.5: Development of the Rhodamine-6G volume stored within the surfactant cap as it rises through the tank for different droplet radii in the main experimental series. Rhodamine-6G concentration of 0.06mg/l.

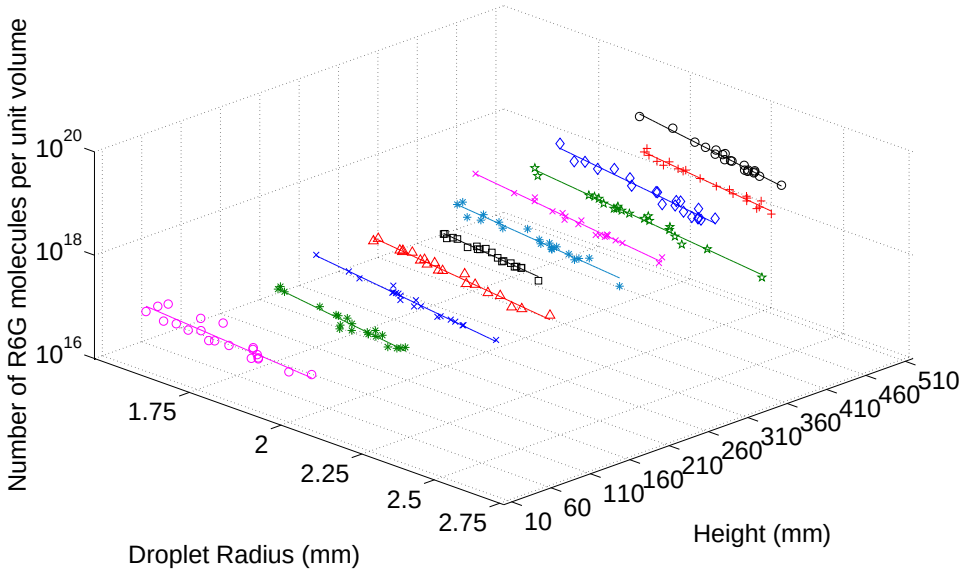

(a) 3-dimensional visualisation,

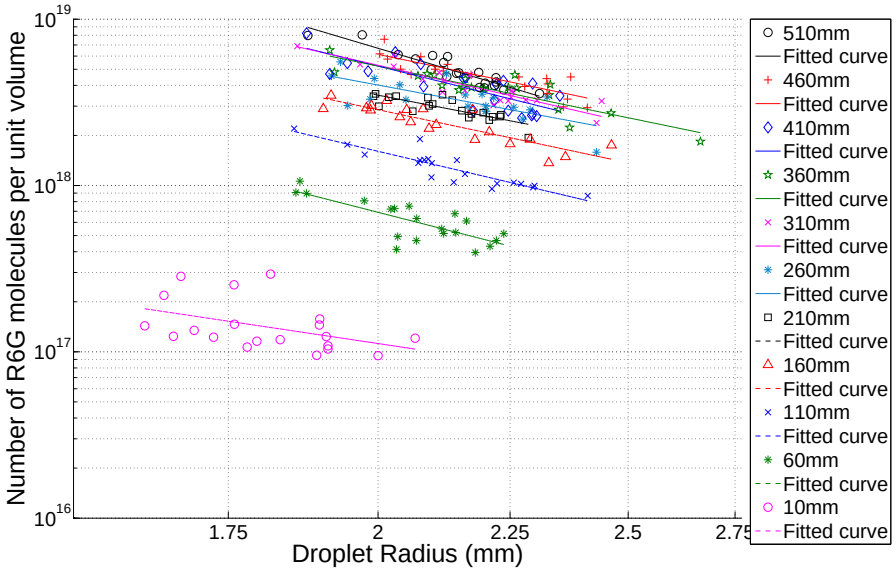

(b) Volume of Rhodamine-6G against droplet radius for different heights in tank.

Figure B.6: Development of the Rhodamine-6G volume stored within the surfactant cap as it rises through the tank for different droplet radii in the main experimental series. Rhodamine-6G concentration of 0.08mg/l.

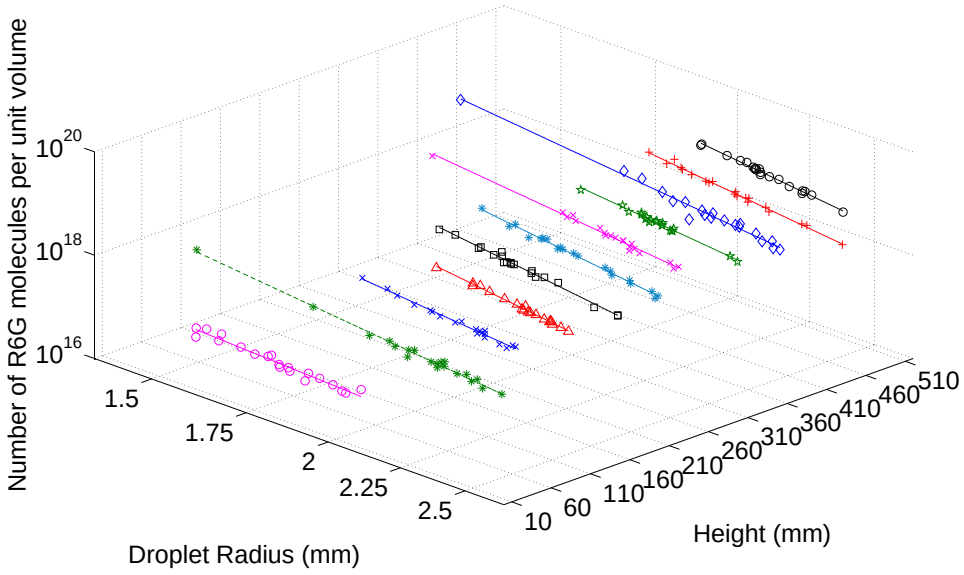

(a) 3-dimensional visualisation,

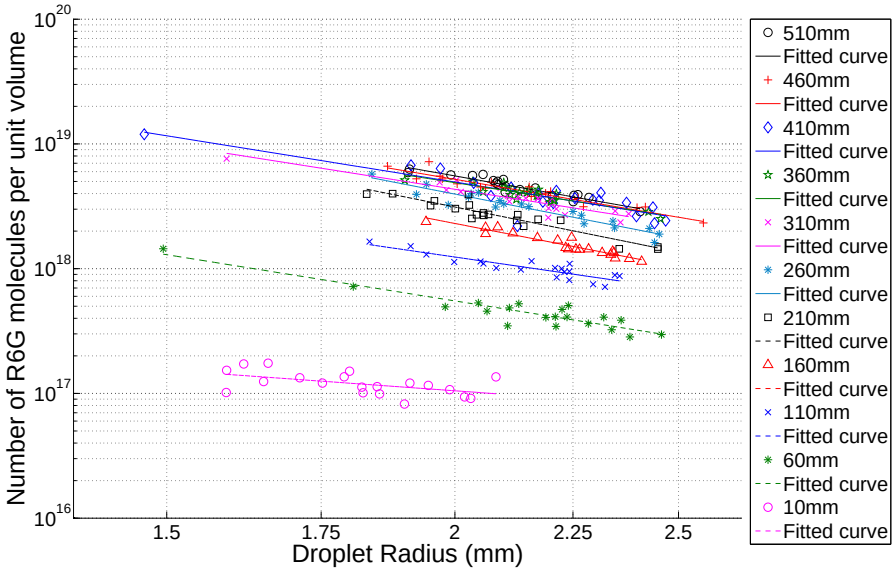

(b) Volume of Rhodamine-6G against droplet radius for different heights in tank.

Figure B.7: Development of the Rhodamine-6G volume stored within the surfactant cap as it rises through the tank for different droplet radii in the main experimental series. Rhodamine-6G concentration of 0.10mg/l.

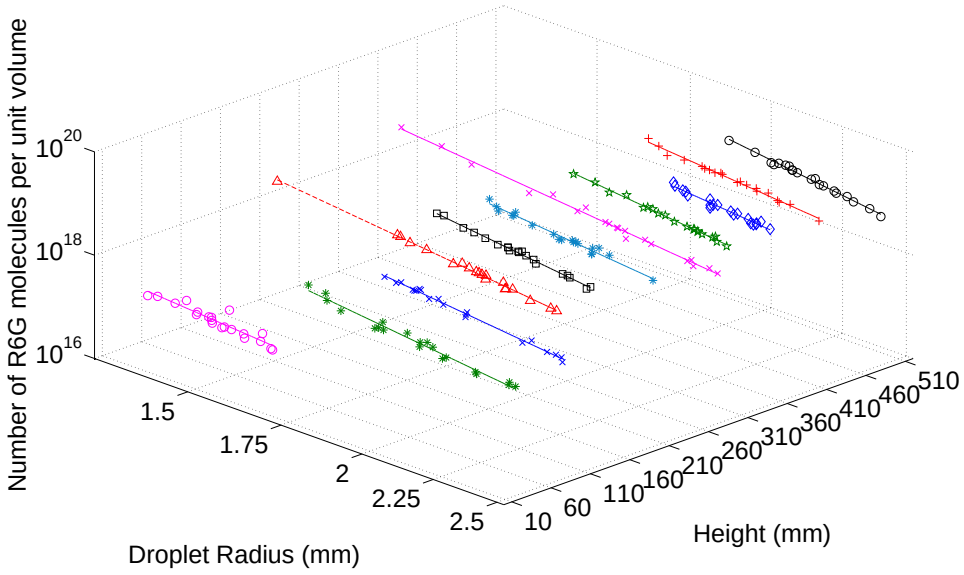

(a) 3-dimensional visualisation,

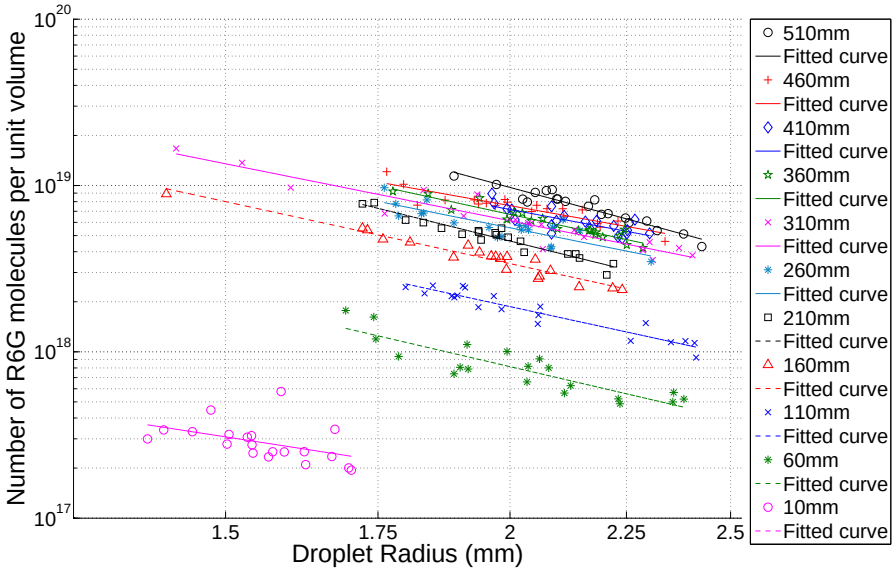

(b) Volume of Rhodamine-6G against droplet radius for different heights in tank.

Figure B.8: Development of the Rhodamine-6G volume stored within the surfactant cap as it rises through the tank for different droplet radii in the main experimental series. Rhodamine-6G concentration of 0.20mg/l.

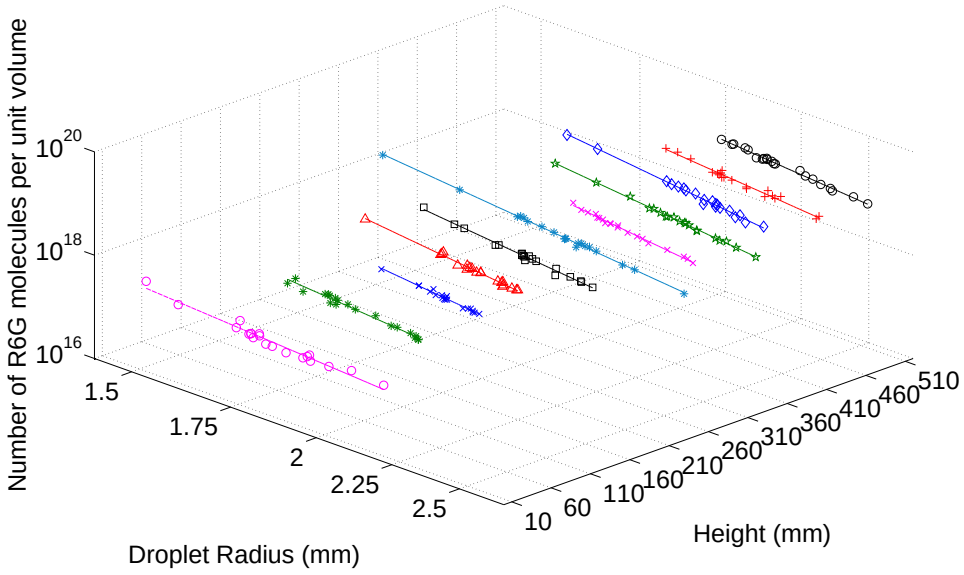

(a) 3-dimensional visualisation,

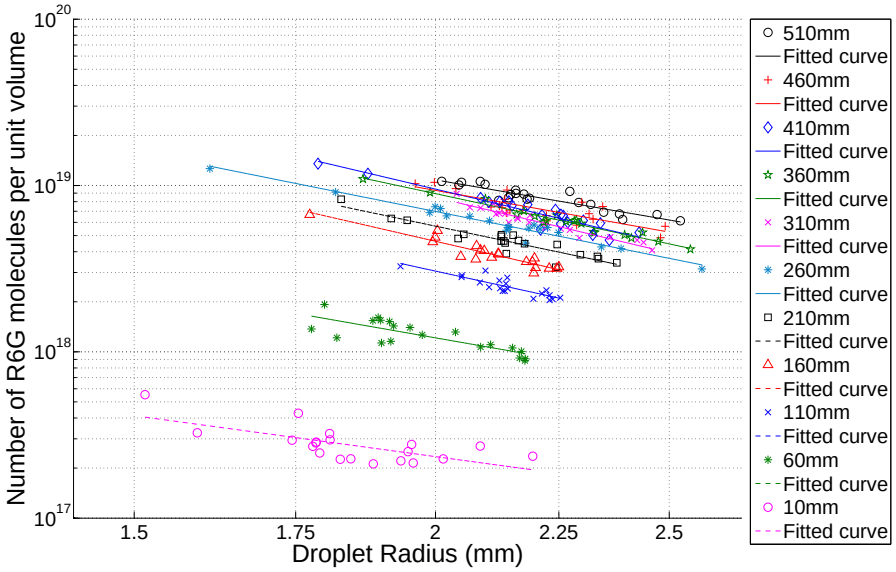

(b) Volume of Rhodamine-6G against droplet radius for different heights in tank.

Figure B.9: Development of the Rhodamine-6G volume stored within the surfactant cap as it rises through the tank for different droplet radii in the main experimental series. Rhodamine-6G concentration of 0.30mg/l.

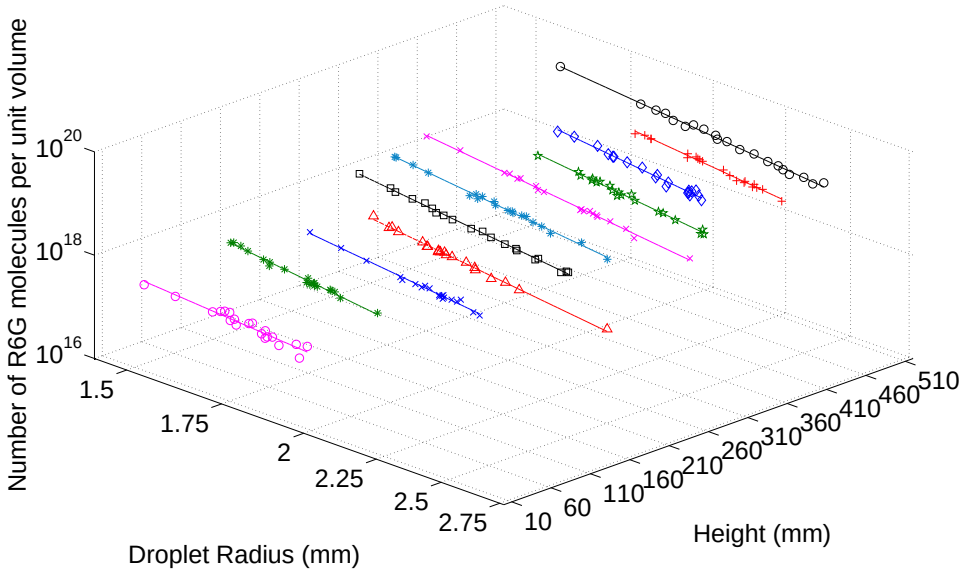

(a) 3-dimensional visualisation,

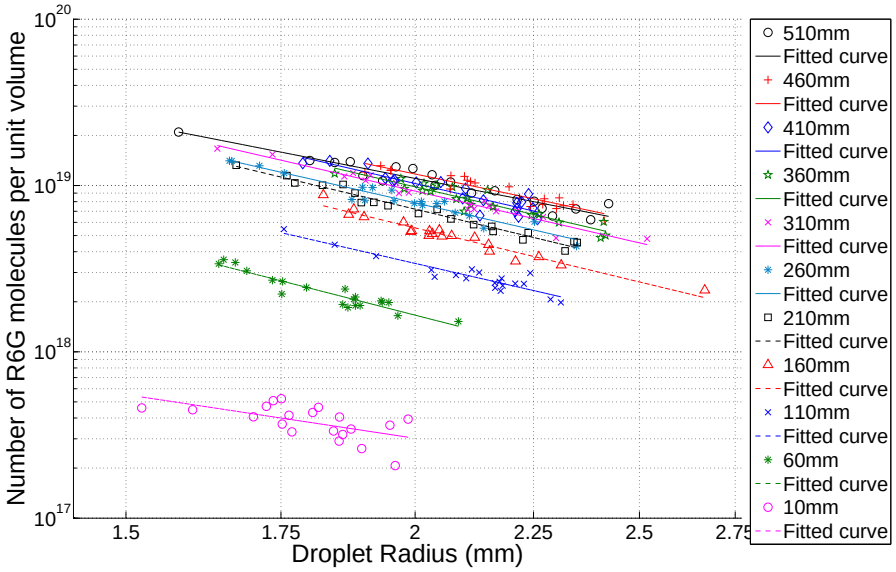

(b) Volume of Rhodamine-6G against droplet radius for different heights in tank.

Figure B.10: Development of the Rhodamine-6G volume stored within the surfactant cap as it rises through the tank for different droplet radii in the main experimental series. Rhodamine-6G concentration of 0.40mg/l.

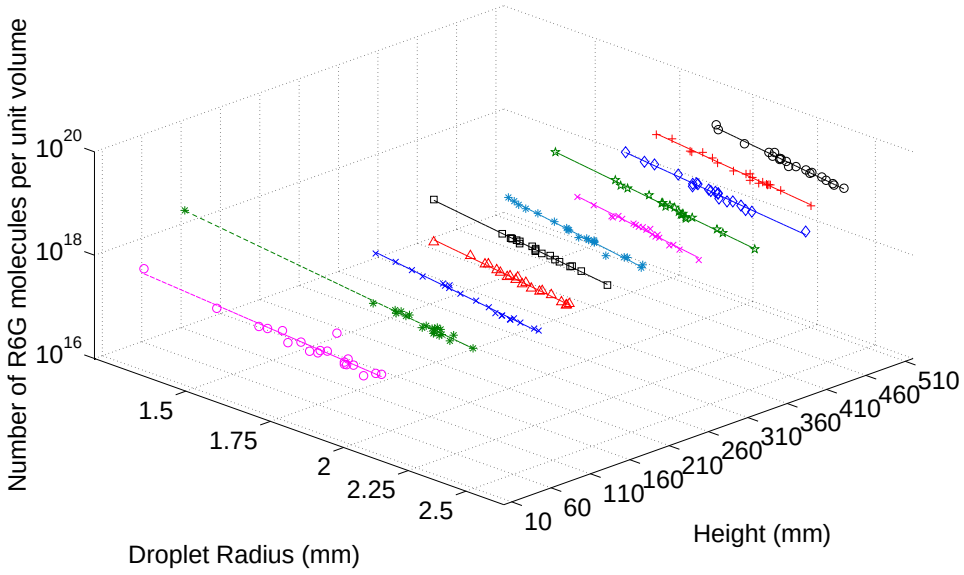

(a) 3-dimensional visualisation,

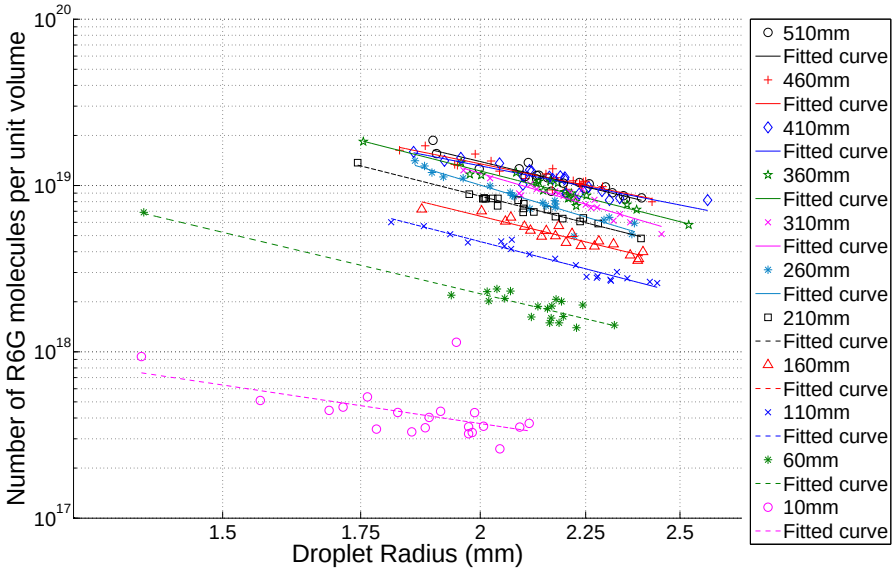

(b) Volume of Rhodamine-6G against droplet radius for different heights in tank.

Figure B.11: Development of the Rhodamine-6G volume stored within the surfactant cap as it rises through the tank for different droplet radii in the main experimental series. Rhodamine-6G concentration of 0.50mg/l.

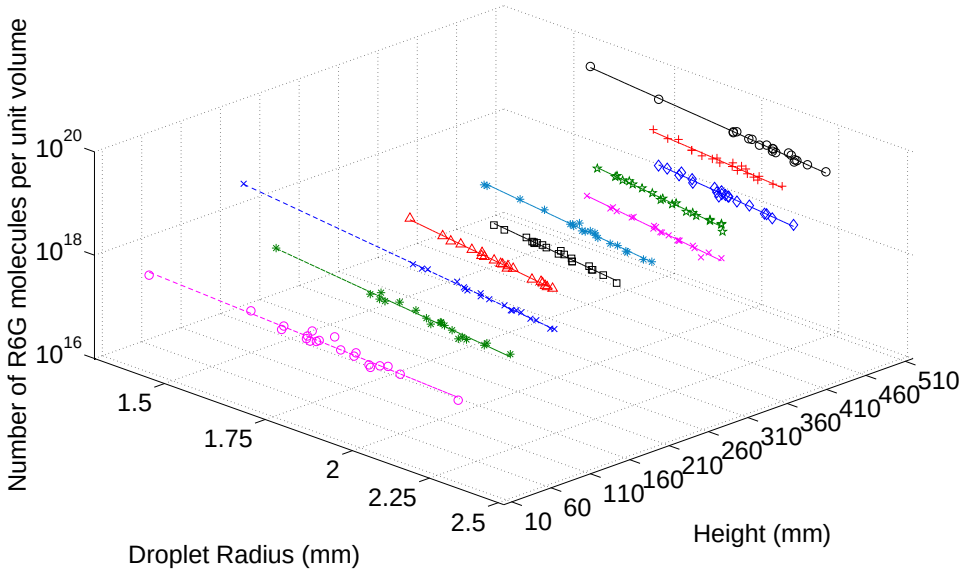

(a) 3-dimensional visualisation,

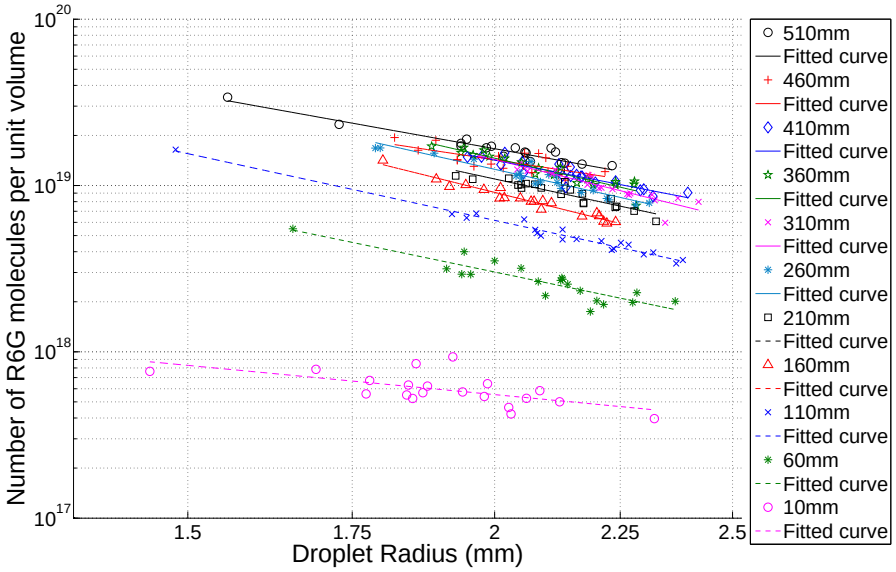

(b) Volume of Rhodamine-6G against droplet radius for different heights in tank.

Figure B.12: Development of the Rhodamine-6G volume stored within the surfactant cap as it rises through the tank for different droplet radii in the main experimental series. Rhodamine-6G concentration of 0.60mg/l.

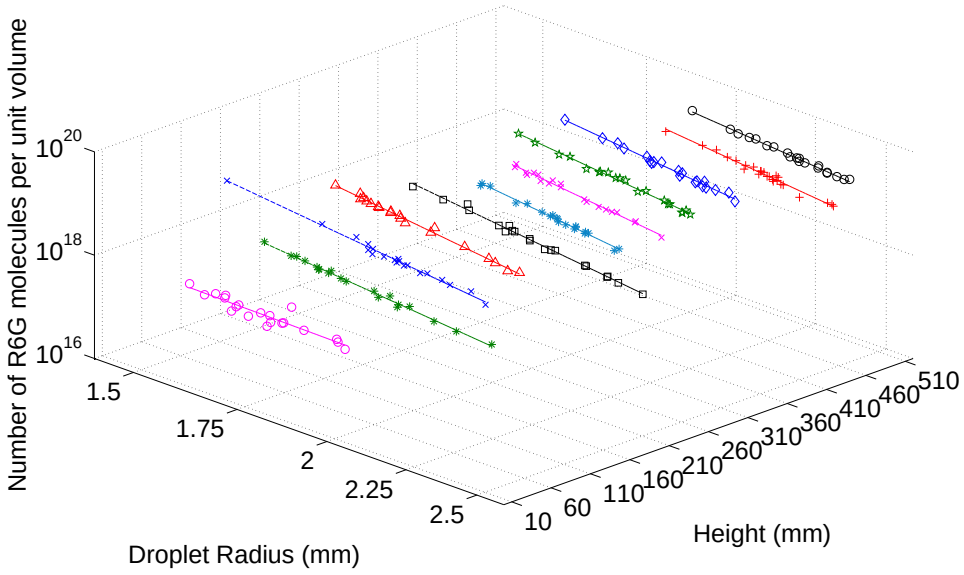

(a) 3-dimensional visualisation,

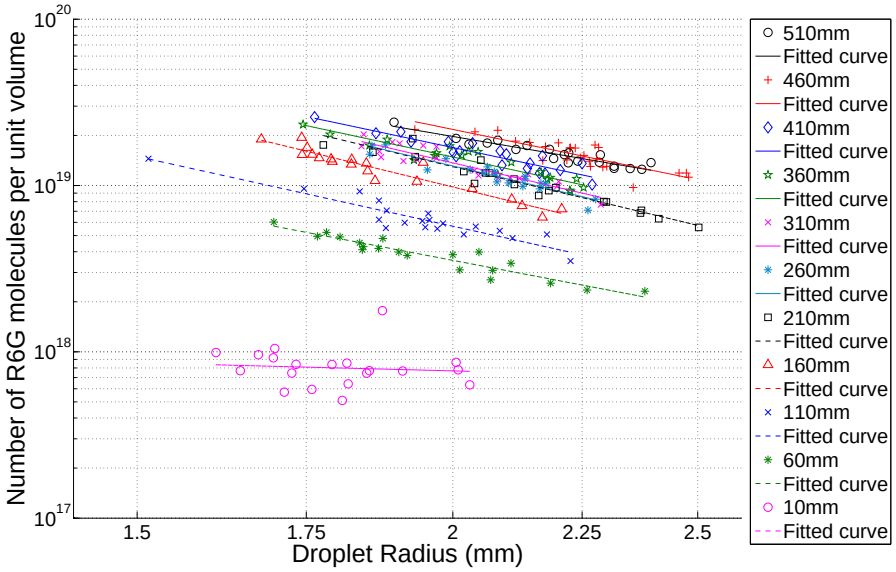

(b) Volume of Rhodamine-6G against droplet radius for different heights in tank.

Figure B.13: Development of the Rhodamine-6G volume stored within the surfactant cap as it rises through the tank for different droplet radii in the main experimental series. Rhodamine-6G concentration of 0.80mg/l.

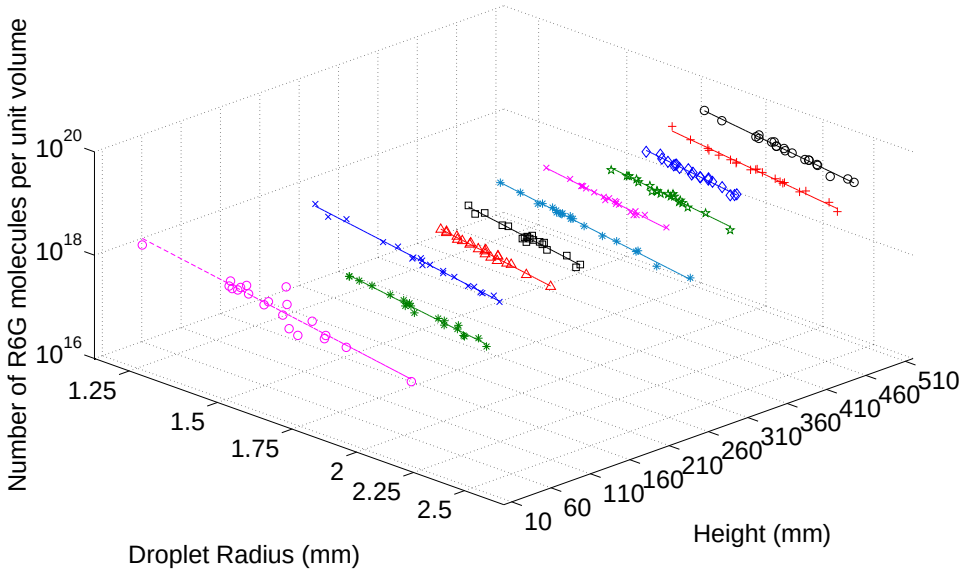

(a) 3-dimensional visualisation,

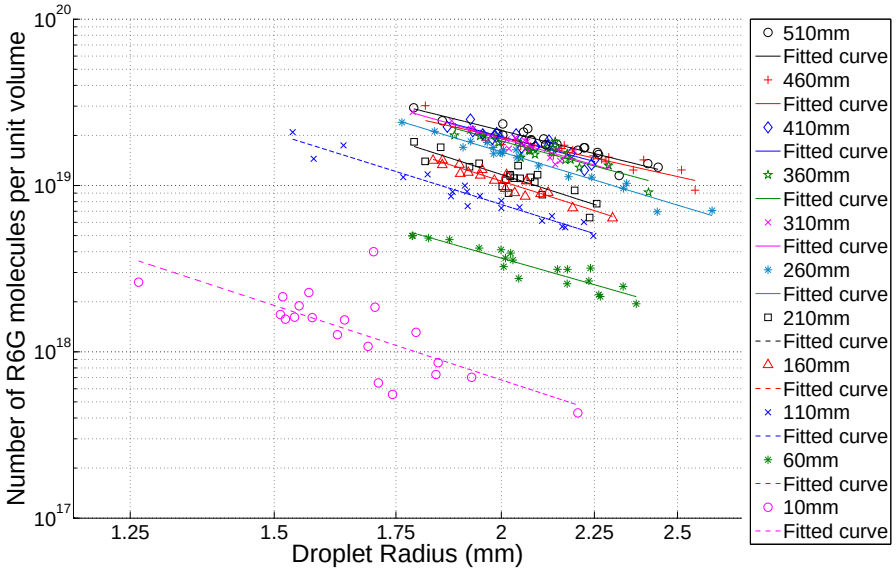

(b) Volume of Rhodamine-6G against droplet radius for different heights in tank.

Figure B.14: Development of the Rhodamine-6G volume stored within the surfactant cap as it rises through the tank for different droplet radii in the main experimental series. Rhodamine-6G concentration of 1.00mg/l.

Appendix C

LIF surfactant cap angles

The surfactant cap angles for the concentrations relating to 0.02mg/l through to 1.00mg/l calculated from the LIF experiments are presented here. All droplets for each concentration are presented having been split into different radius size bands. In general it is observed that smaller droplets possess a larger cap angle although there is an overlap between droplet of different size bands in most cases. For a height of 10mm from the base of the tank it is observed that as the concentration increases, the spread of data increases, reducing the reliability of the results at this height.

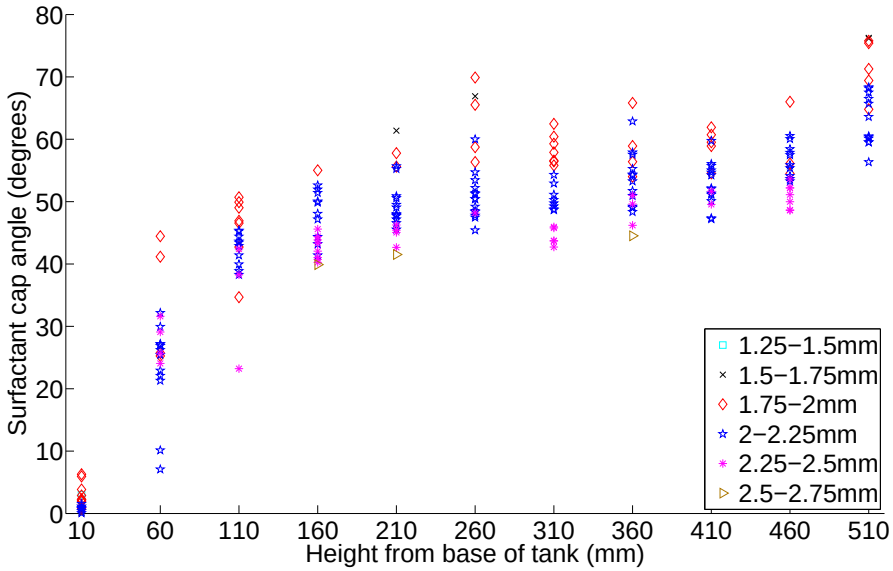

Figure C.1: Development of the surfactant cap angle over the height of the tank for different droplet radii in the main experimental series. Rhodamine-6G concentration of 0.02mg/l.

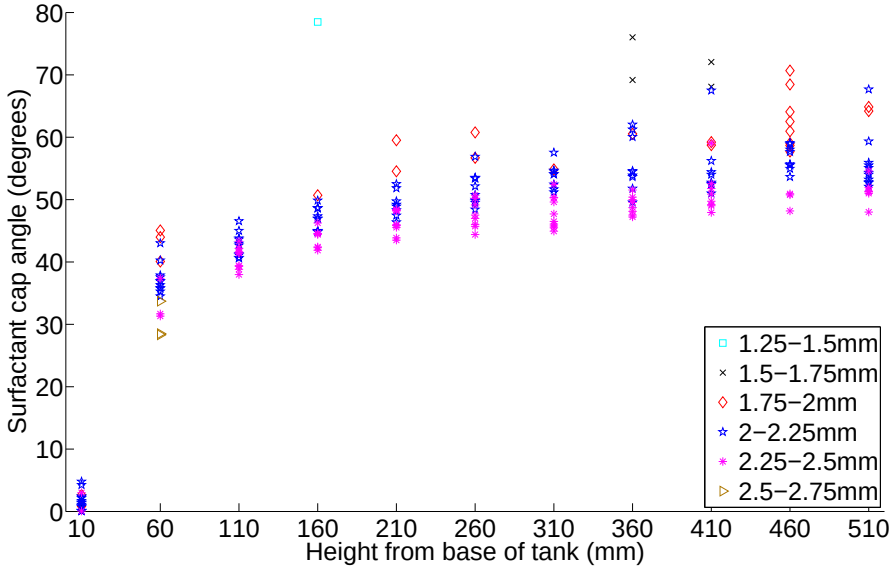

Figure C.2: Development of the surfactant cap angle over the height of the tank for different droplet radii in the main experimental series. Rhodamine-6G concentration of 0.03mg/l.

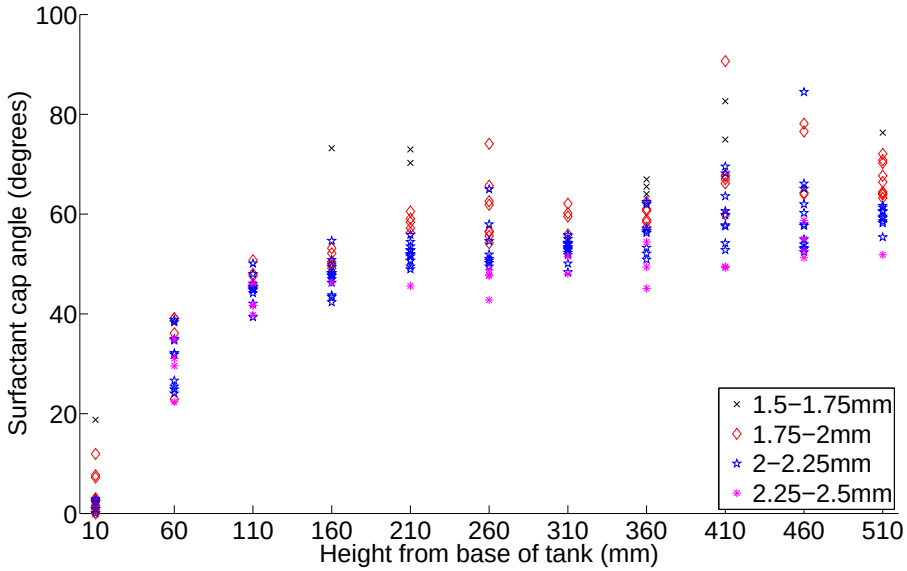

Figure C.3: Development of the surfactant cap angle over the height of the tank for different droplet radii in the main experimental series. Rhodamine-6G concentration of 0.04mg/l.

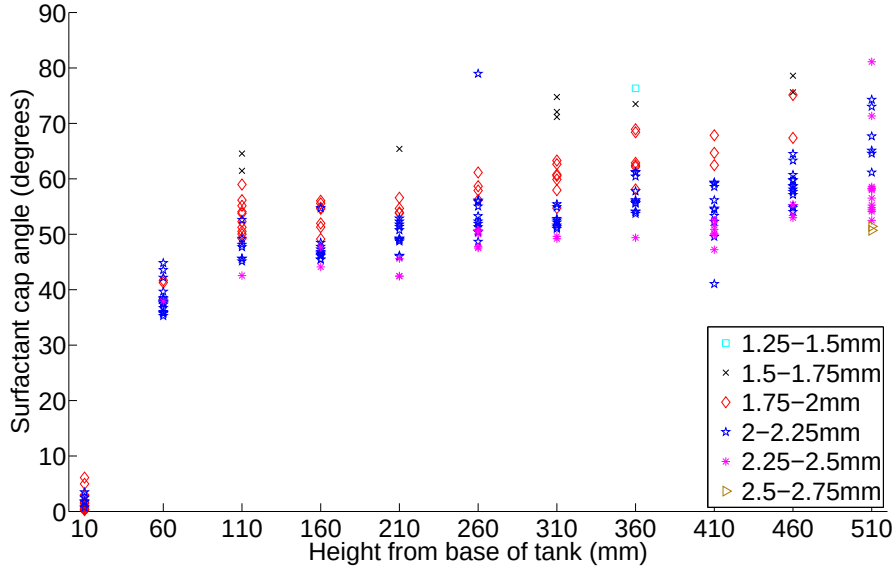

Figure C.4: Development of the surfactant cap angle over the height of the tank for different droplet radii in the main experimental series. Rhodamine-6G concentration of 0.05mg/l.

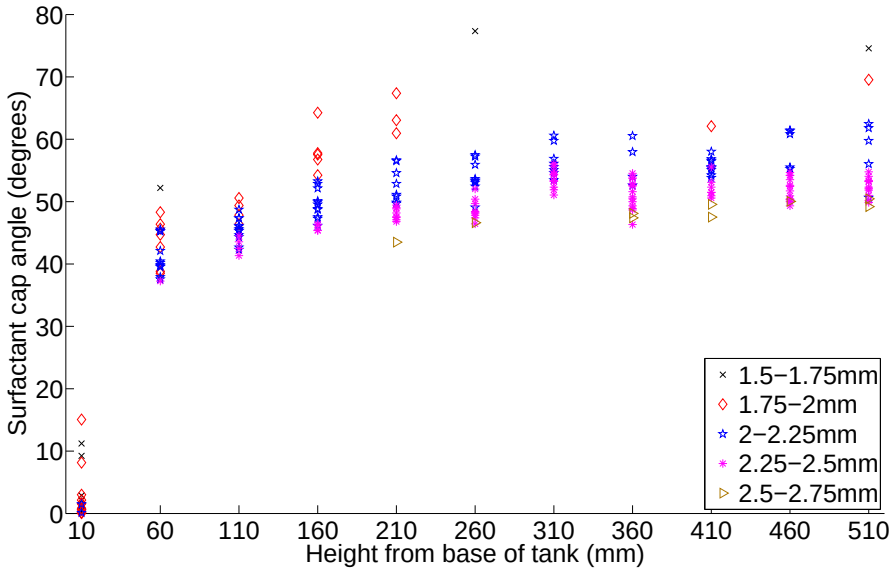

Figure C.5: Development of the surfactant cap angle over the height of the tank for different droplet radii in the main experimental series. Rhodamine-6G concentration of 0.06mg/l.

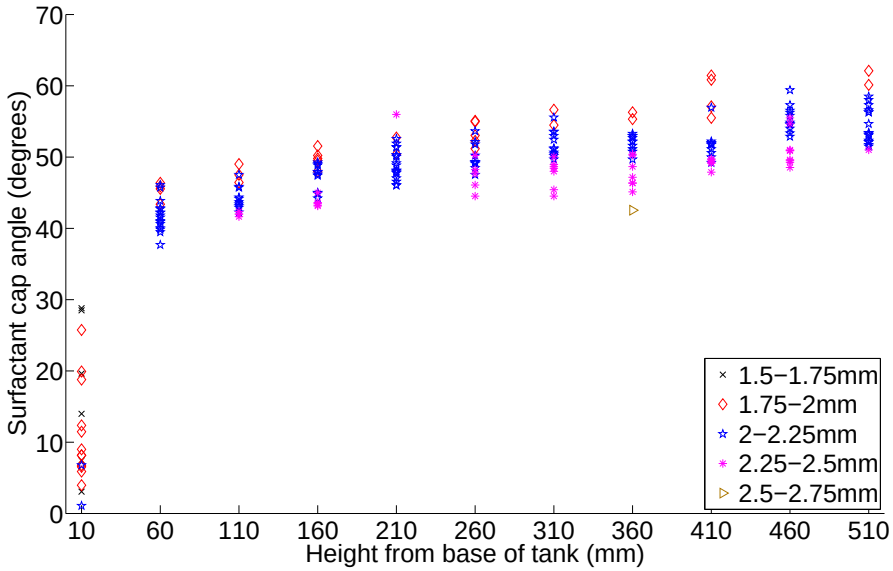

Figure C.6: Development of the surfactant cap angle over the height of the tank for different droplet radii in the main experimental series. Rhodamine-6G concentration of 0.08mg/l.

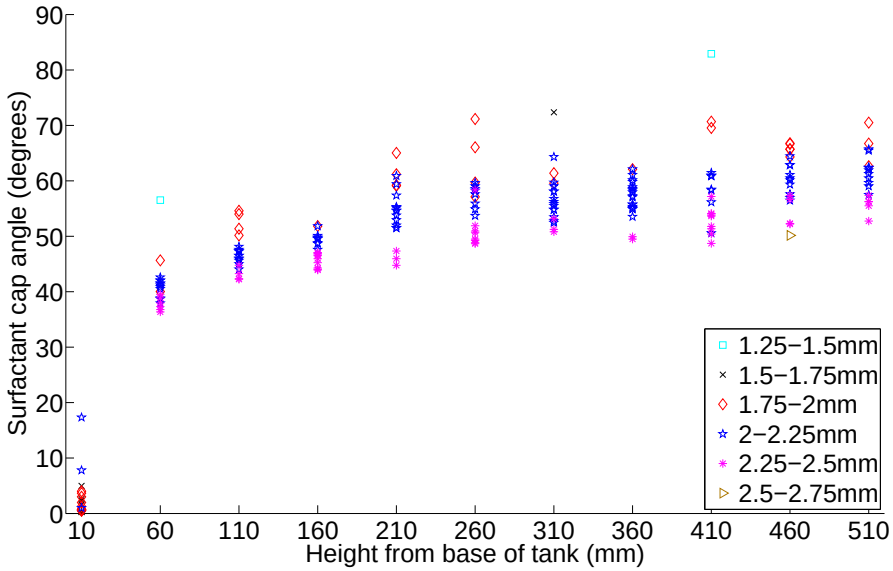

Figure C.7: Development of the surfactant cap angle over the height of the tank for different droplet radii in the main experimental series. Rhodamine-6G concentration of 0.10mg/l.

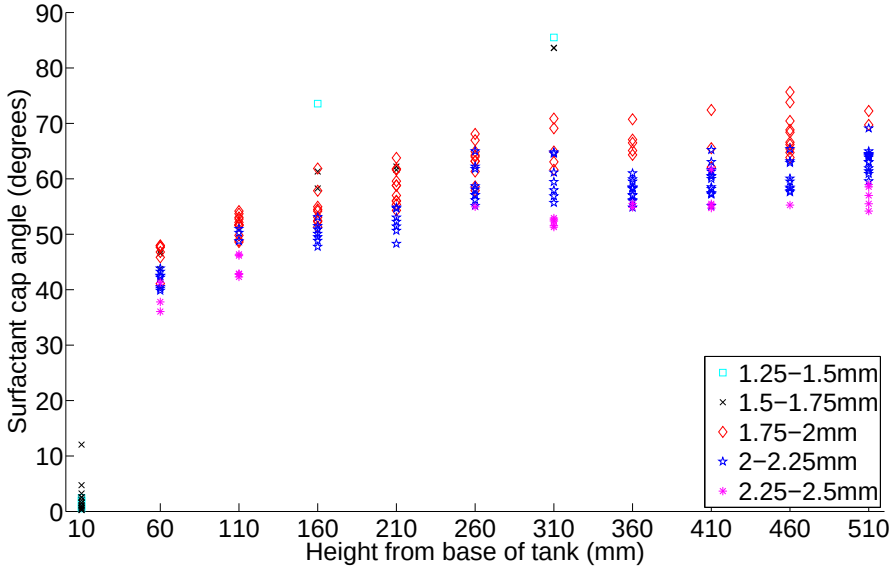

Figure C.8: Development of the surfactant cap angle over the height of the tank for different droplet radii in the main experimental series. Rhodamine-6G concentration of 0.20mg/l.

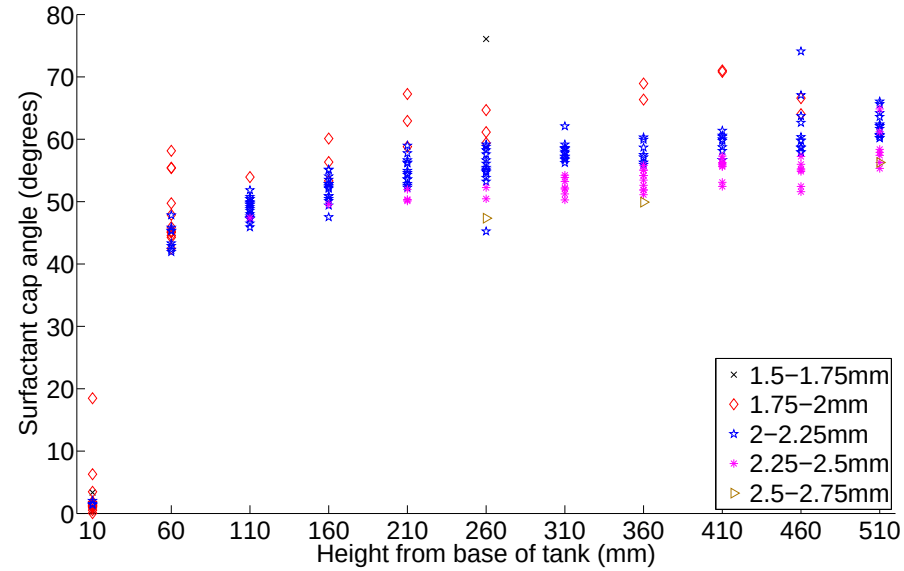

Figure C.9: Development of the surfactant cap angle over the height of the tank for different droplet radii in the main experimental series. Rhodamine-6G concentration of 0.30mg/l.

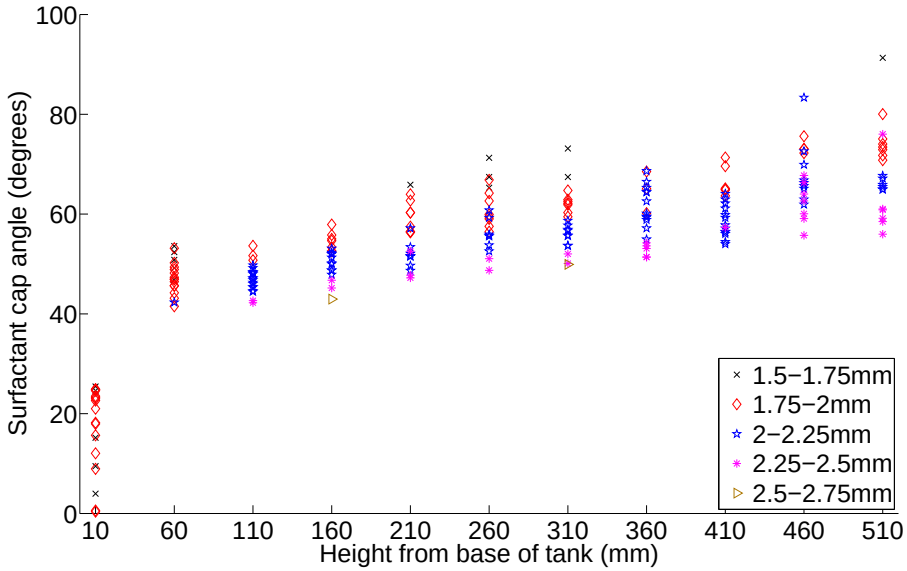

Figure C.10: Development of the surfactant cap angle over the height of the tank for different droplet radii in the main experimental series. Rhodamine-6G concentration of 0.40mg/l.

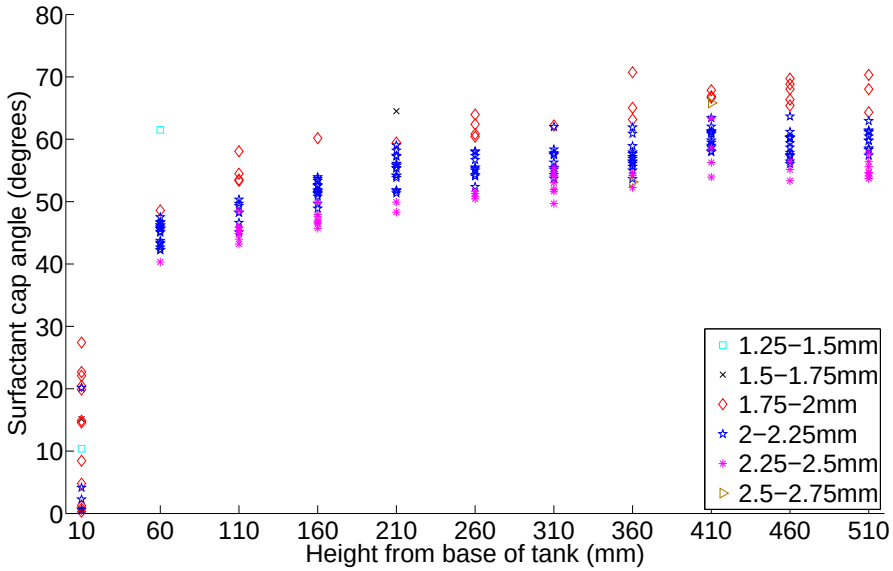

Figure C.11: Development of the surfactant cap angle over the height of the tank for different droplet radii in the main experimental series. Rhodamine-6G concentration of 0.50mg/l.

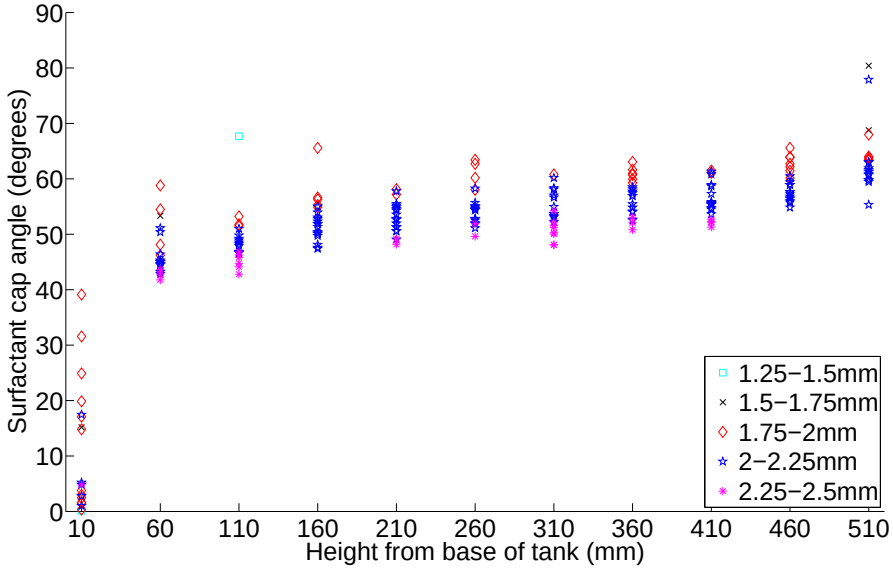

Figure C.12: Development of the surfactant cap angle over the height of the tank for different droplet radii in the main experimental series. Rhodamine-6G concentration of 0.60mg/l.

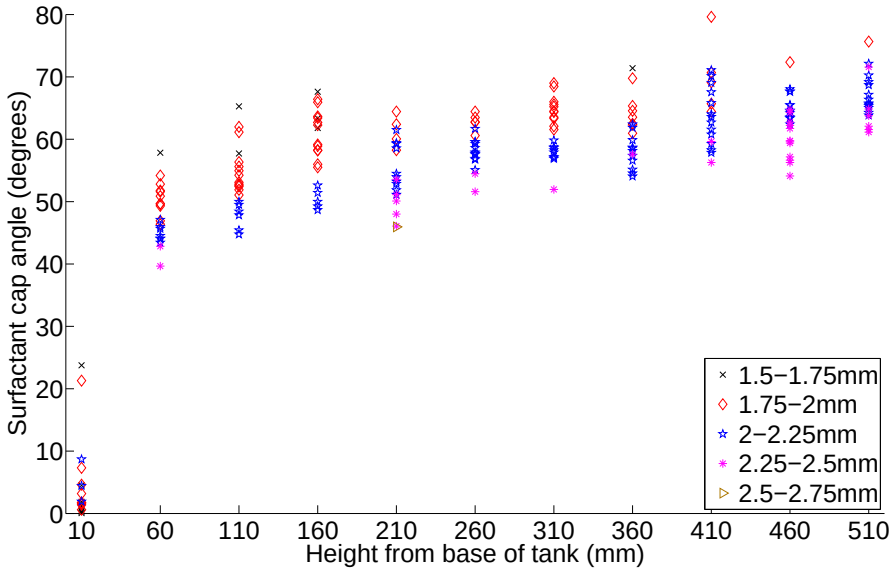

Figure C.13: Development of the surfactant cap angle over the height of the tank for different droplet radii in the main experimental series. Rhodamine-6G concentration of 0.80mg/l.

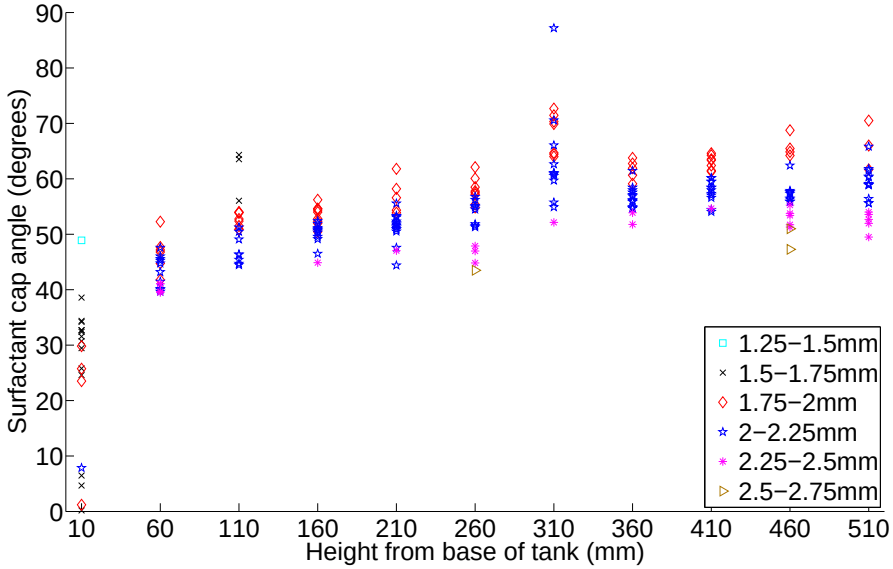

Figure C.14: Development of the surfactant cap angle over the height of the tank for different droplet radii in the main experimental series. Rhodamine-6G concentration of 1.00mg/l.

Appendix D

LIF averaged surfactant distribution profiles

The averaged surfactant distribution profiles for each concentration from 0.02mg/l to 1.00mg/l are presented here. Each concentration starts off very low levels of surfactant at the rear of the droplet. This level has a sharp initial increase in volume which levels off towards the top of the tank. The sharp peak that develops relates to the Rhodamine-6G in the surfactant-rich wake that develops behind the droplet. Higher concentrations exhibit less noise in the profile that the lower concentrations.

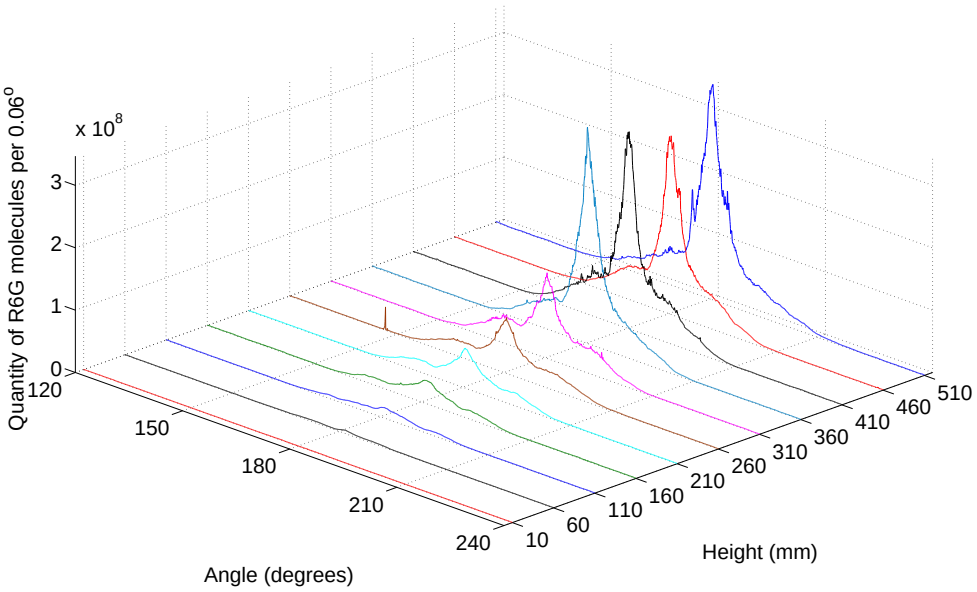

Figure D.1: Averaged surfactant distribution profiles for a Rhodamine-6G concentration of 0.02mg/l at different heights from the base of the tank. Angle measured from the front of the droplet.

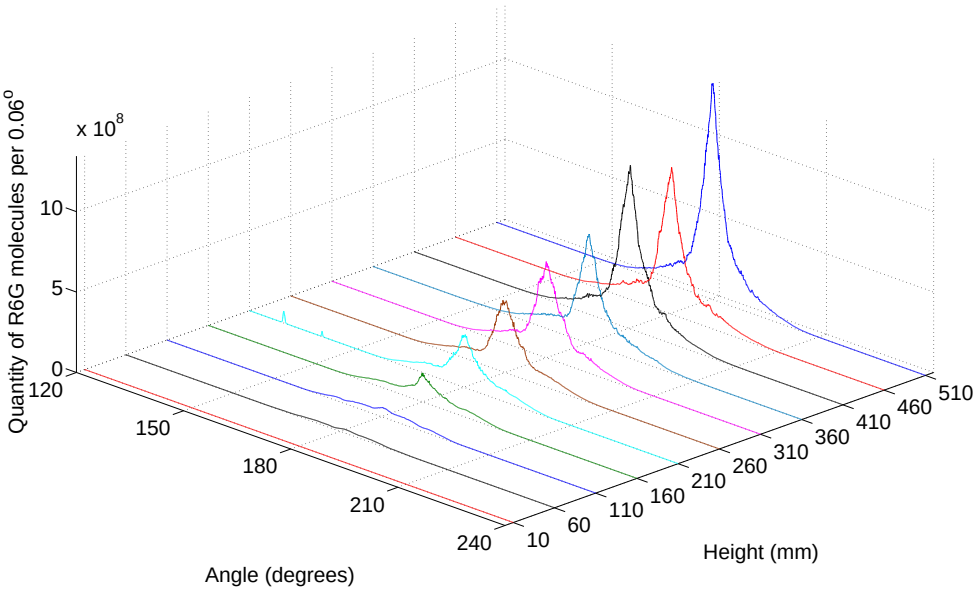

Figure D.2: Averaged surfactant distribution profiles for a Rhodamine-6G concentration of 0.03mg/l at different heights from the base of the tank. Angle measured from the front of the droplet.

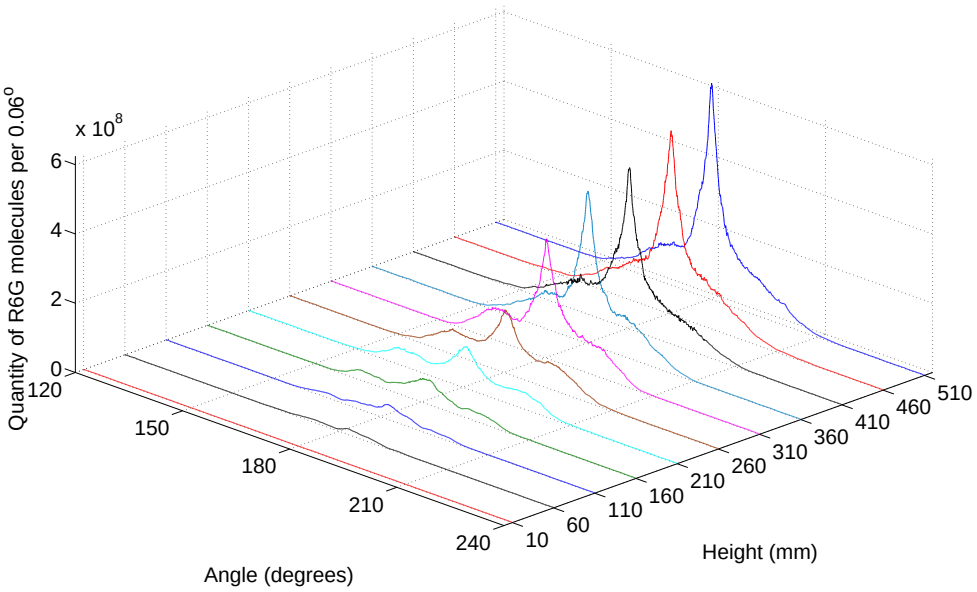

Figure D.3: Averaged surfactant distribution profiles for a Rhodamine-6G concentration of 0.04mg/l at different heights from the base of the tank. Angle measured from the front of the droplet.

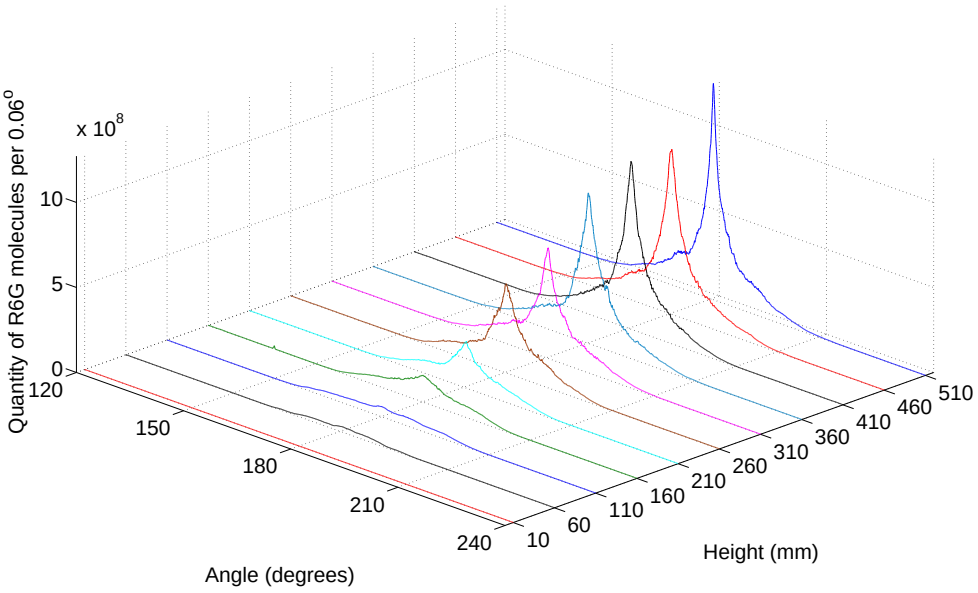

Figure D.4: Averaged surfactant distribution profiles for a Rhodamine-6G concentration of 0.05mg/l at different heights from the base of the tank. Angle measured from the front of the droplet.

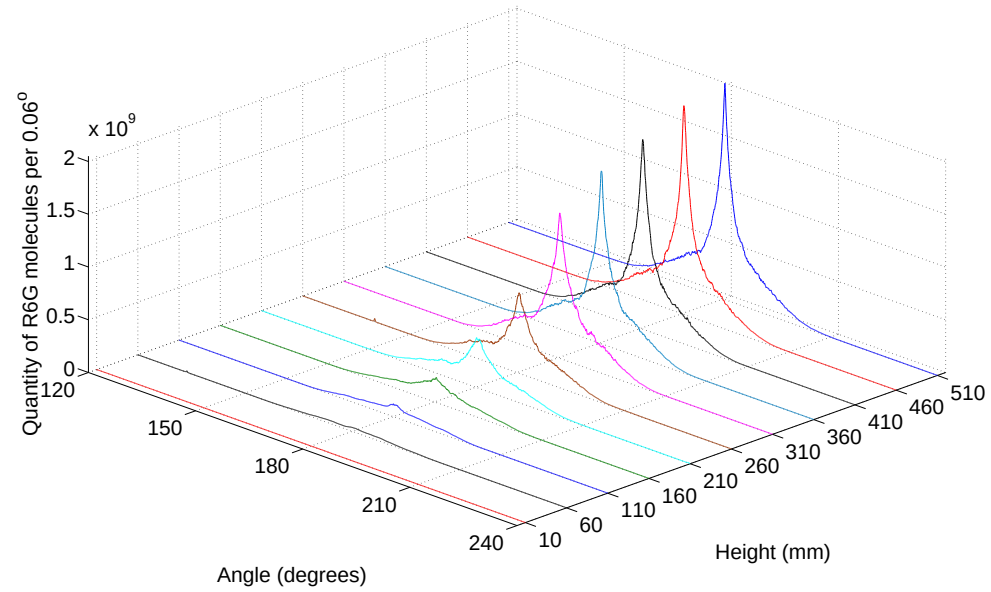

Figure D.5: Averaged surfactant distribution profiles for a Rhodamine-6G concentration of 0.06mg/l at different heights from the base of the tank. Angle measured from the front of the droplet.

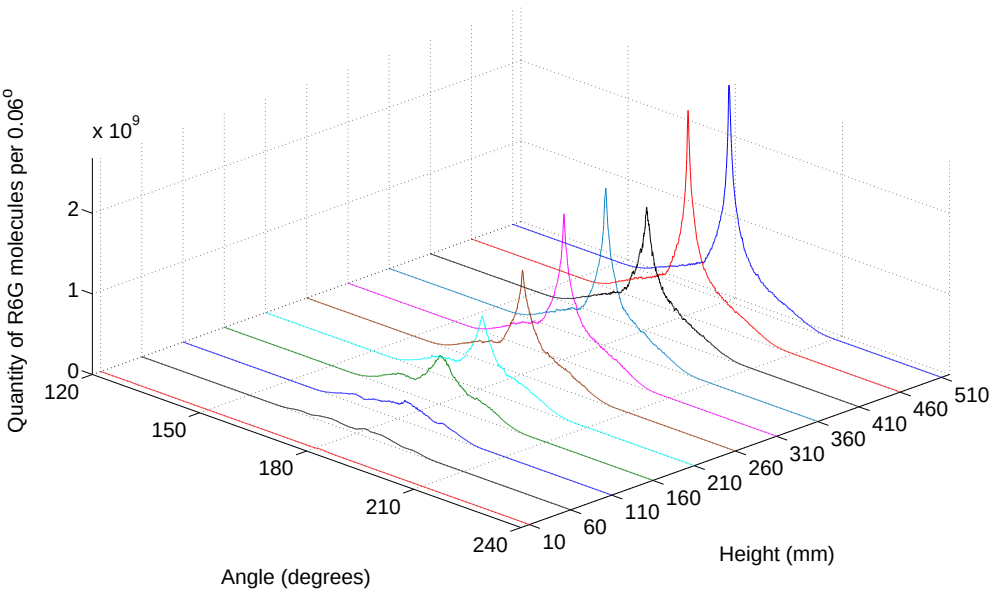

Figure D.6: Averaged surfactant distribution profiles for a Rhodamine-6G concentration of 0.08mg/l at different heights from the base of the tank. Angle measured from the front of the droplet.

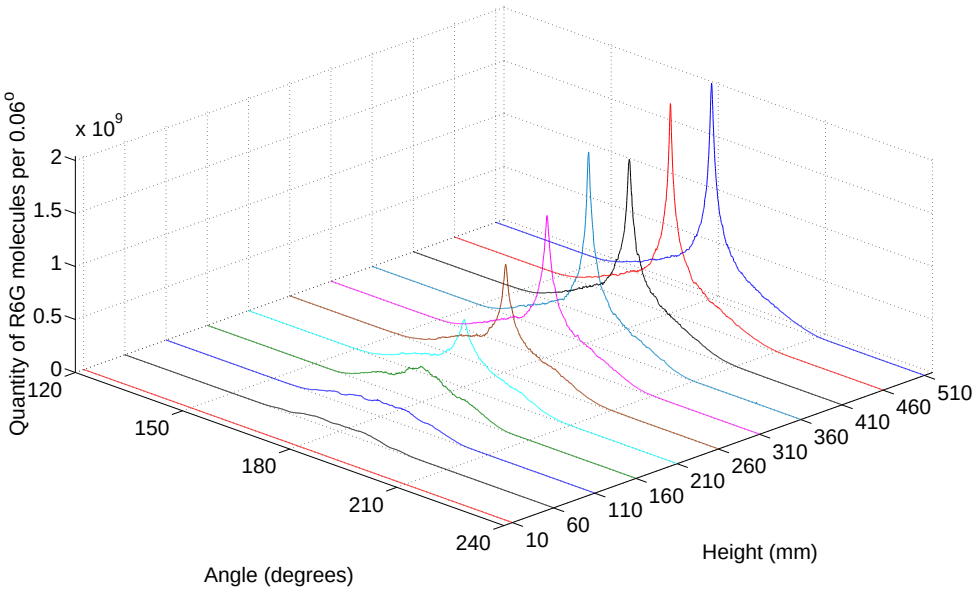

Figure D.7: Averaged surfactant distribution profiles for a Rhodamine-6G concentration of 0.10mg/l at different heights from the base of the tank. Angle measured from the front of the droplet.

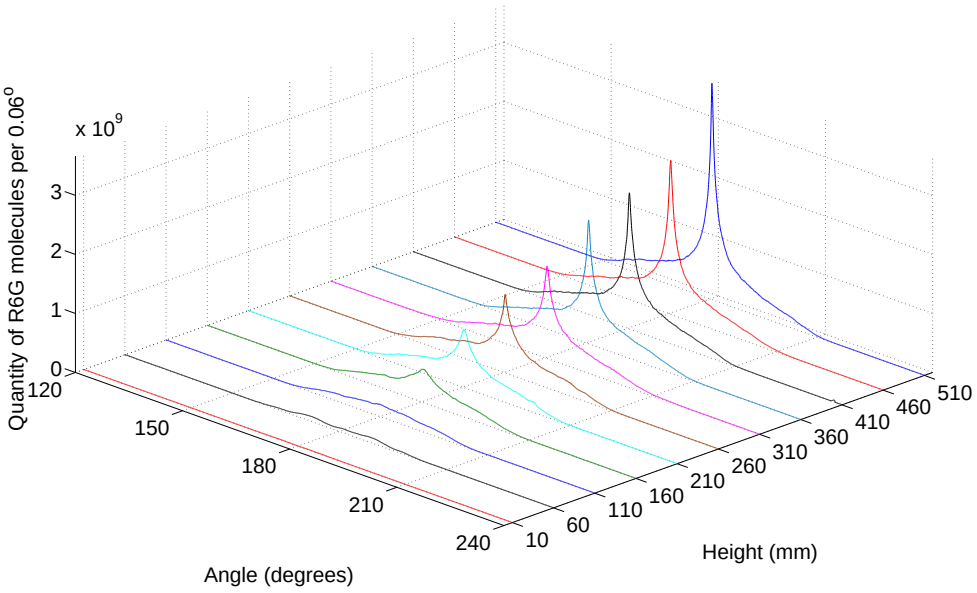

Figure D.8: Averaged surfactant distribution profiles for a Rhodamine-6G concentration of 0.20mg/l at different heights from the base of the tank. Angle measured from the front of the droplet.

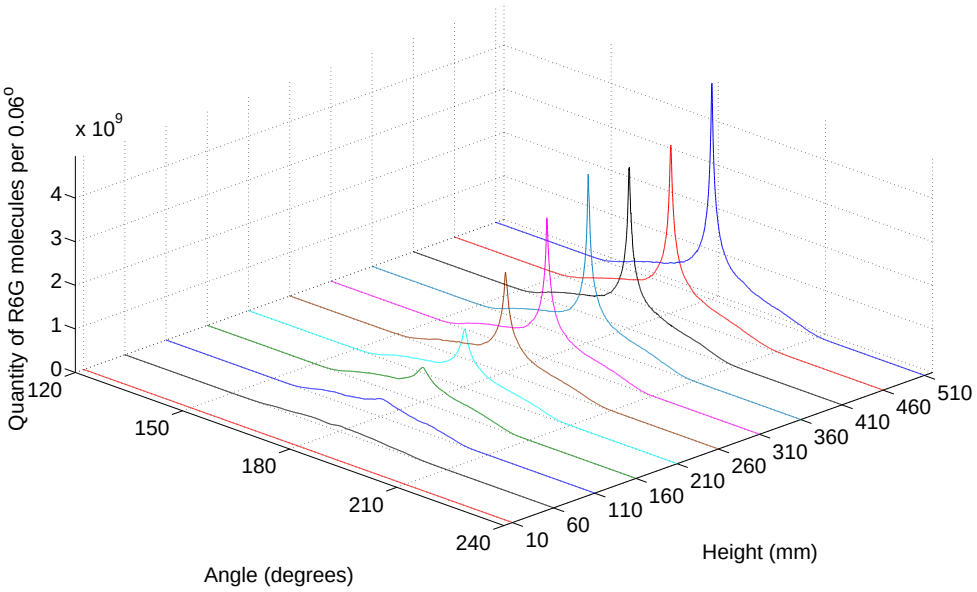

Figure D.9: Averaged surfactant distribution profiles for a Rhodamine-6G concentration of 0.30mg/l at different heights from the base of the tank. Angle measured from the front of the droplet.

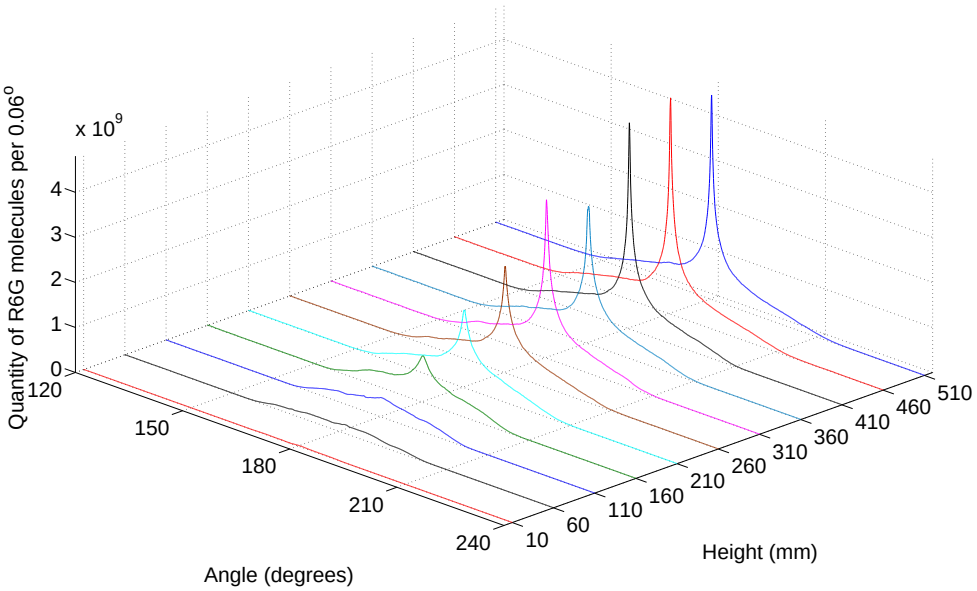

Figure D.10: Averaged surfactant distribution profiles for a Rhodamine-6G concentration of 0.40mg/l at different heights from the base of the tank. Angle measured from the front of the droplet.

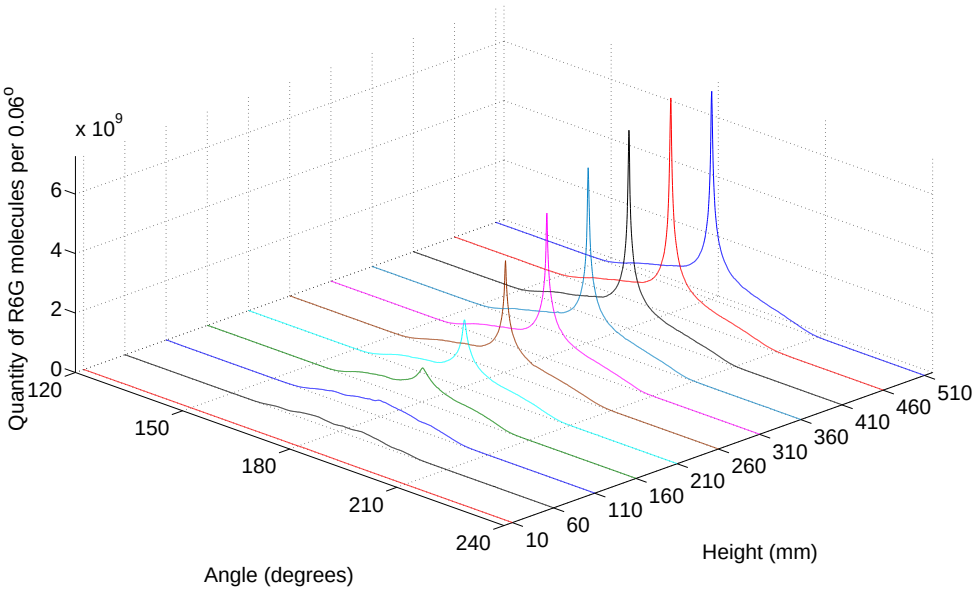

Figure D.11: Averaged surfactant distribution profiles for a Rhodamine-6G concentration of 0.50mg/l at different heights from the base of the tank. Angle measured from the front of the droplet.

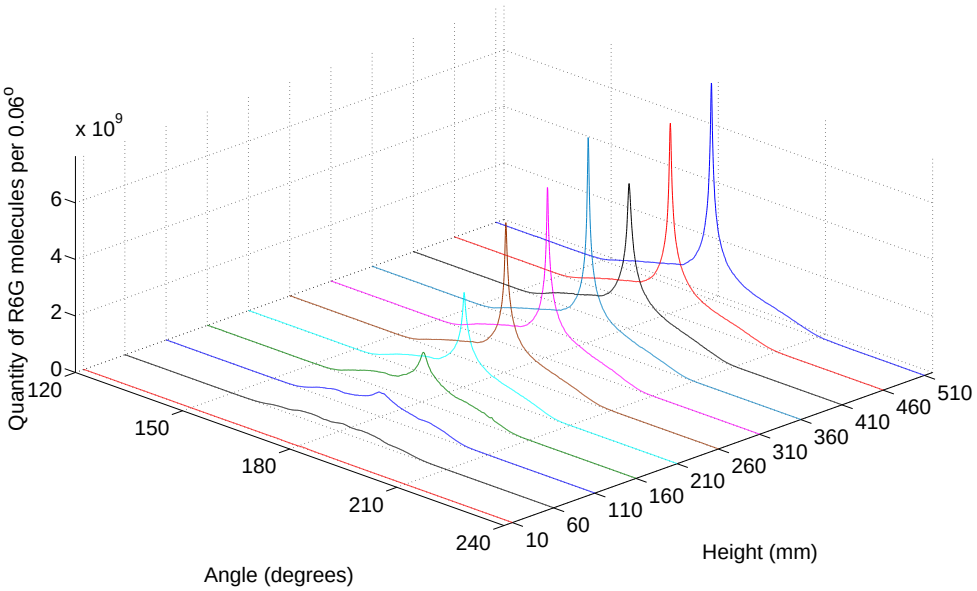

Figure D.12: Averaged surfactant distribution profiles for a Rhodamine-6G concentration of 0.60mg/l at different heights from the base of the tank. Angle measured from the front of the droplet.

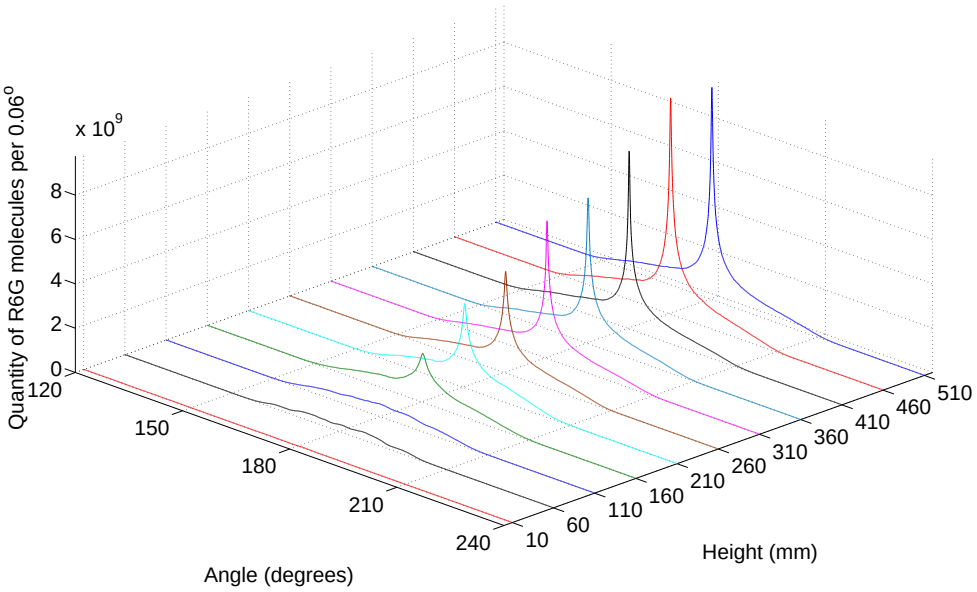

Figure D.13: Averaged surfactant distribution profiles for a Rhodamine-6G concentration of 0.80mg/l at different heights from the base of the tank. Angle measured from the front of the droplet.

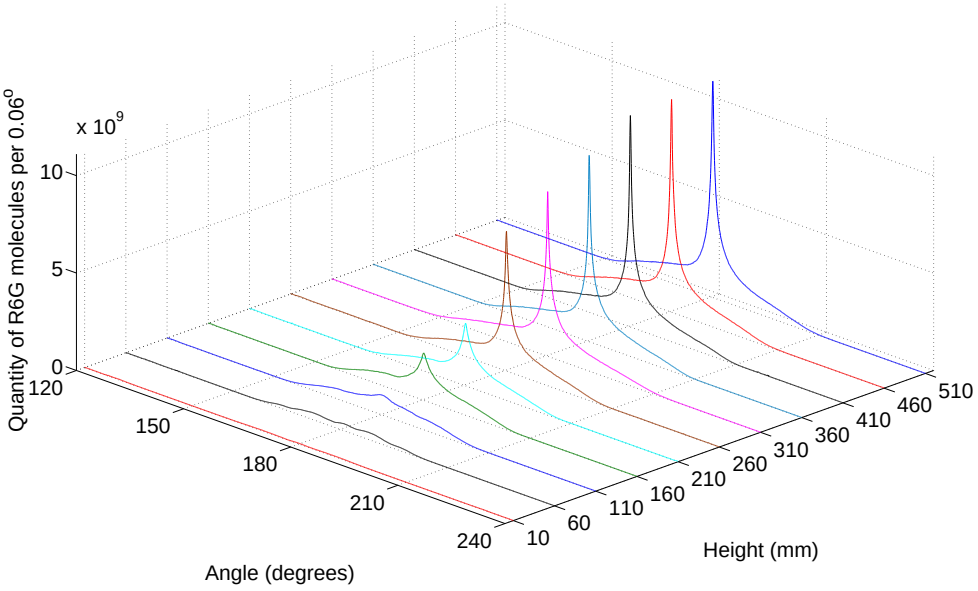

Figure D.14: Averaged surfactant distribution profiles for a Rhodamine-6G concentration of 1.00mg/l at different heights from the base of the tank. Angle measured from the front of the droplet.

Appendix E

PIV internal streamlines

The vector fields generated by the PIV analysis along with the associated streamlines for the Rhodamine-6G concentrations from 0.02mg/l to 1.00mg/l for each position in the tank are presented in Figures E.1-E.14. The aqueous phase is flowing from the top to bottom of the frame with an area of very low velocity growing at the rear of the droplet as the droplet increases in height through the tank.

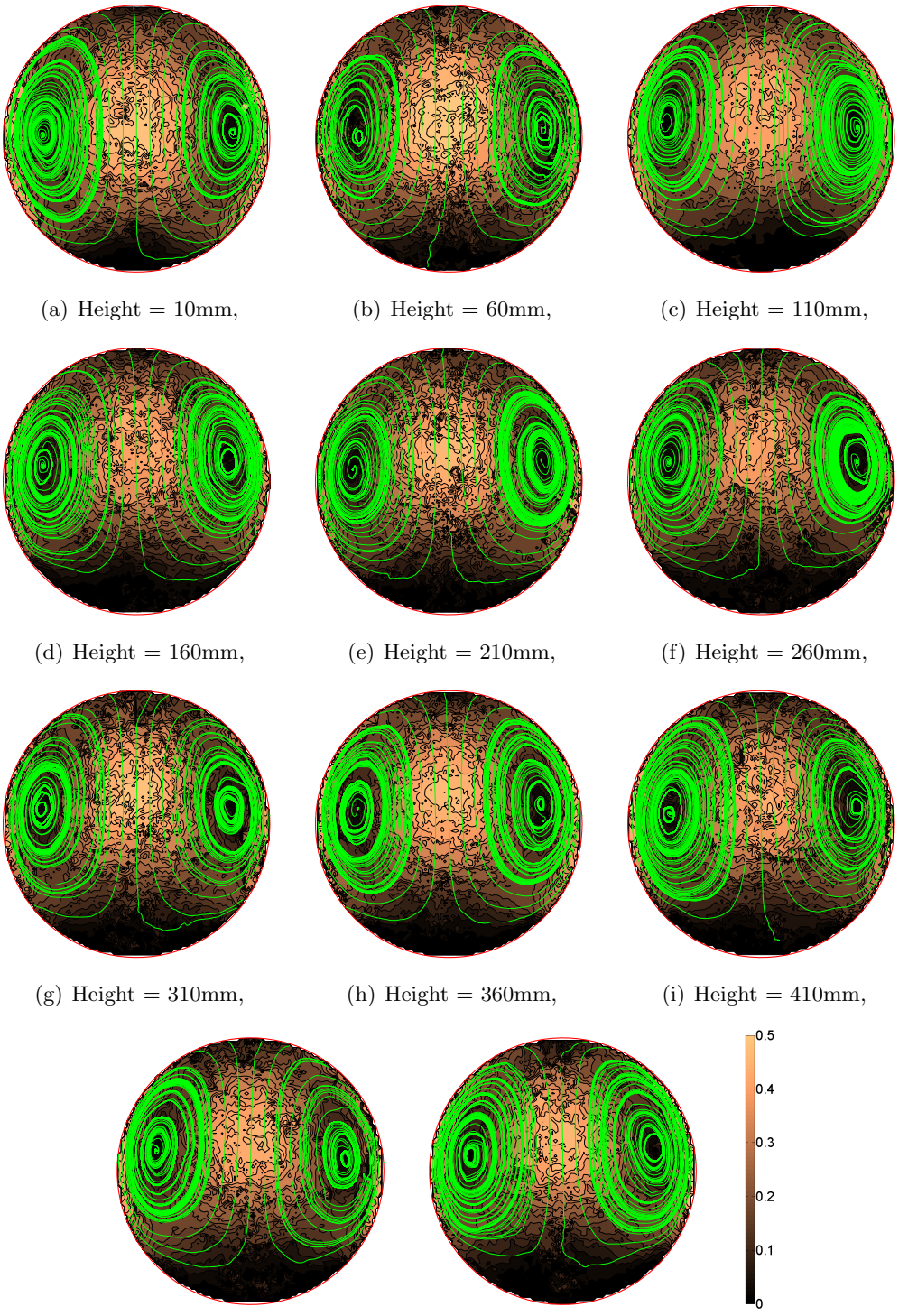

(a) Height = 10mm, (b) Height = 60mm, (c) Height = 110mm,

(d) Height = 160mm, (e) Height = 210mm, (f) Height = 260mm,

(g) Height = 310mm, (h) Height = 360mm, (i) Height = 410mm,

(j) Height = 460mm, (k) Height = 510mm.

Figure E.1: Contour plots calculated from the vector fields superimposed with the internal streamlines (green lines) of the droplet (red outline) rising through the tank at different heights for a Rhodamine-6G concentration of 0.02mg/l. Internal velocities normalised against droplet rising speed.

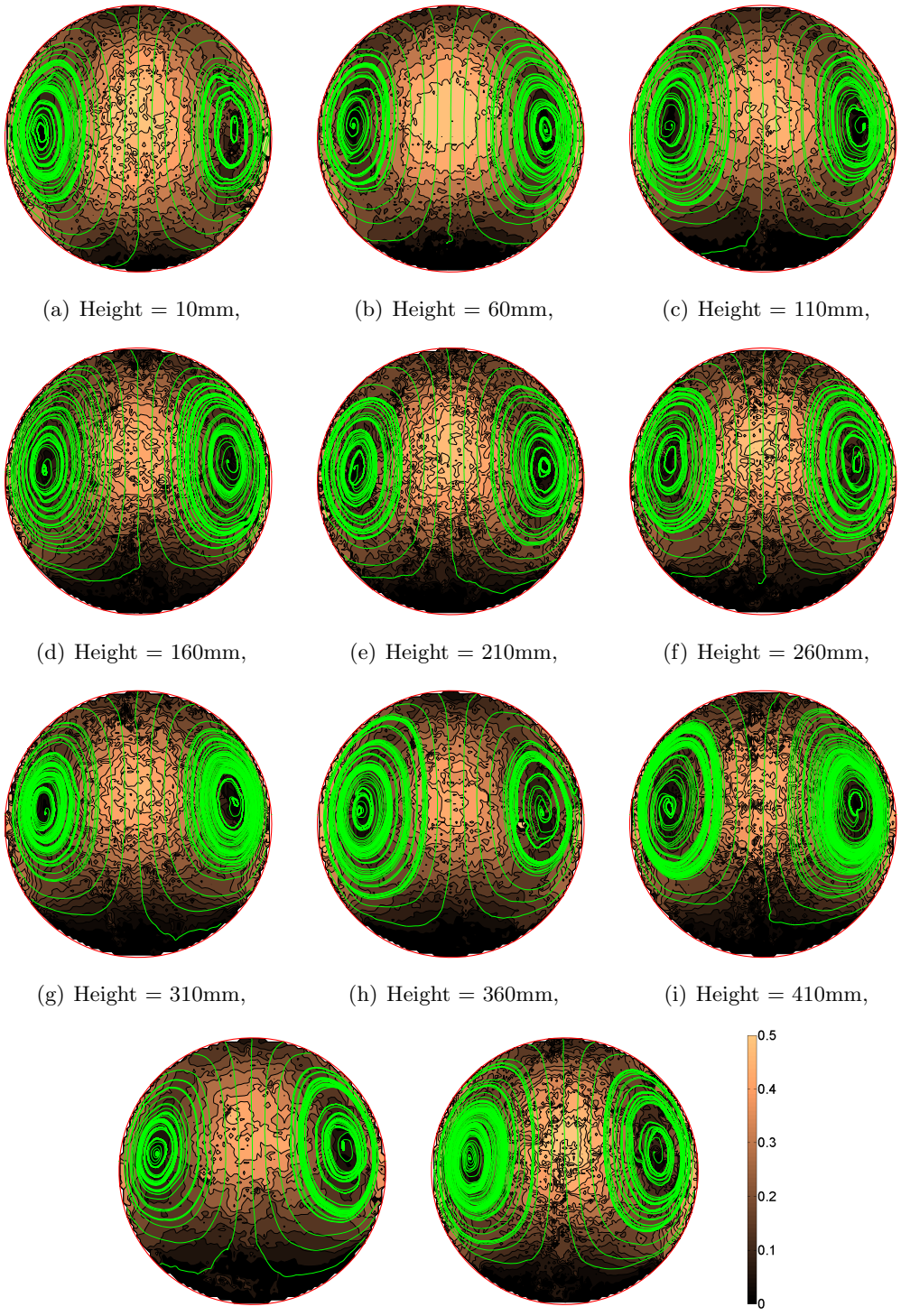

(a) Height = 10mm, (b) Height = 60mm, (c) Height = 110mm,

(d) Height = 160mm, (e) Height = 210mm, (f) Height = 260mm,

(g) Height = 310mm, (h) Height = 360mm, (i) Height = 410mm,

(j) Height = 460mm, (k) Height = 510mm.

Figure E.2: Contour plots calculated from the vector fields superimposed with the internal streamlines (green lines) of the droplet (red outline) rising through the tank at different heights for a Rhodamine-6G concentration of 0.03mg/l. Internal velocities normalised against droplet rising speed.

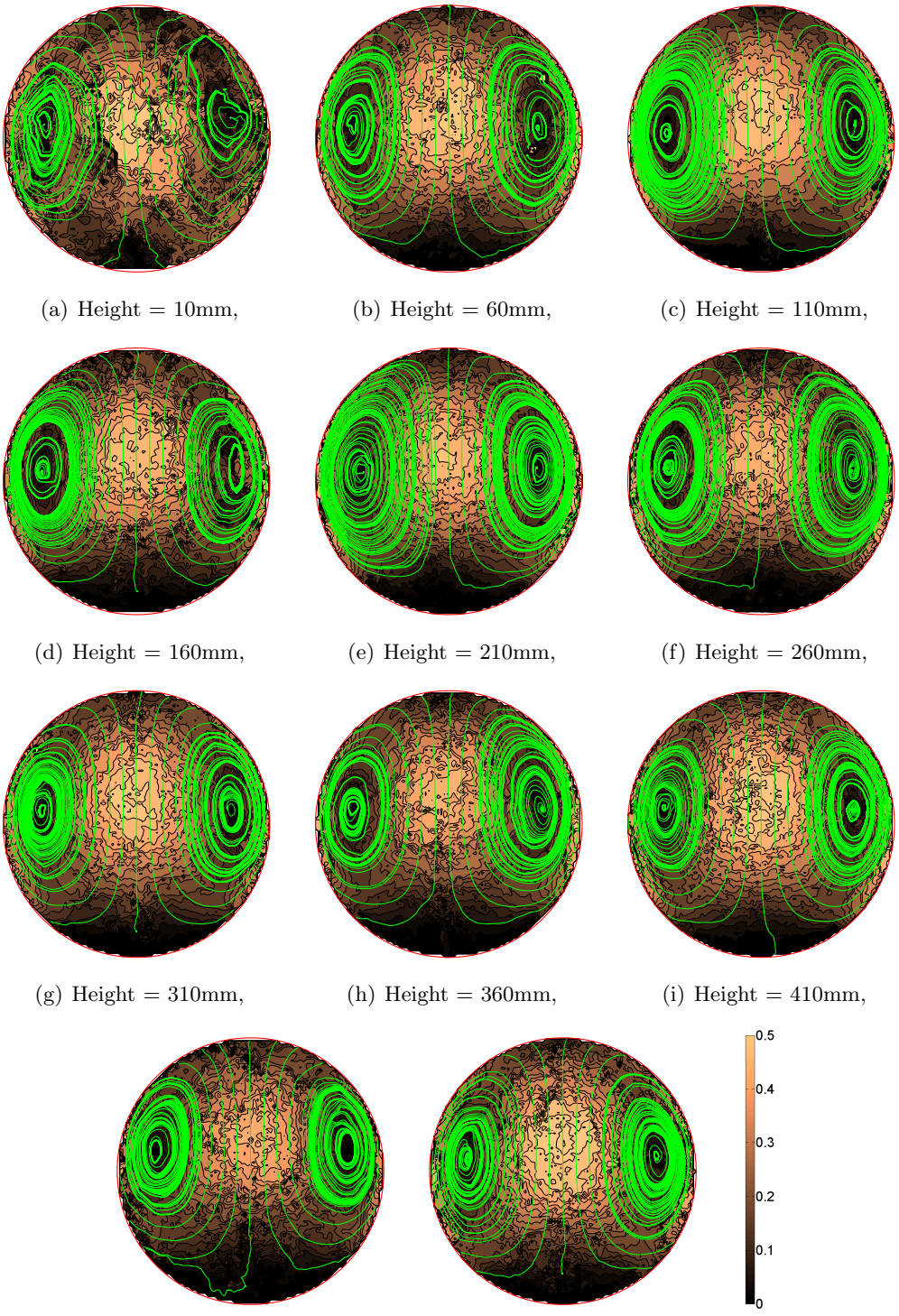

(a) Height = 10mm, (b) Height = 60mm, (c) Height = 110mm,

(d) Height = 160mm, (e) Height = 210mm, (f) Height = 260mm,

(g) Height = 310mm, (h) Height = 360mm, (i) Height = 410mm,

(j) Height = 460mm, (k) Height = 510mm.

Figure E.3: Contour plots calculated from the vector fields superimposed with the internal streamlines (green lines) of the droplet (red outline) rising through the tank at different heights for a Rhodamine-6G concentration of 0.04mg/l. Internal velocities normalised against droplet rising speed.

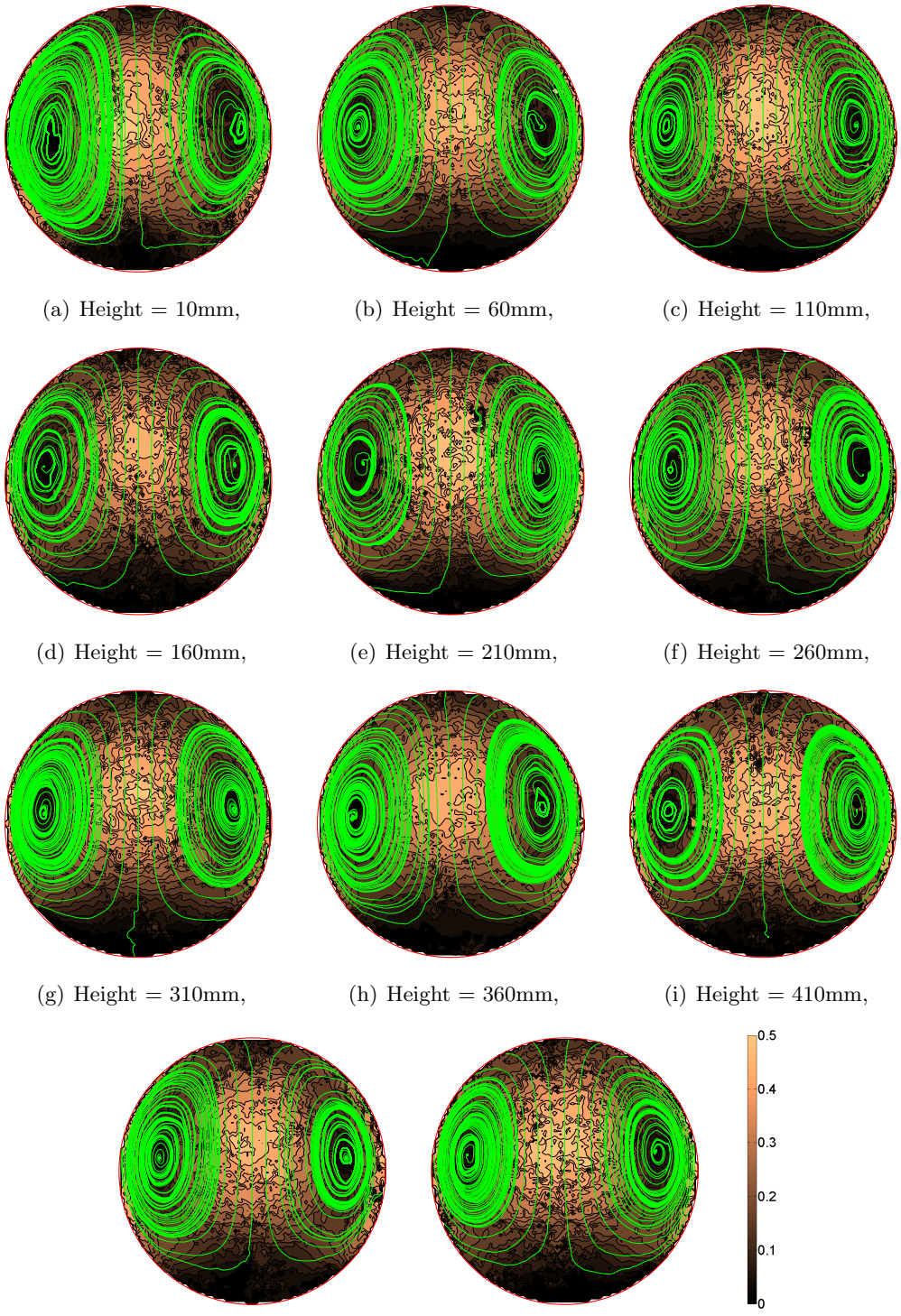

(a) Height = 10mm, (b) Height = 60mm, (c) Height = 110mm,

(d) Height = 160mm, (e) Height = 210mm, (f) Height = 260mm,

(g) Height = 310mm, (h) Height = 360mm, (i) Height = 410mm,

(j) Height = 460mm, (k) Height = 510mm.

Figure E.4: Contour plots calculated from the vector fields superimposed with the internal streamlines (green lines) of the droplet (red outline) rising through the tank at different heights for a Rhodamine-6G concentration of 0.05mg/l. Internal velocities normalised against droplet rising speed.

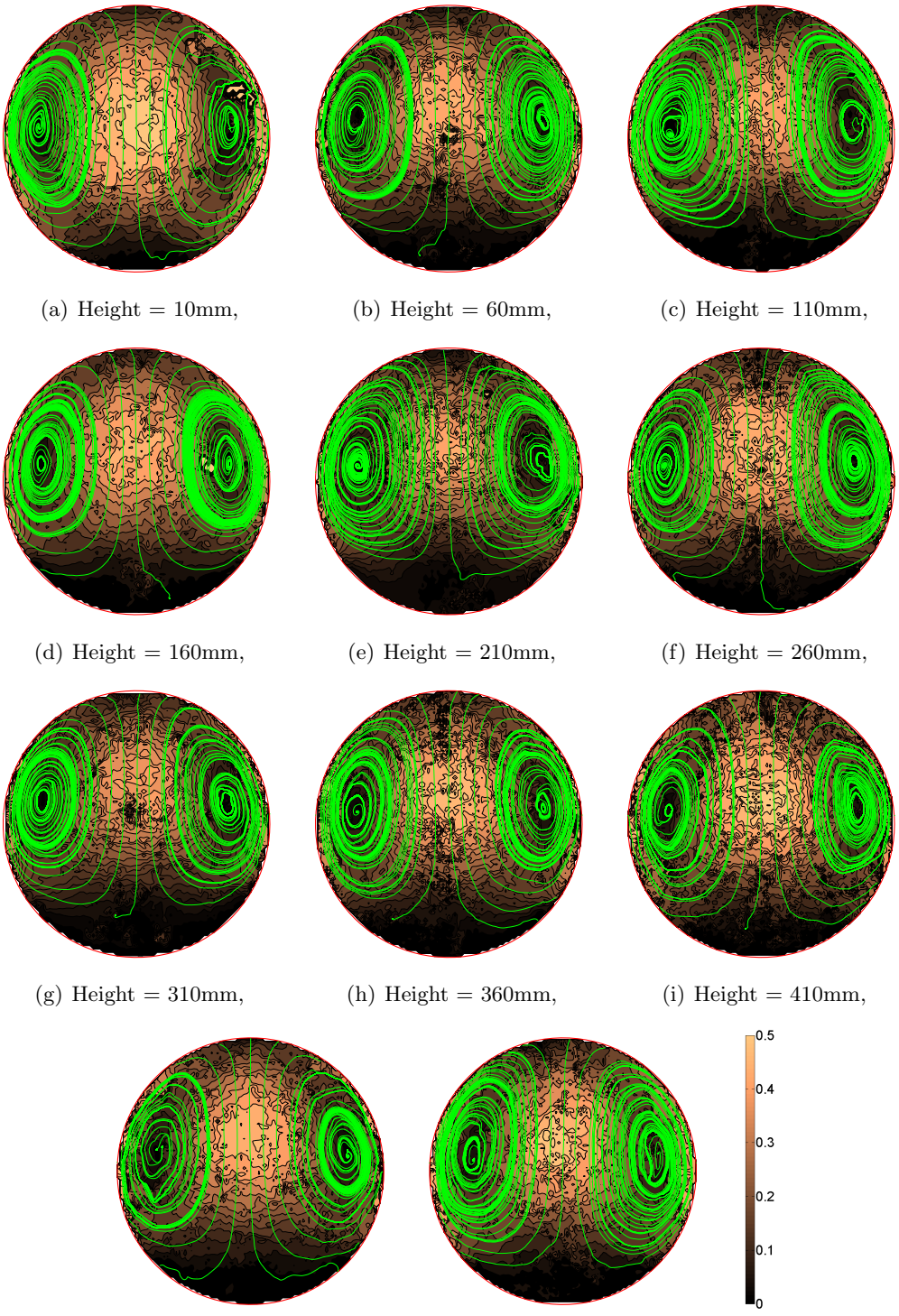

(a) Height = 10mm, (b) Height = 60mm, (c) Height = 110mm,

(d) Height = 160mm, (e) Height = 210mm, (f) Height = 260mm,

(g) Height = 310mm, (h) Height = 360mm, (i) Height = 410mm,

(j) Height = 460mm, (k) Height = 510mm.

Figure E.5: Contour plots calculated from the vector fields superimposed with the internal streamlines (green lines) of the droplet (red outline) rising through the tank at different heights for a Rhodamine-6G concentration of 0.06mg/l. Internal velocities normalised against droplet rising speed.

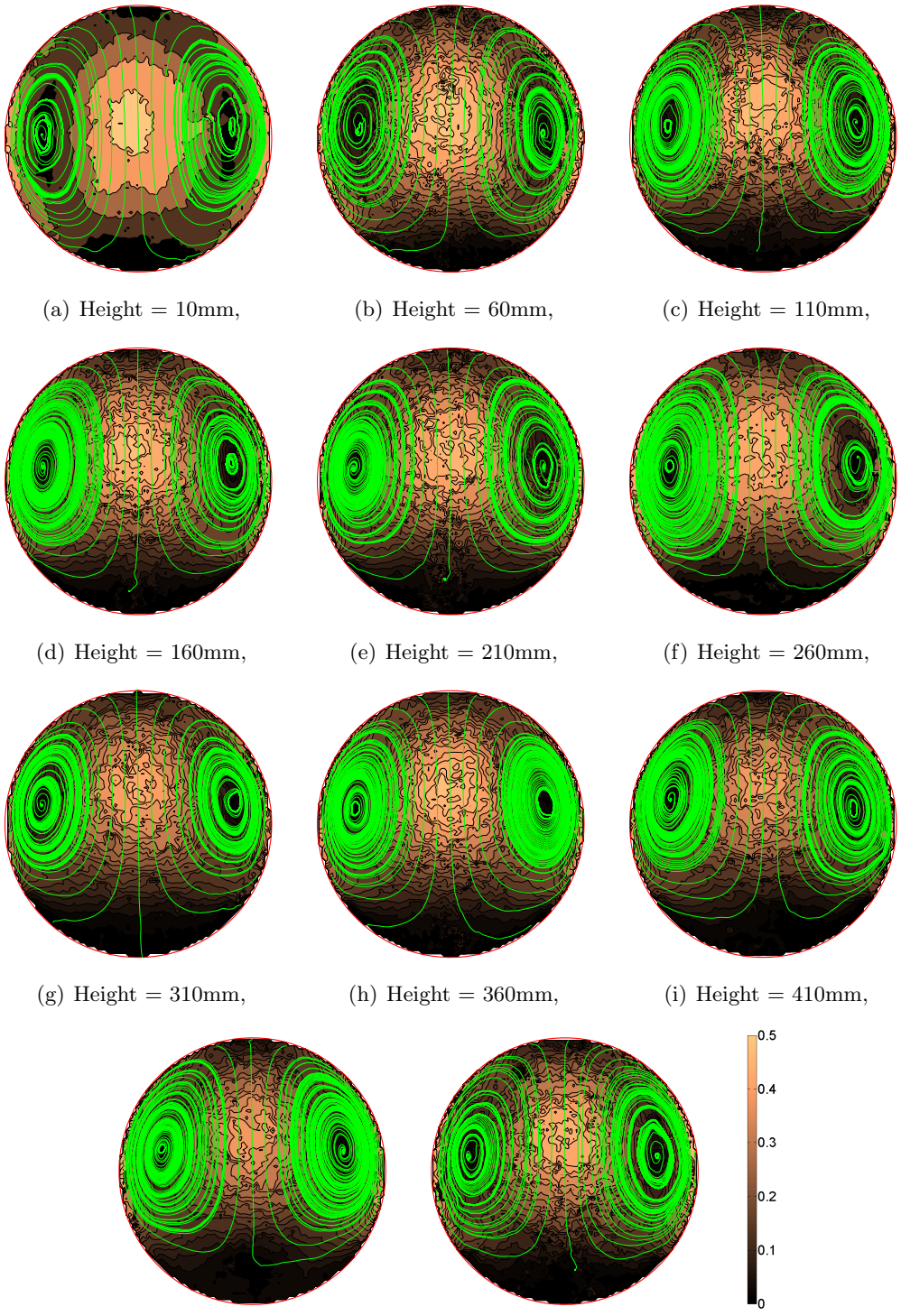

(a) Height = 10mm, (b) Height = 60mm, (c) Height = 110mm,

(d) Height = 160mm, (e) Height = 210mm, (f) Height = 260mm,

(g) Height = 310mm, (h) Height = 360mm, (i) Height = 410mm,

(j) Height = 460mm, (k) Height = 510mm.

Figure E.6: Contour plots calculated from the vector fields superimposed with the internal streamlines (green lines) of the droplet (red outline) rising through the tank at different heights for a Rhodamine-6G concentration of 0.08mg/l. Internal velocities normalised against droplet rising speed.

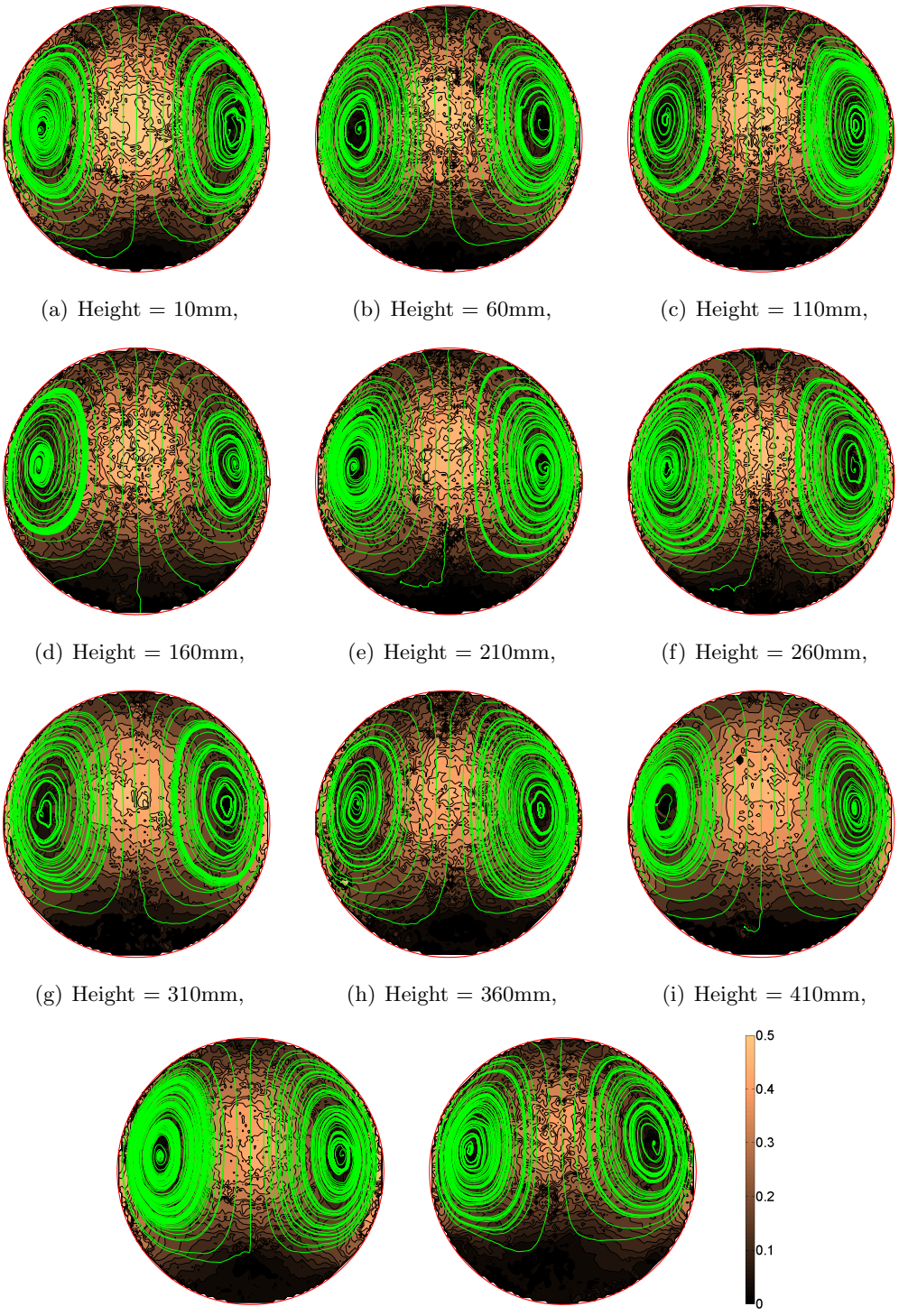

(a) Height = 10mm, (b) Height = 60mm, (c) Height = 110mm,

(d) Height = 160mm, (e) Height = 210mm, (f) Height = 260mm,

(g) Height = 310mm, (h) Height = 360mm, (i) Height = 410mm,

(j) Height = 460mm, (k) Height = 510mm.

Figure E.7: Contour plots calculated from the vector fields superimposed with the internal streamlines (green lines) of the droplet (red outline) rising through the tank at different heights for a Rhodamine-6G concentration of 0.10mg/l. Internal velocities normalised against droplet rising speed.

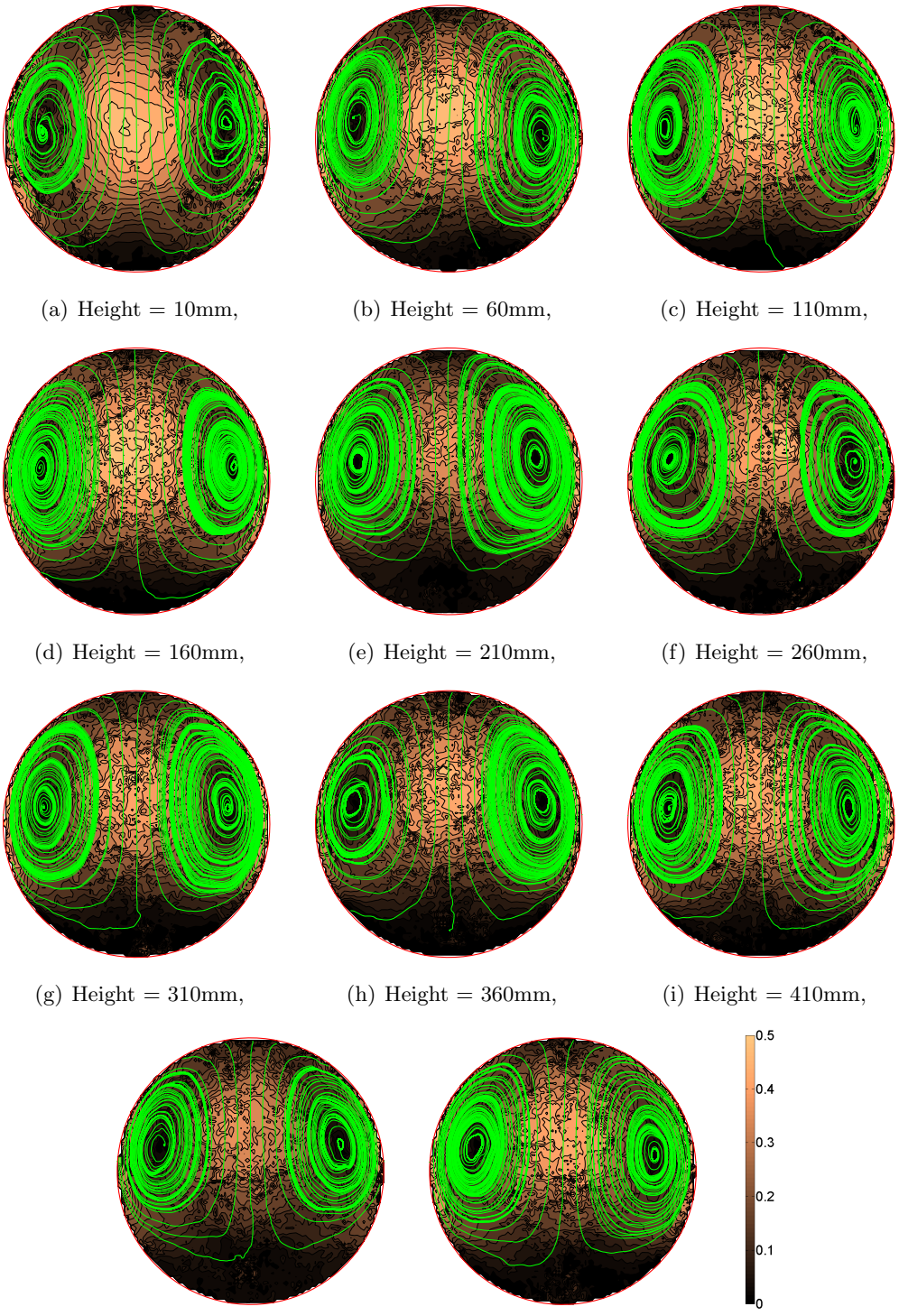

(a) Height = 10mm, (b) Height = 60mm, (c) Height = 110mm,

(d) Height = 160mm, (e) Height = 210mm, (f) Height = 260mm,

(g) Height = 310mm, (h) Height = 360mm, (i) Height = 410mm,

(j) Height = 460mm, (k) Height = 510mm.

Figure E.8: Contour plots calculated from the vector fields superimposed with the internal streamlines (green lines) of the droplet (red outline) rising through the tank at different heights for a Rhodamine-6G concentration of 0.20mg/l. Internal velocities normalised against droplet rising speed.

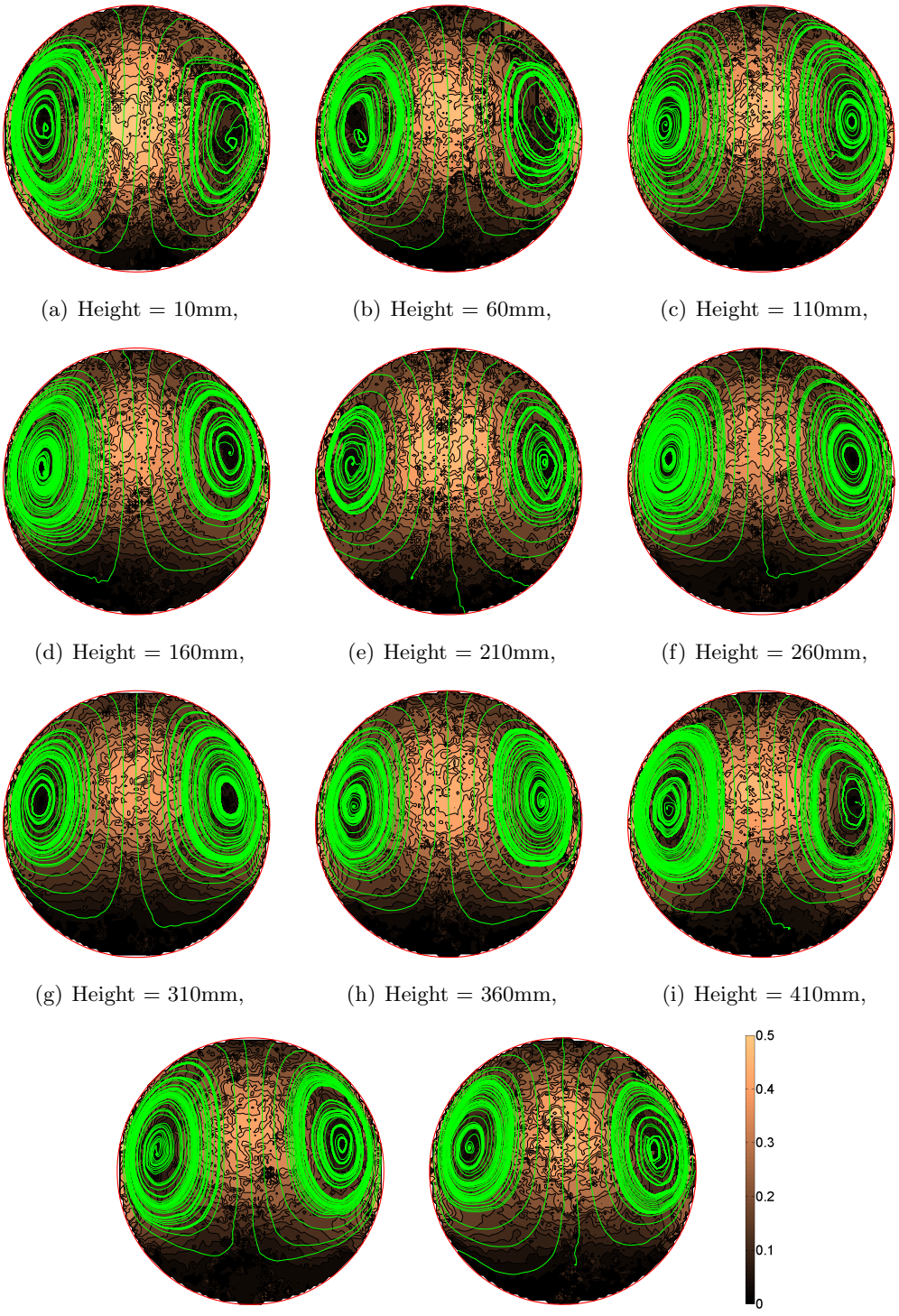

(a) Height = 10mm, (b) Height = 60mm, (c) Height = 110mm,

(d) Height = 160mm, (e) Height = 210mm, (f) Height = 260mm,

(g) Height = 310mm, (h) Height = 360mm, (i) Height = 410mm,

(j) Height = 460mm, (k) Height = 510mm.

Figure E.9: Contour plots calculated from the vector fields superimposed with the internal streamlines (green lines) of the droplet (red outline) rising through the tank at different heights for a Rhodamine-6G concentration of 0.30mg/l. Internal velocities normalised against droplet rising speed.

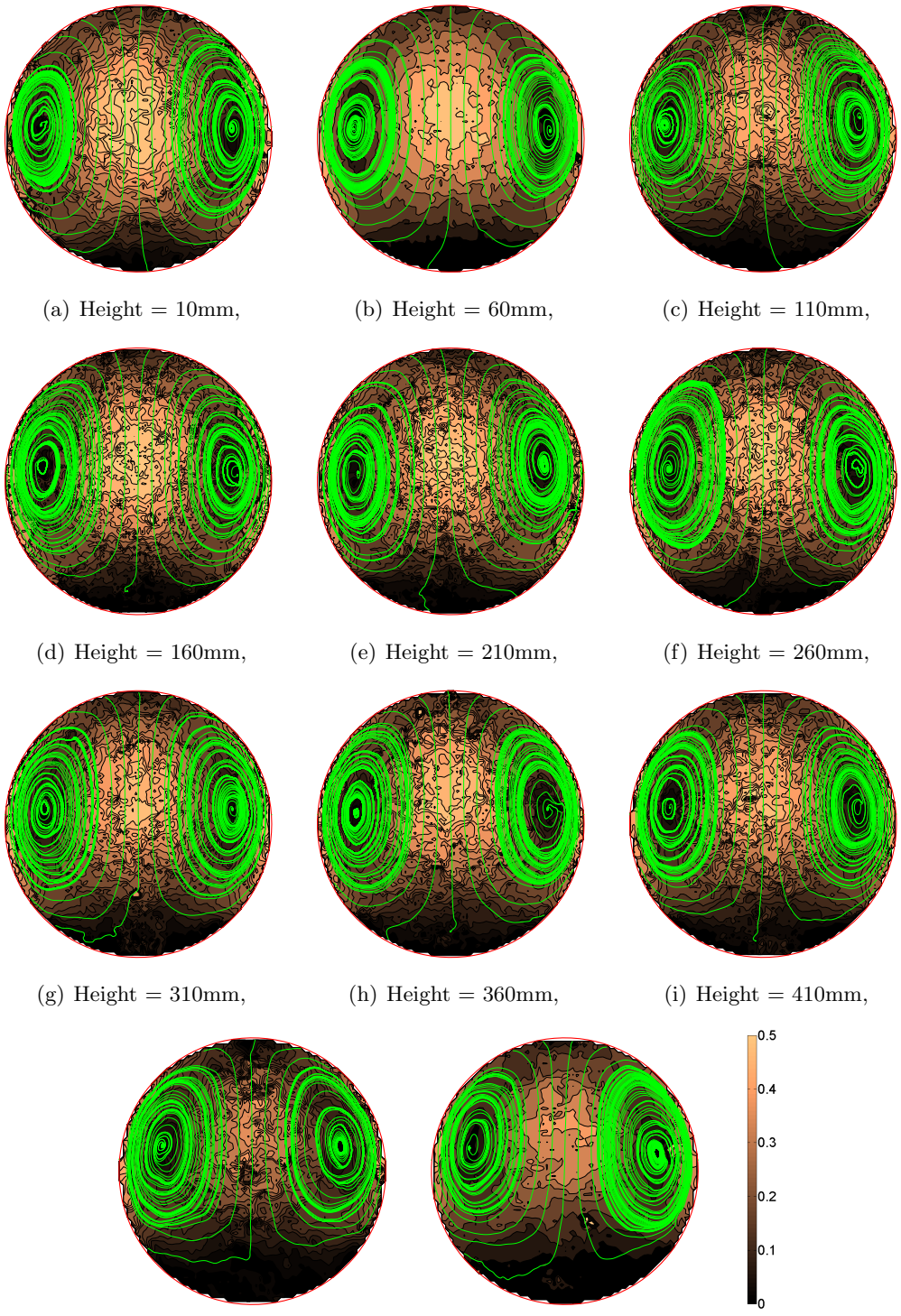

(a) Height = 10mm, (b) Height = 60mm, (c) Height = 110mm,

(d) Height = 160mm, (e) Height = 210mm, (f) Height = 260mm,

(g) Height = 310mm, (h) Height = 360mm, (i) Height = 410mm,

(j) Height = 460mm, (k) Height = 510mm.

Figure E.10: Contour plots calculated from the vector fields superimposed with the internal streamlines (green lines) of the droplet (red outline) rising through the tank at different heights for a Rhodamine-6G concentration of 0.40mg/l. Internal velocities normalised against droplet rising speed.

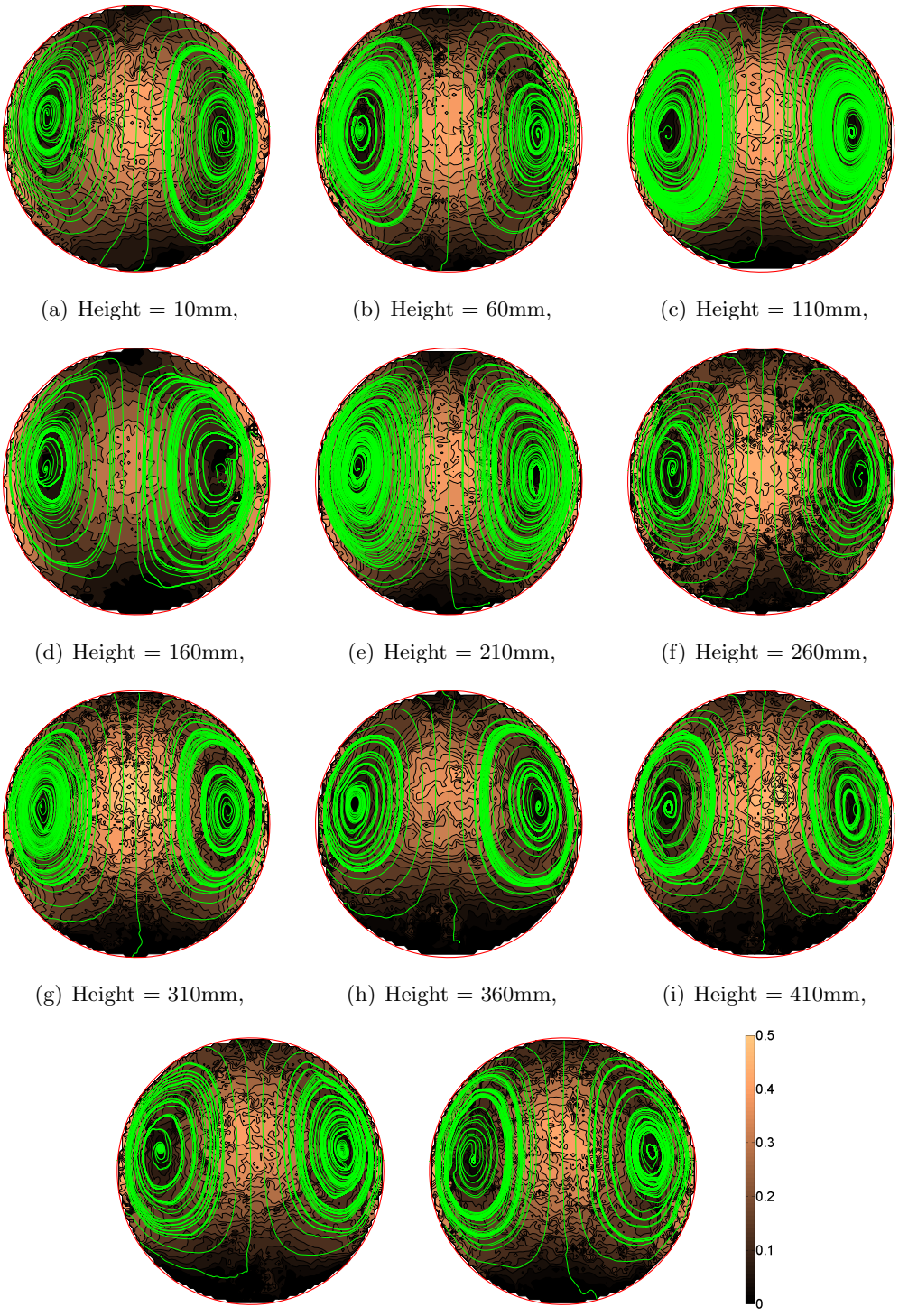

(a) Height = 10mm, (b) Height = 60mm, (c) Height = 110mm,

(d) Height = 160mm, (e) Height = 210mm, (f) Height = 260mm,

(g) Height = 310mm, (h) Height = 360mm, (i) Height = 410mm,

(j) Height = 460mm, (k) Height = 510mm.

Figure E.11: Contour plots calculated from the vector fields superimposed with the internal streamlines (green lines) of the droplet (red outline) rising through the tank at different heights for a Rhodamine-6G concentration of 0.50mg/l. Internal velocities normalised against droplet rising speed.

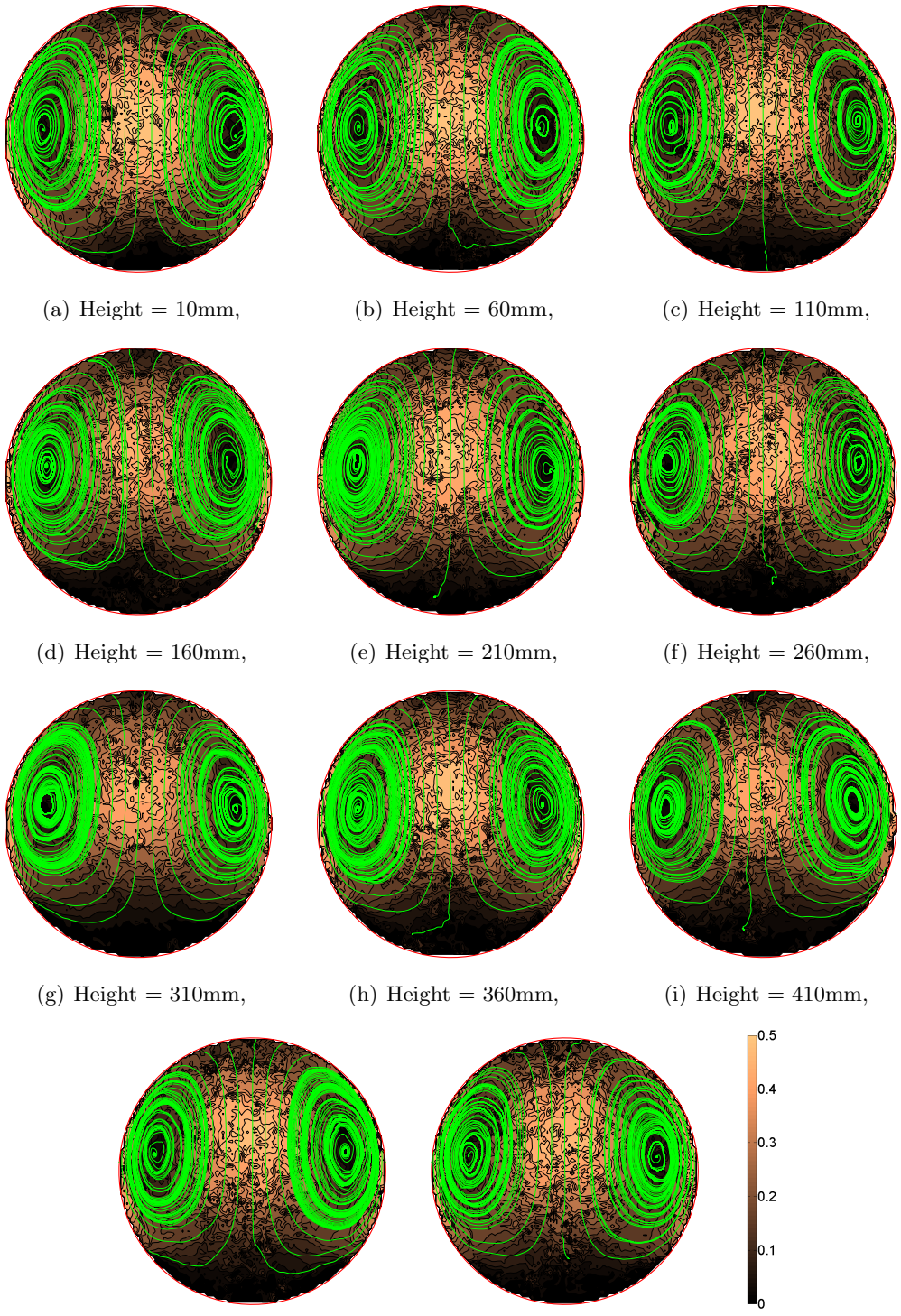

(a) Height = 10mm, (b) Height = 60mm, (c) Height = 110mm,

(d) Height = 160mm, (e) Height = 210mm, (f) Height = 260mm,

(g) Height = 310mm, (h) Height = 360mm, (i) Height = 410mm,

(j) Height = 460mm, (k) Height = 510mm.

Figure E.12: Contour plots calculated from the vector fields superimposed with the internal streamlines (green lines) of the droplet (red outline) rising through the tank at different heights for a Rhodamine-6G concentration of 0.60mg/l. Internal velocities normalised against droplet rising speed.

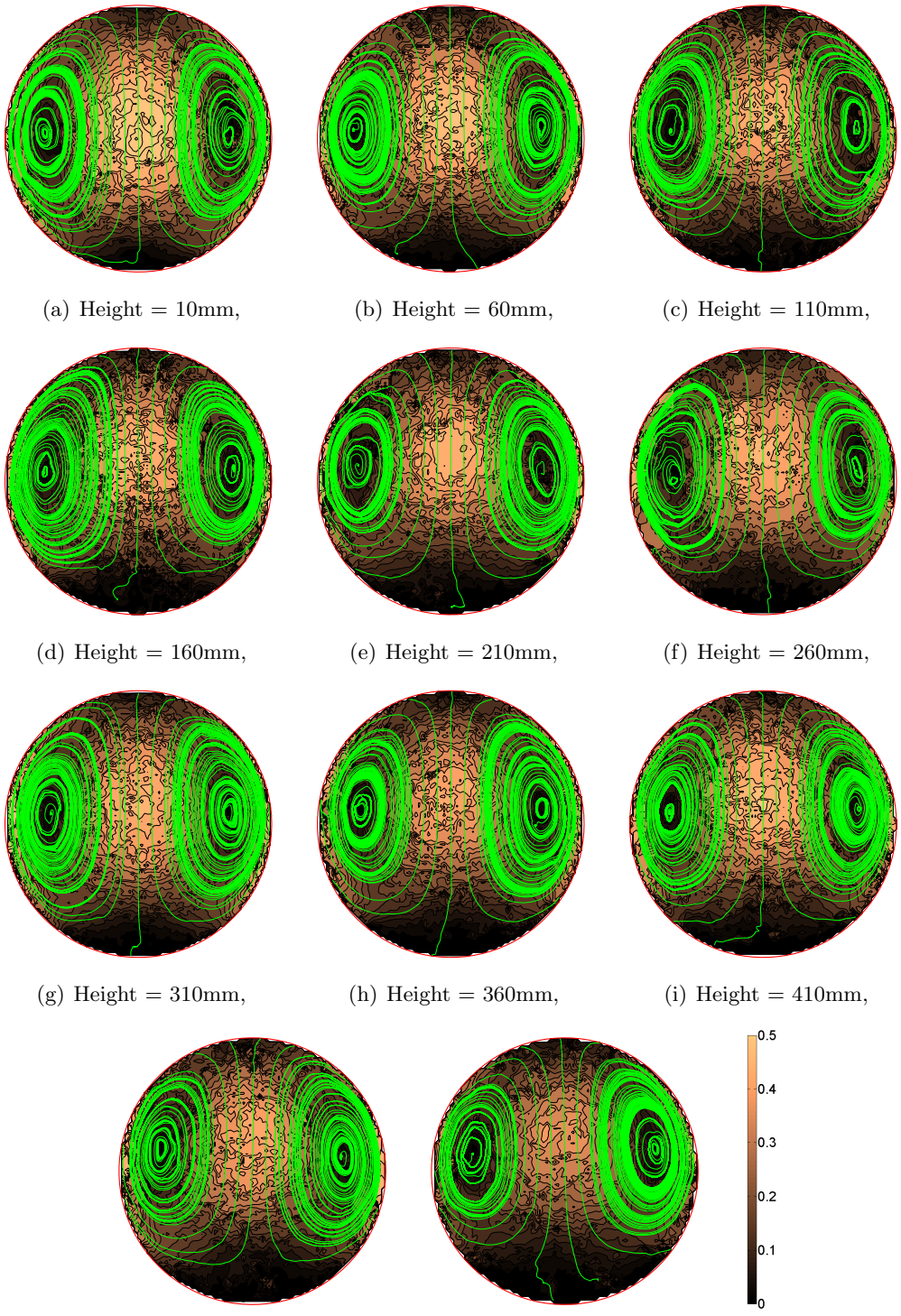

(a) Height = 10mm, (b) Height = 60mm, (c) Height = 110mm,

(d) Height = 160mm, (e) Height = 210mm, (f) Height = 260mm,

(g) Height = 310mm, (h) Height = 360mm, (i) Height = 410mm,

(j) Height = 460mm, (k) Height = 510mm.

Figure E.13: Contour plots calculated from the vector fields superimposed with the internal streamlines (green lines) of the droplet (red outline) rising through the tank at different heights for a Rhodamine-6G concentration of 0.80mg/l. Internal velocities normalised against droplet rising speed.

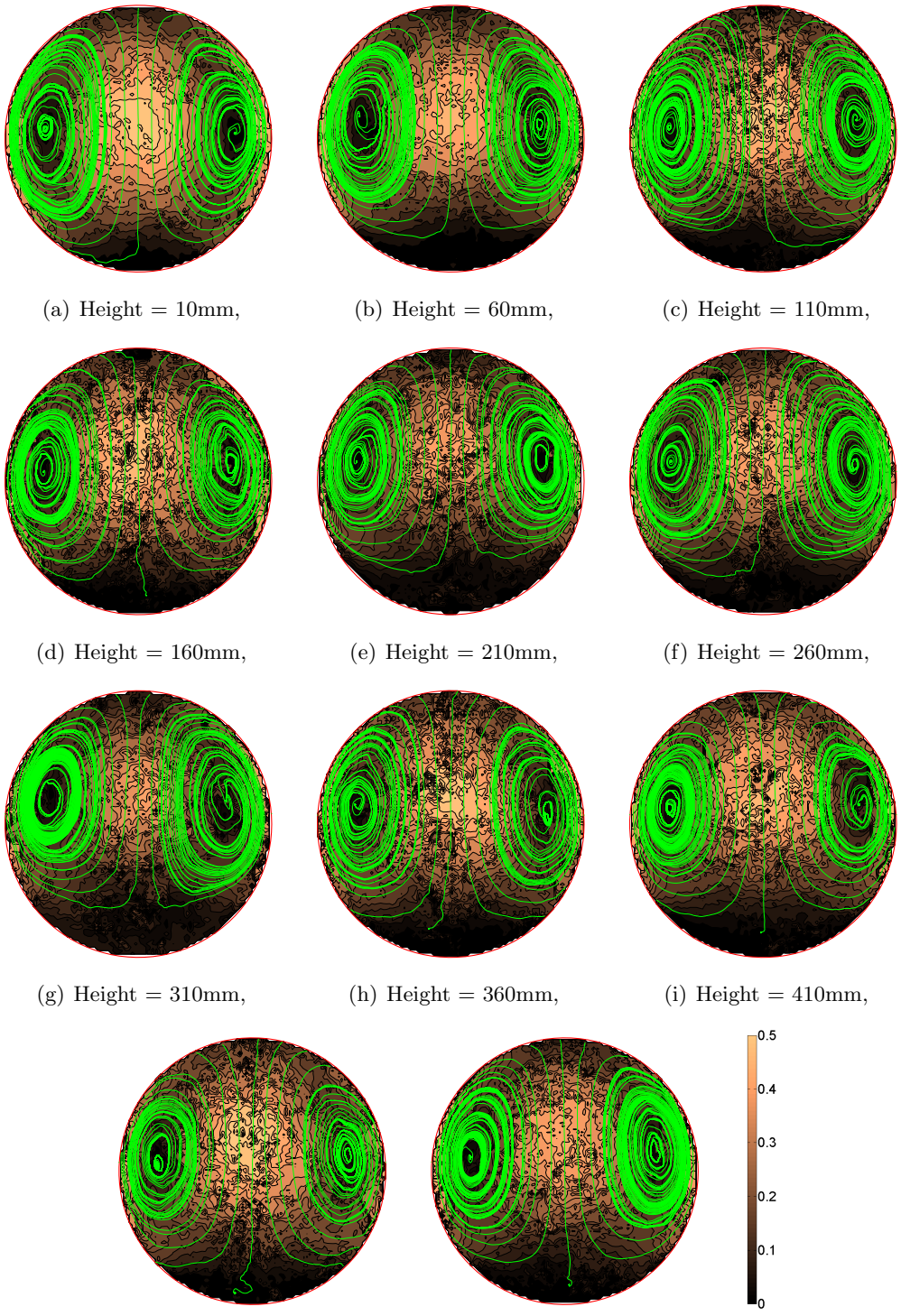

(a) Height = 10mm, (b) Height = 60mm, (c) Height = 110mm,

(d) Height = 160mm, (e) Height = 210mm, (f) Height = 260mm,

(g) Height = 310mm, (h) Height = 360mm, (i) Height = 410mm,

(j) Height = 460mm, (k) Height = 510mm.

Figure E.14: Contour plots calculated from the vector fields superimposed with the internal streamlines (green lines) of the droplet (red outline) rising through the tank at different heights for a Rhodamine-6G concentration of 1.00mg/l. Internal velocities normalised against droplet rising speed.

Appendix F

PIV stagnant cap angles

The stagnant cap angles calculated from the PIV data are presented for Rhodamine-6G concentrations of 0.02mg/l to 1.00mg/l. Each concentration shows each of the droplets for each height with the droplets divided into bands based on radius size in increments of 0.25mm. Despite the results for different sized droplets overlapping the general trend shows that larger droplets obtain a smaller surfactant cap angle.

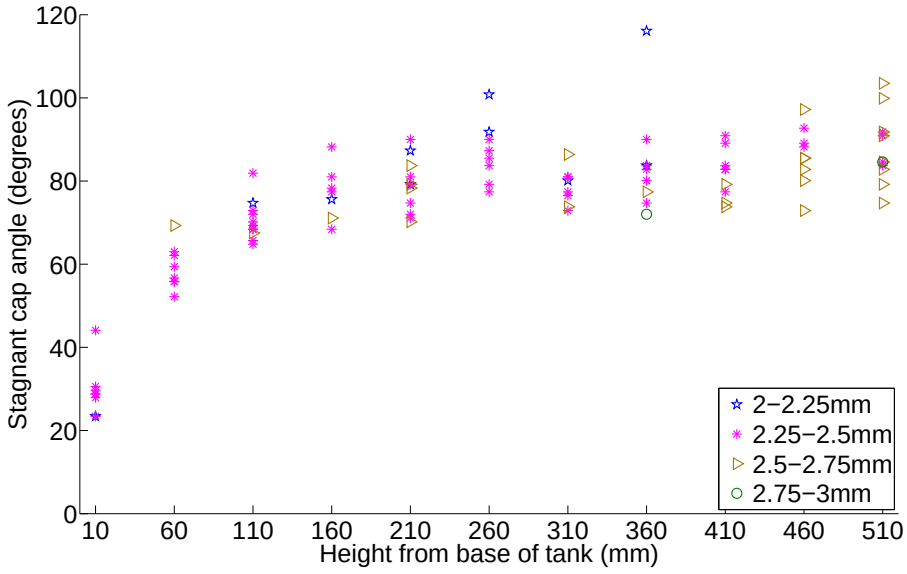

Figure F.1: Development of the stagnant cap angle over the height of the tank for different droplet radii. Rhodamine-6G concentration of 0.02mg/l.

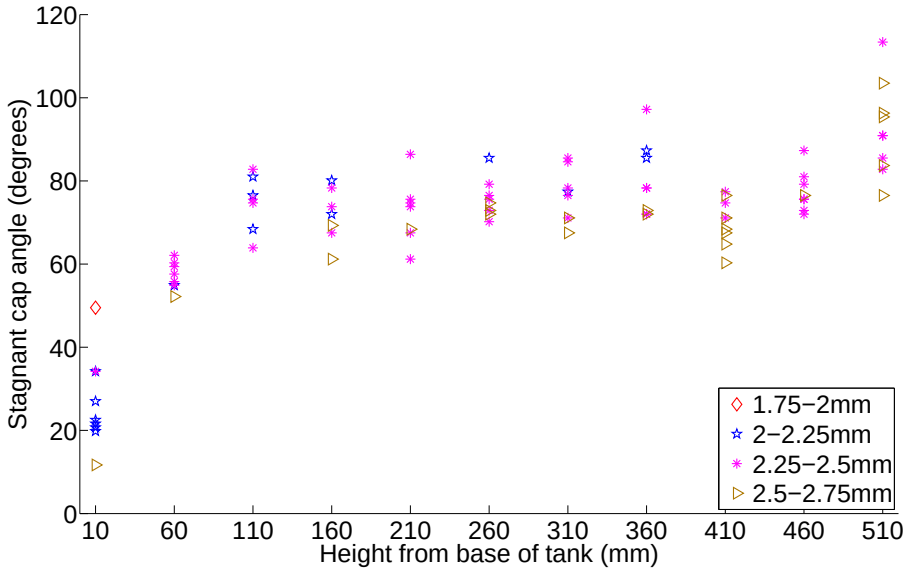

Figure F.2: Development of the stagnant cap angle over the height of the tank for different droplet radii. Rhodamine-6G concentration of 0.03mg/l.

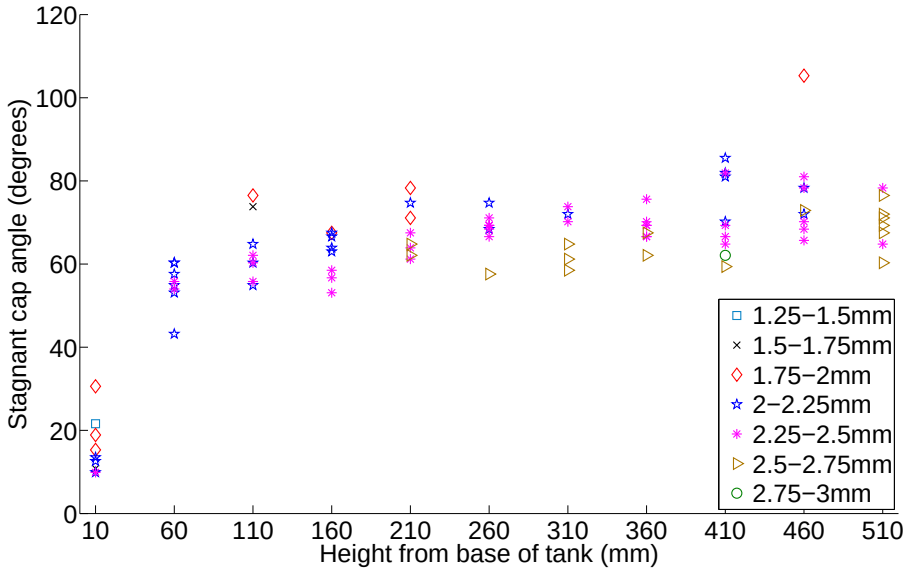

Figure F.3: Development of the stagnant cap angle over the height of the tank for different droplet radii. Rhodamine-6G concentration of 0.04mg/l.

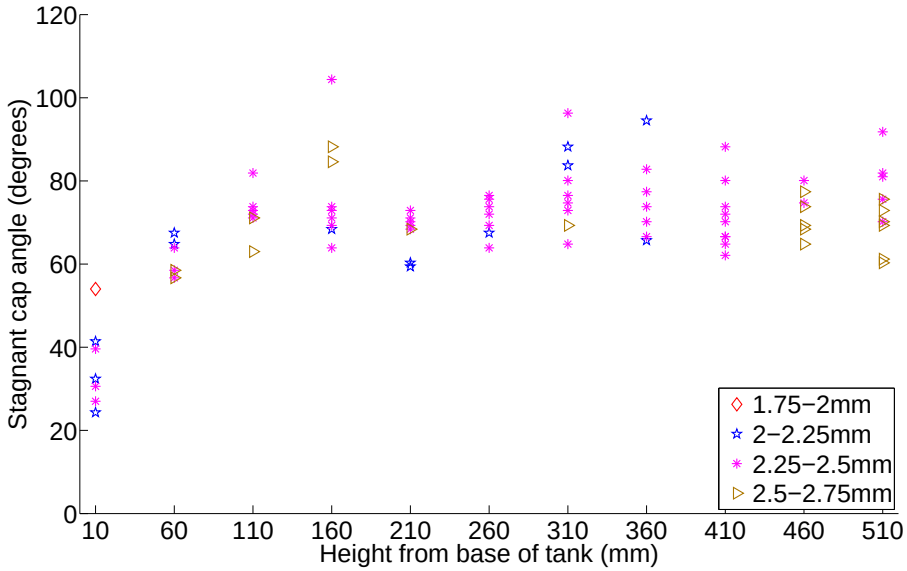

Figure F.4: Development of the stagnant cap angle over the height of the tank for different droplet radii. Rhodamine-6G concentration of 0.05mg/l.

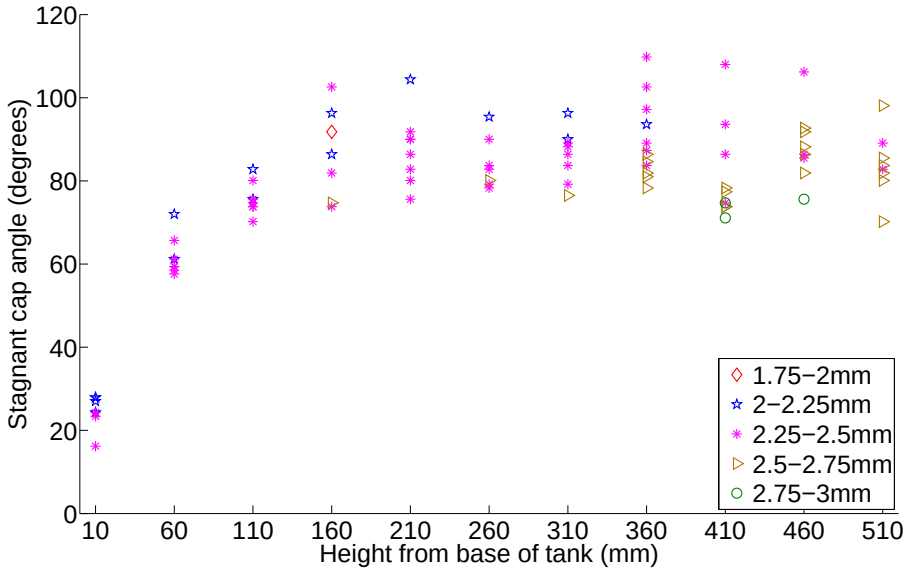

Figure F.5: Development of the stagnant cap angle over the height of the tank for different droplet radii. Rhodamine-6G concentration of 0.06mg/l.

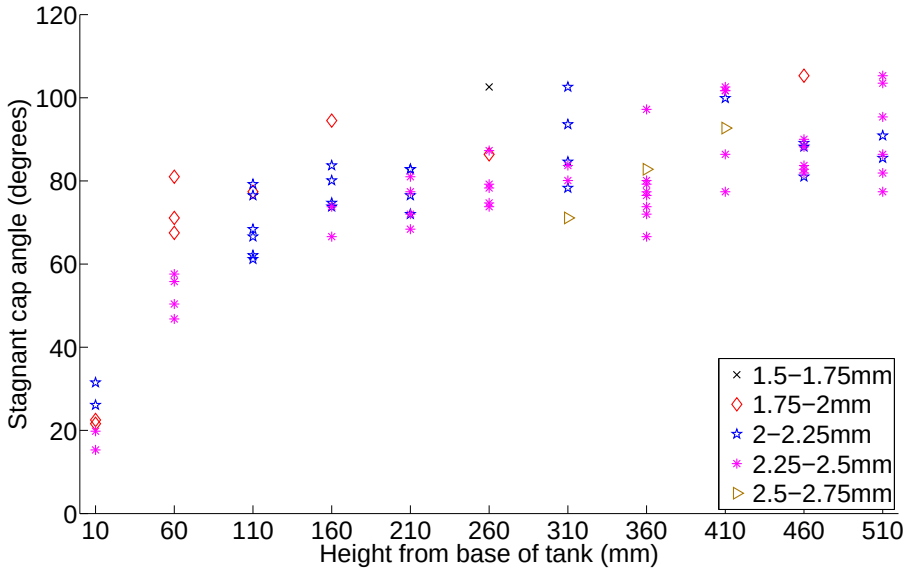

Figure F.6: Development of the stagnant cap angle over the height of the tank for different droplet radii. Rhodamine-6G concentration of 0.08mg/l.

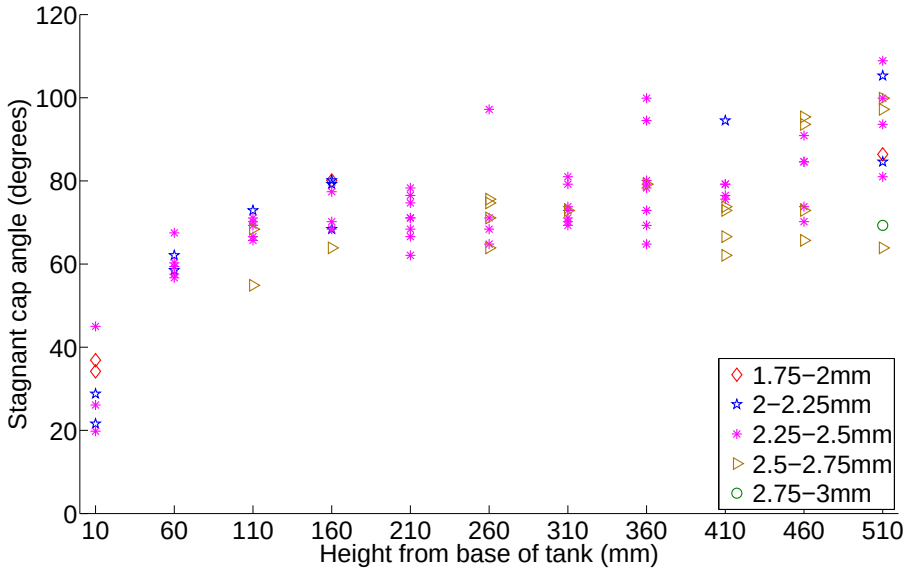

Figure F.7: Development of the stagnant cap angle over the height of the tank for different droplet radii. Rhodamine-6G concentration of 0.10mg/l.

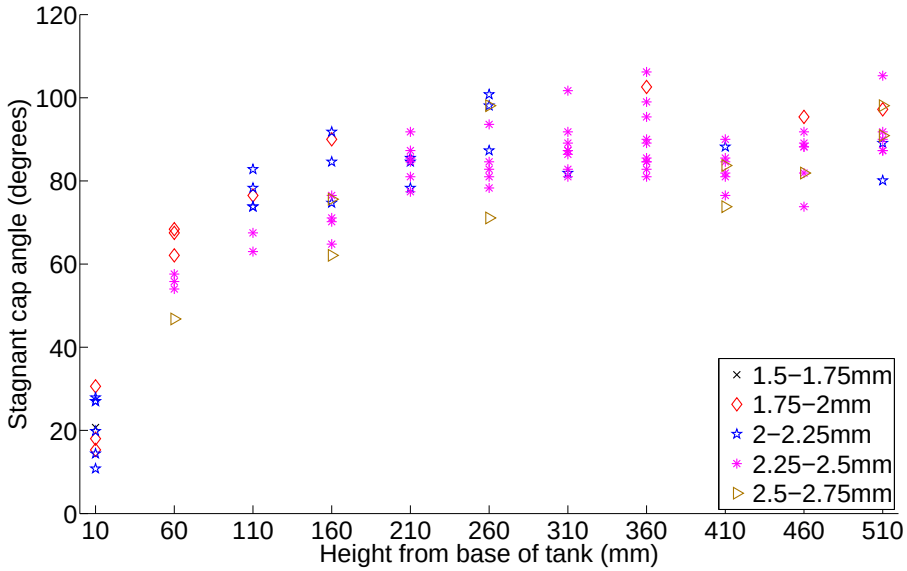

Figure F.8: Development of the stagnant cap angle over the height of the tank for different droplet radii. Rhodamine-6G concentration of 0.20mg/l.

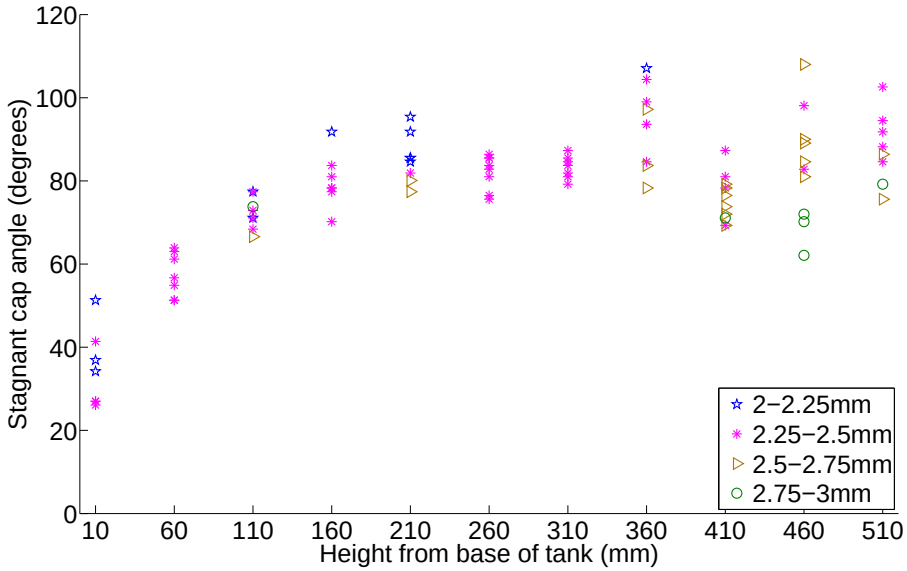

Figure F.9: Development of the stagnant cap angle over the height of the tank for different droplet radii. Rhodamine-6G concentration of 0.30mg/l.

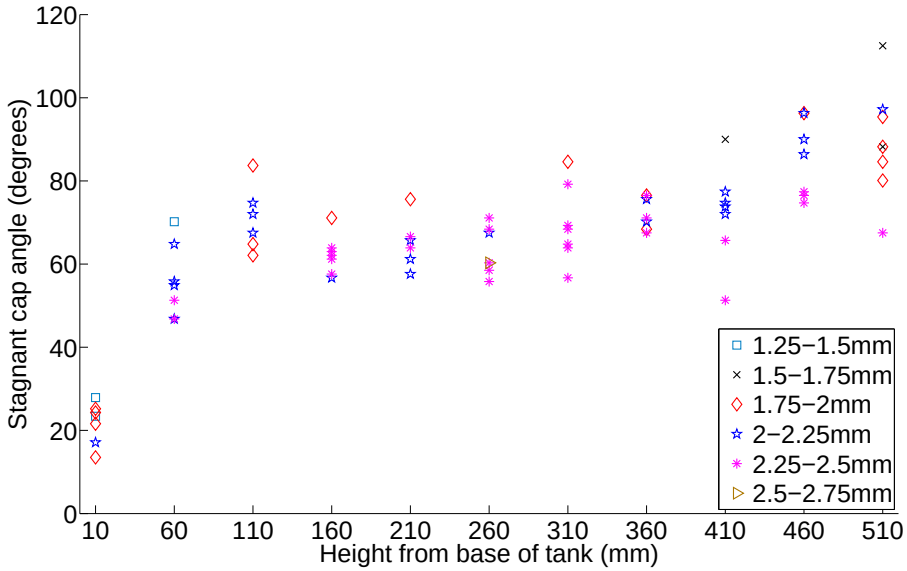

Figure F.10: Development of the stagnant cap angle over the height of the tank for different droplet radii. Rhodamine-6G concentration of 0.40mg/l.

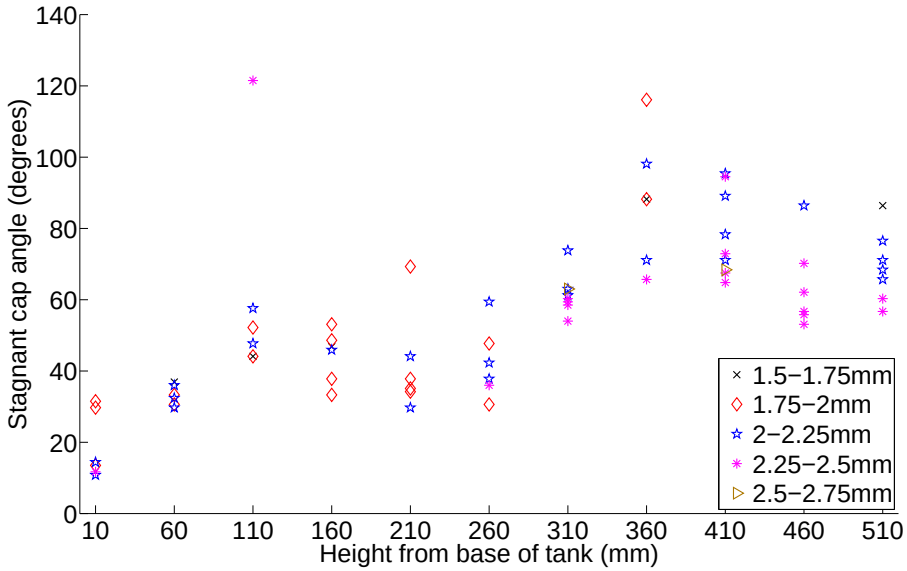

Figure F.11: Development of the stagnant cap angle over the height of the tank for different droplet radii. Rhodamine-6G concentration of 0.50mg/l.

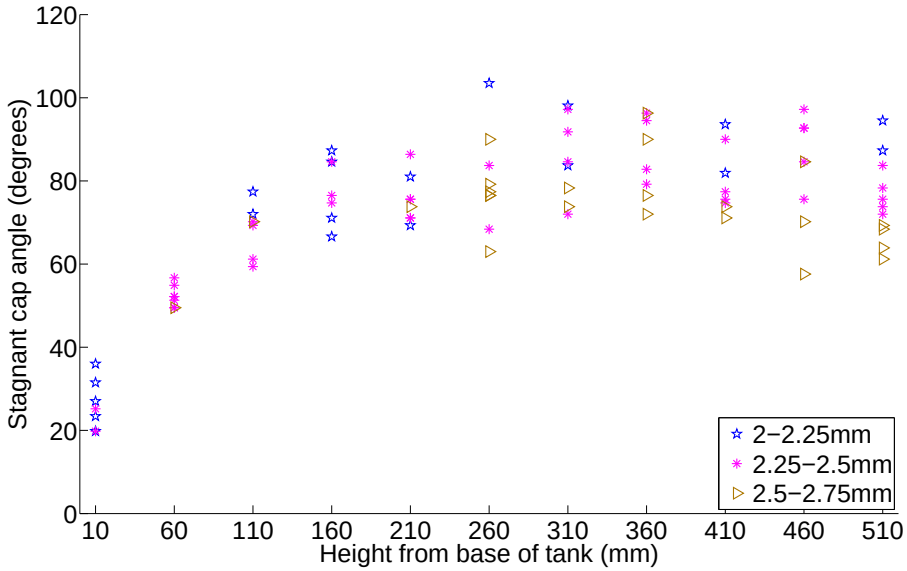

Figure F.12: Development of the stagnant cap angle over the height of the tank for different droplet radii. Rhodamine-6G concentration of 0.60mg/l.

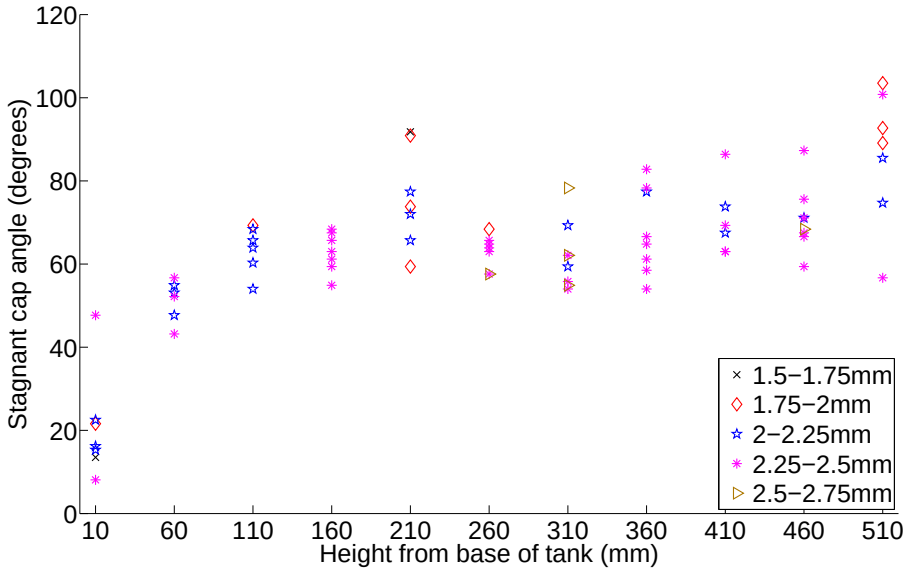

Figure F.13: Development of the stagnant cap angle over the height of the tank for different droplet radii. Rhodamine-6G concentration of 0.80mg/l.

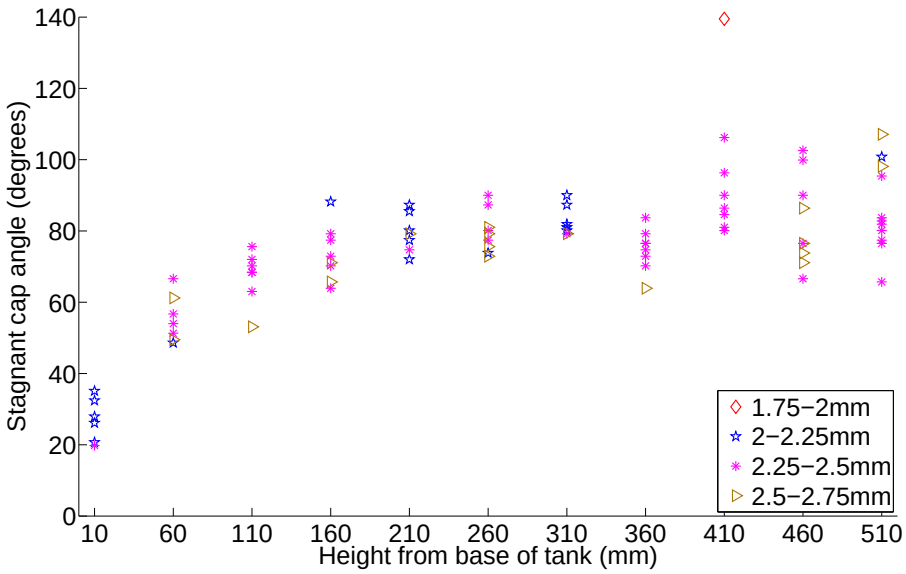

Figure F.14: Development of the stagnant cap angle over the height of the tank for different droplet radii. Rhodamine-6G concentration of 1.00mg/l.

Appendix G

PIV averaged tangential velocity profiles

The averaged tangential velocity profiles around the droplet calculated from the PIV data are presented here for Rhodamine-6G concentrations from 0.02mg/l to 1.00mg/l. Each of the concentrations shows the tangential velocity profile for each height in the tank and shows a large area of low velocity at the rear of the droplet relating to the stagnant cap angle. Each concentration shows an initial large increase in the stagnant cap angle before achieving approximately the same angle over the upper end of the tank.

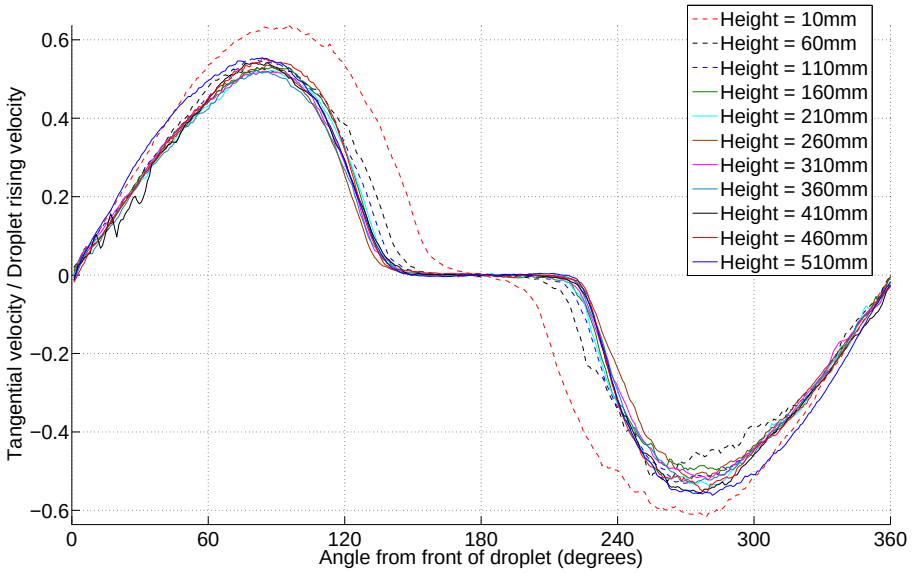

Figure G.1: Averaged tangential velocity profiles around a droplet for a Rhodamine-6G concentration of 0.02mg/l at different heights from the base of the tank.

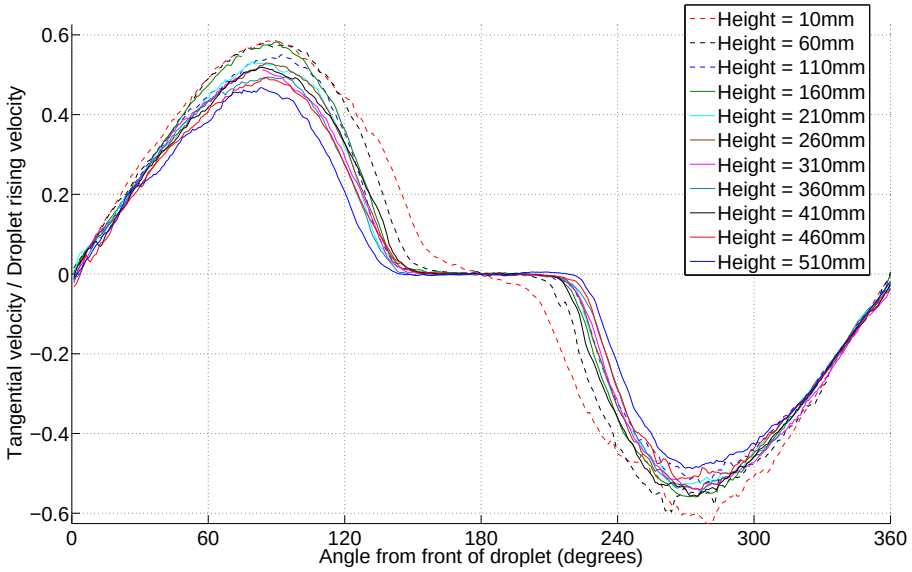

Figure G.2: Averaged tangential velocity profiles around a droplet for a Rhodamine-6G concentration of 0.03mg/l at different heights from the base of the tank.

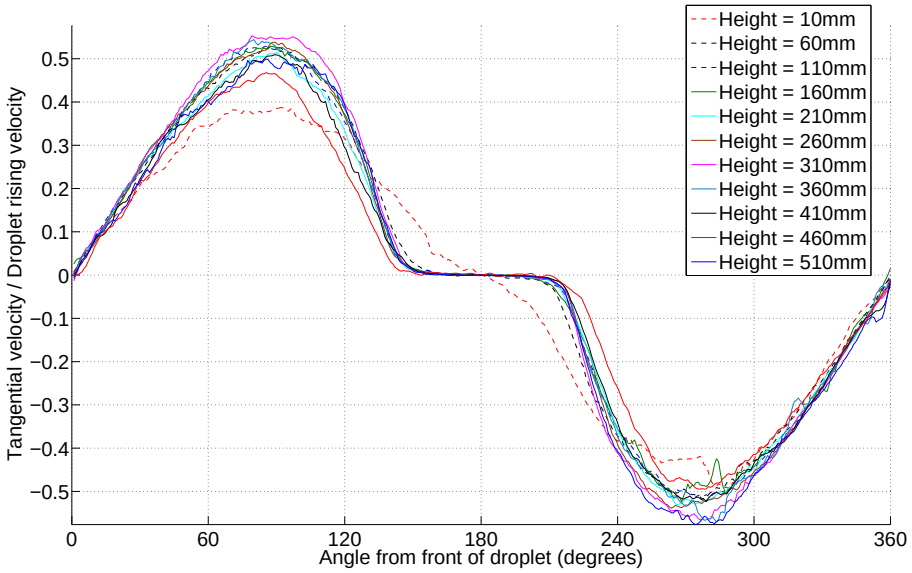

Figure G.3: Averaged tangential velocity profiles around a droplet for a Rhodamine-6G concentration of 0.04mg/l at different heights from the base of the tank.

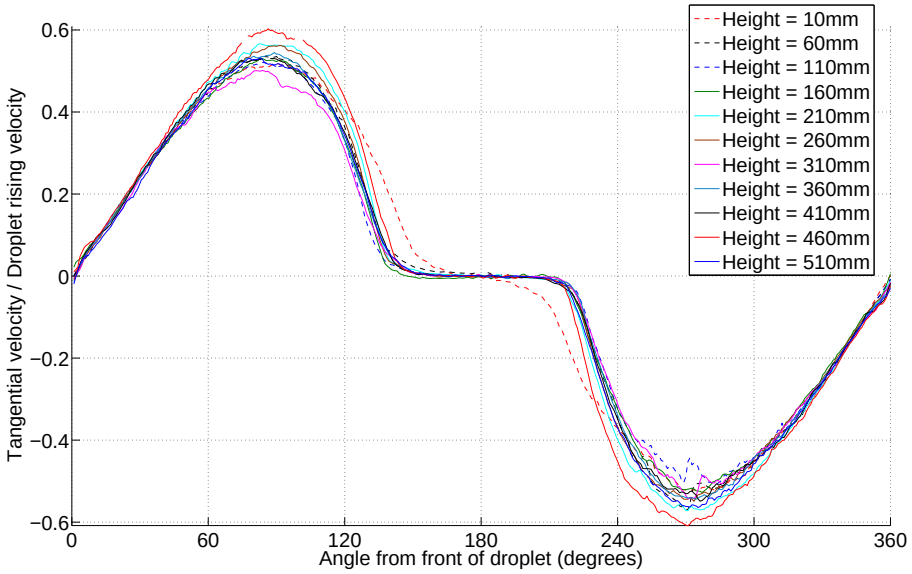

Figure G.4: Averaged tangential velocity profiles around a droplet for a Rhodamine-6G concentration of 0.05mg/l at different heights from the base of the tank.

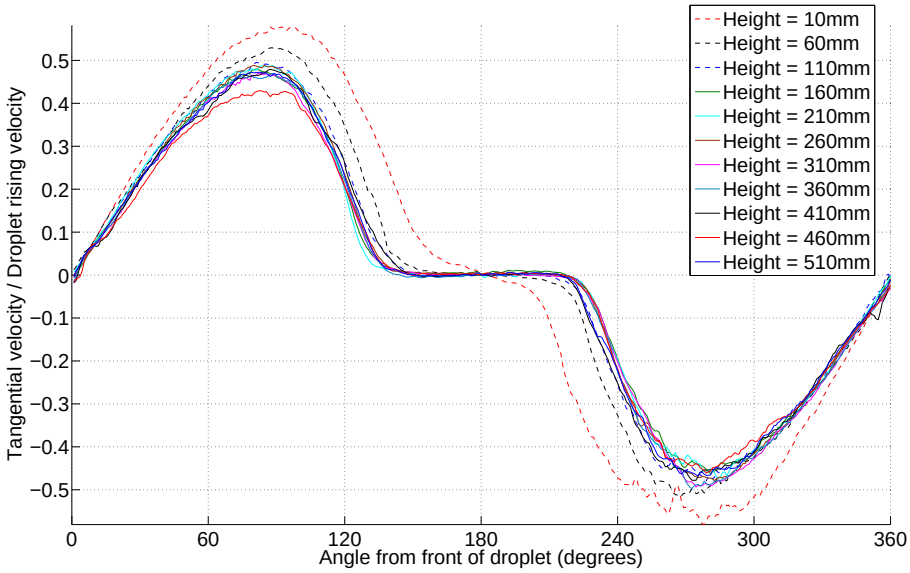

Figure G.5: Averaged tangential velocity profiles around a droplet for a Rhodamine-6G concentration of 0.06mg/l at different heights from the base of the tank.

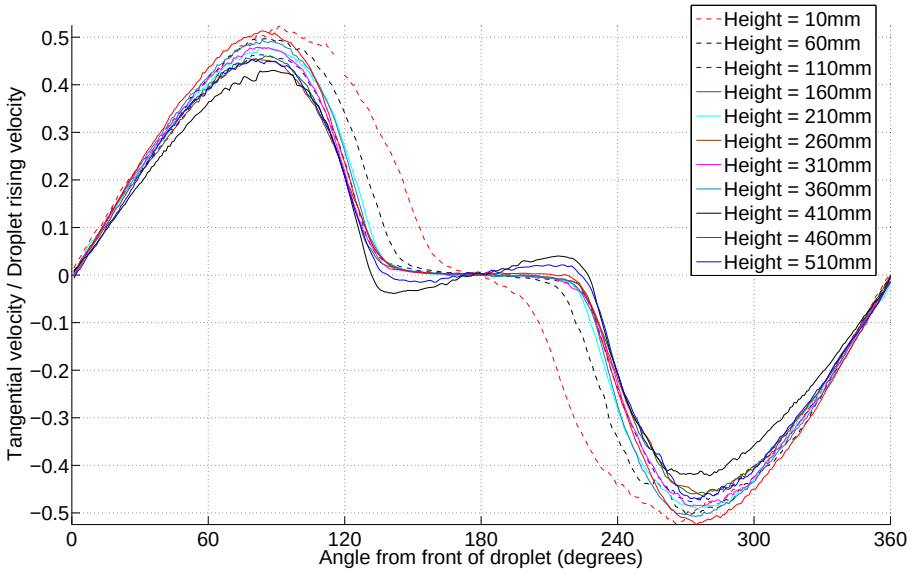

Figure G.6: Averaged tangential velocity profiles around a droplet for a Rhodamine-6G concentration of 0.08mg/l at different heights from the base of the tank.

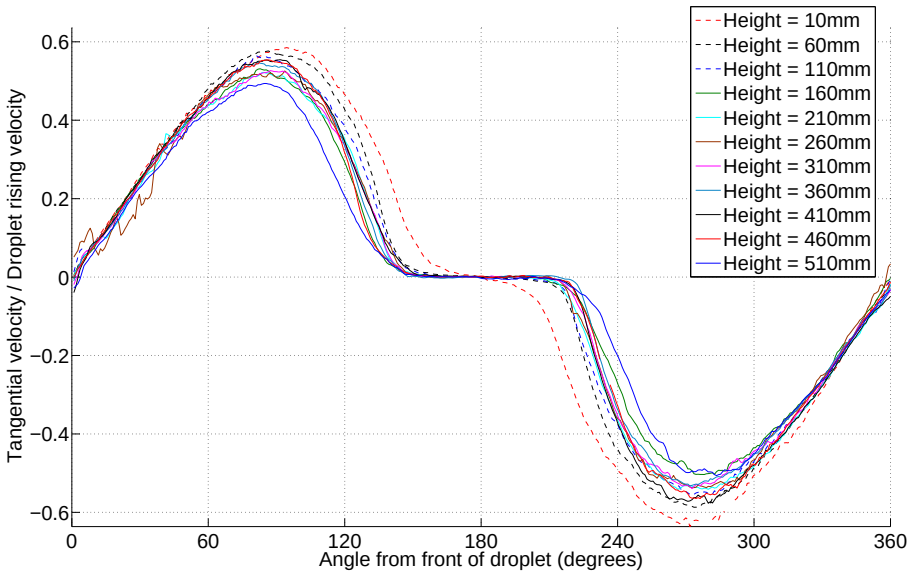

Figure G.7: Averaged tangential velocity profiles around a droplet for a Rhodamine-6G concentration of 0.10mg/l at different heights from the base of the tank.

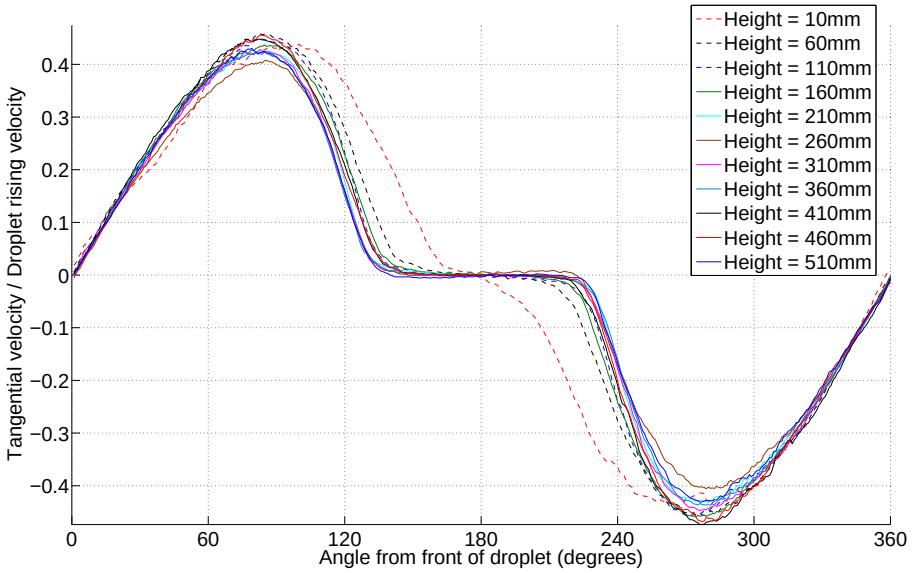

Figure G.8: Averaged tangential velocity profiles around a droplet for a Rhodamine-6G concentration of 0.20mg/l at different heights from the base of the tank.

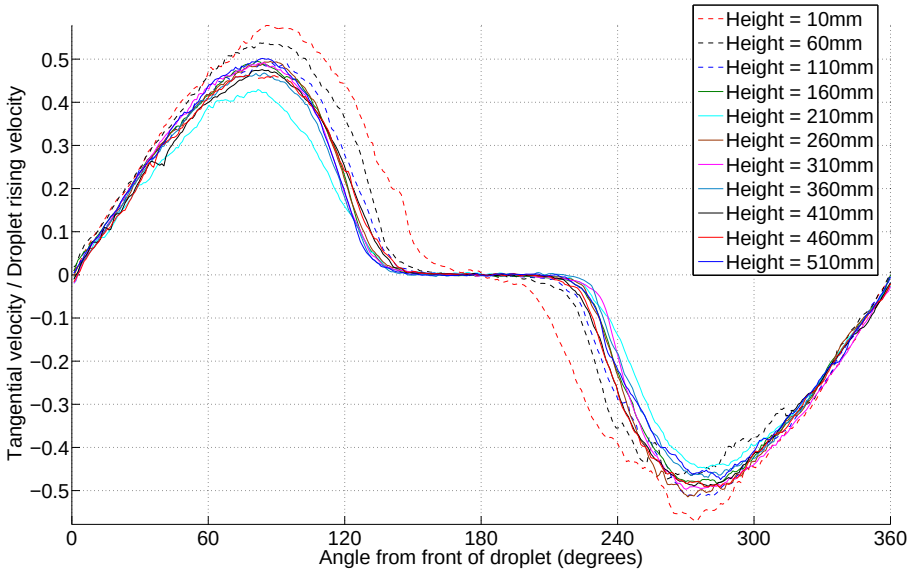

Figure G.9: Averaged tangential velocity profiles around a droplet for a Rhodamine-6G concentration of 0.30mg/l at different heights from the base of the tank.

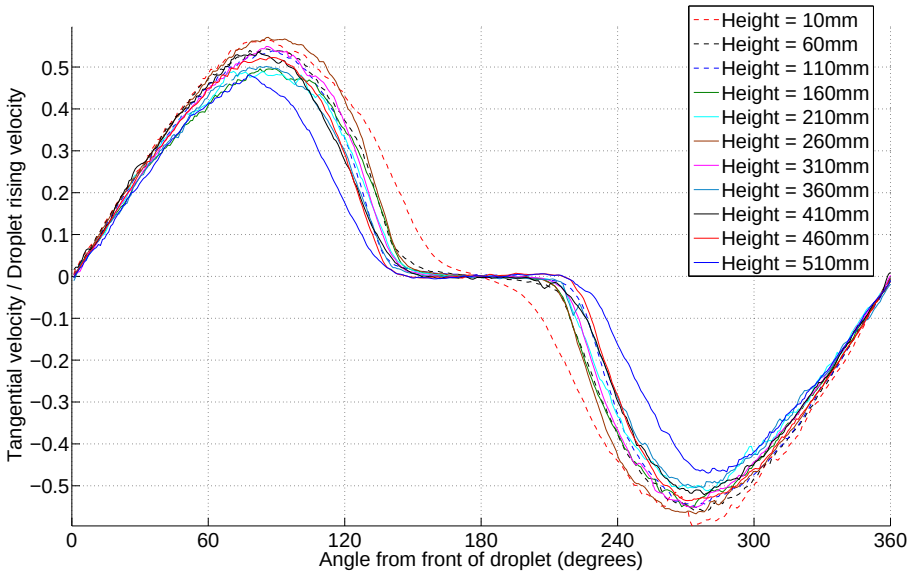

Figure G.10: Averaged tangential velocity profiles around a droplet for a Rhodamine-6G concentration of 0.40mg/l at different heights from the base of the tank.

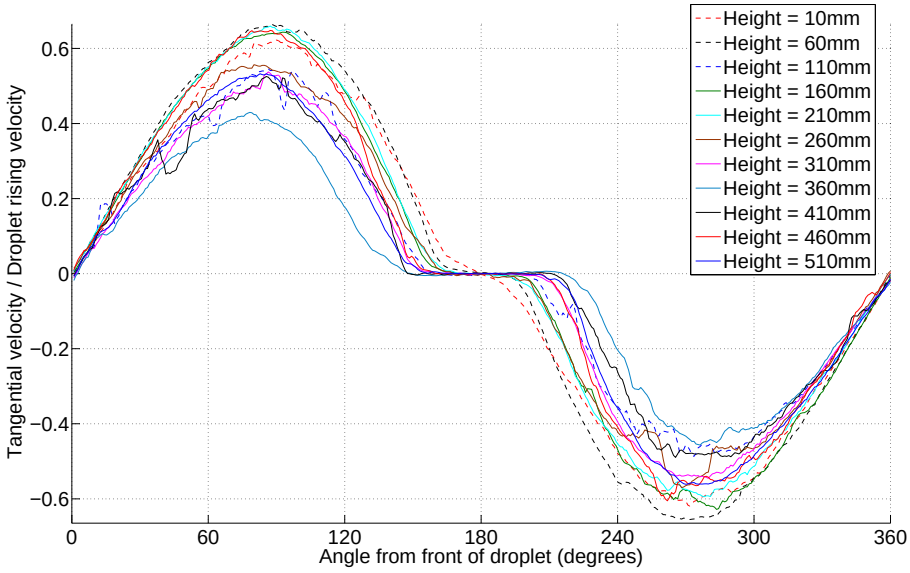

Figure G.11: Averaged tangential velocity profiles around a droplet for a Rhodamine-6G concentration of 0.50mg/l at different heights from the base of the tank.

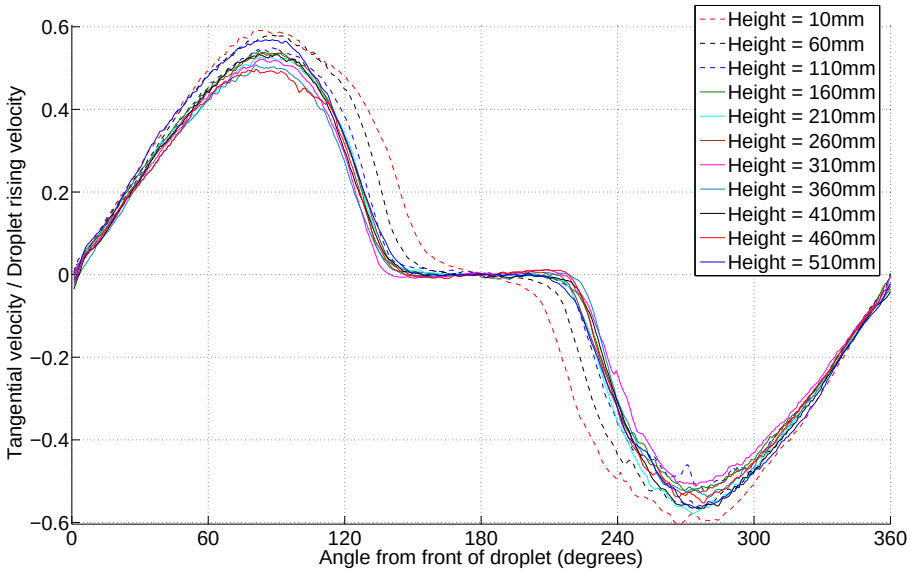

Figure G.12: Averaged tangential velocity profiles around a droplet for a Rhodamine-6G concentration of 0.60mg/l at different heights from the base of the tank.

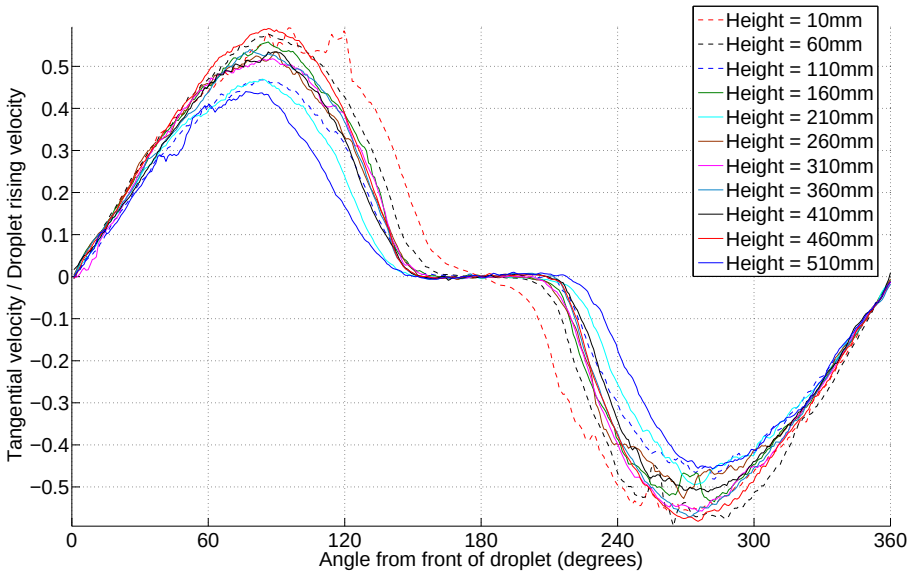

Figure G.13: Averaged tangential velocity profiles around a droplet for a Rhodamine-6G concentration of 0.80mg/l at different heights from the base of the tank.

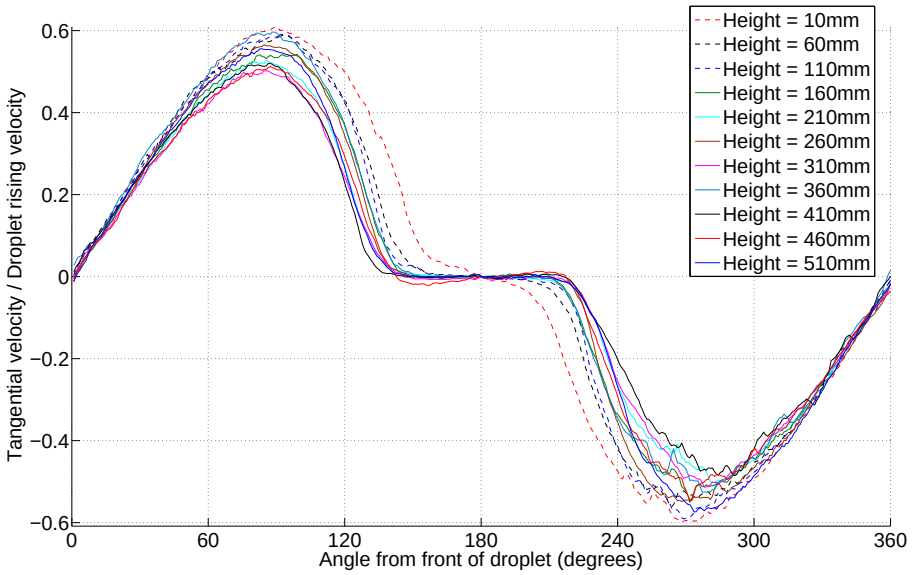

Figure G.14: Averaged tangential velocity profiles around a droplet for a Rhodamine-6G concentration of 1.00mg/l at different heights from the base of the tank.

Appendix H

Comparison of cap angles measured by LIF and PIV

Figures H.1-H.14 show the comparison between the surfactant cap angle measured by LIF and the stagnant cap angle measured by PIV for the concentrations of 0.02mg/l through to 1.00mg/l of Rhodamine-6G. For each concentration there is a comparison at each position of the tank with the LIF surfactant distribution profile given by the blue line and the tangential velocity profile given by the red line.

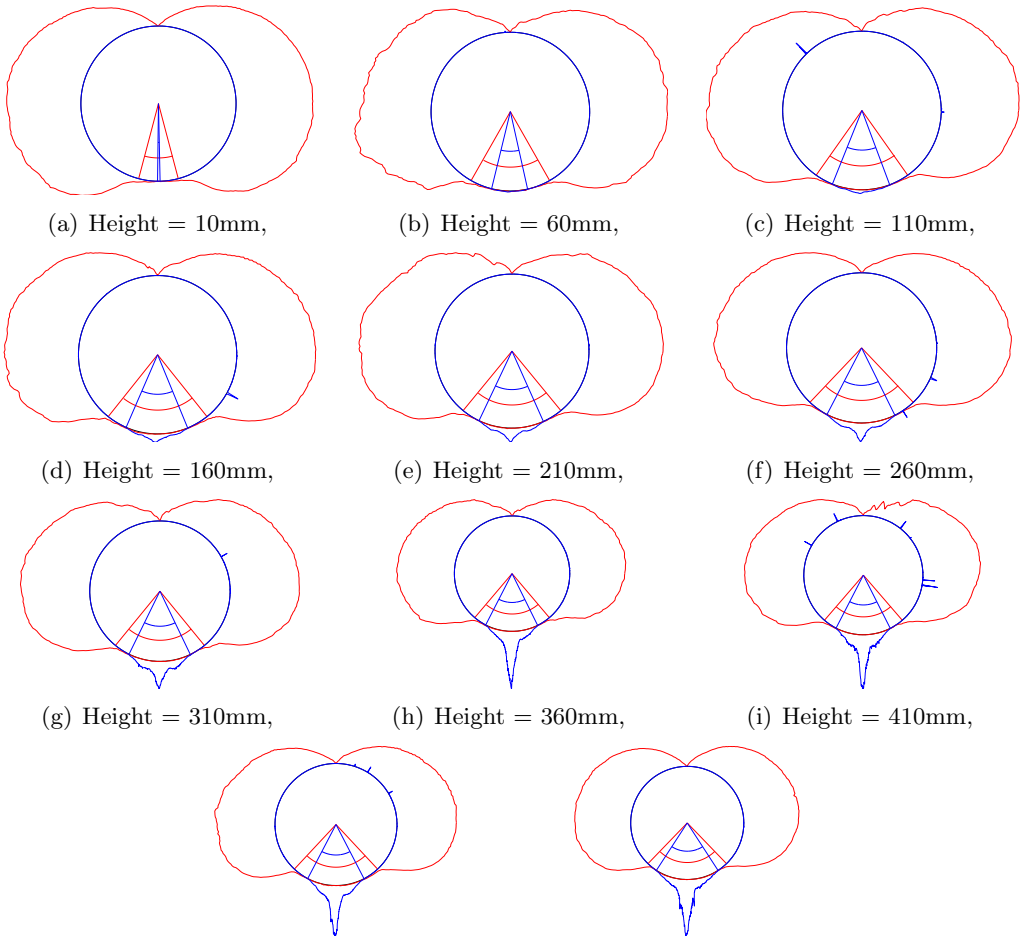

(a) Height = 10mm, (b) Height = 60mm, (c) Height = 110mm,

(d) Height = 160mm, (e) Height = 210mm, (f) Height = 260mm,

(g) Height = 310mm, (h) Height = 360mm, (i) Height = 410mm,

(j) Height = 460mm, (k) Height = 510mm.

Figure H.1: Averaged LIF surfactant distribution profile (blue) compared with the averaged PIV tangential velocity profile (red) over the height of the tank for a Rhodamine-6G concentration of 0.02mg/l.

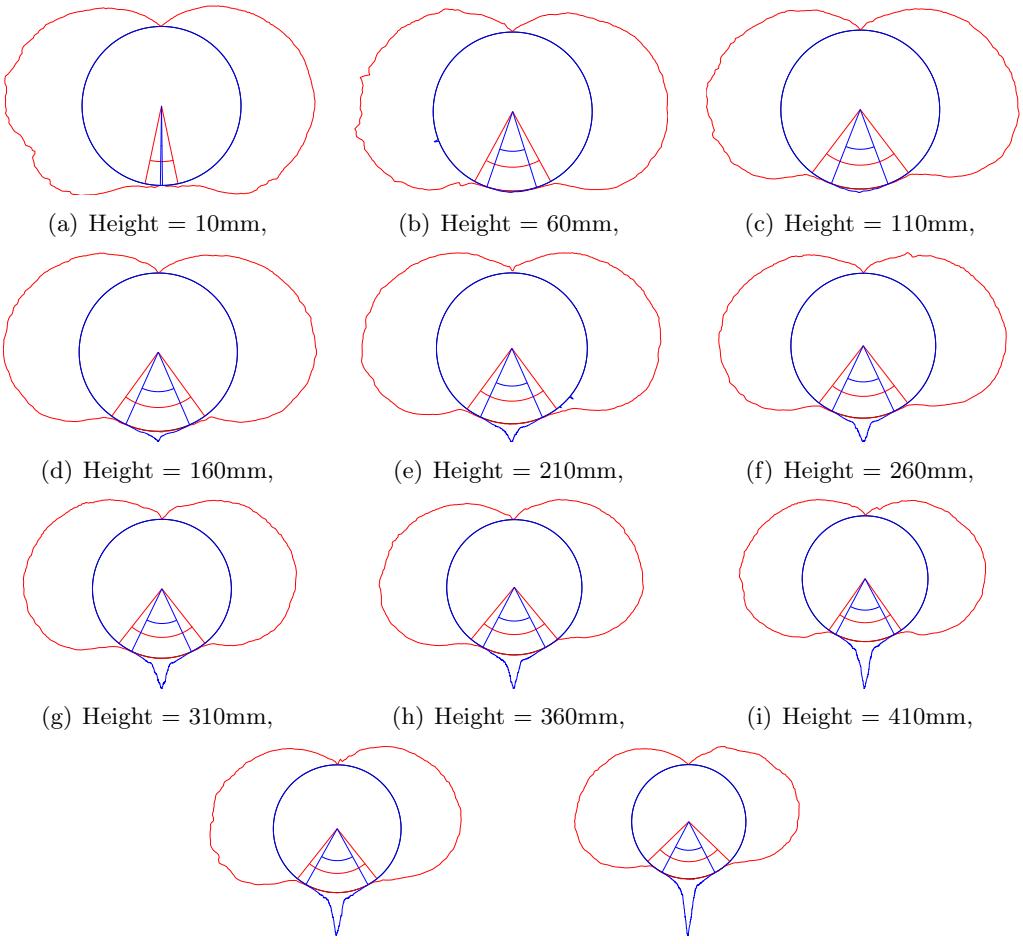

(a) Height = 10mm, (b) Height = 60mm, (c) Height = 110mm,

(d) Height = 160mm, (e) Height = 210mm, (f) Height = 260mm,

(g) Height = 310mm, (h) Height = 360mm, (i) Height = 410mm,

(j) Height = 460mm, (k) Height = 510mm.

Figure H.2: Averaged LIF surfactant distribution profile (blue) compared with the averaged PIV tangential velocity profile (red) over the height of the tank for a Rhodamine-6G concentration of 0.03mg/l.

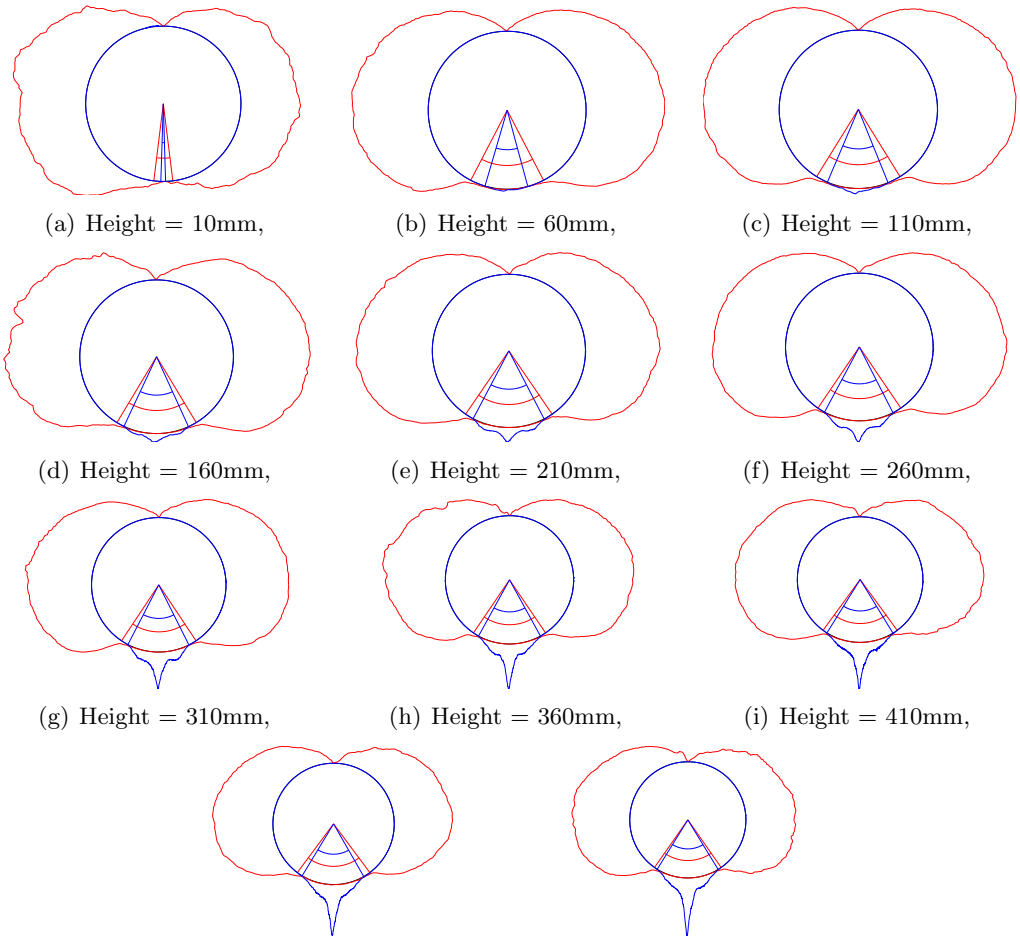

(a) Height = 10mm, (b) Height = 60mm, (c) Height = 110mm,

(d) Height = 160mm, (e) Height = 210mm, (f) Height = 260mm,

(g) Height = 310mm, (h) Height = 360mm, (i) Height = 410mm,

(j) Height = 460mm, (k) Height = 510mm.

Figure H.3: Averaged LIF surfactant distribution profile (blue) compared with the averaged PIV tangential velocity profile (red) over the height of the tank for a Rhodamine-6G concentration of 0.04mg/l.

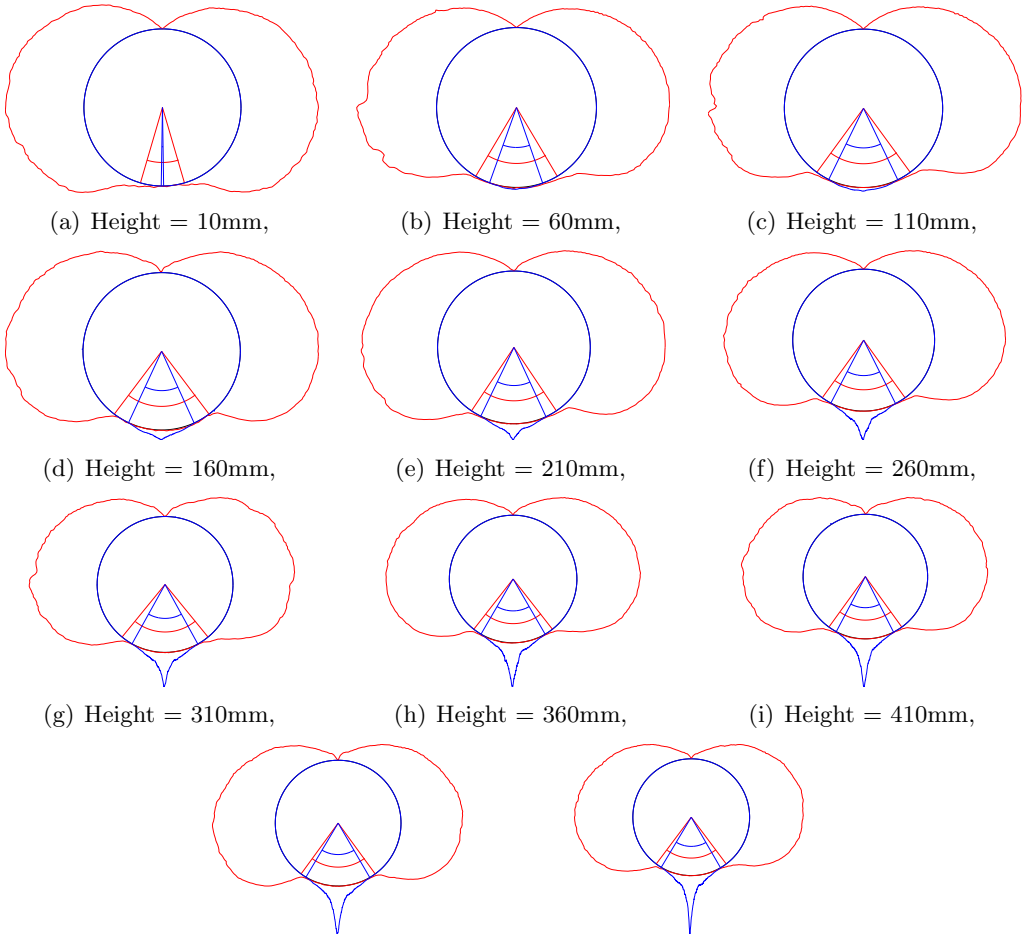

(a) Height = 10mm, (b) Height = 60mm, (c) Height = 110mm,

(d) Height = 160mm, (e) Height = 210mm, (f) Height = 260mm,

(g) Height = 310mm, (h) Height = 360mm, (i) Height = 410mm,

(j) Height = 460mm, (k) Height = 510mm.

Figure H.4: Averaged LIF surfactant distribution profile (blue) compared with the averaged PIV tangential velocity profile (red) over the height of the tank for a Rhodamine-6G concentration of 0.05mg/l.

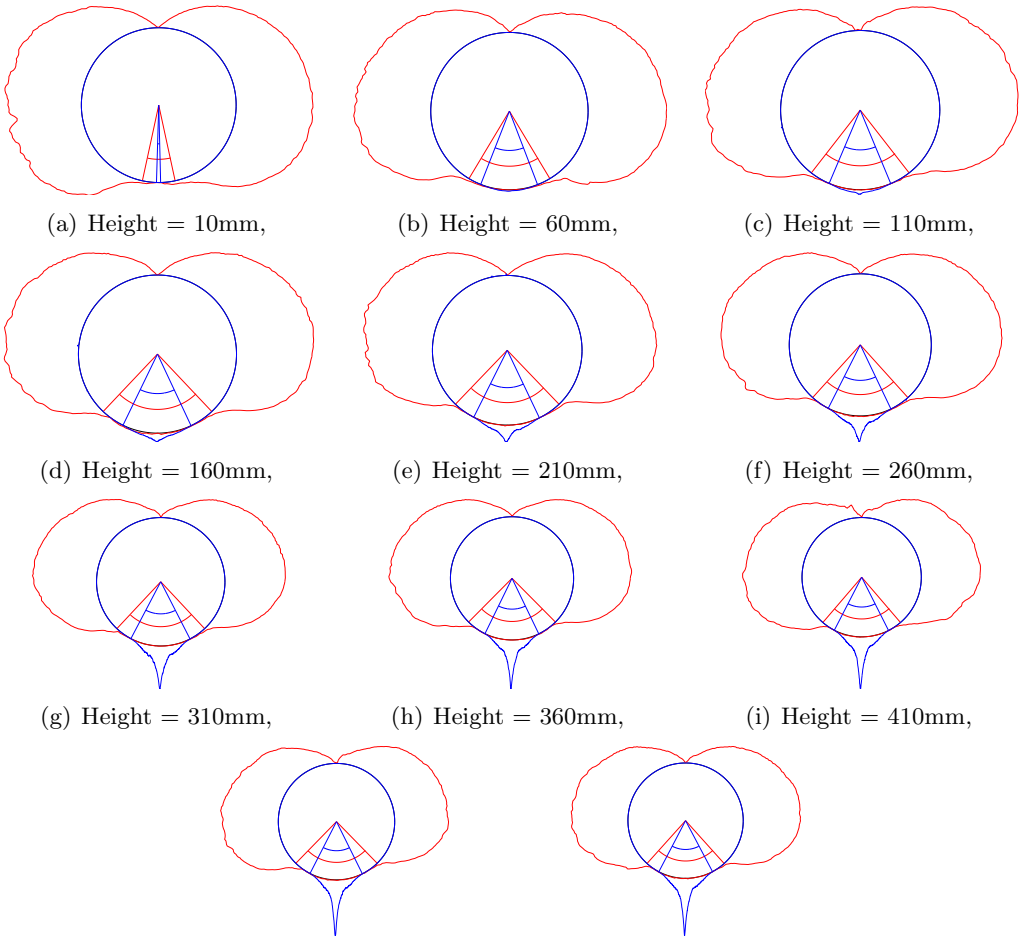

(a) Height = 10mm, (b) Height = 60mm, (c) Height = 110mm,

(d) Height = 160mm, (e) Height = 210mm, (f) Height = 260mm,

(g) Height = 310mm, (h) Height = 360mm, (i) Height = 410mm,

(j) Height = 460mm, (k) Height = 510mm.

Figure H.5: Averaged LIF surfactant distribution profile (blue) compared with the averaged PIV tangential velocity profile (red) over the height of the tank for a Rhodamine-6G concentration of 0.06mg/l.

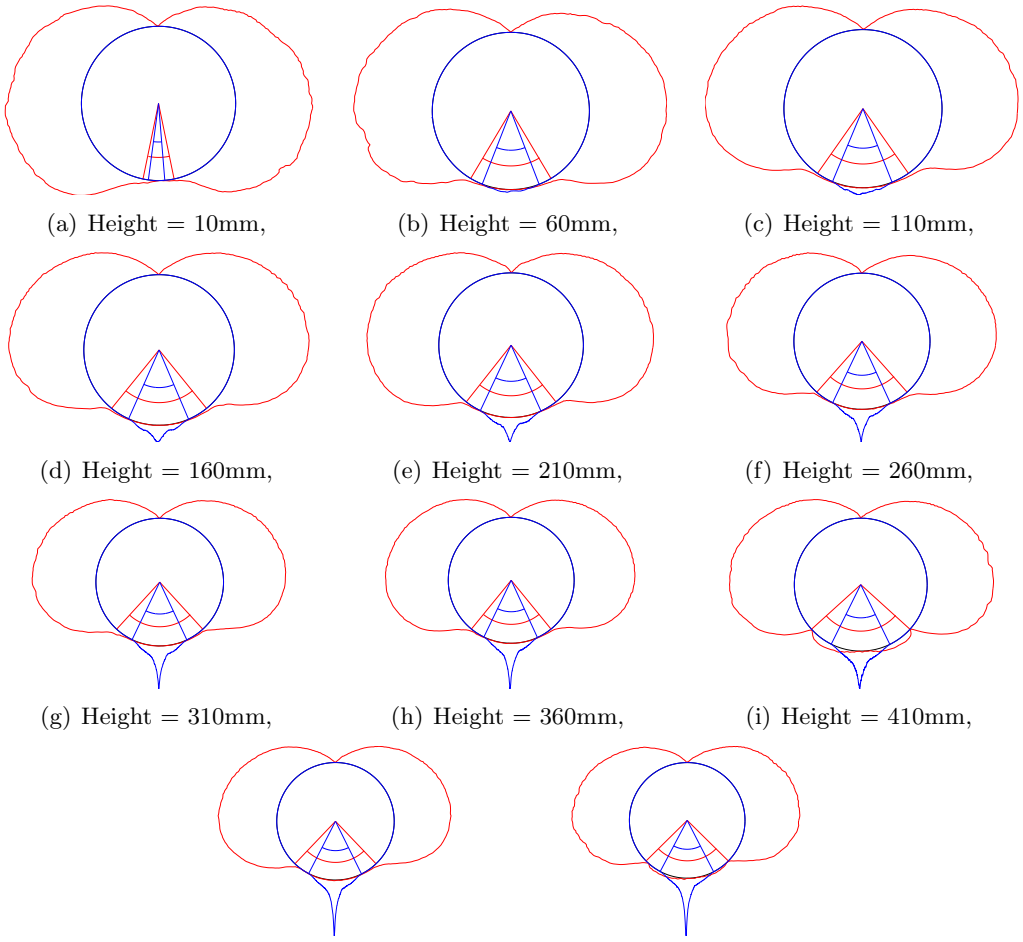

(a) Height = 10mm, (b) Height = 60mm, (c) Height = 110mm,

(d) Height = 160mm, (e) Height = 210mm, (f) Height = 260mm,

(g) Height = 310mm, (h) Height = 360mm, (i) Height = 410mm,

(j) Height = 460mm, (k) Height = 510mm.

Figure H.6: Averaged LIF surfactant distribution profile (blue) compared with the averaged PIV tangential velocity profile (red) over the height of the tank for a Rhodamine-6G concentration of 0.08mg/l.

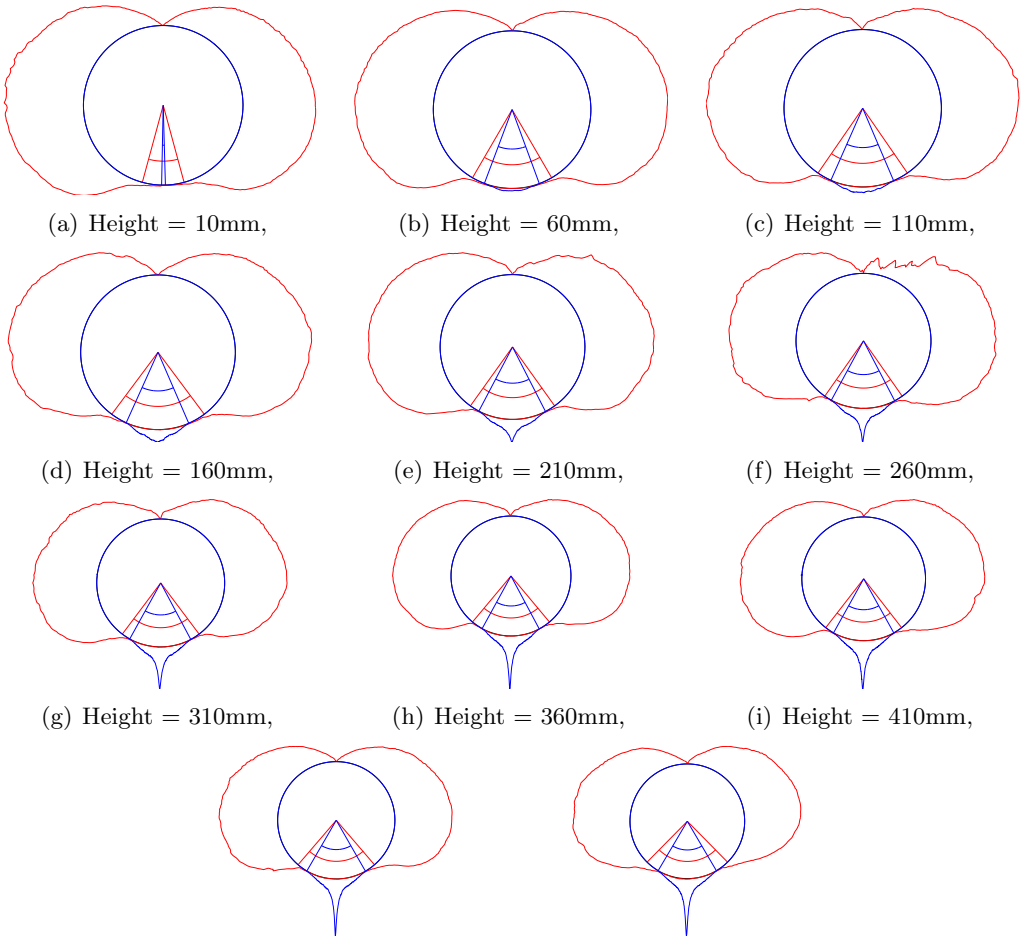

(a) Height = 10mm, (b) Height = 60mm, (c) Height = 110mm,

(d) Height = 160mm, (e) Height = 210mm, (f) Height = 260mm,

(g) Height = 310mm, (h) Height = 360mm, (i) Height = 410mm,

(j) Height = 460mm, (k) Height = 510mm.

Figure H.7: Averaged LIF surfactant distribution profile (blue) compared with the averaged PIV tangential velocity profile (red) over the height of the tank for a Rhodamine-6G concentration of 0.10mg/l.

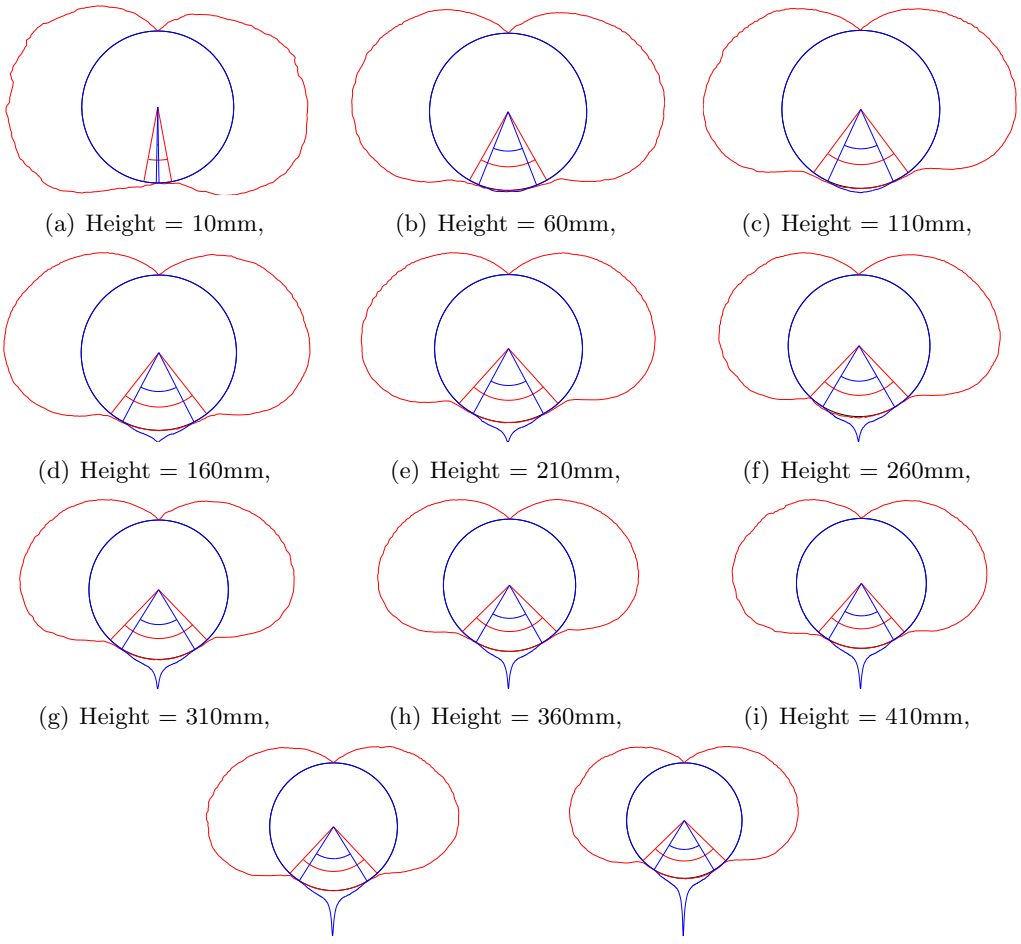

(a) Height = 10mm, (b) Height = 60mm, (c) Height = 110mm,

(d) Height = 160mm, (e) Height = 210mm, (f) Height = 260mm,

(g) Height = 310mm, (h) Height = 360mm, (i) Height = 410mm,

(j) Height = 460mm, (k) Height = 510mm.

Figure H.8: Averaged LIF surfactant distribution profile (blue) compared with the averaged PIV tangential velocity profile (red) over the height of the tank for a Rhodamine-6G concentration of 0.20mg/l.

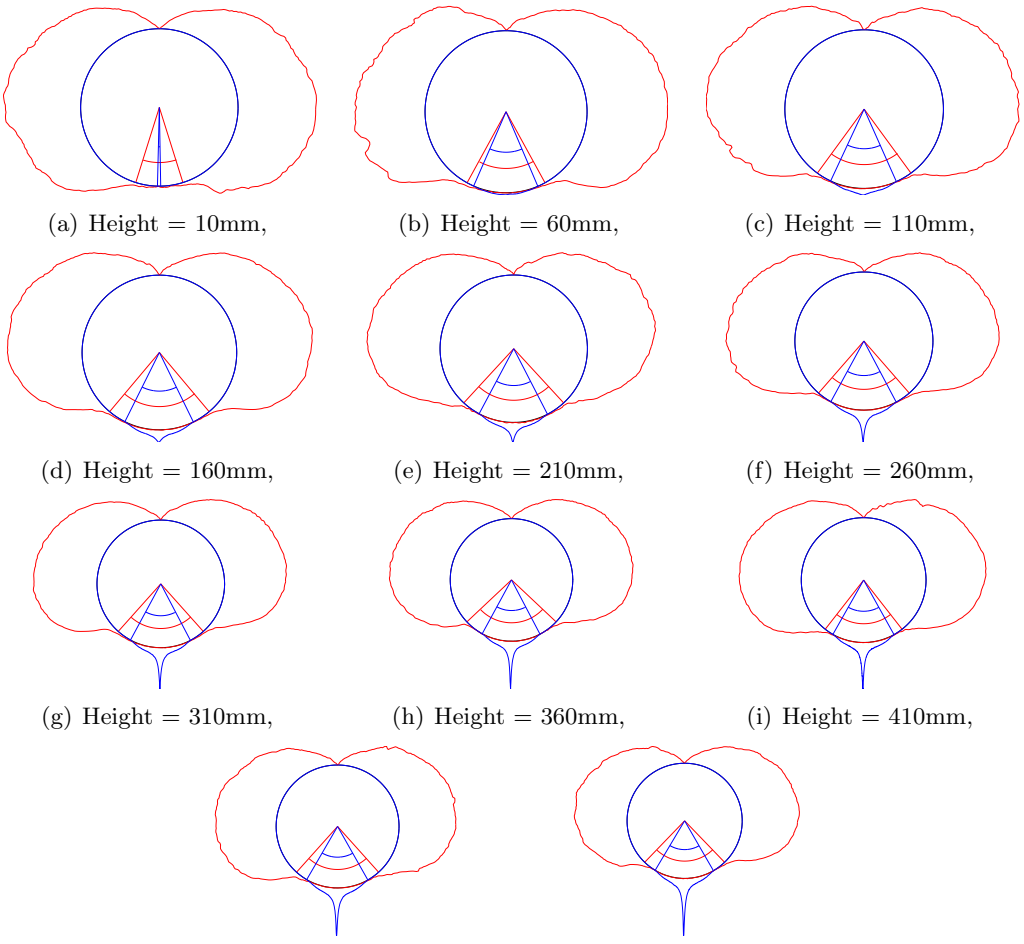

(a) Height = 10mm, (b) Height = 60mm, (c) Height = 110mm,

(d) Height = 160mm, (e) Height = 210mm, (f) Height = 260mm,

(g) Height = 310mm, (h) Height = 360mm, (i) Height = 410mm,

(j) Height = 460mm, (k) Height = 510mm.

Figure H.9: Averaged LIF surfactant distribution profile (blue) compared with the averaged PIV tangential velocity profile (red) over the height of the tank for a Rhodamine-6G concentration of 0.30mg/l.

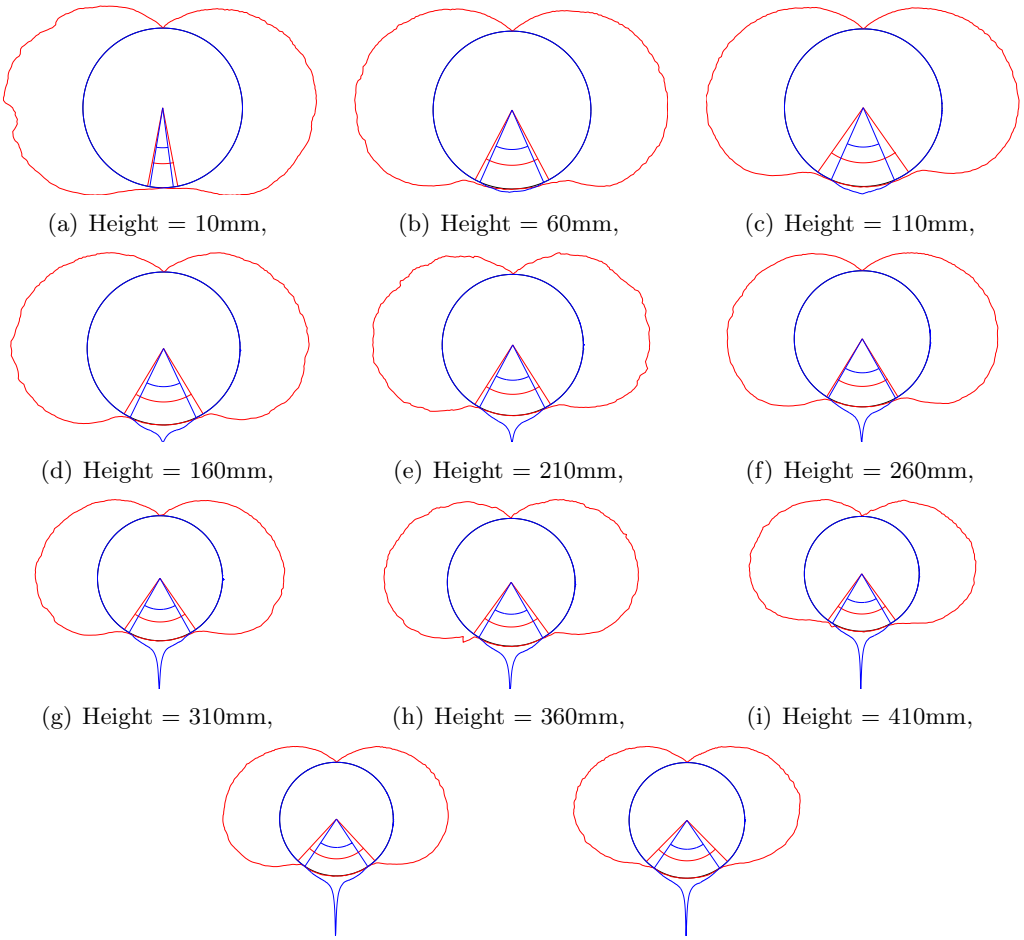

(a) Height = 10mm, (b) Height = 60mm, (c) Height = 110mm,

(d) Height = 160mm, (e) Height = 210mm, (f) Height = 260mm,

(g) Height = 310mm, (h) Height = 360mm, (i) Height = 410mm,

(j) Height = 460mm, (k) Height = 510mm.

Figure H.10: Averaged LIF surfactant distribution profile (blue) compared with the averaged PIV tangential velocity profile (red) over the height of the tank for a Rhodamine-6G concentration of 0.40mg/l.

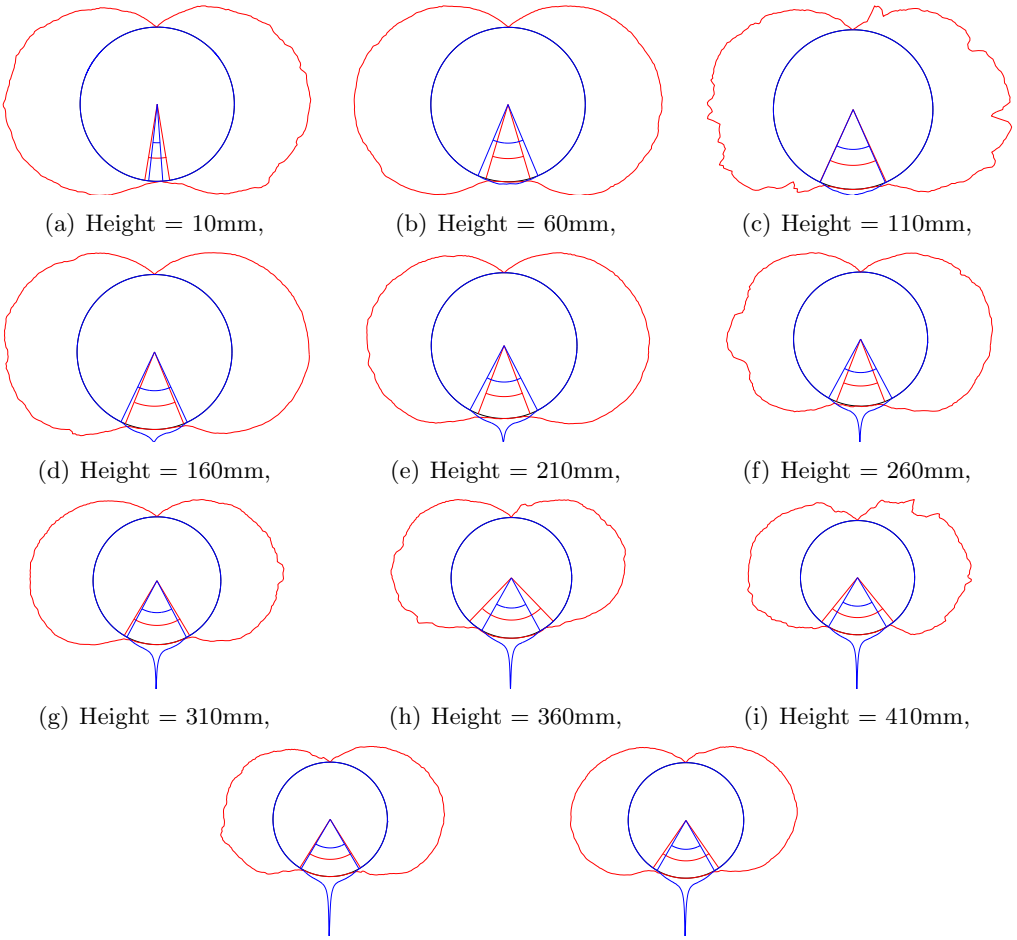

(a) Height = 10mm, (b) Height = 60mm, (c) Height = 110mm,

(d) Height = 160mm, (e) Height = 210mm, (f) Height = 260mm,

(g) Height = 310mm, (h) Height = 360mm, (i) Height = 410mm,

(j) Height = 460mm, (k) Height = 510mm.

Figure H.11: Averaged LIF surfactant distribution profile (blue) compared with the averaged PIV tangential velocity profile (red) over the height of the tank for a Rhodamine-6G concentration of 0.50mg/l.

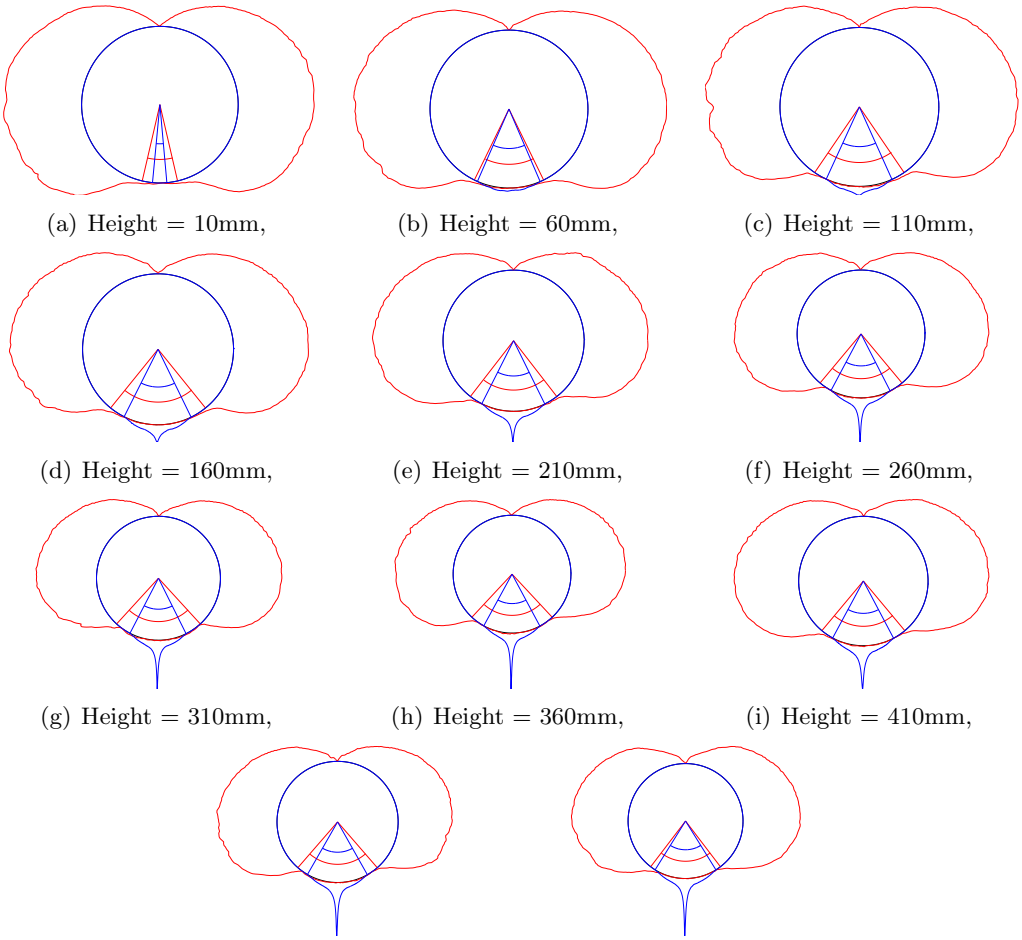

(a) Height = 10mm, (b) Height = 60mm, (c) Height = 110mm,

(d) Height = 160mm, (e) Height = 210mm, (f) Height = 260mm,

(g) Height = 310mm, (h) Height = 360mm, (i) Height = 410mm,

(j) Height = 460mm, (k) Height = 510mm.

Figure H.12: Averaged LIF surfactant distribution profile (blue) compared with the averaged PIV tangential velocity profile (red) over the height of the tank for a Rhodamine-6G concentration of 0.60mg/l.

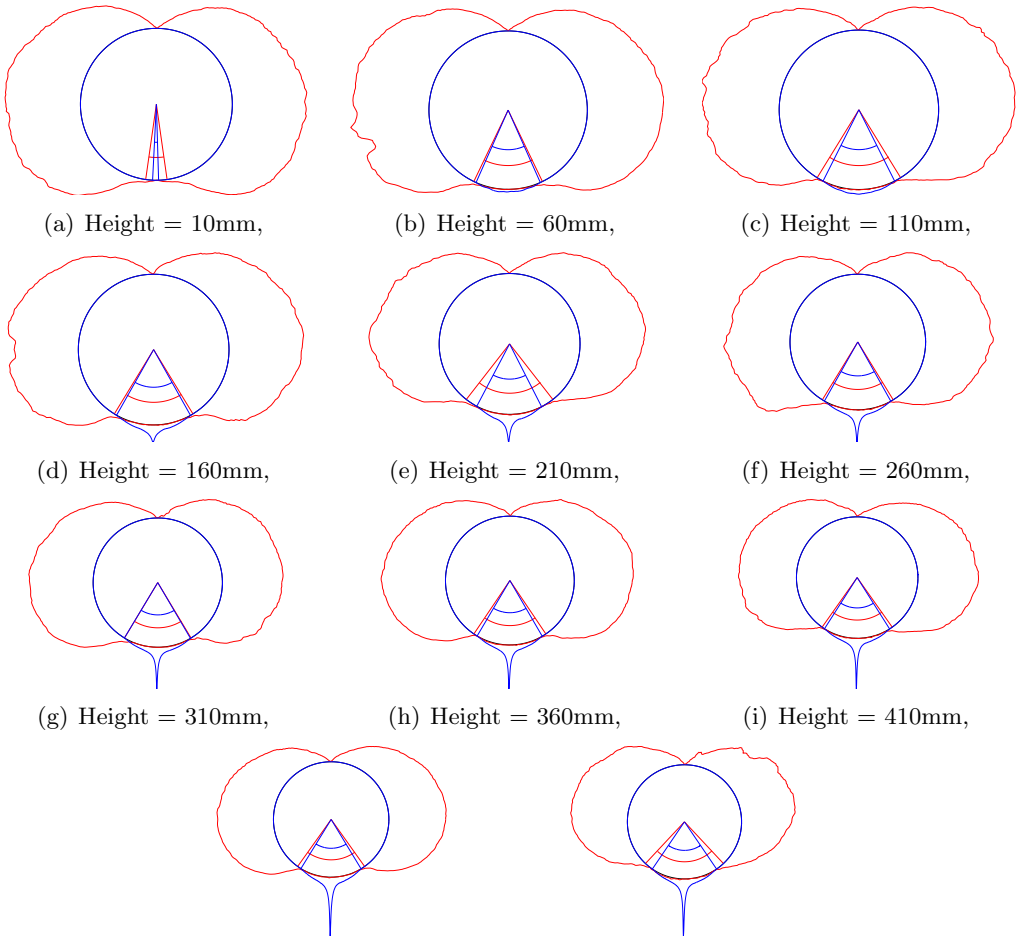

(a) Height = 10mm, (b) Height = 60mm, (c) Height = 110mm,

(d) Height = 160mm, (e) Height = 210mm, (f) Height = 260mm,

(g) Height = 310mm, (h) Height = 360mm, (i) Height = 410mm,

(j) Height = 460mm, (k) Height = 510mm.

Figure H.13: Averaged LIF surfactant distribution profile (blue) compared with the averaged PIV tangential velocity profile (red) over the height of the tank for a Rhodamine-6G concentration of 0.80mg/l.

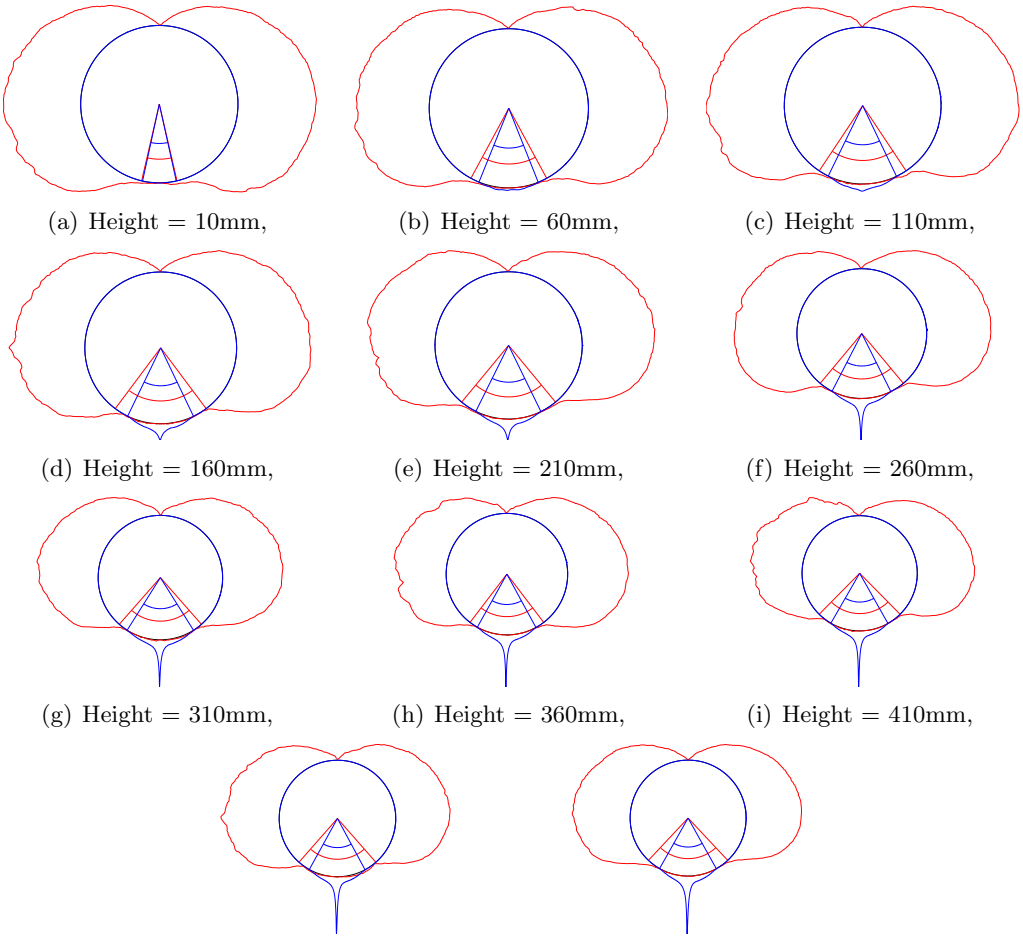

(a) Height = 10mm, (b) Height = 60mm, (c) Height = 110mm,

(d) Height = 160mm, (e) Height = 210mm, (f) Height = 260mm,

(g) Height = 310mm, (h) Height = 360mm, (i) Height = 410mm,

(j) Height = 460mm, (k) Height = 510mm.

Figure H.14: Averaged LIF surfactant distribution profile (blue) compared with the averaged PIV tangential velocity profile (red) over the height of the tank for a Rhodamine-6G concentration of 1.00mg/l.